Excitations, Two-Particle Correlations and Ordering Phenomena in Strongly Correlated Electron Systems from a Local Point of View

Vom Fachbereich Physik
der Technischen Universität Darmstadt
zur Erlangung des Grades
eines Doktors der Naturwissenschaften
(Dr. rer. nat.)
genehmigte

D i s s e r t a t i o n

von
Dipl.-Phys. Sebastian Schmitt
aus Bensheim

Referent:	Prof. Dr. N. Grewe
Korreferent:	Prof. Dr. J. Berges
Tag der Einreichung:	14.10.2008
Tag der Prüfung:	24.11.2008

Darmstadt 2008
D17

It would indeed be remarkable if nature fortified herself against further advances in knowledge behind the analytical difficulties of the many-body problem.

Max Born

Abstract

Strongly correlated electron systems show a rich variety of interesting physical phenomena. However, their theoretical description poses a highly non-trivial task, and even the simplest models cannot be solved exactly.

In this thesis the intricate behavior of the single impurity Anderson model (SIAM) and the Hubbard model is investigated. The main emphasis is laid on two-particle Green functions of these systems. To this end, existing approximation schemes are extended to be capable of treating susceptibilities as well. The quality and range of applicability of these approximations is discussed in detail.

The physical pictures behind the phenomena encountered in these systems are introduced. A prominent many-body effect is the emergence of temperature dependent low energy quasiparticles in both models. The occurrence of such excitations is a result of the dynamical screening of local magnetic moments, a characteristic feature of the Kondo effect. It is argued, that within the presented approximations, the low temperature phase of these models can usually be described as a Fermi liquid. As a counterexample, the Hubbard model is shown to exhibit pronounced non-Fermi liquid behavior in situations, where a van Hove singularity in the non-interacting density of states is found in the vicinity of the Fermi level. The magnetic properties of the Hubbard model are discussed in view of the two archetypical pictures of magnetism: local moment magnetism and itinerant Stoner-magnetism. Critical temperatures for antiferromagnetic, ferromagnetic and incommensurate phase transitions are calculated, and the influence of the lattice structure and frustration is examined. In strongly correlated metallic situations, the complicated competition between Kondo-screening and local moment magnetism can lead to a reentrant behavior of the Néel temperature. A direct signature of the Kondo effect in the Hubbard model is found in the dynamic magnetic susceptibility, where a localized collective mode emerges at very low temperatures. It is connected to the breakup of a singlet formed by the local moments with their Kondo-screening cloud, and consequently the excitation energy is of the order of the low energy scale T^*.

Zusammenfassung

Stark korrelierte Elektronensysteme zeigen eine Vielzahl interessanter physikalischer Phänomene. Ihre theoretische Beschreibung stellt aber ein höchst nicht-triviales Problem dar und selbst einfachste Modelle können nicht mehr exakt gelöst werden.

In der vorliegenden Arbeit wird das komplexe Verhalten des Ein-Störstellen Anderson Modells (SIAM) und des Hubbard Modells untersucht. Das Hauptaugenmerk ist auf die Berechnung von Zweiteilchen-Greenfunktionen gelegt. Aus diesem Grund werden schon existierende Näherungsverfahren auf die Berechnung von Zweiteilchengrößen erweitert. Die Qualität und der Anwendungsbereich dieser Näherungen werden im Detail diskutiert.

Es werden die physikalischen Bilder eingeführt, die hinter den in den untersuchten Systemen gefundenen Phänomenen stehen. Ein prominenter Vielteilcheneffekt ist das Entstehen von temperaturabhängigen Niederenergie-Quasiteilchen in beiden Modellen. Das Auftreten solcher Anregungen ist das Resultat dynamischer Abschirmung lokaler magnetischer Momente und repräsentiert eine charakteristische Eigenschaft des Kondo-Effekts. Es wird argumentiert, daß die Tieftemperaturphase in den vorgestellten Näherungen meistens durch einen Fermiflüssigkeitszustand beschrieben werden kann. Als ein Gegenbeispiel hierzu wird gezeigt, daß das Hubbard Modell ausgeprägtes Nicht-Fermiflüssigkeitsverhalten an den Tag legt, sofern eine van Hove Singularität in der nichtwechselwirkenden Zustandsdichte nahe der Fermikante auftritt. Die magnetischen Eigenschaften des Hubbard Modells werden unter Berücksichtigung der beiden prototypischen Bilder des Magnetismus diskutiert: Magnetismus lokalisierter Momente und itineranter Stoner-Magnetismus. Es werden kritische Temperaturen für antiferromagntische, ferromagnetische und inkommensurable Phasenübergänge berechnet und der Einfluß der Gitterstruktur und Frustrationen untersucht. In stark korrelierten metallischen Situationen kann der komplizierte Wettbewerb zwischen Kondo-Abschirmung und lokalem Moment-Magnetismus zu einem Wiedereintrittsverhalten der Néel-Temperatur führen. Eine direkte Signatur des Kondo-Effekts im Hubbard Modell wird in der dynamischen magnetischen Suszeptibilität gefunden, in der bei sehr tiefen Temperaturen eine lokalisierte kollektive Mode auftritt. Diese ist mit dem Aufbrechen eines Singulett-Zustands zwischen einem lokalen Moment und der Kondo-Abschirmwolke verbunden und daher ist die Anregungsenergie von der Größenordung der Tieftemperaturskala T^*.

Contents

1 Introduction

The field of strong correlations in electronic and spin systems constitutes a major area of modern solid state research. Amongst the physical phenomena encountered in such systems are mixed valence and heavy fermion behavior, quantum criticality, superconductivity, in particular heavy fermion and high-temperature superconductivity, the quantum Hall effect, Wigner crystals, colossal magnetoresistance, magnetism and Mott-Hubbard metal-insulator transitions. Especially the microscopic description of magnetism is one of the longstanding problems in solid state theory. Along with the description of itinerant ferromagnetism like in iron or the spin density wave state of chromium, the transmutation of the two archetypical pictures underlying the understanding of magnetism is of interest: on the one side the picture of weakly interacting itinerant electrons bearing the notion of Stoner- or band-magnetism and on the other side the picture of localized spins interacting via effective exchange interactions, best described with Heisenberg-type models.

Strongly correlated systems usually involve atoms with partially filled d- or f-shells as they are found in transition-metals, rare-earth elements and actinides. When embedded into a crystalline environment, the valence d- or f-orbitals are still quite localized, which leads to narrow valence bands. Taking crystal field effects into account, the valence states are split up in energy and usually one is left with only a small number of $\sim 1-3$ relevant bands in the vicinity of the Fermi level. Therefore it is usually sufficient to consider single-band, two-band or at most three-band models for the theoretical description. Due to the localized nature of the relevant valence states it is clear, that the Coulomb interaction within the localized shells plays a major role for the properties of those materials.

In situations, where the Coulomb interaction is assumed to be the largest scale in the system, a theoretical treatment becomes complicated. Conventional theories start by describing the system in the non-interacting limit. The interaction is then included and treated perturbatively. Such an approach clearly fails if the interaction matrix elements are larger than the other matrix elements involved, because higher order terms dominate the expansion and must not be omitted. One could argue that utilizing some skeleton expansion, i.e. choosing certain classes of perturbative contributions and summing these in a self-consistent manner up to infinite order, might remedy this breakdown. But in general this is still not sufficient as it just extends the region of validity of the generated approximation and does not lead to an accurate description of the fully interacting system.

The physical reason of the failure of usual perturbation theory for correlated systems lies in the unfavorable starting point for the description. By choosing the non-interacting system, the basic degrees of freedom, i.e. itinerant infinitely long-lived electrons, are too far away from the actual interacting degrees of freedom which determine the behavior of the system. The actual physical degrees of freedom might for example consist of strongly localized correlated electronic excitations with finite lifetimes, which behave a lot more like spins than electrons. Consequently, trying to describe these by some linear combination of itinerant electrons is very disadvantageous and might lead to serious difficulties.

More technically speaking, choosing Bloch functions as the one-particle basis in order to build up Fock space is disadvantageous when trying to describe rather localized excitations. This is one of the reasons why conventional density functional theory (DFT) fails in strongly correlated systems. Another reason for the failure of DFT, shared by all other one-particle approaches, lies in this very fact of using a one-particle basis. The effective states occuring in the Kohn-Sham equations, for example, are those of well-defined electronic particles with an infinite lifetime and a definite energy. In realistic situations the relevant excitations are not infinitely long-lived and might not even resemble particles at all.

This already hints at the fact, that localized basis states should be more appropriate to build up Fock-space instead of itinerant Bloch-states. The most prominent localized basis set are the so-called Wannier states, where each state is chosen to resemble an atomic orbital at some lattice site, but they are mutually orthogonalized and thus form an orthonormal basis set for the lattice.

This thesis is organized as follows:

In chapter 2 the basics of a cumulant perturbation theory capable of describing strong interactions is reviewed. The strict formal reasoning is mostly discarded and only those points necessary to understand the essentials of the *locally complete approximation* are presented. The diagrams included in this approximation are characterized, and a special emphasis is laid on the mapping of the lattice model onto an effective impurity model embedded in a self-consistently determined medium. This effective physical picture is then extended to an approximation for the two-particle properties of the lattice system and a set of coupled Bethe-Salpeter equations is derived. A simple decoupling scheme is employed to yield a very intuitive but non-trivial approximation for lattice susceptibilities. Aspects concerning the physical content and the quality of this approximative form are discussed.

Chapter 3 deals with the approximative solution of the single Anderson impurity model (SIAM), an essential step in the self-consistent mapping of the lattice model. An existing approximation within the direct perturbation theory, the *extended non-crossing approximation* (ENCA), is extended to provide charge and magnetic susceptibilities. The numerical and especially the physical merits and shortcomings are discussed in detail.

The approximations developed in previous chapters are then applied to the Hubbard model, the simplest model for correlated electrons on a crystal lattice, in chapter 4. One- and two-particle Green functions are calculated and the physical pictures necessary to understand the results are introduced. One major point is the question whether the low temperature phase of the model is a realization of a Fermi liquid state or not. The second major topic concerns the magnetic properties of the model. Therefore static and dynamic susceptibilities are calculated and critical temperatures for magnetic phase transition derived.

This thesis is concluded by a summary and an outlook in chapter 5.

Throughout this work natural units will be used, i.e. $\hbar = c = k_B = 1$. To further enhance the readability, the lattice constant a of all lattices is taken to be unity as well, $a = 1$.

2 Formal development

In this chapter the perturbation theory with respect to the hopping matrix elements is shortly introduced. It is indicated how the use of local cumulant averages circumvents the excluded volume problem and makes the reformulation of this expansion as a Feynman-like perturbation theory possible.

The usefulness of the cumulant averages in physics was already recognized by Kubo [Kub62]. General introductions can be found in [Kla98] and [Ful91, Appendix]. First ideas of their use in the field of strongly correlated electron system was already proposed by Hubbard himself [Hub64b] and later on made more explicit by [Kur85b, Gre87, Vak90, Vla90, Met91, Coj93, Cit97, Mos97a, Mos97b, Mos98, She05, She06].

In the first part 2.1 of this chapter the general setup of a perturbation expansion involving local cumulant averages is outlined. The focus is on those aspects necessary to understand the approximations made in the following sections. For more details and some examples refer to appendix A. In sections 2.2 and 2.3 the *locally complete approximation* for the one- and two-particle quantities of lattice systems is constructed. The explicit reasoning concerning the algebraic structure of this theory is given in the original document [Gre96].

This theory represents the matrix generalization of the *dynamical mean field theory* (DMFT) [Geo96], but due to the derivations in terms of a diagrammatic expansion, all contributing diagrams are specified and extensions such as non-local correlation effects can be formulated.

Within this work, the term "locally complete approximation" will be exclusively used, while in the literature this approximation is usually denoted by DMFT.

2.1 Cumulant expansion

Crystal lattices consist of sites amongst which electrons are transfered, thereby introducing valence fluctuations to the ions at theses sites. Usually most of the electrons are tightly bound to the nucleus, forming an inert core not excitable on the relevant energy scale. Only the few outermost shell electrons are loosely bound and can be excited and therefore they dominate the electronic properties of the ion embedded in the lattice. Due to the charging energy [Hub64a] of the ion, there are commonly only three valence states for the ion possible which have n_0, $n_0 + 1$ and $n_0 + 2$ electrons, where n_0 is the number of electrons in the core.

Choosing the state with only n_0 core electrons at a site to be the local vacuum state, the localized valence states with a few additional electrons can be accurately modelled with the help of Wannier functions. Wannier functions resemble atomic orbitals and are characterized by a lattice index i, indicating the spacial position at which the function is localized, and a set of orbital quantum numbers α, representing spin and angular momentum. By construction, the Wannier states form an orthonormal basis of the one-particle

Hilbert space for the complete lattice and, as mentioned above, are used to build up Fock space by orthonormalizing the wave functions of the valence states on different lattice sites. The Wannier basis can be viewed as being complementary to the Bloch basis, which constitutes an alternative one-particle basis set of itinerant electronic states spread over the whole crystal volume.

Generally the Hamiltonian in the Wannier representation can be written as a sum of terms $\hat{h}_i$, acting on a specific lattice site i, terms $\hat{T}_{ij}$ connecting sites i and j via the one-particle transfer and all sorts of interaction terms between lattice sites $\Delta\hat{V}$,

$$\hat{H} = \hat{H}_0 + \hat{T} + \Delta\hat{V} \tag{2.1.1}$$

$$\begin{aligned} \hat{H}_0 &= \sum_i \hat{h}_i \\ \hat{T} &= \sum_{i,j} \hat{T}_{ij} \quad . \end{aligned}$$

According to the general reasoning in the introduction, the local Coulomb matrix elements included into $\hat{h}_i$ should be dominant for the situations and materials considered here. Since calculations from first principles will not be made in this work and effective model Hamiltonians will exclusively be considered later on, the term $\Delta\hat{V}$ is thought to be included in a mean-field manner into $\hat{h}_i$ and $\hat{T}_{ij}$. Therefore $\Delta\hat{V}$ will be subsequently neglected.

The isolated local part of the Hamiltonian can generally be written as

$$\hat{h}_i = \sum_{\alpha,\beta} \epsilon_{\alpha\beta}\, \hat{c}^\dagger_{i,\alpha}\hat{c}_{i,\beta} + \sum_{\alpha,\beta,\gamma,\delta} U_{\alpha\beta\gamma\delta}\, \hat{c}^\dagger_{i,\alpha}\hat{c}^\dagger_{i,\beta}\hat{c}_{i,\delta}\hat{c}_{i,\gamma} \quad , \tag{2.1.2}$$

where $\hat{c}^\dagger_{i,\alpha}$ ($\hat{c}_{i,\alpha}$) is the creation (annihilation) operator for an electron in a Wannier state at site i and orbital quantum number α. The $\epsilon_{\alpha\beta}$ are the single-particle matrix elements of $\hat{H}_0$ and the $U_{\alpha\beta\gamma\delta}$ are the afore mentioned local Coulomb interaction matrix elements for Wannier states with orbital quantum numbers α, β, γ and δ.

The local problem characterized by $\hat{h}_i$ is in principle exactly solvable, if the set of local quantum numbers characterized by α, β, γ, δ is taken to be finite. The resulting diagonal Hamiltonian has the form

$$\hat{h}_i = \sum_M E_M\, \hat{X}^{(i)}_{MM} \quad . \tag{2.1.3}$$

The E_M are the eigenvalues to the eigenstates $|i, M\rangle$, which apart from the lattice site i, are characterized by the many-body quantum numbers M. The quantum numbers represented through M are the number of electrons (valence), orbital quantum numbers and spin or angular momentum. The introduced operators $\hat{X}^{(i)}_{MM} = |i, M\rangle\langle i, M|$ are projection operators onto the many-body eigenstates and are specializations of the more general ionic transfer operators, or Hubbard's X-operators [Hub65],

$$\hat{X}^{(i)}_{MM'} = |i, M\rangle\langle i, M'| \quad . \tag{2.1.4}$$

This operator transfers the ionic many-body state M' into M at a given lattice site i. The two equivalent forms of the local ionic Hamiltonian (2.1.3) and (2.1.2) imply a transformation between the ionic transfer operators and the annihilation operators,

$$\hat{c}_{i,\alpha} = \sum_{MM'} a_{\alpha}^{MM'} \hat{X}_{MM'}^{(i)} \tag{2.1.5}$$

and the analog for the creation operators $\hat{c}_{i,\alpha}^{\dagger}$. The ionic states labeled with the quantum numbers M in (2.1.5) must have one electron less than the ones labeled with M'.

The ionic transfer operators and their relation to the creation and annihilation operators are introduced here because they prove to be very useful in order to describe the local dynamics and will be frequently used later on.

From the local point of view, the natural starting point for a perturbation theory is the atomic limit. Thus, the local problem described by $\hat{H}_0 = \sum_i \hat{h}_i$ is considered to be solved and the one-body transfer term in (2.1.1) $\hat{T} = \sum_{i,j} \hat{T}_{ij}$ constitutes the perturbation. Within second quantization this transfer operator reads

$$\hat{T} = \sum_{i,j;\alpha\beta} t_{ij}^{\alpha\beta} \hat{c}_{i,\alpha}^{\dagger} \hat{c}_{j,\beta} \quad . \tag{2.1.6}$$

The matrix elements $t_{ij}^{\alpha\beta}$ contain all the information on the lattice structure, the geometry of the possible electron hoppings in the lattice and the different hybridization processes between orbitals at different sites.

The goal is to calculate time-ordered thermodynamic expectation values

$$\langle \mathcal{T}\left[\hat{A}_{1,H}(\tau_1) \cdot \ldots \cdot \hat{A}_{n,H}(\tau_n)\right]\rangle = \frac{1}{Z} Tr\left(e^{-\beta\hat{H}} \mathcal{T}\left[\hat{A}_{1,H}(\tau_1) \ldots \hat{A}_{n,H}(\tau_n)\right]\right) \quad , \tag{2.1.7}$$

where the operators $\hat{A}_{n,H}$ are taken to be in the imaginary time Heisenberg picture

$$\hat{A}_{n,H}(\tau_n) = e^{\tau_n \hat{H}} \hat{A}_n e^{-\tau_n \hat{H}} \quad , \tag{2.1.8}$$

which is also frequently called thermodynamic Heisenberg picture. $\beta = \frac{1}{T}$ is the inverse temperature T and the imaginary times take values out of the interval $-\beta \leq \tau_n \leq \beta$. The trace Tr occuring in (2.1.7) has to be taken over all many-body states in Fock space. Z is the partition function of the system,

$$Z = Tr\left(e^{-\beta\hat{H}}\right) \quad . \tag{2.1.9}$$

The time-ordering operator $\mathcal{T}$ in (2.1.7) organizes the operators $\hat{A}_{n,H}(\tau_n)$ according to their imaginary time arguments in a descending manner from left to right. For a given set of times $\tau_1, \ldots \tau_n$, every permutation of two fermionic operators necessary to achieve this order produces a minus sign, due to their anticommutation relations.

Transforming all operators into the interaction picture,

$$\hat{A}_{n,I}(\tau_n) = e^{\tau_n \hat{H}_0} \hat{A}_n e^{-\tau_n \hat{H}_0} \tag{2.1.10}$$

and expanding the exponential in (2.1.7), the perturbation series is obtained as

$$\langle \mathcal{T}\big[\hat{A}_1(\tau_1)\dots\hat{A}_n(\tau_n)\big]\rangle = \frac{Z_0}{Z}\sum_{l=0}^{\infty}\frac{(-1)^l}{l!}\int_0^\beta\dots\int_0^\beta d\tau^{(1)}\dots d\tau^{(l)}. \tag{2.1.11}$$
$$\cdot\,\langle \mathcal{T}\big[\hat{T}_I(\tau^{(1)})\dots\hat{T}_I(\tau^{(l)})\,\hat{A}_{1,I}(\tau_1)\dots\hat{A}_{n,I}(\tau_n)\big]\rangle_0 \quad .$$

The subscripts 0 on the right-hand side denote the unperturbed average and partition function

$$\begin{aligned}\langle\hat{A}\rangle_0 &= \frac{1}{Z_0}Tr\big(e^{-\beta\hat{H}_0}\hat{A}\big)\\ Z_0 &= Tr\big(e^{-\beta\hat{H}_0}\big)=\prod_i Z^{(i)} \quad ,\end{aligned} \tag{2.1.12}$$

where $Z^{(i)}$ is the partition function of the isolated lattice site i,

$$Z^{(i)} = \sum_M \langle i,M|e^{-\beta\hat{h}_i}|i,M\rangle = \sum_M e^{-\beta E_M^{(i)}} \quad , \tag{2.1.13}$$

with the local eigenenergies $E_M^{(i)}$ from (2.1.3).

From now on all operators are taken to be in the interaction picture and the subscript I is dropped.

Physically relevant thermal averages are the partition function Z and N-body Green functions, most notably one- and two-body Green functions,

$$G^1_{i\alpha;j\beta}(\tau_1;\tau_1') = -\langle \mathcal{T}\big[\hat{c}_{i\alpha}(\tau_1)\,\hat{c}^\dagger_{j\beta}(\tau_1')\big]\rangle \equiv G^1(1;1') \tag{2.1.14}$$

$$G^2_{i\alpha,j\beta;k\gamma,l\delta}(\tau_1,\tau_2;\tau_2',\tau_1') = \langle \mathcal{T}\big[\hat{c}_{i\alpha}(\tau_1)\,\hat{c}_{j\beta}(\tau_2)\,\hat{c}^\dagger_{k\gamma}(\tau_2')\,\hat{c}^\dagger_{l\delta}(\tau_1')\big]\rangle \equiv G^2(1,2;2',1') \quad . \tag{2.1.15}$$

Notice the short hand notation introduced on the right-hand side, where time-arguments and quantum numbers of creation (annihilation) operators are summarized by primed (unprimed) numbers. Another useful notation encodes the orbital quantum numbers in a matrix structure (see appendix B),

$$\begin{aligned}G^1_{i\alpha;j\beta}(\tau_1;\tau_1') &\equiv \big(\underset{\approx}{G}_{ij}(\tau_1;\tau_1')\big)_{\alpha\beta}\\ G^2_{i\alpha,j\beta;k\gamma,l\delta}(\tau_1,\tau_2;\tau_2',\tau_1') &\equiv \Big(\underline{\underline{G}}_{ijkl}(\tau_1,\tau_2;\tau_2',\tau_1')\Big)_{\alpha\beta\gamma\delta} \quad .\end{aligned} \tag{2.1.16}$$

To explicitly distinguish between one- and two-particle quantities a wavy and straight double underline is used, respectively. These short hand notations will be used frequently and interchangeably whichever seems to be more convenient.

In the following the reorganization of the perturbation expansion (2.1.11) in order to derive diagrammatic rules for the calculation of time-ordered expectation is shortly sketched. The focus lies on the necessary and crucial steps to obtain a self-consistent approximation

scheme, the *locally complete approximation*. Some more details and examples are give in the appendix A.

The analysis of the perturbation expansion (2.1.11) is conducted in the usual manner. Since the unperturbed Hamiltonian does not mix different lattice sites, any contribution factorizes in a product of local expectation values of creation and annihilation operators on the same lattice site connected by the perturbation, i.e. the hopping matrix elements.

But one crucial difference arises at this point: since the unperturbed local Hamiltonian $\hat{H}_0$ incorporates a two-particle interaction $\sim U_{\alpha\beta\gamma\delta}$, Wick's theorem is not applicable. Therefore local averages involving more than two creation and annihilation operators, i.e. higher order local Green functions, cannot be decomposed into products of one-particle Green functions; any term involving higher order Green functions at some sites must be taken as it is. As a consequence no products of local Green function at the same lattice sites do occur in the whole perturbation expansion. This implies for a given contribution, that the summation over lattice indices has to respect this fact and thus a self-exclusion constraint is included in the terms of the sum. The problem of summing (or even enumerating) all paths on a lattice not intersecting themselves is known in the literature as the self-avoiding random walk or excluded volume problem and remains unsolved up to today.

For the same reason, i.e. the lack of Wick's theorem, the linked cluster theorem is not applicable. Therefore the partition function cannot be factorized and canceled from every connected diagram, resulting in the necessity to consider disconnected diagrams as well.

The formal solution to this problem lies in the usage of cumulant Green functions (cumulants for short). Pictorially, the N-body cumulant is the N-body Green function minus all the terms generated by a generalized Wick-decomposition. Generalized in a sense, that it does not only include products of one-body Green functions, but also all possible decomposition into $m, n, \ldots$-body Green functions, where $m, n, \cdots < N$. One can think of the N-body cumulant representing only the N-body correlations present in the Green function. Therefore we can express the N-body Green function as a sum over products of cumulants. The first few cumulant decompositions of Green functions are

$$G^1(1;1') = G^{1\,c}(1;1') \tag{2.1.17}$$

$$\begin{aligned} G^2(1,2;2',1') = {} & G^{2\,c}(1,2;2',1') \\ & + G^{1\,c}(1;1')G^{1\,c}(2;2') - G^{1\,c}(1;2')G^{1\,c}(2;1') \end{aligned} \tag{2.1.18}$$

$$\begin{aligned} G^3(1,2,3;3',2',1') = {} & G^{3\,c}(1,2,3;3',2',1') \\ & + G^{2\,c}(1,2;2',1')G^{1\,c}(3;3') - G^{2\,c}(1,2;3',1')G^{1\,c}(3;2') + \ldots \\ & + G^{1\,c}(1;1')G^{1\,c}(2;2')G^{1\,c}(3;3') + \ldots \quad . \end{aligned} \tag{2.1.19}$$

The dots in equation (2.1.19) stand for terms with the same structure, but permutated arguments. The signs in front of the cumulant correction terms are determined by the

parity of the permutation necessary to achieve the order of the creation and annihilation operators[1].

The cumulant perturbation expansion is obtained be inserting the cumulant decomposition for every encountered local N-body Green function. An in-depth analysis of symmetry factors, signs and possible paths on the lattice reveals, that in turn the lattice summations in all diagrams can be done freely over the lattice without any self-exclusions. The cumulant correction terms included at every local vertex, composed of products of local Green functions, exactly cancel all unphysical terms generated through the free lattice summations. A direct consequence is the applicability of the linked cluster theorem, i.e. the factorization and cancelation of the partition function for every connected diagram. Connected with respect to hopping processes on the lattice which join N-body cumulant vertices.

The derivation of the diagrammatic rules for the cumulant perturbation theory now proceeds along the same lines as in the usual Feynman-case and the explicit rules are stated in appendix A.

Even so the perturbation theory sketched above makes strong use of the local picture of the lattice, it is useful to transform into the delocalized Fourier space. The creation and annihilation operators in position and Fourier space are related trough the following transformations

$$\begin{aligned} \hat{c}_{j\alpha} &= \frac{1}{\sqrt{N_0}} \sum_{\underline{k}} e^{-i\underline{k}\cdot\underline{R}_j} \hat{c}_{\underline{k}\alpha} \quad , \qquad \hat{c}^\dagger_{j\alpha} = \frac{1}{\sqrt{N_0}} \sum_{\underline{k}} e^{i\underline{k}\cdot\underline{R}_j} \hat{c}^\dagger_{\underline{k}\alpha} \quad , \\ \hat{c}_{\underline{k}\alpha} &= \frac{1}{\sqrt{N_0}} \sum_{j} e^{i\underline{k}\cdot\underline{R}_j} \hat{c}_{j\alpha} \quad , \qquad \hat{c}^\dagger_{\underline{k}\alpha} = \frac{1}{\sqrt{N_0}} \sum_{j} e^{-i\underline{k}\cdot\underline{R}_j} \hat{c}^\dagger_{j\alpha} \quad . \end{aligned} \tag{2.1.22}$$

N_0 is the total number of lattice sites in the volume, $\underline{R}_j$ the lattice vector of site j and $\underline{k}$ a crystal momentum vector.

It is also convenient to go into Matsubara frequency space [Neg88] and transform the time arguments accordingly. For time translationally invariant systems, i.e. the Hamiltonian is independent of τ, expectation values depend only on time differences, e.g.

$$G(\tau;\tau') = G(\tau-\tau';0) \equiv G(\tau-\tau') \quad . \tag{2.1.23}$$

[1] The N-th order cumulant can be calculated from the generating functional $G^{0\,c}[\xi,\xi^*]$

$$G^{0\,c}[\xi,\xi^*] = \ln\Big\langle \mathcal{T} \exp\Big\{ -\sum_{i,\alpha} \int_0^\beta d\tau \, \Big[\xi^*_{i\alpha}(\tau)\,\hat{c}_{i\alpha}(\tau) + \hat{c}^\dagger_{i\alpha}(\tau)\,\xi_{i\alpha}(\tau)\Big] \Big\}\Big\rangle_0 \tag{2.1.20}$$

by functional derivatives with respect to the Grassmann fields ξ and ξ^* [Hub67, Neg88, Met91]

$$G^{N\,c}(1,\ldots,N;N',\ldots,1') = \frac{\delta}{\delta\xi^*(1)}\cdots\frac{\delta}{\delta\xi^*(N)}\frac{\delta}{\delta\xi(N')}\cdots\frac{\delta}{\delta\xi(1')} G^{0\,c}[\xi,\xi^*]\Big|_{\xi=\xi^*=0} \quad . \tag{2.1.21}$$

For the case the $\hat{c}_{i\alpha}$ and $\hat{c}^\dagger_{i\alpha}$'s are classical statistical variables or bosonic operators (instead of anticommuting operators), the $\xi_{i\alpha}$ and $\xi^*_{i\alpha}$ are just regular commuting functions [Kub62].

In frequency space this translates into energy conservation. The transformation for the one-body Green function reads

$$G_A(\tau) = \frac{1}{\beta}\sum_n e^{-i\omega_n\tau} G_A(i\omega_n) \quad , \tag{2.1.24}$$

$$G_A(i\omega_n) = \int_0^\beta d\tau\, e^{i\omega_n\tau} G_A(\tau) \quad .$$

The $\omega_n = \frac{(2n+1)\pi}{\beta}$, $n = 0, \pm1, \pm2, \ldots$ are fermionic Matsubara frequencies and A is an index denoting orbital quantum numbers, lattice sites or momentum vectors. The fact that the fermionic Matsubara frequencies are discrete and odd multiples of $\frac{\pi}{\beta}$ reflects the antiperiodicity of the Green function in time [Neg88]. For a bosonic Green function the same transformation (2.1.24) applies, but with even Matsubara frequencies $\nu_n = \frac{2n\pi}{\beta}$, $n = 0, \pm1, \pm2, \ldots$ [2], reflecting the periodicity of the Green function.

Since all systems considered in this work are translational invariant in space and time, crystal momentum and energy are conserved at every vertex and for every hopping process.

The use of the cumulant Green functions as local vertices make it possible to formulate the expansion as a Feynman-like perturbation theory with all its characteristic features: diagrams can be expressed in momentum and frequency space with the conservation of both implied for homogeneous systems. Diagrams are defined by the participating graphical elements and their topological assembly. All quantum number assigned to inner lines (momentum or lattice indices, energy, orbital quantum numbers, ...) are to be summed freely. Only connected diagrams have to be considered as it is implied by the applicability of the linked cluster theorem.

The basic graphical elements are elementary transfers $t_{ij}^{\alpha\beta}$ ($t_{\underline{k}}^{\alpha\beta} = \frac{1}{N_0}\sum_{i,j} e^{i\underline{k}(\underline{R}_i - \underline{R}_j)}\, t_{ij}^{\alpha\beta}$ in momentum space) and local cumulants $\underline{\underline{\underline{\underline{G}}}}^{N\,c}_{iiii}$ ($\underline{\underline{\underline{\underline{G}}}}^{N\,c}_{iiii}\delta_{\underline{k}_1,0}\delta_{\underline{k}_2,0}\delta_{\underline{k}_3,0}\delta_{\underline{k}_4,0}$) as vertices.

The major practical drawback of this method is certainly the appearance of local cumulant vertices up to infinite order. These have to be calculated separately and become quite cumbersome for larger N.

2.2 Dyson equations and the locally complete approximation

In this section an approximation for the one-particle Green function is developed. It is convenient to group together all one-particle irreducible (1PI) diagrams starting and ending with a cumulant vertex and thus define the cumulant self-energy $\underline{\underline{\Sigma}}^c(\underline{k}, i\omega_n)$. A diagram is said to be 1PI, if any single inner line can be cut without separating it into two disconnected pieces. With this self-energy the Dyson equation for the one-body lattice Green function can be formulated in momentum and Matsubara space as shown in figure 2.1. The double line with open circles on both ends represents the full lattice Green function $\underline{\underline{G}}(\underline{k}, i\omega_n)$ for crystal momentum $\underline{k}$ and fermionic Matsubara frequency $i\omega_n$. The shaded box with open half-circles stands for the cumulant self-energy $\underline{\underline{\Sigma}}^c(\underline{k}, i\omega_n)$ and an isolated open circle for the atomic one-body Green function $\underline{\underline{G}}(i\omega_n)|^{(0)}$. The dashed line is the single-electron transfer $\underline{\underline{t}}_{\underline{k}}$.

[2] Fermionic Matsubara frequencies are denoted by ω_n and bosonic ones by ν_n.

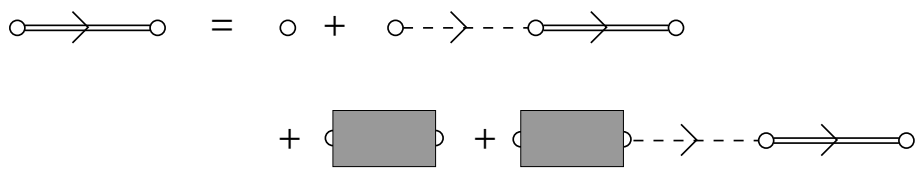

Figure 2.1: Dyson equation for the one-particle Green function with a cumulant self-energy

Diagrams constructed in the cumulant perturbation theory must not have two (or more) cumulant vertices occur on the same lattice site; these only implicitly occur due to the free lattice sums (cf. appendix A). Therefore the single-electron transfers $\underset{\approx}{t_{\underline{k}}}$ have to be made explicit in the Dyson equation to ensure this.

Notice, in contrast to the usual definition of a self-energy, Σ^c has the dimension $1/Energy$ instead of $Energy$ and therefore is a Green function regarded from its dimension. The reason for this lies in the fact that the start and end points are accounted for in the self-energy. This becomes more apparent from the analytic version of the Dyson equation[3]

$$\underset{\approx}{G}(\underline{k}, i\omega_n) = \underset{\approx}{G}(i\omega_n)|^{(0)} + \underset{\approx}{\Sigma}^c(\underline{k}, i\omega_n) + \underset{\approx}{G}(\underline{k}, i\omega_n)\, \underset{\approx}{t_{\underline{k}}}\, \left[\underset{\approx}{G}(i\omega_n)|^{(0)} + \underset{\approx}{\Sigma}^c(\underline{k}, i\omega_n)\right] \quad , \tag{2.2.1}$$

where Σ^c occurs as an additional contribution to the local Green function $\underset{\approx}{G}(i\omega_n)|^{(0)}$. Equation (2.2.1) can be formally solved to give

$$\underset{\approx}{G}(\underline{k}, i\omega_n) = \left[\underset{\approx}{\tilde{G}}(\underline{k}, i\omega_n)^{-1} - \underset{\approx}{t_{\underline{k}}}\right]^{-1} \quad , \tag{2.2.2}$$

where we introduced the effective cumulant Green function

$$\underset{\approx}{\tilde{G}}(\underline{k}, i\omega_n) = \underset{\approx}{G}(i\omega_n)|^{(0)} + \underset{\approx}{\Sigma}^c(\underline{k}, i\omega_n) \quad . \tag{2.2.3}$$

This quantity represents the collection of all possible 1PI cumulant terms, local and non-local, while the one-particle reducible ones are accounted for in the Dyson equation (2.2.1).

The open task is to select and calculate a set of diagrams defining the cumulant self-energy.

But before this is done explicitly, it is appropriate to mention how the atomic and the non-interacting limit are correctly produced in this theory:

- In the atomic limit the hopping matrix elements vanish, i.e. $\underset{\approx}{t_{\underline{k}}} = 0$. Substituting this into the Dyson's equation (2.2.1) we see that the one-particle Green function reduces to $\underset{\approx}{G}(i\omega_n)|^{(0)} + \underset{\approx}{\Sigma}^c(\underline{k}, i\omega_n)$. But since the self-energy includes necessarily inner lines which are proportional to $\underset{\approx}{t_{\underline{k}}}$ it vanishes as well. Therefore we indeed recover the atomic Green function and describe a system of independent ions.

- In the non-interacting limit the Coulomb matrix elements vanish, i.e. $U_{\alpha\beta\gamma\delta} = 0$ in (2.1.2). In that case all local cumulant averages of order $n \geq 2$ vanish identically since the local Hamiltonian $\hat{h}_0$ is bi-linear and Wick's theorem applies. Thus the cumulant self-energy is zero and we recover the usual tight-binding model, i.e. non-interacting electrons in a band structure specified by $\underset{\approx}{t_{\underline{k}}}$.

[3] See appendix B for details on the matrix notation.

Both limits are thus exactly reproduced by this theory, regardless of the approximation made for the self-energy. This is very promising in view of the goal to describe the transition of physical systems from phases with itinerant, almost free particles to systems with heavy, localized degrees of freedom.

Certainly the calculation of the exact self-energy $\underset{\approx}{\Sigma}^c$ is not possible in general and one has to employ approximations. The simplest approximation is to neglect all local n-body cumulant vertices with $n > 1$, i.e. ignoring $\underset{\approx}{\Sigma}^c$ altogether. The resulting Green function is of the form,

$$\underset{\approx}{G}(\underline{k}, i\omega_n)|^{(1)} = \left[\underset{\approx}{G}(i\omega_n)|^{(0)^{-1}} - \underset{\approx}{t}_k\right]^{-1} \quad . \tag{2.2.4}$$

This type of approximation was first done by Hubbard for the single-band Hubbard model [Hub63] and a multi-band model [Hub64a] and is known as the *Hubbard-I* approximation. In the present setup this type of approximation is termed *free theory*, since all cumulant vertices with $n > 1$ are neglected and therefore a theory without interaction vertices remains. But this by no means implies that a non-interacting case is considered as the atomic Green function is calculated with the local interaction matrix elements $U_{\alpha\beta\gamma\delta}$.

One step further is to include the first cumulant diagram, which is the one shown in figure A.2(a) of appendix A. The calculation was performed in [Gre96, Vla90, Vak90] for the Hubbard model and termed *Hartree-type* approximation, because of the similarity of the diagram to the usual Hartree diagram. But as the local two-particle cumulant is a dynamic quantity, this does produce a dynamic, i.e. frequency dependent, self-energy, not just a shift in the chemical potential. One possible choice for this type of self-energy is to take the diagram as drawn and use the Green function of the free theory $\underset{\approx}{G}(\underline{k}, i\omega_n)|^{(1)}$ for the inner line. Another choice is to interpret the diagram as a skeleton and use the full Hartree-type Green function for the inner line. By doing the latter, a self-consistency equation is derived, which is solved by the physical Green function.

Better approximations obtained by selecting a set of specific diagrams soon become quite cumbersome, because of the occurrence of higher order cumulants and the increasing number of frequency and momentum sums to be performed.

In order to describe magnetic screening effects and the formation of heavy quasiparticles, it is necessary to go beyond skeleton expansions with only a finite number of cumulant vertices, but infinite order vertices have to be retained. Since local correlations are believed to play a major role, only pseudo-local diagrams, i.e. those which start and end at the same lattice site, are included into the self-energy. With this, explicit non-local correlations are neglected and the resulting self-energy is momentum independent,

$$\underset{\approx}{\Sigma}^c(\underline{k}, i\omega_n) \rightarrow \underset{\approx}{\Sigma}^c(i\omega_n) \quad .$$

In order to obtain a manageable selection of diagrams a further restriction is imposed, which excludes *all* non-local correlations from the self-energy. The resulting selection of diagrams within this approximation can be characterized as follows:

From all possible connected one-particle irreducible graphs constituting the exact cumulant self-energy, those are selected

a) which are pseudo-local, i.e. have the external lines attached to the same lattice site,

b) where any two cumulant vertices sitting on *different* lattice sites are connected by not more than two electronic lines.

The term "all possible graphs" does not only refer to all topological distinct diagrams in accord with the diagram rules of the cumulant perturbation theory as described in appendix A, but those terms generated in the free lattice sums are taken into account as well. So the contributing terms are selected from all diagrams *after* expanding all lattice sums. This means, products of cumulant averages on equal lattice sites, which do not appear in diagrams of the cumulant perturbation theory, *will* explicitly occur in this approximation. This procedure therefore discards some terms of a topological diagram, whilst keeping others depending on the arrangement of the cumulant vertices on the lattice. The graphs included in this approximation can therefore not be strictly characterized as diagrams in the sense of the cumulant perturbation theory, where every diagram represents one topology of an arrangement and the lattice sums are performed freely.

To make it clear, condition b) does not exclude graphs where two lattice sites are joined by more than two electronic lines, but only those where two cumulant vertices sitting on different lattice sites are connected by more than two lines.

The above stated selection of diagrams constitute the *locally complete approximation* and quantities calculated within it will be denoted with a trailing $|^{(lc)}$.

The cumulant self-energy $\underset{\approx}{\Sigma}^{c}|^{(lc)}$ can be expressed through a skeleton expansion with the following diagrams: at the site with the external lines attached – which is called site 0 for further reference – all possible combinations of two- and higher-particle cumulant vertices are summed. The external lines can be attached to any of those vertices and the connections of the cumulants are done by fully dressed one-particle loop-propagations as inner lines. Due to the condition b) all these inner lines have the structure of nested loops, i.e. they start and end at site 0 and lattice sites visited during such a loop can have more loops attached. But no two loops based at site 0 must be connected, i.e. correlated, through a cumulant average situated at any site other than 0! Due to the free lattice sums present in these loops, contributions where a local cumulant or a cluster of local cumulants is connected to another cumulant or cluster of cumulants on the same site by only two lines have to be excluded from site 0. And additionally all terms involving one-body cumulants have to be omitted at the site 0, since they are either generated by the free lattice sums of the inner loops or are not 1PI.

The usage of the fully dressed propagators for the inner loops is justified by the observation, that the same selection of diagrams is made at any other site visited during a loop-propagation, with the modification that the 1PI diagrams involving one-body Green functions are retained and thus build up the full lattice Green function.

The resulting skeleton expansion is sketched in figure 2.2, where symmetry and sign factors are omitted.

To get an insight in the physical processes included in this approximation, first notice that the difference between the effective local cumulant Green function $\underset{\approx}{\tilde{G}}|^{(lc)}$ and the real physical Green function $\underset{\approx}{G}|^{(lc)}$ lies in the one-particle *reducible* terms present in $\underset{\approx}{G}|^{(lc)}$ but not in $\underset{\approx}{\tilde{G}}|^{(lc)}$. This becomes apparent by looking at the Dyson equation shown in figure 2.1, or analytically

$$\underset{\approx}{G}(\underline{k}, i\omega_n)|^{(lc)} = \underset{\approx}{\tilde{G}}(i\omega_n)|^{(lc)} + \underset{\approx}{G}(\underline{k}, i\omega_n)|^{(lc)} \, \underset{\approx}{t}_{\underline{k}} \, \underset{\approx}{\tilde{G}}(i\omega_n)|^{(lc)} \quad , \tag{2.2.5}$$

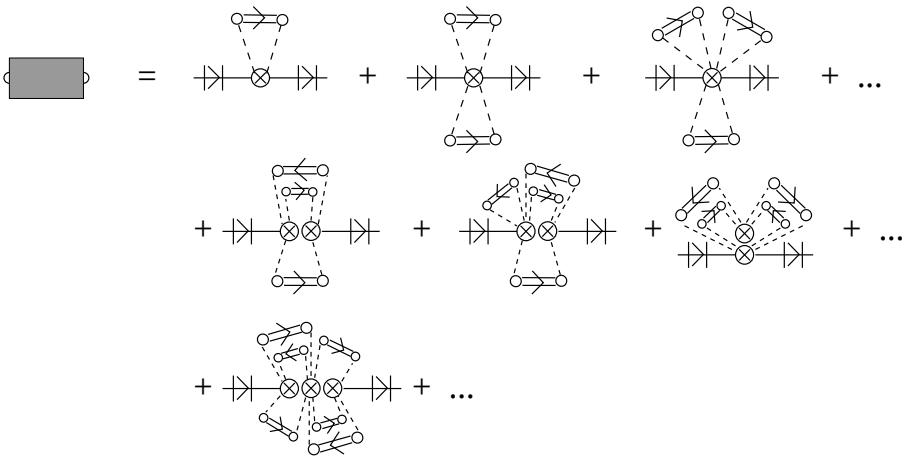

Figure 2.2: Structure of the skeleton expansion of the self-energy in the local approximation. Symmetry and sign factors of the diagrams are omitted. The local cumulant Green functions (crossed circles) drawn right next to each other are taken to be at the same lattice site.

where only one-particle reducible terms are summed. From the above lattice Green function, the local Green function is obtained by performing the momentum sum

$$\underset{\approx}{G}^{(loc)}(i\omega_n)|^{(lc)} = \frac{1}{N_0}\sum_{\underline{k}} \underset{\approx}{G}(\underline{k}, i\omega_n)|^{(lc)} \quad . \tag{2.2.6}$$

In order to clarify the following argument, a specific site is considered, again labeled by 0[4]. In this local Green function for the site 0, all those terms are generated by the lattice sum which have products of cumulant vertices on this site and which are only connected by a *single* electronic line, i.e. which are one-particle reducible. Combining these with all the 1PI terms incorporated into the cumulant self-energy, the cumulant decomposition at this local site can be partially reversed. This is explicitly done by expressing all the local cumulant averages by their decomposition into local physical Green functions, i.e. by inverting the formulas for the cumulant decomposition indicated in the equations (2.1.17) to (2.1.19) (thus leaving the realm of the cumulant perturbation theory and returning to contributions of the original perturbation theory with respect to the hopping amplitude (2.1.11)). Doing this, a multitude of terms is generated which involve unphysical products of local (physical) Green functions at site 0. But by construction of the cumulant averages, almost all of these terms cancel. Each of the remaining terms consists of only *one* local physical N-particle Green function with the external lines and $N-1$ inner loops attached to it. All additional local Green functions which occur at the site 0 can only be of the following two types:

1. Part of a nested loop: an inner loop starting and ending at site 0 can have a higher order Green function at some site different than 0. This higher order Green functions then necessarily has an inner loop which in turn can visit site 0, so that an unphysical product occurs at 0. Clearly these terms arise as a direct consequence of the neglect of correlated loops. Including those terms would subtract the unphysical products and

[4] Due to the translational invariance of the lattice, the local Green function is the same for any site and the following argument applies anywhere.

replace them with the physical ones, consisting of two higher order Green functions at two different sites connected by four (or more) lines. But since correlated loops are discarded in this approximations, the unphysical product terms remain and constitute the approximation for the correlated loops.
To make it clear, an inner loop based at site 0 must no visit it directly during the loop-propagation (terms where it did cancel with terms stemming from a cumulant decomposition of some higher-order local cumulant). In contrast, a nested loop, i.e. a loop based on any site on an inner propagation, may return to site 0.
All those nested loop-terms can be grouped in such as way, that a so-called *irreducible transfer matrix* $\underset{\approx}{\tilde{T}}(i\omega_n)$ can be defined, which describes a fully dressed loop-propagation without visiting the base site of the loop.

2. Part of a factorized diagram: the additional local Green functions at site 0 are part of a diagram which is not connected to the external lines and thus just represents a factorized contribution. Apart from the fact, that they are unconnected to the external lines, these terms have the same loop-structure as the connected ones: they have inner loops attached, starting at ending at site 0, but which do not visit it in-between. Nested loops starting at different sites of such a loop do visit site 0 and produce unphysical products, which is again due to the neglect of correlated loops. All these loops just represented the irreducible transfer matrix $\underset{\approx}{\tilde{T}}(i\omega_n)$.
For any connected diagram including the external lines, an infinite sum of unconnected ones is produced as a factor. Due to the fact that these terms stem from the inverted cumulant decomposition and that all local cumulant diagrams up to infinite order are summed, the *same* factor is produced for each of these connected diagrams! This is the same argument, why a linked cluster theorem was valid in the cumulant perturbation theory and the partition function could be factorized there, only now reversed. This factor consists of all possible closed diagrams in accord with the diagrammatic selection rules and thus defines the partition function Z_{loc} of this approximation which in turn is used to define an effective local average.

Putting these two points together, the local Green function can be expressed as a functional of the irreducible transfer matrix $\underset{\approx}{\tilde{T}}(i\omega_n)$ and the effective local average defined by Z_{loc}. With the exact same reasoning, the local partition function can also be expressed as a functional of $\underset{\approx}{\tilde{T}}(i\omega_n)$, which is intimately connected to that for the local Green function.

The structure of the resulting $\underset{\approx}{G}^{(loc)}|^{(lc)}$ is shown in figure 2.3, where the double zig-zag line with the two attached transfers denotes $\underset{\approx}{\tilde{T}}(i\omega_n)$ and the nested circle the effective local average. This form makes the name "locally complete" evident, since all local correlations are taken into account, i.e. all local Green functions up to infinite order with all possible inner loops are summed.

At this point a physical picture of this approximation can be introduced: all inner irreducible loops can be regarded to represent a fictitious non-interacting medium, since they are all uncorrelated from each other. The successive propagations in this medium are linked together by the effective local site, where all dynamic correlations are respected. The local Green function of the lattice model can thus be identified with that of an interacting impurity embedded into an effective medium characterized by $\underset{\approx}{\tilde{T}}$,

$$\underset{\approx}{G}^{(loc)}|^{(lc)} = \underset{\approx}{G}^{(imp)}[\underset{\approx}{\tilde{T}}|^{(lc)}] \quad . \tag{2.2.7}$$

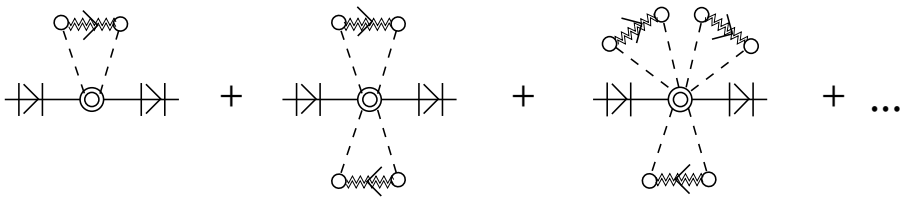

Figure 2.3: Structure of the local one-particle Green function in terms of the irreducible transfer matrix $\tilde{T}$, which is denoted as a double zig-zag line with two attached transfers. The nested circles are local averages with the corresponding partition functions Z_{loc} and represent effective local Green functions. Sign and symmetry factors are omitted.

The partition function Z_{loc} can also be identified with the one of that impurity model.

The conceptual difficulty here is certainly the determination of the effective medium $\underset{\approx}{\tilde{T}}|^{(lc)}$. It has to be obtained in self-consistent manner, since it is build from fully dressed lattice propagations involving local Green functions, which in turn already incorporate $\underset{\approx}{\tilde{T}}$ itself. Thus a set of equations needs to be derived from which the Green function and the effective medium can be determined.

Another problem is to solve the effective impurity model given an effective medium $\underset{\approx}{\tilde{T}}$. But due to their long history and focus of attention, impurity models can be solved quite effectively with a variety of methods and the solution of this task is described in chapter 3.

In order to determine $\underset{\approx}{\tilde{T}}$, the Dyson equation (2.2.5) is iterated once and then the momentum sum is used to calculate the local Green function (cf. (2.2.6)). Since the elementary hopping always transfers to a different lattice site, i.e.

$$\underset{\approx}{t}_{ii} = \frac{1}{N_0} \sum_{\underline{k}} \underset{\approx}{t}_{\underline{k}} = 0 \quad , \tag{2.2.8}$$

the local Green function can be expressed as[5]

$$\underset{\approx}{G}^{(loc)}(i\omega_n) = \underset{\approx}{\tilde{G}}(i\omega_n) + \underset{\approx}{\tilde{G}}(i\omega_n)\, \underset{\approx}{T}(i\omega_n)\, \underset{\approx}{\tilde{G}}(i\omega_n) \quad , \tag{2.2.9}$$

$$\underset{\approx}{T}(i\omega_n) = \frac{1}{N_0} \sum_{\underline{k}} \underset{\approx}{t}_{\underline{k}}\, \underset{\approx}{G}(\underline{k}, i\omega_n)\, \underset{\approx}{t}_{\underline{k}} \tag{2.2.10}$$

with the *reducible transfer matrix* $\underset{\approx}{T}(i\omega_n)$, which is shown in figure 2.4. To connect the reducible transfer matrix $\underset{\approx}{T}$ to the irreducible $\underset{\approx}{\tilde{T}}$, another Dyson equation has to be deduced. $\underset{\approx}{T}$ incorporates all paths starting and ending at the base site 0, irregardless how these are arranged on the lattice. It therefore represents the sum of all random walks starting and ending at 0, where each visited lattice site contributes with a factor $\underset{\approx}{\tilde{G}}$ and each link with an elementary hopping. In contrast to that, the irreducible transfer matrix counts only those random walks where the base site 0 is excluded. It is evident that $\underset{\approx}{T}$ can be expressed in terms of repeated visits to site 0 as (see figure 2.5)

$$\underset{\approx}{T}(i\omega_n) = \underset{\approx}{\tilde{T}}(i\omega_n) + \underset{\approx}{T}(i\omega_n)\, \underset{\approx}{\tilde{G}}(i\omega_n)\, \underset{\approx}{\tilde{T}}(i\omega_n) \quad . \tag{2.2.11}$$

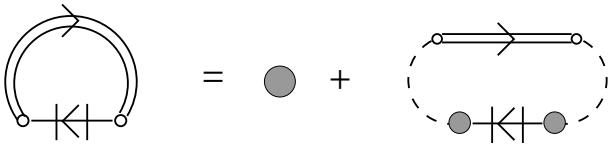

Figure 2.4: Equation for the local one-particle Green function in terms of the T-matrix. The shaded circle represents the effective local cumulant Green function $\tilde{G} = G|^{(0)} + \Sigma^c$.

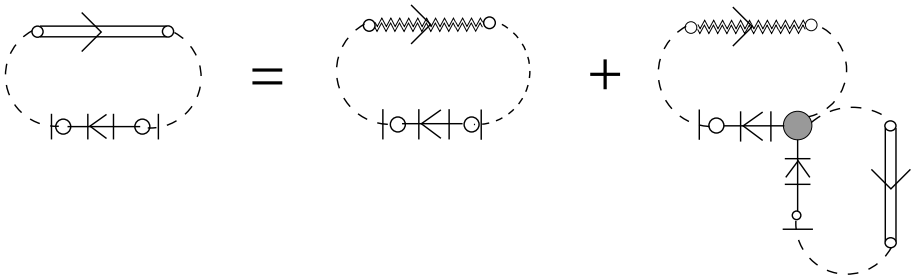

Figure 2.5: Equation for the local reducible T-matrix in terms of the irreducible T-matrix $\tilde{T}$.

Before proceeding with the argument, notice the identity

$$\underset{\approx}{G}^{(loc)}(i\omega_n)\,\underset{\approx}{\tilde{T}}(i\omega_n) = \underset{\approx}{\tilde{G}}(i\omega_n)\,\underset{\approx}{T}(i\omega_n) \quad , \tag{2.2.12}$$

which is gained by comparing equations (2.2.11) and (2.2.9). An equivalent form of this identity will be useful for the corresponding two-particle quantities in section 2.3.

Putting equations (2.2.11) and (2.2.9) together yields the local Green function

$$\underset{\approx}{G}^{(loc)}(i\omega_n) = \left[\underset{\approx}{\tilde{G}}(i\omega_n)^{-1} - \underset{\approx}{\tilde{T}}(i\omega_n)\right]^{-1} \quad , \tag{2.2.13}$$

or solved for the effective local cumulant Green function

$$\underset{\approx}{\tilde{G}}(i\omega_n) = \left[\underset{\approx}{G}^{(loc)}(i\omega_n)^{-1} + \underset{\approx}{\tilde{T}}(i\omega_n)\right]^{-1} \quad . \tag{2.2.14}$$

In case the effective medium $\underset{\approx}{\tilde{T}}$ is known, the solution of the impurity model yields the local Green function $\underset{\approx}{G}^{(loc)}$. Equation (2.2.14) can then be used to calculate the effective cumulant Green function $\underset{\approx}{\tilde{G}}$ which in turn determines the lattice Green function via the Dyson equation (2.2.5),

$$\underset{\approx}{G}(\underline{k}, i\omega_n) = \left[\underset{\approx}{\tilde{G}}(i\omega_n)^{-1} - \underset{\approx}{t}_{\underline{k}}\right]^{-1} \quad . \tag{2.2.15}$$

This can be used to calculate the local Green function via (2.2.6) and compared to the local Green function from the effective impurity model.

The crucial point certainly is, that the effective medium is not known a priori. But at this point all necessary equations needed to determine the lattice Green function are

[5] For the sake of simplicity regarding the notation, the trailing $|^{(lc)}$ will be omitted. From now on all quantities are assumed to be calculated in the locally complete approximation, unless stated otherwise.

already given. Under the assumption, that a model describing an impurity embedded in a non-interacting, dynamically reacting host can be solved, an iterative self-consistency cycle can be set up. For completeness, this cycle is stated:

0. initialize the cycle by guessing an effective medium $\underline{\underline{\tilde{T}}}_0(i\omega_n)$
1. use the effective medium from the previous $(i-1)$th iteration $\underline{\underline{\tilde{T}}}_{i-1}(i\omega_n)$ to solve the effective impurity model and obtain the local Green function $\underline{\underline{G}}_i^{(loc)}(i\omega_n)$
2. calculate the local cumulant Green function

$$\underline{\underline{\tilde{G}}}_i(i\omega_n) = \left[\underline{\underline{G}}_i^{(loc)}(i\omega_n)^{-1} + \underline{\underline{\tilde{T}}}_{i-1}(i\omega_n)\right]^{-1} \tag{2.2.16}$$

3. obtain the local Green function

$$\underline{\underline{G}}_i^{(loc)}(i\omega_n) = \frac{1}{N_0}\sum_{\underline{k}}\left[\underline{\underline{\tilde{G}}}_i(i\omega_n)^{-1} - \underline{\underline{t}}_{\underline{k}}\right]^{-1} \tag{2.2.17}$$

4. check whether self-consistency is reached, e.g.

$$\underline{\underline{G}}_i^{(loc)}(i\omega_n) \stackrel{?}{=} \underline{\underline{G}}_{i-1}^{(loc)}(i\omega_n) \quad . \tag{2.2.18}$$

   - if true, stop this cycle
   - if not true, get a new guess for the effective medium

$$\underline{\underline{\tilde{T}}}_i(i\omega_n) = \underline{\underline{\tilde{G}}}_i(i\omega_n)^{-1} - \underline{\underline{G}}_i^{(loc)}(i\omega_n)^{-1} \quad . \tag{2.2.19}$$

     and proceed with step 1.

In [Pru01] it is shown, that the solution obtained in this iterative manner indeed represents a physical solution.

The equivalent self-consistent scheme for the Periodic Anderson Model was already proposed by Kuramoto and is known as the XNCA [Kur85a, Kim90]. But since it was developed from the direct perturbation theory for impurity models [Kei70, Kei71a, Gre81, Kei84], this method of solving the impurity was already build into the scheme and not rendered exchangeable as described above.

A similar self-consistent scheme for the Periodic Anderson Model, the LNCA, was introduced by Grewe [Gre87, Gre88] which also used effective local cumulant averages, but the self-consistency was formulated in a different manner.

For the Falicov-Kimball model the above stated setup was already used by Brandt and Mielsch [Bra89, Bra90, Bra91] and for the Hubbard model by Jarrell [Jar92].

Metzner [Met91] developed the formulation of the cumulant perturbation theory with effective renormalized local cumulants and a dressed-atom picture, but failed to produce a self-consistent mapping onto an impurity model.

In the literature the scalar version of this self-consistent scheme is known as the *dynamical mean field theory* (DMFT) [Geo96] and is usually introduced as the exact solution in the limit of infinite lattice dimensions, $d \to \infty$ [Met89, MH89a, MH89b, Bra89, Bra90]. Diagrams in the cumulant perturbation theory depend on the lattice dimension through

the lattice sums included in every diagram. It can be shown, that lattice sums produce terms with higher powers in d whenever the cumulant vertices are situated at the same lattice site, in contrast to those, where they are arranged on different sites[6]. If the hopping matrix elements $\underset{\approx}{t}$ are rescaled properly with a factor of $1/\sqrt{d}$, the infinite dimensional limit $d \to \infty$ yields a non-trivial theory and only the terms of the locally complete approximation as characterized in this section survive. The intuitive physical reason for the existence of this exact limit is, that in infinite lattice dimensions the probability for two random walks starting at the same site to meet at any other site vanishes. This assures the neglect of correlated loops.

Even so we introduced the effective cumulant Green function or equivalently the cumulant self-energy to describe the effects of the interaction, it is convenient to introduce the more common correlation self-energy $\underset{\approx}{\Sigma}^U$. The lattice Green function is expressed in the usual form

$$\underset{\approx}{G}(\underline{k}, i\omega_n) = \left[i\omega_n - \underset{\approx}{\epsilon} - \underset{\approx}{\Sigma}^U(i\omega_n) - \underset{\approx}{t}_k\right]^{-1} \quad , \tag{2.2.20}$$

where $\underset{\approx}{\epsilon}$ are the one-body matrix elements of equation (2.1.2). From this form it is clear, that $\underset{\approx}{\Sigma}^U$ represents the standard self-energy of perturbation theory with respect to the interaction matrix elements $U_{\alpha\beta\gamma\delta}$. Additionally, it directly lends itself to a physical interpretation: The real part describes the shift of energy levels and the imaginary part life-time effects due to the interactions. But from the foregoing derivation of this approximation it should be clear, that the locally complete approximation does *not* represent any finite or infinite order expansion in the interaction matrix elements. The form (2.2.20) merely bridges the formalism to a more common form of the lattice Green function known from the literature.

The connection between the effective cumulant Green function $\underset{\approx}{\tilde{G}}$ by and $\underset{\approx}{\Sigma}^U$ is obtained by comparison of equation (2.2.15) with (2.2.20),

$$\underset{\approx}{\tilde{G}}(i\omega_n) = \left[i\omega_n - \underset{\approx}{\epsilon} - \underset{\approx}{\Sigma}^U(i\omega_n)\right]^{-1} \quad . \tag{2.2.21}$$

Notice, that the effective cumulant Green function $\underset{\approx}{\tilde{G}}$ is build up from infinitely many one-particle *reducible* terms, when it is expressed in terms of physical interaction vertices represented by $\underset{\approx}{\Sigma}^U$; in contrast to that, it is the sum of one-particle *irreducible* terms only, when expressed in terms of cumulant vertices.

The local Green function for the lattice system can be equally well expressed with the help of the U-self-energy,

$$\underset{\approx}{G}^{(loc)}(i\omega_n) = \left[i\omega_n - \underset{\approx}{\epsilon} - \underset{\approx}{\Sigma}^U(i\omega_n) - \underset{\approx}{\tilde{T}}(i\omega_n)\right]^{-1} \tag{2.2.22}$$

$$\equiv \left[i\omega_n - \underset{\approx}{\epsilon} - \underset{\approx}{\Sigma}^{tot}(i\omega_n)\right]^{-1} \quad . \tag{2.2.23}$$

This form makes another connection to a more common form of a Green function known from the literature, namely that of a magnetic impurity embedded in a host characterized by $\underset{\approx}{\tilde{T}}$. Whereas the form (2.2.22) is certainly instructive from the lattice point of view and the effective impurity picture, in the second equation (2.2.23) a total self-energy

$$\underset{\approx}{\Sigma}^{tot}(i\omega_n) = \underset{\approx}{\Sigma}^U(i\omega_n) + \underset{\approx}{\tilde{T}}(i\omega_n) \tag{2.2.24}$$

is introduced, which is more commonly found in the literature on magnetic impurities.

[6] For the detailed argument see [Met91] and the article by J.L. Martin in [Dom74].

2.3 Bethe-Salpeter equations and susceptibilities

Having constructed a non-trivial approximation for the one-particle propagator, the focus will now be on two-particle properties. The Bethe-Salpeter equations for the lattice susceptibilities are presented for a general two-particle cumulant vertex. It is argued that the strict implementation of the locally complete scheme is not feasible, but a slightly modified effective impurity picture has to be used. This is then utilized to derive a simple instructive form for the dynamic susceptibility matrix.

2.3.1 Definitions and notation

The susceptibility function characterizes the response of the system to an external perturbation and within linear response theory is given by a two-particle Green function. While the two-particle Green functions in general have three independent time or frequency arguments, the dynamic susceptibility only has one. This is evident from the zz-component of the lattice- and time-dependent magnetic susceptibility tensor

$$\chi_{ij}^{zz,mag}(\tau) = \langle \mathcal{T}\left[\hat{M}_i^z(\tau)\,\hat{M}_j^z(0)\right]\rangle \quad , \tag{2.3.1}$$

with the total magnetization operator at site i given by

$$\hat{M}_i = \sum_{m\sigma} \gamma_\alpha\, \hat{n}_{i,\alpha} = \sum_{m\sigma} \gamma_\alpha\, \hat{c}_{i,\alpha}^\dagger \hat{c}_{i,\alpha} \quad . \tag{2.3.2}$$

The index α collects all local shell, orbital and spin quantum numbers and the γ_α are the matrix elements determining the z-component of the spin on the local site. For the case of a single orbital with total orbital angular momentum l the relevant quantum numbers are the orbital angular momentum m ($-l \leq m \leq l$) and spin $s = \frac{\sigma}{2}$ ($\sigma = \pm 1$) and thus $\alpha = \{m, \sigma\}$ and

$$\gamma_{m\sigma} = -\mu_B\big(m + \frac{g}{2}\sigma\big) \quad , \tag{2.3.3}$$

with g the electron Landé factor and μ_B the Bohr magneton.

Throughout this work only isotropic paramagnetic situations are considered and therefore the susceptibility tensor is diagonal and all diagonal elements are equal,

$$\chi_{ij}^{mag}\,\delta_{ab} \equiv \chi_{ij}^{ab,mag} = \chi_{ij}^{zz,mag}\,\delta_{ab} \quad , \qquad a,b = \{x,y,z\} \quad , \tag{2.3.4}$$

and the transverse susceptibility is just given by twice this value, i.e. $\chi^\perp = 2\chi^{zz}$. For brevity the superscript zz will be dropped from now on and whenever the magnetic susceptibility is mentioned, it refers to the zz-component of the magnetic susceptibility tensor.

Inserting equation (2.3.2) into (2.3.1) yields

$$\chi_{ij}^{mag}(\tau) = \sum_{\alpha\beta} \gamma_\alpha\gamma_\beta \lim_{\delta\to 0^+} \langle \mathcal{T}\big[\hat{c}_{i,\alpha}^\dagger(\tau{+}\delta)\hat{c}_{i,\alpha}(\tau)\hat{c}_{j,\beta}^\dagger(\delta)\hat{c}_{j,\beta}(0)\big]\rangle \tag{2.3.5}$$

$$= \sum_{\alpha\beta} \gamma_\alpha\gamma_\beta \lim_{\delta\to 0^+} G^2_{i\alpha,j\beta;j\beta,i\alpha}(\tau,0;\delta,\tau{+}\delta) \tag{2.3.6}$$

$$\equiv \sum_{\alpha\beta} \gamma_\alpha\gamma_\beta \lim_{\delta\to 0^+} \Big\{ G^1_{i\alpha;i\alpha}(\tau;\tau{+}\delta)\, G^1_{j\beta;j\beta}(0;\delta) + G^{2D}_{i\alpha,j\beta;j\beta,i\alpha}(\tau,0;\delta,\tau{+}\delta)\Big\} \tag{2.3.7}$$

$$= \sum_{\alpha\beta} \gamma_\alpha\gamma_\beta \langle \hat{n}_{i\alpha}\rangle\langle \hat{n}_{j\beta}\rangle + \sum_{\alpha\beta} \gamma_\alpha\gamma_\beta \lim_{\delta\to 0^+} G^{2D}_{i\alpha,j\beta;j\beta,i\alpha}(\tau,0;\delta,\tau{+}\delta) \quad .$$

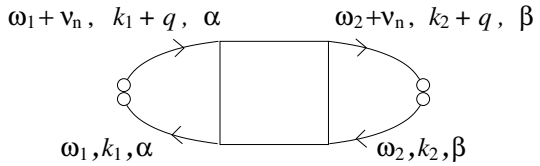

Figure 2.6: Graphical representation of the susceptibility matrix

Owing to the fact that no time ordering can be defined for equal times, a so-called convergence factor δ had to be introduced, which is chosen to be positive to preserve the order of the creation and annihilation operator in (2.3.2) and (2.3.1).

In (2.3.6) the specific arguments for the two-particle Green function are visible and equation (2.3.7) introduces the *direct* two-particle Green function G^{2D}, where a product of two time-independent one-particle Green functions is separated. It is this quantity determining the dynamic susceptibility which will be in the focus of the following considerations.

For the charge susceptibility the magnetization from (2.3.2) has to be replaced with the charge operator at site i,

$$\hat{Q}_i = -|e| \sum_{\alpha} \hat{n}_{i,\alpha} = -|e| \sum_{\alpha} \hat{c}^{\dagger}_{i,\alpha} \hat{c}_{i,\alpha} \quad . \tag{2.3.8}$$

Therefore the susceptibility is given by the same expression (2.3.6), only the coefficients γ_α are to be replaced with the appropriate matrix elements $-|e|$, i.e. a different linear combination of the orbital matrix elements of $\underline{\underline{G}}^{2D}$ is relevant.

Transforming the susceptibility into the energy and momentum representation,

$$\chi(\underline{q}, i\nu_n) = \frac{1}{(N_0)^2} \sum_{ij} \int_0^{\beta} d\tau \; e^{i\nu_n \tau} \; e^{i\underline{q}(\underline{R}_i - \underline{R}_j)} \chi_{ij}(\tau) \quad , \tag{2.3.9}$$

with the bosonic Matsubara frequency $i\nu_n = \frac{2\pi}{\beta} in$, $n = 0, \pm 1, \pm 2, \ldots$. Using the matrix formulation introduced in (2.1.16) (see also appendix B) an equivalent form of (2.3.7) is obtained,

$$\chi_{mag}(\underline{q}, i\nu_n) = \sum_{\alpha\beta} \gamma_\alpha \gamma_\beta \langle \hat{n}_{i\alpha} \rangle \langle \hat{n}_{j\beta} \rangle \; \delta_{i\nu_n, 0} + \sum_{\alpha\beta} \gamma_\alpha \gamma_\beta \lim_{\delta \to 0^+} \left[\underline{\underline{\chi}}(\underline{q}, i\nu_n) \right]_{\alpha\beta\beta\alpha} \quad . \tag{2.3.10}$$

The central quantity is the susceptibility matrix $\underline{\underline{\chi}}(\underline{q}, i\nu_n)$, which is given in terms of the momentum- and frequency-dependent direct two-particle Green function

$$\underline{\underline{\chi}}(\underline{q}, i\nu_n) = \frac{1}{\beta} \sum_{i\omega_1, i\omega_2} \frac{1}{N_0} \sum_{\underline{k}_1, \underline{k}_2} \underline{\underline{G}}^{2D}(\underline{k}_1, i\omega_1, \underline{k}_2 + \underline{q}, i\omega_2 + i\nu_n; \underline{k}_2, i\omega_2, \underline{k}_1 + \underline{q}, i\omega_1 + i\nu_n) \; e^{(i\omega_1 + i\omega_2)\delta} \tag{2.3.11}$$

$$\equiv \frac{1}{\beta} \sum_{i\omega_1, i\omega_2} \frac{1}{N_0} \sum_{\underline{k}_1, \underline{k}_2} \underline{\underline{\chi}}(q, i\nu_n | \underline{k}_1, \underline{k}_2 | i\omega_1, i\omega_2) \; e^{(i\omega_1 + i\omega_2)\delta} \tag{2.3.12}$$

$$\equiv \frac{1}{\beta} \sum_{i\omega_1, i\omega_2} \underline{\underline{\chi}}(q, i\nu_n | i\omega_1, i\omega_2) \; e^{(i\omega_1 + i\omega_2)\delta} \quad . \tag{2.3.13}$$

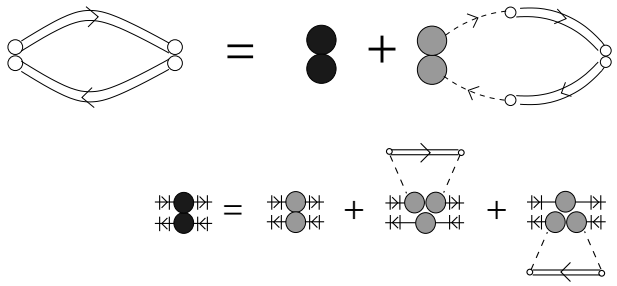

Figure 2.7: The particle-hole propagator expressed through $\underline{J}$ and $\underline{\underline{\Lambda}}\,\underline{\underline{\tilde{G}\tilde{G}}}$. The quantity $\underline{\underline{\Lambda}}\,\underline{\underline{\tilde{G}\tilde{G}}}$ is shown in the lower part, where the external lines are made explicitly for clarity.

$i\omega_1$ and $i\omega_2$ are short hand notations for sets of fermionic Matsubara frequencies $i\omega_{n_1}$ and $i\omega_{n_2}$, $n_1, n_2 = 0, \pm 1, \pm 2, \ldots$, respectively. The notation $\underline{\underline{\chi}}(q, i\nu_n|\underline{k}_1, \underline{k}_2|i\omega_1, i\omega_2)$ for the susceptibility matrix is introduced in (2.3.12) to explicitly discriminate it from a general two-particle Green function and to automatically imply the indicated choice of arguments with it. In equation (2.3.13) the $\underline{k}$-sums are absorbed into the definition, which will abbreviate expressions later on. The graphical representation of $\underline{\underline{\chi}}$ is shown in figure 2.6. The two external, pairwise contracted lines indicate the specific choice of variables also depicted in the graph.

Another quantity of interest is the so-called *particle-hole propagator*. It describes the uncorrelated propagation of an electron and a hole trough the lattice and it is build up from two one-particle Green functions,

$$\underline{\underline{P}}(\underline{q}, i\nu_n \,|\, i\omega_1) \equiv \frac{1}{N_0} \sum_{\underline{k}} \underline{\underline{GG}}(q, i\nu_n|\underline{k}|i\omega_1) \quad . \tag{2.3.14}$$

The notation $\underline{\underline{GG}}$ indicates a two-particle matrix which is build up from two one-particle quantities and is explained in appendix B. Using the Dyson equation (2.2.5) and the fact that $\sum_{\underline{k}} \underline{\underline{t}}_{\underline{k}} = 0$, the particle-hole propagator can be separated into a momentum dependent and momentum independent part

$$\underline{\underline{P}}(\underline{q}, i\nu_n \,|\, i\omega_1) = \underline{\underline{\Lambda}}(i\nu_n \,|\, i\omega_1)\, \underline{\underline{\tilde{G}\tilde{G}}}(i\nu_n \,|\, i\omega_1) + \underline{\underline{J}}(\underline{q}, i\nu_n \,|\, i\omega_1) \quad , \tag{2.3.15}$$

with

$$\underline{\underline{J}}(\underline{q}, i\nu_n \,|\, i\omega_1) = \frac{1}{N_0} \sum_{\underline{k}} \underline{\underline{GG}}(q, i\nu_n|\underline{k}|i\omega_1)\ \underline{\underline{tt}}(\underline{q} \,|\, \underline{k})\ \underline{\underline{\tilde{G}\tilde{G}}}(i\nu_n \,|\, i\omega_1) \quad , \tag{2.3.16}$$

$$\underline{\underline{\Lambda}}(i\nu_n \,|\, i\omega_1) = \underline{\underline{1}} \otimes \underline{\underline{1}} + \underline{\underline{1}} \otimes \left[\underline{\underline{\tilde{G}}}(i\omega_1 + i\nu_n)\, \underline{\underline{T}}(i\omega_1 + i\nu_n)\right] + \left[\underline{\underline{T}}(i\omega_1)\, \underline{\underline{\tilde{G}}}(i\omega_1)\right] \otimes \underline{\underline{1}} \quad , \tag{2.3.17}$$

as it is show in figure 2.7. The functions $\underline{\underline{\Lambda}}$ incorporate processes, where only one electron leaves a site and propagates through the lattice, while the other remains at this site.

2.3.2 Locally complete approximation

In close analogy to the one-particle cumulant self-energy $\underset{\approx}{\Sigma}^c$, an effective two-particle cumulant vertex can be defined, which generally depends on three independent energy and momentum variables,

$$\underline{\underline{\underline{\underline{\Pi}}}}^c(i\omega_1, \underline{k}_1, i\omega_2, \underline{k}_2; i\omega_2', \underline{k}_2', i\omega_1', \underline{k}_1') \quad . \tag{2.3.18}$$

This vertex is build from all two-particle irreducible (2PI) diagrams. Two-particle irreducible means, that a diagram does not separate into two disconnected pieces by cutting any two inner lines, and thus is the direct extension of the concept of one-particle irreducibility.

In the spirit of the locally complete approximation and in analogy to the cumulant self-energy, as a first step this vertex is assumed to be momentum independent,

$$\underline{\underline{\underline{\underline{\Pi}}}}^c(i\omega_1, \underline{k}_1, i\omega_2, \underline{k}_2; i\omega_2', \underline{k}_2', i\omega_1', \underline{k}_1') \rightarrow \underline{\underline{\underline{\underline{\Pi}}}}^c(i\omega_1, i\omega_2; i\omega_2', i\omega_1') \quad . \tag{2.3.19}$$

Therefore only pseudo-local diagrams contribute, where all four external lines are attached to the same lattice site.

Before proceeding with the explicit selection of diagrams to be included in $\underset{\approx}{\underline{\underline{\underline{\underline{\Pi}}}}}^{c}|^{(lc)}$, Bethe-Salpeter equations will be given, which are valid for any choice of the cumulant vertex[7]. These describe the relations between the various two-particle lattice Green functions and constitute the two-particle analog of the Dyson equation.

Due to the rich structure of possible two-particle excitations on a lattice, additional lattice propagators and equations have to be introduced, which do not have their direct counterpart in the one-particle case. In order to keep track of the various functions, table 2.2 provides an overview and lists the equivalent one-particle functions, if possible.

The Bethe-Salpeter equation for the susceptibility matrix is obtained by explicitly summing all two-particle *reducible* diagrams not yet accounted for in the 2PI cumulant vertex,

$$\begin{aligned}\underline{\underline{\underline{\underline{\chi}}}}(\underline{q}, i\nu_n \,|\, i\omega_1, i\omega_2) = &-\underline{\underline{\underline{\underline{P}}}}(\underline{q}, i\nu_n \,|\, i\omega_1)\, \delta_{\omega_1,\omega_2} + \underline{\underline{\underline{\underline{P}}}}(\underline{q}, i\nu_n \,|\, i\omega_2)\, \underline{\underline{\underline{\underline{\Pi}}}}^{c,(amp)}(i\nu_n \,|\, i\omega_1, i\omega_2)\, \underline{\underline{\underline{\underline{P}}}}(\underline{q}, i\nu_n \,|\, i\omega_1) \\ &- \sum_{i\omega_3} \underline{\underline{\underline{\underline{S}}}}^c(\underline{q}, i\nu_n \,|\, i\omega_3, i\omega_2)\, \underline{\underline{\underline{\underline{\Pi}}}}^{c,(amp)}(i\nu_n \,|\, i\omega_1, i\omega_3) \underline{\underline{\underline{\underline{P}}}}(\underline{q}, i\nu_n \,|\, i\omega_1) \quad .\end{aligned} \tag{2.3.20}$$

Here, the two-particle cumulant transfer-propagator $\underset{\approx}{\underline{\underline{\underline{\underline{S}}}}}^c$ is introduced. It describes the correlated two-particle propagation, which starts with two elementary transfers and a Bethe-Salpeter equation can be formulated for it,

$$\begin{aligned}\underline{\underline{\underline{\underline{S}}}}^c(\underline{q}, i\nu_n \,|\, i\omega_1, i\omega_2) = &\underline{\underline{\underline{\underline{P}}}}(\underline{q}, i\nu_n \,|\, i\omega_2)\, \underline{\underline{\underline{\underline{\Pi}}}}^{c,(amp)}(i\nu_n \,|\, i\omega_1, i\omega_2)\, \underline{\underline{\underline{\underline{J}}}}(\underline{q}, i\nu_n \,|\, i\omega_1) \\ &- \sum_{i\omega_3} \underline{\underline{\underline{\underline{S}}}}^c(\underline{q}, i\nu_n \,|\, i\omega_3, i\omega_2)\, \underline{\underline{\underline{\underline{\Pi}}}}^{c,(amp)}(i\nu_n \,|\, i\omega_1, i\omega_3)\, \underline{\underline{\underline{\underline{J}}}}(\underline{q}, i\nu_n \,|\, i\omega_1) \quad .\end{aligned} \tag{2.3.21}$$

$\underline{\underline{\underline{\underline{P}}}}(\underline{q}, i\nu_n)$ and $\underline{\underline{\underline{\underline{J}}}}(\underline{q}, i\nu_n)$ are the full particle-hole propagator and its momentum dependent part as introduced in equations (2.3.14) to (2.3.16).

[7] Most of the lattice equations are even valid for a momentum dependent cumulant vertex, if the additional momentum dependencies and summations are re-introduced.

Two-particle quantity	**One-particle counterpart**	**Short description**
Local quantities		
$\underline{\underline{\underline{\underline{\tilde{G}\tilde{G}}}}}(i\nu_n\|i\omega_1)$ $\underline{\underline{\underline{\underline{\Lambda\tilde{G}\tilde{G}}}}}(i\nu_n\|i\omega_1)$	$\underline{\underline{G}}(i\omega_n)\|^{(0)}$	"non-interacting" local Green functions
$\underline{\underline{\underline{\Lambda}}}(i\nu_n\|i\omega_1)$	–	pseudo-local one-particle excitations
$\underline{\underline{\underline{\underline{\chi}}}}^{(loc)}(i\nu_n\|i\omega_1, i\omega_2)$	$\underline{\underline{G}}^{(loc)}(i\omega_n)$	local Green function
$\underline{\underline{\underline{\underline{\Pi}}}}^c(i\nu_n\|i\omega_1, i\omega_2)$	$\underline{\underline{\Sigma}}^c(i\omega_n)$	cumulant vertex/self-energy
$\underline{\underline{\underline{\underline{\tilde{G}^2}}}}(i\nu_n\|i\omega_1, i\omega_2)$ $\underline{\underline{\underline{\underline{\tilde{G}^{2,\Lambda}}}}}(i\nu_n\|i\omega_1, i\omega_2)$ $\underline{\underline{\underline{\underline{\Lambda\tilde{G}^{2,\Lambda}}}}}(i\nu_n\|i\omega_1, i\omega_2)$	$\underline{\underline{\tilde{G}}}(i\omega_n)$	effective local cumulant Green functions
$\underline{\underline{\underline{\underline{TT}}}}(i\nu_n\|i\omega_1, i\omega_2)$	$\underline{\underline{T}}(i\omega_n)$	reducible transfer matrix
$\widetilde{\underline{\underline{\underline{\underline{TT}}}}}(i\nu_n\|i\omega_1, i\omega_2)$	$\underline{\underline{\tilde{T}}}(i\omega_n)$	irreducible transfer matrix
Lattice quantities		
$\underline{\underline{\underline{\underline{tt}}}}(\underline{q}\|\underline{k})$	$\underline{\underline{t_k}}$	elementary transfer
$\underline{\underline{\underline{\underline{P}}}}(\underline{q}, i\nu_n\|\omega_1)$ $\underline{\underline{\underline{\underline{J}}}}(\underline{q}, i\nu_n\|\omega_1)$	$\underline{\underline{G}}(\underline{k}, i\omega_n)\|^{(1)}$	"non-interacting" lattice props. i.e. free theory
$\underline{\underline{\underline{\underline{\chi}}}}(\underline{q}, i\nu_n\|i\omega_1, i\omega_2)$	$\underline{\underline{G}}(\underline{k}, i\omega_n)$	lattice Green function
$\underline{\underline{\underline{\underline{S}}}}(\underline{q}, i\nu_n\|\omega_1, i\omega_2)$	$\underline{\underline{G}}(\underline{k}, i\omega_n)\underline{\underline{t_k}}$	transfer propagator
$\underline{\underline{\underline{\underline{S}}}}^c(\underline{q}, i\nu_n\|\omega_1, i\omega_2) =$ $\underline{\underline{\underline{\underline{S}}}}(\underline{q}, i\nu_n\|\omega_1, i\omega_2) + J(\underline{q}, \nu_n\|i\omega_1)\delta_{\omega_1,\omega_2}$	–	cumulant transfer-propagator

Table 2.2: Listing of the two-particle quantities and their corresponding one-particle counterparts. The term "non-interacting" refers to the absence of the explicit cumulant interaction vertex $\underline{\underline{\underline{\underline{\Pi}}}}^c$ and Σ^c for two- and one-particle quantities, respectively. It does not mean the standard non-interaction limit with $U_{\alpha\beta\gamma\delta} = 0$.

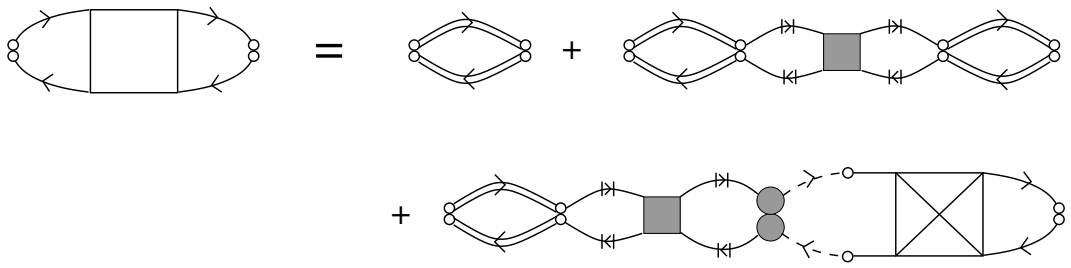

Figure 2.8: Bethe-Salpeter equation for the two-particle cumulant Green function

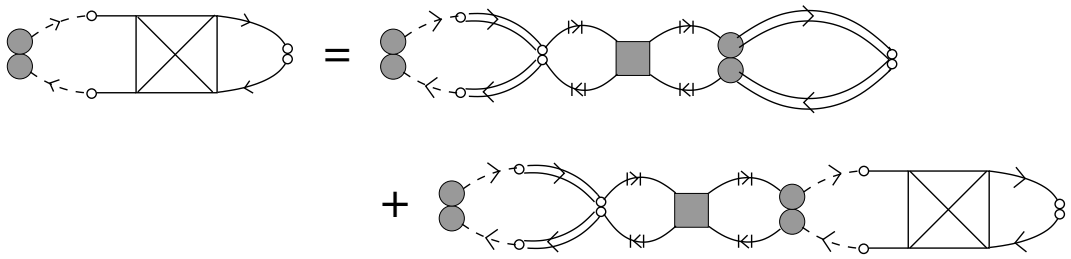

Figure 2.9: Equation for the two-particle cumulant transfer propagator $\underline{\underline{S}}^c$.

In the Bethe-Salpeter equation (2.3.20) the two-particle cumulant transfer-propagator $\underline{\underline{S}}^c(\underline{q}, i\nu_n \,|\, i\omega_3, i\omega_2)$ has to be introduced, because of the occurrence of the two explicit transfers attached to the cumulant vertex. The graphical representations of both equations is shown in figures 2.8 and 2.9. The crossed box signals, that only terms with at least one two-particle cumulant interaction vertex involving all four external lines contribute. The negative signs in front of the particle-hole propagators in equations (2.3.20) and (2.3.21) stem from the permutations necessary to obtain the ordering of the creation- and annihilation operators. These are viewed as part of the diagrammatic rules – for every closed fermionic loop a minus sign has to be included – and thus do not explicitly occur in the figures.

No explicit momentum sums appear in the Bethe-Salpeter equations as they are absorbed into the definitions of the quantities $\underline{\underline{P}}$, $\underline{\underline{S}}^c$ and $\underline{\underline{\chi}}$, cf. (2.3.13). Since no assumption regarding the frequency dependence of the effective local vertex are made, the sums over Matsubara frequencies remain and cannot be absorbed.

In the Bethe-Salpeter equation (2.3.20) the amputated version of the effective vertex is used and depicted as a shaded square. It is obtained by factorizing the one-particle contributions of the local site,

$$\underline{\underline{\Pi}}^c(i\nu_n \,|\, i\omega_1, i\omega_2) \equiv \underline{\underline{\tilde{G}\tilde{G}}}(i\nu_n \,|\, i\omega_2)\, \underline{\underline{\Pi}}^{c,(amp)}(i\nu_n \,|\, i\omega_1, i\omega_2)\, \underline{\underline{\tilde{G}\tilde{G}}}(i\nu_n \,|\, i\omega_1) \quad . \tag{2.3.22}$$

This is necessary because the particle-hole propagator already includes the start- and endpoint of the propagation and these must not be accounted for twice.

Having the locally complete approximation in mind, it is instructive to reformulate the Bethe-Salpeter equation (2.3.20). The aim is to summarize pseudo-local processes into an

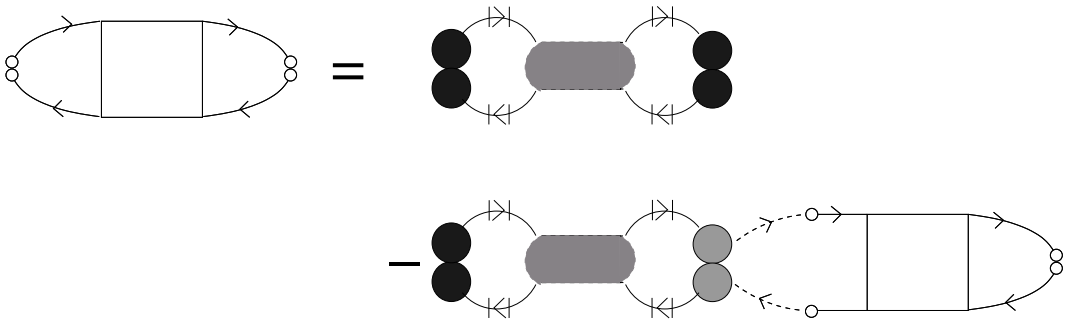

Figure 2.10: Alternative Bethe-Salpeter equations for the lattice susceptibility expressed with the effective local two-particle cumulant Green functions

effective local two-particle cumulant Green function analog to $\tilde{\underline{\underline{G}}}$. Using the expansion of the particle-hole propagator (2.3.15) in the Bethe-Salpeter equation (2.3.20), an alternative formulation can be deduced (see figure 2.10)

$$\underline{\underline{\chi}}(\underline{q}, i\nu_n \,|\, i\omega_1, i\omega_2) = \underline{\underline{\Lambda}}(i\nu_n \,|\, i\omega_2)\, \underline{\underline{\tilde{G}}}^{2,\Lambda}(i\nu_n \,|\, i\omega_1, i\omega_2) \tag{2.3.20a}$$
$$- \sum_{i\omega_3} \underline{\underline{\tilde{G}\tilde{G}}}(i\nu_n \,|\, i\omega_2)\, \underline{\underline{S}}^{(amp)}(\underline{q}, i\nu_n \,|\, i\omega_3, i\omega_2)\, \underline{\underline{\tilde{G}}}^{2,\Lambda}(i\nu_n \,|\, i\omega_1, i\omega_3) \quad ,$$

where the amputated two-particle transfer propagator $\underline{\underline{S}}^{(amp)}$ is introduced. The (unamputated) two-particle transfer propagator $\underline{\underline{S}}$ is closely related to the two-particle cumulant transfer propagator $\underline{\underline{S}}^c$ via

$$\underline{\underline{S}}(\underline{q}, i\nu_n \,|\, i\omega_1, i\omega_2) = -\underline{\underline{J}}(\underline{q}, i\nu_n \,|\, i\omega_1)\delta_{i\omega_1, i\omega_2} + \underline{\underline{S}}^c(\underline{q}, i\nu_n \,|\, i\omega_1, i\omega_2) \quad . \tag{2.3.23}$$

The effective local two-particle cumulant Green function introduced in (2.3.20a) is (see figure 2.11)

$$\underline{\underline{\tilde{G}}}^{2,\Lambda}(i\nu_n \,|\, i\omega_1, i\omega_2) = -\underline{\underline{\tilde{G}\tilde{G}}}(i\nu_n \,|\, i\omega_1)\, \delta_{i\omega_1, i\omega_2} + \underline{\underline{\Pi}}^c(i\nu_n \,|\, i\omega_1, i\omega_2)\, \underline{\underline{\Lambda}}(i\nu_n \,|\, i\omega_1) \quad . \tag{2.3.24}$$

The first term on the right $\underline{\underline{\tilde{G}\tilde{G}}}$ represents the effective two-particle cumulant Green function without any explicit two-particle interaction. The minus sign associated with it reflects the fact that this term originates from the particle-hole propagator, but the closed fermion loop is no longer visible in the diagrammatic representation.

The modification $\underline{\underline{\Lambda}}$ at the cumulant vertex stems from the momentum independent part of the particle-hole propagator (see equations (2.3.17) and (2.3.15)) and represents a particle-hole propagation where only one particle (or hole) leaves the site. These processes must necessarily be considered when separating the Bethe-Salpeter equation into pseudo-local and non-local parts. The reason for their inevitable appearance lies in the momentum sums already performed in the quantity $\underline{\underline{\chi}}(\underline{q}, i\nu_n \,|\, i\omega_1, i\omega_2)$, see (2.3.13). Equations (2.3.20) and (2.3.21) represent the fundamental equations in accord with the diagrammatic rules of the cumulant perturbation theory. They are also valid, if generalized to a momentum dependent cumulant vertex $\underline{\underline{\Pi}}^c(q, i\nu_n | \underline{k}_1, \underline{k}_2 | i\omega_1, i\omega_2)$, omitting the external momentum sums,

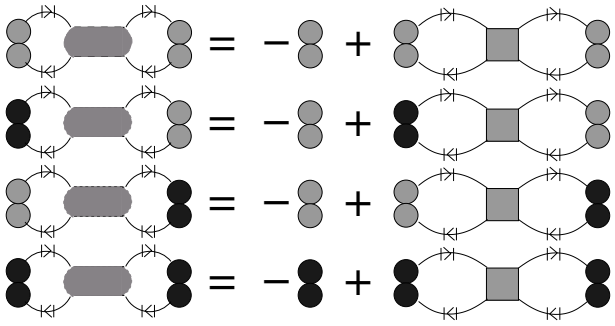

Figure 2.11: The effective local two-particle cumulant Green functions $\underline{\underline{\tilde{G}}}^2$, $\underline{\underline{\tilde{G}}}^{2,\Lambda}$, $\underline{\underline{\Lambda}}\underline{\underline{\tilde{G}}}^{2,\Lambda}\underline{\underline{\Lambda}}^{-1}$ (see footnote 8), and $\underline{\underline{\Lambda}}\underline{\underline{\tilde{G}}}^{2,\Lambda}$ (from top to bottom).

and stating the explicit momentum dependencies of all quantities. But in the reformulation (2.3.20a) the external momentum sums appearing in $\underline{\underline{P}}$ are partially performed and therefore terms occur, which were originally not allowed.

Equation (2.3.20a) is the two-particle analog of the Dyson equation (2.2.5) with 1PI diagrams replaced by 2PI diagrams, along with the resulting factors of $\underline{\underline{\Lambda}}$, and the complication of a second equation needed for the two-particle transfer propagator $\underline{\underline{S}}$.

After having presented all necessary equations for lattice Green functions, the remaining task is to implement the locally complete approximation for the cumulant vertex. The goal is to establish an effective impurity picture for the two-particle quantities in close analogy to the one-particle case of the previous section.

From equation (2.3.20a) the local two-particle Green function can be constructed: iterating it once using the equation for $\underline{\underline{S}}$ and the fact that $\sum_{\underline{q},\underline{k}} \underline{\underline{tt}}(\underline{q}|\underline{k}) = 0$ yields[8]

$$\begin{aligned}\underline{\underline{\chi}}^{(loc)}(i\nu_n \,|\, i\omega_1, i\omega_2) &\equiv \frac{1}{N_0}\sum_{\underline{q}} \underline{\underline{\chi}}(\underline{q}, i\nu_n \,|\, i\omega_1, i\omega_2) \\ &= \underline{\underline{\Lambda}}(i\nu_n \,|\, i\omega_2)\, \underline{\underline{\tilde{G}}}^{2,\Lambda}(i\nu_n \,|\, i\omega_1, i\omega_2) \qquad (2.3.25) \\ &+ \sum_{i\omega_3, i\omega_4} \underline{\underline{\Lambda}}(i\nu_n \,|\, i\omega_2)\underline{\underline{\tilde{G}}}^{2,\Lambda}(i\nu_n \,|\, i\omega_4, i\omega_2)\underline{\underline{\Lambda}}(i\nu_n \,|\, i\omega_4)^{-1}\, \underline{\underline{TT}}(i\nu_n \,|\, i\omega_3, i\omega_4)\, \underline{\underline{\tilde{G}}}^{2,\Lambda}(i\nu_n \,|\, i\omega_1, i\omega_3) \quad .\end{aligned}$$

The quantity $\underline{\underline{TT}}$ is closely related to the $\underline{q}$-summed two-particle transfer propagator and represents the two-particle scattering matrix, where both particles leave the local site and propagate through the lattice (see figure 2.12).

Equation (2.3.25) is the analog of the one-particle equation (2.2.9) and establishes the connection between the effective local two-particle cumulant Green function $\underline{\underline{G}}^{2,\Lambda}$ (or equivalently the local cumulant vertex $\underline{\underline{\Pi}}^c$) and the local physical Green function.

[8] The cumbersome expression $\underline{\underline{\Lambda}}\,\underline{\underline{\tilde{G}}}^{2,\Lambda}\underline{\underline{\Lambda}}^{-1}$ just represents $\underline{\underline{\tilde{G}}}^{2,\Lambda}$, but with the factor of $\underline{\underline{\Lambda}}$ at the other side of the vertex, i.e. $\underline{\underline{\Lambda}}\,\underline{\underline{\tilde{G}}}^{2,\Lambda}\underline{\underline{\Lambda}}^{-1} = -\underline{\underline{\tilde{G}\tilde{G}}}\,\delta_{i\omega_1,i\omega_2} + \underline{\underline{\Lambda}}\,\underline{\underline{\Pi}}^c$ (see figure 2.11). This form is used to avoid another abbreviation.

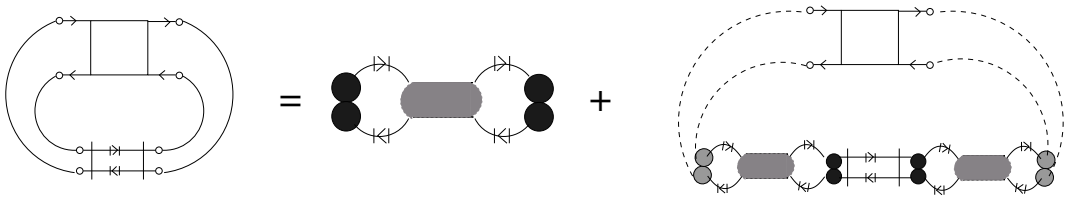

Figure 2.12: Bethe-Salpeter equation for the local two-particle Green function $\underline{\underline{\chi}}^{(loc)}$.

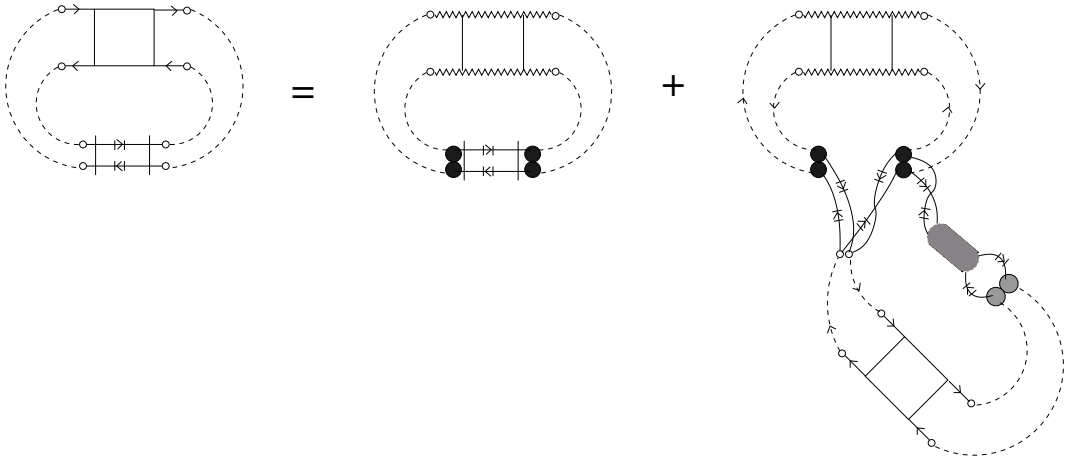

Figure 2.13: The decomposition of the two-particle scattering matrix $\underline{\underline{\underline{\underline{TT}}}}$ into irreducible propagations $\widetilde{\underline{\underline{\underline{\underline{TT}}}}}$ and repeated visits to the local site.

In complete analogy to the one-particle case (2.2.11), the scattering matrix $\underline{\underline{\underline{\underline{TT}}}}$ can be constructed from an irreducible scattering matrix $\widetilde{\underline{\underline{\underline{\underline{TT}}}}}$, which describes the simultaneous propagation of two particles starting and ending at the same site without any intermediate returns to this specific site. The full scattering matrix is then build up from repeated visits to the local site with irreducible loop-propagations in between (see figure 2.13),

$$\begin{aligned}\underline{\underline{\underline{\underline{TT}}}}(i\nu_n \,|\, i\omega_1, i\omega_2) = \underline{\underline{\Lambda}}(i\nu_n \,|\, i\omega_2)\, \widetilde{\underline{\underline{\underline{\underline{TT}}}}}(i\nu_n \,|\, i\omega_1, i\omega_2)\, \underline{\underline{\Lambda}}(i\nu_n \,|\, i\omega_1) \qquad (2.3.26)\\ + \sum_{i\omega_3, i\omega_4} \underline{\underline{\underline{\underline{TT}}}}(i\nu_n \,|\, i\omega_4, i\omega_2)\, \underline{\underline{\tilde{G}}}^{2,\Lambda}(i\nu_n \,|\, i\omega_3, i\omega_4) \widetilde{\underline{\underline{\underline{\underline{TT}}}}}(i\nu_n \,|\, i\omega_1, i\omega_3)\, \underline{\underline{\Lambda}}(i\nu_n \,|\, i\omega_1) \quad .\end{aligned}$$

The only structural difference of this form to the one-particle case lies in the appearance of the factors $\underline{\underline{\Lambda}}$, representing the single electron recurrence procedure.

At this point the identity

$$\sum_{i\omega_3} \underline{\underline{\underline{\underline{TT}}}}(i\nu_n \,|\, i\omega_3, i\omega_2)\, \underline{\underline{\tilde{G}}}^{2,\Lambda}(i\nu_n \,|\, i\omega_1, i\omega_3) = \sum_{i\omega_3} \underline{\underline{\Lambda}}(i\nu_n \,|\, i\omega_2)\, \widetilde{\underline{\underline{\underline{\underline{TT}}}}}(i\nu_n \,|\, i\omega_3, i\omega_2)\, \underline{\underline{\chi}}^{(loc)}(i\nu_n \,|\, i\omega_1, i\omega_3) \qquad (2.3.27)$$

and the equivalent form with the order of the matrix products reversed,

$$\sum_{i\omega_3} \underline{\underline{\Lambda}}(i\nu_n \,|\, i\omega_2)\underline{\underline{\tilde{G}}}^{2,\Lambda}(i\nu_n \,|\, i\omega_3, i\omega_2)\, \underline{\underline{\Lambda}}(i\nu_n \,|\, i\omega_3)^{-1}\underline{\underline{TT}}(i\nu_n \,|\, i\omega_1, i\omega_3) \tag{2.3.28}$$
$$= \sum_{i\omega_3} \underline{\underline{\chi}}^{(loc)}(i\nu_n \,|\, i\omega_3, i\omega_2)\, \widetilde{\underline{\underline{TT}}}(i\nu_n \,|\, i\omega_1, i\omega_3)\, \underline{\underline{\Lambda}}(i\nu_n \,|\, i\omega_1)$$

can be proven by comparing equations (2.3.25) and (2.3.26). These are the two-particle versions of (2.2.12) and as in the one-particle case, reflect the topology of the decompositions of the local Green function and the effective local cumulant in terms of reducible and irreducible loops.

Utilizing the the above identities in equation (2.3.25) a closed equation for the local Green function is obtained

$$\underline{\underline{\chi}}^{(loc)}(i\nu_n \,|\, i\omega_1, i\omega_2) = \underline{\underline{\Lambda}}(i\nu_n \,|\, i\omega_2)\, \underline{\underline{\tilde{G}}}^{2,\Lambda}(i\nu_n \,|\, i\omega_1, i\omega_2) \tag{2.3.29}$$
$$+ \sum_{i\omega_3, i\omega_4} \underline{\underline{\chi}}^{(loc)}(i\nu_n \,|\, i\omega_3, i\omega_2)\, \widetilde{\underline{\underline{TT}}}(i\nu_n \,|\, i\omega_4, i\omega_3)\, \underline{\underline{\Lambda}}(i\nu_n \,|\, i\omega_3)\, \underline{\underline{\tilde{G}}}^{2,\Lambda}(i\nu_n \,|\, i\omega_1, i\omega_3) \quad .$$

All equations derived so far incorporate inner frequency sums and thus have the character of integral equations for the unknown functions. In order to get an insight into the structure of the above equations, it is beneficial to switch to a slightly different notation: the dependence on the discrete Matsubara frequencies can be interpreted as an additional matrix structure. In this Matsubara-matrix space representation of dynamic quantities frequency sums transform into simple matrix multiplications.

Equation (2.3.29) can be solved in Matsubara-matrix space to give

$$\underline{\underline{\chi}}^{(loc)} = \left[\left(\underline{\underline{\Lambda}}\, \underline{\underline{\tilde{G}}}^{2,\Lambda} \right)^{-1} - \widetilde{\underline{\underline{TT}}} \right]^{-1} \quad . \tag{2.3.30}$$

This clearly demonstrates the resemblance to the one-particle equation (2.2.13), as the physical local Green function has exactly the same structure expressed in terms of a effective local cumulant and an effective irreducible loop propagator.

To derive a closed form for the lattice susceptibility, equation (2.3.30) is used to express the effective local vertex in terms of the local Green function, i.e.

$$\underline{\underline{\Pi}}^{c,(amp)} = \left(\underline{\underline{\Lambda}}\, \underline{\underline{\tilde{G}\tilde{G}}} \right)^{-1} + \underline{\underline{\chi}}^{(loc)} \left[\underline{\underline{\Lambda}}\, \underline{\underline{\tilde{G}\tilde{G}}} \left(1 + \underline{\underline{\chi}}^{(loc)}\, \widetilde{\underline{\underline{TT}}} \right) \underline{\underline{\Lambda}}\, \underline{\underline{\tilde{G}\tilde{G}}} \right]^{-1} \quad . \tag{2.3.31}$$

Eliminating the cumulant vertex from equations (2.3.20) and (2.3.21), the resulting lattice susceptibility matrix can be stated (in orbital and Matsubara-matrix space)

$$\underline{\underline{\chi}}_{\underline{q}, i\nu_n} = \left[-\underline{\underline{P}}^{-1}_{\underline{q}, i\nu_n} + \underline{\underline{\chi}}^{(loc)^{-1}}_{i\nu_n} + \left(\underline{\underline{\Lambda}}\, \underline{\underline{\tilde{G}\tilde{G}}}_{i\nu_n} \right)^{-1} + \widetilde{\underline{\underline{TT}}}_{i\nu_n} \right]^{-1} \quad , \tag{2.3.32}$$

where the dependence on the external variables is indicated as subscripts.

Formulas (2.3.30)-(2.3.32) clearly suggest the same interpretation as in the one-particle case: when expressed in terms of physical local averages, the effective local cumulant Green

function and vertex incorporate a multitude of unphysical products connected by irreducible two-particle loops. These must be subtracted with the help of the irreducible scattering matrix to yield a physical two-particle Green function.

The interpretation of $\widetilde{\underline{\underline{TT}}}$ as an effective medium, which seems familiar with respect to the analogy to the one-particle case, is somewhat misleading: the connection of all the above formulas, which are valid for the lattice model, to an effective impurity embedded self-consistently into a non-interacting medium has not been established.

Up to now, diagrams contributing to the effective cumulant vertex $\underline{\underline{\Pi}}^c$ have not been specified in detail. The only assumption was its momentum independence and all above formulas are valid for any selection of diagrams So of the selection rules characterizing the locally complete approximation (see page 11) only the first one is utilized. As for the second rule, diagrams containing local cumulant vertices connected by two or more lines are not only implicitly present in the the effective vertex $\underline{\underline{\Pi}}^c$, but also explicitly in all the above Bethe-Salpeter equations, irregardless of the diagrams selected for $\underline{\underline{\Pi}}^c$! Any two-particle lattice propagator, such as $\underline{\underline{\chi}}$, $\underline{\underline{S}}$, or $\underline{\underline{TT}}$, is build from local two-particle interactions with free particle-hole propagations in between. A contribution incorporating more than one effective cumulant vertex $\underline{\underline{\Pi}}^c$ has necessarily two cumulant vertices sitting on different sites joined by more than two electronic lines. Thus, the second defining rule b) for the locally complete approximation can strictly not be implemented for the two-particle properties (unless in the trivial approximation without explicit two-particle interactions, where the lattice susceptibility is given by the particle-hole propagator). Consequently, the construction of a fully self-consistent theory analog to the one-particle approximation is not possible and the self-consistent impurity picture of the one-particle case not directly applicable.

However, the impurity picture does not need to be discarded as a whole. The physical local Green function as described by equations (2.3.25) and (2.3.26) could be characterized as that of an effective impurity embedded in an *interacting* medium. The local two-particle Green function could be expressed as a functional of the effective one- and two-particle media,

$$\underline{\underline{\chi}}^{(loc)} = \underline{\underline{\chi}}^{(imp)}[\underline{\tilde{\underline{T}}}, \widetilde{\underline{\underline{TT}}}] \quad . \tag{2.3.33}$$

To obtain a consistent approximation, the effective media $\underline{\tilde{\underline{T}}}$ and $\widetilde{\underline{\underline{TT}}}$ must be determined self-consistently from the lattice equations. Since the two-particle medium in general incorporates explicit two-particle interactions, these must be respected in the one-particle quantities as well (which is not done in the locally complete approximation). Such a self-consistent formulation poses a highly non-trivial task and will not be considered further.

As an alternative route, an approximation is made to the effective two-particle medium $\widetilde{\underline{\underline{TT}}}$, which is assumed to incorporate no correlated loops. For the effective cumulant vertex $\underline{\underline{\Pi}}^c$ this implies, that it can be calculated along the very same line as the cumulant self-energy in section 2.2 (with the only modification of four attached external lines). The selection rules of the locally complete approximation a) and b) are strictly implemented for it and inner lines have the structure of uncorrelated nested loops. Therefore the physical local two-particle Green function $\underline{\underline{\chi}}^{(loc)}$ can be obtained by summing all two-particle reducible processes via equation (2.3.29), but using the *non-interacting* medium $\widetilde{\underline{\underline{TT}}}|^{(lc)}$. So the

picture of an effective impurity embedded in a non-interacting medium is again suitable for the local Green function.

The difference to the one-particle case lies in the processes explicitly incorporated into the lattice susceptibility. These include graphs, which *do* produce correlated loops in the local Green function when calculated by a momentum sum of the lattice Green function. As a consequence, the local two-particle Green function calculated as a momentum sum from the lattice Green function does not equal the one calculated from the effective impurity picture with the uncorrelated medium,

$$\frac{1}{N_0}\sum_{\underline{q}} \underline{\underline{\chi}}(\underline{q}, i\nu_n \,|\, i\omega_1, i\omega_2)|^{(lc)} \neq \underline{\underline{\chi}}^{(loc)}(i\nu_n \,|\, i\omega_1, i\omega_2)|^{(imp)} \quad . \tag{2.3.34}$$

Therefore the self-consistency of the local and lattice two-particle propagator is not achieved.

In order to model the non-interacting two-particle medium, correlations are neglected in the effective two-particle medium and thus loop-propagations reduce to one-particle propagations only. This implies the irreducible two-particle scattering matrix $\widetilde{\underline{\underline{TT}}}$ is solely determined by its one-particle counterpart $\tilde{\underline{\underline{T}}}$,

$$\widetilde{\underline{\underline{TT}}}(i\nu_n \,|\, i\omega_1, i\omega_2)|^{(lc)} = -\left(\tilde{\underline{\underline{T}}}(i\omega_1) \otimes \tilde{\underline{\underline{T}}}(i\omega_1 + i\nu_n)\right) \underline{\underline{\Lambda}}(i\nu_n \,|\, i\omega_1)^{-1}\delta_{\omega_1,\omega_2} \quad . \tag{2.3.35}$$

The negative sign here stems from the fact that the scattering matrices are derived from the $\underline{q}$-summed two-particle transfer propagator, where the start- and endpoint of the propagation are subtracted. Without explicit two-particle interactions during the propagation, this quantity just reduces to some amputated part of the q-summed particle-hole propagator (2.3.15) (i.e. $\sum_{\underline{q}} \underline{\underline{J}}^{(amp)}(\underline{q}, i\nu_n|i\omega_1)$ from (2.3.16)) and thus carries a minus sign due to the closed fermion loop. The inverse factor of $\underline{\underline{\Lambda}}$ is due to the definition of the irreducible scattering matrix, as the amplitude where *both* electrons simultaneously leave the local site.

Notice that in this approximation the scattering matrix $\underline{\underline{TT}}$ is not just the product of the uncorrelated one-particle scattering matrices, i.e.

$$\underline{\underline{TT}}(i\nu_n \,|\, i\omega_1, i\omega_2)|^{(lc)} \neq -\underline{\underline{T}}(i\omega_1) \otimes \underline{\underline{T}}(i\omega_1 + i\nu_n)\delta_{\omega_1,\omega_2} \quad , \tag{2.3.36}$$

as it could be suspected naïvely. Two-particle correlations are only discarded in the medium, but locally all cumulant vertices are retained, since the second term in equation (2.3.26) or figure 2.13 involving $\tilde{\underline{\underline{G}}}^{2,\Lambda}$ is not dropped. The Matsubara-matrix space representation reveals the structure of $\underline{\underline{TT}}|^{(lc)}$

$$\underline{\underline{TT}}|^{(lc)} = -\left(\underline{\underline{T}} \otimes \underline{\underline{T}}\right) \left[1 + \underline{\underline{\Pi}}^{c}|^{(lc)} \left(\underline{\underline{T}} \otimes \underline{\underline{T}}\right)\right]^{-1} \quad , \tag{2.3.37}$$

which can be derived by using equations (2.3.26), (2.3.17) and (2.2.11). This very instructive form confirms the insight, that the uncorrelated one-particle loops get renormalized by interaction vertices whenever the particles visit the local lattice site.

The explicit form (2.3.35) can be used to express the irreducible scattering matrix as

$$\widetilde{\underline{\underline{TT}}}(i\nu_n|i\omega_1, i\omega_2)|^{(lc)} = \left[-\left(\underline{\underline{\Lambda}}(\underline{q}, i\nu_n \,|\, i\omega_1)\, \underline{\underline{\tilde{G}\tilde{G}}}(i\nu_n \,|\, i\omega_1)\right)^{-1} + \underline{\underline{P}}^{(loc)}(i\nu_n|i\omega_1)^{-1}\right] \delta_{\omega_1,\omega_2} \quad , \tag{2.3.38}$$

where the local particle-hole propagator is the $\underline{q}$-summed lattice particle-hole propagator and is just given by the product of two local one-particle Green functions,

$$\begin{aligned}\underline{\underline{P}}^{(loc)}(\underline{q}, i\nu_n|i\omega_1) &\equiv \frac{1}{N_0}\sum_{\underline{q}} \underline{\underline{P}}(\underline{q}, i\nu_n \,|\, i\omega_1) = \frac{1}{N_0^2}\sum_{\underline{q},\underline{k}} \underline{\underline{GG}}(q, i\nu_n|\underline{k}|i\omega_1) \\ &= \underline{\underline{G^{(loc)}G^{(loc)}}}(i\nu_n \,|\, i\omega_1) \quad .\end{aligned} \tag{2.3.39}$$

Inserting this form into the equation (2.3.32), the final form for the lattice susceptibility in Matsubara-matrix space can be stated

$$\underline{\underline{\chi}}_{q,i\nu_n}|^{(lc)} = \left[-\underline{\underline{P}}^{-1}_{\underline{q},i\nu_n} + \underline{\underline{\chi}}^{(loc)^{-1}}_{i\nu_n} + \underline{\underline{P}}^{(loc)^{-1}}_{i\nu_n}\right]^{-1} \quad . \tag{2.3.40}$$

Again, in the above equation $\underline{\underline{\chi}}^{(loc)}$ is the susceptibility calculated for an impurity model with the uncorrelated effective medium $\underline{\underline{\tilde{T}}}$. This form of the susceptibility is a generalization to orbital matrices of the usual scalar one known from the DMFT [Zla90, Jar92, Jar95][9].

Expressions (2.3.32) and (2.3.40) are presented in order to clarify the structure of the investigated equations for the susceptibility. The Matsubara-matrix representations will not be used for calculations in this work. Instead, the analytic continuation of all Matsubara frequencies to the real axis is the principal goal of the above treatment. This seems possible, since by means of the effective impurity picture the local susceptibility function $\underline{\underline{\chi}}^{(loc)}(i\nu_n|i\omega_1, i\omega_2)$, along with its analytical continuations to the real axis $\underline{\underline{\chi}}^{(loc)}(\nu_n \pm i\delta_\nu|\omega_1 \pm i\delta_1, \omega_2 \pm i\delta_2)$ are known. Thus equation (2.3.29), along with the irreducible scattering matrix (2.3.35), can be continued to the real axis, transforming into an set of integral equations for the unknown effective vertex functions $\underline{\underline{\Pi}}^c(\nu_n \pm i\delta_\nu|\omega_1 \pm i\delta_1, \omega_2 \pm i\delta_2)$. After obtaining the vertex functions, the analog procedure can be applied to equation (2.3.21) yielding the analytically continued transfer propagators $\underline{\underline{S}}$. The lattice susceptibility can then be calculated via (2.3.20) or (2.3.20a). All other functions can be directly calculated using one-particle Green functions.

With this rather involved procedure, the shortcomings of the Matsubara-space formalism are circumvented: the Fermi and Bose frequencies form countable infinite sets, which make the Matsubara-space matrices formally infinite dimensional. This can obviously not be sustained in practical calculations. The sets of frequencies must be truncated to some finite number N, so that any two-particle quantity $\underline{\underline{A}}(i\omega_1, i\omega_2)$ can be represented as a

[9] In the DMFT this equation is usually motivated by applying the $D \to \infty$ limit and the effective impurity picture directly to show the momentum independence of the vertex function Γ (see page 17) and then constituting the lattice Bethe-Salpeter equation

$$\chi(\underline{q}, \nu_n) = -P(\underline{q}, \nu_n) - P(\underline{q}, \nu_n)\Gamma(\nu_n)\chi(\underline{q}, \nu_n)$$

along with an analog local one

$$\chi^{(loc)}(\nu_n) = -P^{(loc)}(\nu_n) - P^{(loc)}(\nu_n)\Gamma^{(loc)}(\nu_n)\chi^{(loc)}(\nu_n) \quad .$$

Equating the unknown vertex functions $\Gamma = \Gamma^{(loc)}$ and eliminating it from the two equations directly yields (2.3.40).

$N \times N$-matrix. The frequency $\omega_N = (2N+1)\pi T$ then represents an energy cut-off proportional to the temperature T. Therefore the truncation error becomes worse, the lower the temperature.

A more severe point in connection with the Matsubara-space formulation is, that the desired quantities are obtained as sets of discrete Fourier coefficients evaluated at imaginary frequencies only. In order to obtain a physical observable function depending on real frequencies, these discrete sets need to be analytically continued to the real axis. Since the data points are known only numerically, the analytical continuation must be performed numerically as well, with maximum entropy-, Padé-, or other methods. This poses a non-trivial, generally ill-conditioned problem and therefore involves a considerable amount of arbitrariness.

Decoupling scheme

Instead of employing the afore mentioned involved procedure of solving sets of integral equations at the real frequency axis, it is instructive to study the results obtained within a decoupling scheme for the frequency sums. The sums in equations (2.3.20), (2.3.21) and (2.3.29) are decoupled in a manner similar to the random phase approximation (RPA), i.e.

$$\sum_{i\omega_3} \underline{\underline{A}}(i\nu_n \,|\, i\omega_3, i\omega_2)\underline{\underline{B}}(i\nu_n \,|\, i\omega_1, i\omega_3) \rightarrow \underline{\underline{A}}(i\nu_n \,|\, i\omega_1, i\omega_2) \sum_{i\omega_3} \underline{\underline{B}}(i\nu_n \,|\, i\omega_1, i\omega_3) \quad . \tag{2.3.41}$$

After performing sums over the frequencies $i\omega_1$ and $i\omega_2$, the physical lattice susceptibility (2.3.13) is obtained and the resulting form is in a directly analogy to (2.3.40),

$$\underline{\underline{\chi}}(\underline{q}, \nu) = \left[-\underline{\underline{P}}(\underline{q}, \nu)^{-1} - \underline{\underline{\Gamma}}(\nu) \right]^{-1} \quad , \tag{2.3.42}$$

where the abbreviation

$$\underline{\underline{\Gamma}}(\nu) = -\underline{\underline{\chi}}^{(loc)}(\nu)^{-1} - \underline{\underline{P}}^{(loc)}(\nu)^{-1} \tag{2.3.43}$$

was introduced. The indicated matrices represent the orbital structure only and all quantities are functions of the real frequency ν. The local and lattice particle-hole propagators for real frequencies can be calculated using standard techniques for the evaluation of Matsubara sums,

$$\underline{\underline{P}}^{(loc)}(\nu) = \int_{-\infty}^{\infty} d\omega \; f(\omega) \left[\underline{\underline{\rho}}(\omega) \otimes \underline{\underline{G}}(\omega+\nu+i\delta) + \underline{\underline{G}}(\omega-\nu-i\delta) \otimes \underline{\underline{\rho}}(\omega) \right] \tag{2.3.44}$$

$$\underline{\underline{P}}(\underline{q}, \nu) = \int_{-\infty}^{\infty} d\omega \int_{BZ} \frac{d^D\underline{k}}{(2\pi)^D} \; f(\omega) \Big[\underline{\underline{\rho}}(\underline{k}, \omega) \otimes \underline{\underline{G}}(\underline{k}+\underline{q}, \omega+\nu+i\delta) \tag{2.3.45}$$

$$+ \underline{\underline{G}}(\underline{k}, \omega-\nu-i\delta) \otimes \underline{\underline{\rho}}(\underline{k}+\underline{q}, \omega) \Big] \quad ,$$

with the spectral functions

$$\underset{\approx}{\rho}(\underline{k},\omega) = -\frac{1}{2\pi i}\left(\underset{\approx}{G}(\underline{k},\omega+i\delta) - \underset{\approx}{G}(\underline{k},\omega-i\delta)\right) \tag{2.3.46}$$

$$\underset{\approx}{\rho}(\omega) = \frac{1}{N_0}\sum_{\underline{k}} \underset{\approx}{\rho}(\underline{k},\omega) = -\frac{1}{2\pi i}\left(\underset{\approx}{G}(\omega+i\delta) - \underset{\approx}{G}(\omega-i\delta)\right) \tag{2.3.47}$$

and the momentum integral over the whole Brillouin-Zone (BZ) in D space-dimensions.

The susceptibility of equation (2.3.42) has the typical RPA or Stoner-form and lends itself to a direct physical interpretation: the freely propagating electron-hole excitations, represented by the "non-interacting" particle-hole susceptibility $-\underline{\underline{P}}(\underline{q},\nu)$, interact via the *dynamic* local interaction vertex $\underline{\underline{\Gamma}}(\nu)$. But the particle-hole excitations are certainly not non-interacting, since the propagator is calculated with the fully interacting one-particle Green function, and only the explicit two-particle interactions are excluded.

In contrast to that, in the usual weak-coupling RPA [Don74, Whi83, Sch99a] or extensions thereof, such as the fluctuation exchange approximation (FLEX) [Bic89a, Bic89b, Bic91] and the two-particle self-consistent approach (TPSC) [Vil94a, Vil94b], $\underline{\underline{P}}(\underline{q},\nu)$ is either calculated without the interaction, or interaction processes are included only at a very crude level. The same is true in the auxiliary boson approach [Kha96, Sai98] and equation of motion decoupling schemes [Row68, Ere01, Uld05]. The neglect of life-time and many-body effects in the one-particle Green function can lead to considerably different particle-hole propagators than the ones calculated with the strongly renormalized particles.

Furthermore, in the above mentioned approximation schemes the two-particle interaction vertices are given by weighted linear combinations of bare interaction matrix elements $U_{\alpha\beta\gamma\delta}$, i.e. numbers. The frequency dependence of two-particle vertices is usually ignored.

Finite order cumulant expansions in t as [Mos97b, She07, She08] do respect the leading frequency dependence of the two-particle vertex and include leading order non-local effects, but again life-time effects and Kondo physics are completely ignored.

Notice that the interpretation of equation (2.3.42) is not mandatory since the susceptibility can be re-written as

$$\underline{\underline{\chi}}(\underline{q},\nu) = \left[\underline{\underline{\chi}}^{(loc)}(\nu)^{-1} - \underline{\underline{J}}(\underline{q},\nu)\right]^{-1} \quad , \tag{2.3.42a}$$

with

$$\underline{\underline{J}}(\underline{q},\nu) = \underline{\underline{P}}(\underline{q},\nu)^{-1} - \underline{\underline{P}}^{(loc)}(\nu)^{-1} \quad . \tag{2.3.48}$$

This form would suggest the interpretation of localized magnetic moments, described by the local susceptibility $\underline{\underline{\chi}}^{(loc)}(\nu)$, interacting via a lattice dependent effective exchange interaction $\underline{\underline{J}}(\underline{q},\nu)$. This is the extreme opposite of the interpretation above, since localized moments are expected in the strong-coupling limit, where the electrons tend to be localized.

The two opposing viewpoints on equations (2.3.42) and (2.3.42a) already hint at the fact, that the atomic and the non-interacting band limit are correctly reproduced:

- In the atomic limit the hopping matrix elements vanish, i.e. $\underset{\approx}{t_{\underline{k}}} = 0$, and the lattice particle-hole propagator becomes identical to the local one, $\underline{\underline{P}}(\underline{q},\nu)|^{(t=0)} = \underline{\underline{P}}(\nu)|^{(loc)}$ and the susceptibility correctly reduces to the fully interacting susceptibility of an isolated ion,

$$\underline{\underline{\chi}}(\underline{q},\nu)|^{(t=0)} = \underline{\underline{\chi}}^{(loc)}(\nu) \quad . \tag{2.3.49}$$

- In the non-interacting limit the Coulomb matrix elements vanish, i.e. $U_{\alpha\beta\gamma\delta} = 0$, Wick's theorem is applicable and the local susceptibility reduces to the negative local particle-hole propagator $\underline{\underline{\chi}}^{(loc)}(\nu)|^{(U=0)} = -\underline{\underline{P}}(\nu)|^{(loc)}$. The resulting susceptibility is that of non-interacting particles on a lattice,

$$\underline{\underline{\chi}}(\underline{q},\nu)|^{(U=0)} = -\underline{\underline{P}}(\underline{q},\nu)|^{(U=0)} \quad . \tag{2.3.50}$$

So the resemblance of (2.3.42) and (2.3.42a) to RPA forms is only superficial, since the two opposite limits of weak and strong coupling are incorporated correctly into the theory and, more importantly, in any of the two opposite interpretations, the form of the *dynamic* interaction vertices $\underline{\underline{\Gamma}}(\nu)$ or $\underline{\underline{J}}(\underline{q},\nu)$ are explicitly known.

These considerations spur the hope, that the above developed theory is able to correctly describe the regime of intermediate coupling strength. Especially the transition from itinerant to localized pictures of magnetism or other effective excitations in solids should be controllable.

At this point a comment on the expected advantages and shortcomings of the form (2.3.42) is in place. The major advantage of this formula is its simplicity in combination with the correct description of the weak and strong coupling limits. And as it will be shown in subsequent chapters, the qualitative and quantitative description, even for intermediate coupling, is very good and in many aspects superior to other methods. In particular Kondo physics and life-time effects are accounted for in a non-perturbative manner.

The major deficit represents the RPA-like decoupling of local and lattice particle-hole excitations. For instance, the momentum dependence of any susceptibility is solely determined by the particle-hole excitations and thus without any two-particle interaction. The detailed frequency dependence of intermediate local excitations is neglected by the decoupling. As a direct consequence, the qualitative momentum dependence of any susceptibility calculated is the same: if the particle-hole propagator shows an enhanced response at some wave vector, any susceptibility will show this tendency as well. As an example, it will be impossible to obtain an enhanced antiferromagnetic spin susceptibility ($\underline{q} = \pi(1,1)$-component large) and simultaneously a tendency towards phase separation in the charge susceptibility ($\underline{q} = 0$-component large).

In general this is not problematic and the RPA-like decoupling is a good approximation, where the major physical effects are captured correctly. For propagating modes the dominating influences are the lattice structure, i.e. the Fermi surface, and the lifetime effects, which are both incorporated into the particle-hole propagator. The local two-particle interactions and the dynamics are correctly captured by the local susceptibility. So generally any trend in one of these quantities, such as an enhanced $\underline{\underline{P}}$ due to a large phase space

volume for some scattering process, will also be present in the exact (i.e. non-decoupled) lattice susceptibility.

Another source of inaccuracies stems from the method chosen to solve the effective impurity model. In most cases, the drawbacks of the impurity solver pose the strongest limitations on the accuracy and validity of the calculated Green functions.

3 The single impurity Anderson model

In the foregoing chapter, the effective impurity picture of the locally complete approximation for the approximate solution of a strongly correlated lattice system was introduced. The physical quantities describing the lattice system, such as local Green function and the correlation self-energy, were reduced to quantities of an effective impurity in an uncorrelated host. What remains in the nontrivial task of solving this reduced model, which is done in this chapter.

Even though the formulation in the preceding chapter was done for an arbitrary orbital structure, this chapter is specified for the simplest case of a single s-orbital coupled to a single conduction electron band, which is known as the single impurity Anderson model (SIAM). This is done, because this simplified model is sufficient to solve the Hubbard model considered later in this work. However, the formalism presented in this chapter can be generalized to more complicated orbital structures in a straightforward manner.

3.1 Hamiltonian

The single impurity Anderson model was proposed by Anderson [And61] (see also [And78]) and describes an interacting magnetic impurity of localized f-states hybridizing with a non-interacting band of c-electrons. Therefore the Hamiltonian consists of the three parts

$$\hat{H} = \hat{H}_c + \hat{H}_f + \hat{V} \tag{3.1.1}$$

where

$$\hat{H}_f = \sum_\sigma \left(\epsilon_\sigma^f \, \hat{f}_\sigma^\dagger \hat{f}_\sigma + \frac{U}{2} \, \hat{n}_\sigma^f \hat{n}_{\bar{\sigma}}^f \right) \quad , \quad \hat{H}_c = \sum_{\underline{k},\sigma} \epsilon_{\underline{k}}^c \, \hat{c}_{\underline{k}\sigma}^\dagger \hat{c}_{\underline{k}\sigma}$$
$$\hat{V} = \frac{1}{\sqrt{N_0}} \sum_{\underline{k}} \left(V_{\underline{k}} \, \hat{f}_\sigma^\dagger \hat{c}_{\underline{k}\sigma} + h.c. \right) \quad ,$$

where $\hat{H}_f$ describes the impurity with local one-particle energies ϵ_σ^f a local Coulomb interaction U. The $\hat{f}_\sigma^\dagger$ ($\hat{f}_\sigma$) are the creation (annihilation) operators for local f-states with spin σ. $\hat{H}_c$ describes the free band of c-electrons (operators $\hat{c}_{\underline{k}\sigma}^\dagger$ and $\hat{c}_{\underline{k}\sigma}$), while the hybridization $\hat{V}$ mixes the two systems with an amplitude $V_{\underline{k}}$.

Due to the presence of the interaction term $\sim U$ this model is not exactly solvable and one has to rely on approximations. Common approximation methods are second order perturbation theory in U and modifications thereof, higher order series expansions, strong coupling perturbation theory in $1/U$, the local moment approach (LMA), direct numerical evaluation of observables via quantum Monte Carlo methods (QMC), exact diagonalization of finite systems, the numerical renormalization group (NRG) and the (dynamic) density-matrix renormalization group ((D-)DMRG). For introductory reviews see [Hew93, Geo96,

Bul08, Gre08] and references therein. The thermodynamics of the model can be solved exactly with the Bethe ansatz method [And83, Wie83, Tsv83b, Tsv83a].

In this work, the direct perturbation theory with respect to the hybridization strength V [Kei71a, Kei71b, Gre81, Kei84] is utilized. In the next section, the basic setup of this approach is shortly introduced and the calculation of one-particle quantities sketched. Only those points are emphasized, which are necessary to understand the approximation for the two-particle quantities introduced in section 3.3.

3.2 Direct perturbation theory

In the direct perturbation theory the partition function and dynamic Green function are expressed in terms of a contour integration in the complex plane,

$$Z = Tr\, e^{-\beta \hat{H}} = \oint_{\mathcal{C}} \frac{dz}{2\pi i}\, e^{-\beta z}\, Tr\, \left[z - \hat{H}\right]^{-1} \tag{3.2.1}$$

$$G_{A,B}(i\eta) = \frac{1}{Z} \oint_{\mathcal{C}} \frac{dz}{2\pi i}\, e^{-\beta z}\, Tr\, \left[z - \hat{H}\right]^{-1} \hat{A}\, \left[z + i\eta_n - \hat{H}\right]^{-1} \hat{B} \quad , \tag{3.2.2}$$

with $i\eta$ either a fermionic or bosonic Matsubara frequency depending on the type of the operators $\hat{A}$ and $\hat{B}$. The contour $\mathcal{C}$ encircles all singularities of the integrand, which are situated on the $\mathrm{Im}\, z = 0$ and $\mathrm{Im}\, z + i\eta = 0$ axes in a mathematical positive sense. Because of the appearance of the resolvent operator $[z - \hat{H}]^{-1}$ the name *resolvent perturbation theory* is sometime used as well. Splitting the trace into two traces over the c- and f-electrons separately, the reduced f-partition function Z_f and the f-electron one-body Green function $F_\sigma \equiv G_{f_\sigma, f_\sigma^\dagger}$ can be reformulated

$$Z_f = \sum_M \oint_{\mathcal{C}} \frac{dz}{2\pi i}\, e^{-\beta z}\, P_M(z) \tag{3.2.3}$$

$$F_\sigma(i\omega_n) = \frac{1}{Z_f} \oint_{\mathcal{C}} \frac{dz}{2\pi i}\, e^{-\beta z} \Big[P_0(z)\, P_\sigma(z + i\omega_n)\, \Lambda_{0,\sigma}(z, i\omega_n) \tag{3.2.4}$$

$$+ P_{\bar{\sigma}}(z)\, P_2(z + i\omega_n)\, \Lambda_{2,\bar{\sigma}}(z + i\omega_n, i\omega_n) \Big] \quad ,$$

with the so-called ionic propagators

$$P_M(z) = \langle M | \frac{1}{Z_c} Tr_c\, e^{-\beta \hat{H}_c} \left[z - \hat{H} + \hat{H}_c\right]^{-1} | M \rangle = \langle M | \langle \left[z - \hat{H} + \hat{H}_c\right]^{-1} \rangle_c | M \rangle \tag{3.2.5}$$

$$\equiv \frac{1}{z - E_M - \Sigma_M(z)} \quad , \tag{3.2.6}$$

which describe the dynamics, i.e. the time evolution, of a ionic state $|M\rangle$. The trace Tr_c in equation (3.2.5), as well as the expectation value $\langle \ldots \rangle_c$, are to be taken over the c-states only and Z_c represents the partition function of the isolated c-system. In equation (3.2.6) the ionic propagator is expressed through the ionic self-energy $\Sigma_M(z)$ and the eigenvalue E_M of the unperturbed f-system,

$$\hat{H}_f |M\rangle = E_M |M\rangle \quad . \tag{3.2.7}$$

For the simple orbital structure of a s-shell considered in the SIAM (3.1.1), the ionic many-body quantum numbers are

$$M \in \{0; \sigma; 2\} \tag{3.2.8}$$

and represent the empty, singly occupied with spin σ and doubly occupied s-shell, respectively. The corresponding eigenenergies read

$$E_0 = 0\,, \qquad E_\sigma = \epsilon^f_\sigma\,, \qquad E_2 = \epsilon^f_\uparrow + \epsilon^f_\downarrow + U \quad . \tag{3.2.9}$$

In equation (3.2.4) the $\Lambda_{M,M'}(z,z')$ represent vertex functions which are specified at a later point.

Expanding the resolvent operator with respect to $\hat{V}$,

$$\left[z - \hat{H}\right]^{-1} = \left[z - \hat{H}_f - \hat{H}_c\right]^{-1} \sum_{n=0}^{\infty} \left[\hat{V}\left[z - \hat{H}_f - \hat{H}_c\right]^{-1}\right]^n \tag{3.2.10}$$

and expressing the local f-electron creation and annihilation operators appearing in $\hat{H}_f$ and $\hat{V}$ in terms of the ionic transfer operators $\hat{X}_{M,M'} = |M\rangle\langle M'|$ (see (2.1.4)), this perturbation theory can be visualized with time-ordered Goldstone diagrams, which describe the evolution and dynamics of the ionic f-states.

As an alternative, the ionic transfer operators can be avoided by enlarging the Hilbert space and introducing auxiliary bosons (slave-bosons), representing the empty state [Col84]. The resulting standard Feynman perturbation-theory is in a one-to-one correspondence to the non-standard time-ordered Goldstone expansion described here, but will not be considered further.

The ionic self-energies and f-electron Green function are expressed in terms of the ionic propagators and vertex functions as shown in figure 3.1. Since the self-energies depend on the ionic propagators themselves, this represents a set of coupled non-linear integral equations for the self-energies

$$\begin{aligned}
\Sigma_0(z) &= \sum_\sigma \int dx\; \Delta(x) f(x)\; P_\sigma(z+x)\; \Lambda_{0,\sigma}(z,x) \\
\Sigma_\sigma(z) &= \int dx\; \Delta(x) f(-x)\; P_0(z-x)\; \Lambda_{0,\sigma}(z-x,x) \\
&\quad + \int dx\; \Delta(x) f(x)\; P_2(z+x)\; \Lambda_{2,\sigma}(z+x,x) \\
\Sigma_2(z) &= \sum_\sigma \int dx\; \Delta(x) f(-x)\; P_\sigma(z-x)\; \Lambda_{2,\sigma}(z,x) \quad ,
\end{aligned} \tag{3.2.11}$$

with the hybridization function

$$\Delta(x) = \frac{1}{N_0} \sum_{\underline{k}} |V_{\underline{k}}|^2\, \delta(x - \epsilon^c_{\underline{k}}) \quad , \tag{3.2.12}$$

and the Fermi function

$$f(x) = \frac{1}{e^{\beta x} + 1} \quad ,$$

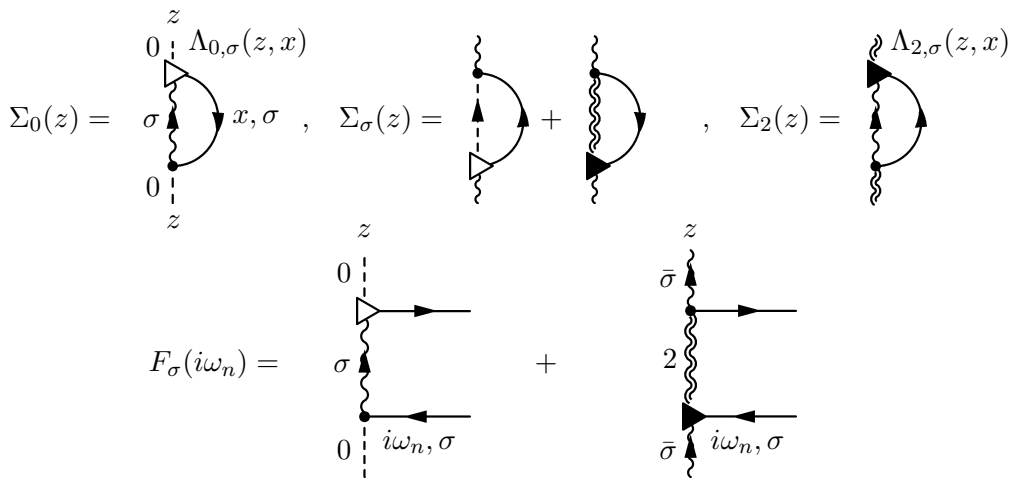

Figure 3.1: Diagrammatic equations for the ionic self-energies (upper) and f-electron Green function (lower). The dashed, wiggly and double-wiggly lines represent the empty, singly occupied ($\bar{\sigma}$ represents the opposite of the spin σ) and doubly occupied ionic propagators, respectively. The full lines represent an uncorrelated propagation in the c-band (upper) or the injection and ejection of the external electron (lower).

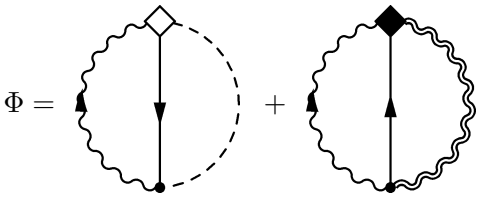

Figure 3.2: The Luttinger-Ward functional for the ionic propagators and self-energies. The vertex functions (filled and empty diamonds) differ from the $\Lambda_{M,M'}(z,z')$ by symmetry factors (see text).

where $\beta = 1/T$ and T the temperature. The vertex functions $\Lambda_{M,M'}(z,z')$, depicted as empty and filled triangles, incorporate the bare vertex and higher order vertex corrections. For given vertex functions, the solutions to these equations yield the ionic propagators which then are used to calculate the one-particle f-electron Green function as shown in the lower part of figure 3.1.

When formulated in such a self-consistent manner, the resulting approximations lead to thermodynamically consistent solutions. This can be seen from the fact, that the set of equations (3.2.11) can be obtained by functional derivatives with respect to the corresponding propagators of a Luttinger-Ward functional Φ [Lut60a, Lut60b, Lut61, Bay61, Bay62], i.e.

$$\Sigma_M = \frac{\delta \Phi}{\delta P_M} \quad , \tag{3.2.13}$$

which is depicted in figure 3.2. The vertex functions appearing in Φ (indicated by diamonds) are closely related to the $\Lambda_{M,M'}(z,z')$ from above: they have the same diagrammatic contributions, but additional symmetry factors appear in front of each diagram. For an explicit example see [Pru89]. The two-particle quantities and equations in the following section can be derived from the same functional, which guarantees their thermodynamic consistency as well.

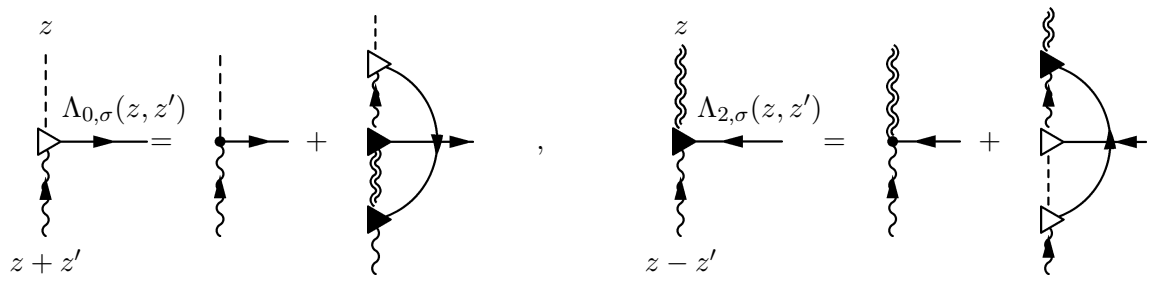

Figure 3.3: Self-consistency equations for the vertex functions within the FNCA. Neglecting all vertex corrections on the right-hand side (i.e. $\Lambda_{M,M'}(z,z')=1$) results in the ENCA.

The different approximations are defined by their corresponding choice of vertex functions $\Lambda_{M,M'}(z,z')$. The first approximation to be made is named the *simple non-crossing approximation* (SNCA), where vertex corrections are neglected altogether and only bare vertices are used, i.e.

$$\text{SNCA}: \quad \Lambda_{M,M'}(z,z') = 1 \quad . \tag{3.2.14}$$

The name stems from the fact, that in the skeleton expansion for this approximation no crossing of band electron lines occurs. This represents the finite-U generalization of the *non-crossing approximation* (NCA) [Gre83, Koj84, Bic87], by simply including the double occupied ionic valence state $|2\rangle$ into the dynamics.

In order to incorporate the correct exchange coupling in the Kondo regime for finite U

$$J = \frac{V^2}{|\epsilon^f|} + \frac{V^2}{|\epsilon^f + U|} \quad , \tag{3.2.15}$$

which is acquired via a Schrieffer-Wolff transformation [Sch66], vertex corrections must be taken into account. Starting from the SNCA and including diagrams generated by exchanging the sequence of incoming and outgoing band electron lines, the *full non-crossing approximation* (FNCA) is obtained, which is defined by the vertex functions shown in figure 3.3. It has been shown [Pru89] that the order of magnitude of the exchange coupling and the Kondo scale are already correctly reproduced by incorporating only the first non-trivial vertex correction, where bare vertices are used on the right-hand sides of figure 3.3. This *extended non-crossing approximation* (ENCA) is defined by the vertex functions

$$\text{ENCA}: \quad \Lambda_{0,\sigma}(z,z') = 1 + \int dx\, \Delta(x) f(x)\, P_{\bar{\sigma}}(z+x)\, P_2(z+z'+x) \tag{3.2.16}$$

$$\Lambda_{2,\sigma}(z,z') = 1 + \int dx\, \Delta(x) f(-x)\, P_{\bar{\sigma}}(z-x)\, P_0(z-z'-x) \tag{3.2.17}$$

and is extensively used in this work.

In the case of infinitely large Coulomb repulsion $U \to \infty$, the approximations SNCA, FNCA and ENCA all reduce to the same theory, i.e. NCA, because the doubly occupied state is then excluded from the dynamics resulting in $P_2(z) = 0$. Therefore the second term in the ionic self-energy $\Sigma_\sigma(z)$ vanishes while $\Lambda_{0,\sigma}(z,z')$ reduces to the bare vertex. In this sense, all these approximations are still referred to as non-crossing. For approximations involving "real" crossing diagrams see [And95, Gre08, Kro97, Kro05].

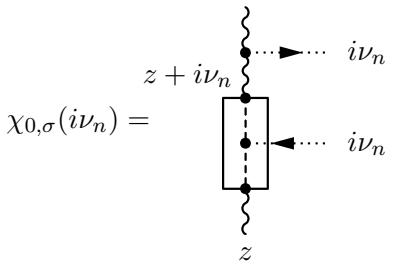

Figure 3.4: The bosonic Green function $\chi_{\sigma,0}(i\nu_n)$

3.3 Susceptibilities

For susceptibilities within the resolvent perturbation theory the relevant dynamic quantities are the bosonic Green functions (see (3.3.2))

$$\chi_{M,M'}(i\nu_n) = \int_0^\beta d\tau\, e^{i\nu_n \tau} \langle \mathcal{T} \left[\hat{X}_{MM}(\tau)\, \hat{X}_{M'M'}(0) \right] \rangle \tag{3.3.1}$$

$$= -\frac{1}{Z_f} \oint_{\mathcal{C}} \frac{dz}{2\pi i}\, e^{-\beta z} Tr \left(\left[z - \hat{H} \right]^{-1} \hat{X}_{MM} \left[z + i\nu_n - \hat{H} \right]^{-1} \hat{X}_{M'M'} \right) \tag{3.3.2}$$

$$= -\frac{1}{Z_f} \oint_{\mathcal{C}} \frac{dz}{2\pi i}\, e^{-\beta z}\, \chi_{M,M'}(z, z + i\nu_n) \tag{3.3.3}$$

$$= -\frac{1}{Z_f} \oint_{\mathcal{C}} \frac{dz}{2\pi i}\, e^{-\beta z}\, \Gamma_{M,M'}(z, z + i\nu_n)\, P_{M'}(z)\, P_{M'}(z+i\nu_n) \quad , \tag{3.3.4}$$

with M and M' many-body quantum numbers of the local shell and $i\nu_n$ a bosonic Matsubara frequency. The contour $\mathcal{C}$ encircles all singularities of the integrand in a mathematical positive sense. In equation (3.3.3) the functions $\chi_{M,M'}(z, z')$ are introduced as a shorthand notation for the integrand, being the dynamic quantities of interest. As an example, the graphical representation of the quantity $\chi_{0,\sigma}(i\nu_n)$ is shown in figure 3.4 where the box represents the vertex functions $\Gamma_{0,\sigma}(z, z + i\nu_n)$.

Before explicit approximative formulas for the susceptibility functions $\chi_{M,M'}(z, z')$ are considered, it is worthwhile to observe some exact properties of these. Exact statements provide essential checks for approximations and serve as valuable benchmarks for all numeric calculations.

As a bosonic Green function $\chi_{M,M'}(i\nu_n)$ fulfills the symmetry property

$$\chi_{M,M'}(-i\nu_n) = \chi_{M',M}(i\nu_n) \quad , \tag{3.3.5}$$

which can be seen by shifting the integration variable in equation (3.3.2), $z \to z + i\nu_n$, using that $e^{\beta i\nu_n} = 1$ and the invariance of the trace with respect to cyclic permutations.

Further exact statements are obtained with the help of the completeness relation of the ionic many-body states, $\sum_M \hat{X}_{MM} = 1$, which implies the sum rules for the susceptibility functions[1]

$$\sum_{M'} \chi_{M',M}(i\nu_n) = \langle \hat{X}_{MM} \rangle \, \delta_{i\nu_n,0} \tag{3.3.6}$$

$$\sum_{M} \chi_{M',M}(i\nu_n) = \langle \hat{X}_{M'M'} \rangle \, \delta_{i\nu_n,0} \tag{3.3.7}$$

$$\sum_{M,M'} \chi_{M',M}(i\nu_n) = \delta_{i\nu_n,0} \quad . \tag{3.3.8}$$

The translation of symmetry relations as (3.3.5) or (3.3.6) into equivalent versions for the functions $\chi_{M,M'}(z,z')$ requires some caution. Within the resolvent perturbation theory, rotated diagrams[2] are considered equivalent. That is, a diagram and all of its rotated versions represent the same physical process and hence their analytic representations as contour integrations yield the same result. This certainly does not imply the equality of the integrands under the contour integration for rotated diagrams. Actually, in general these *must not* be equal, since rotated versions might have inverted band electron lines and a different number of crossing electronic lines with equal spin. The former are accompanied by a different thermal occupation number, i.e. $f(\pm x) \to f(\mp x)$, while the latter are associated with different factors of (-1) in the diagrammatic rules.

The steps necessary to bring the integrands of rotated diagrams into the same analytical expression involve (a) shifts of the complex energy variable $z \to z \pm i\eta$, which produce factors of $e^{-\beta i\eta} = \pm 1$, depending on the nature of the Matsubara frequency $i\eta$, and (b) shifts by a real frequency of a band electron line, which produces factors of $e^{\pm\beta x}$ effectively transforming the thermal occupation numbers $f(\pm x)e^{\pm\beta x} = f(\mp x)$ and adjusting the arguments of the ionic propagators.

Quite generally, integrands of the contour integration can differ substantially but still describe the same process and yield the exact same physical result. The symmetry operations connecting these integrands are rotations and shifts of the complex frequency z.

The selection of a representative for a diagrammatic family is arbitrary. Here, the introduction of the vertex functions in equation (3.3.4) defines the way all diagrams are organized. All vertex corrections are taken at the lower, incoming Bose frequency corresponding to the first index M in $\chi_{M,M'}(z,z')$. Taking all vertex corrections at the top vertex will produce no difference in the calculated susceptibilities $\chi_{M,M'}(i\nu_n)$, but it will result in different functions $\chi_{M,M'}(z,z')$! In that sense a specific arrangement of diagrams is chosen from all possible rotations. As it will be seen shortly, this leads to the failure of the transformation of (3.3.7) into a sum rule for the $\chi_{M,M'}(z,z')$

[1] The third equation (3.3.8) rather provides a check for the one-body quantities, i.e. the defect propagator sum rule $\sum_M \langle \hat{X}_{MM} \rangle = 1$, where $\langle \hat{X}_{MM} \rangle = \int dx \xi_M(x)$ and $\xi_M(x)$ is the defect propagator for the state M (see (C.21)).

[2] For physical quantities the ionic state at the bottom and the top of a diagram have to be the same and it is only accounted for once in the analytic representation. The vertical line carries the internal complex frequency z and has the topology of a cylinder. The rotated version of some diagram is the cyclic permutations of the vertices on that cylinder, thereby keeping all orders of vertices and connections intact.

The transformation of (3.3.6) into the complex plane is done by analyzing the defining formula (3.2.2) with the specifications $\hat{A} = \sum_{M'} \hat{X}_{M'M'} = 1$ and $\hat{B} = \hat{X}_{MM}$

$$\begin{aligned}\sum_{M'} \chi_{M',M}(z,z') &= \langle M| \Big\langle \big[z - \hat{H}\big]^{-1} \overbrace{\sum_{M'} \hat{X}_{M'M'}}^{=1} \big[z' - \hat{H}\big]^{-1} \Big\rangle_c |M\rangle \\ &= \langle M| \Big\langle \big[z - \hat{H}\big]^{-1} \big[z' - \hat{H}\big]^{-1} \Big\rangle_c |M\rangle \\ &= -\frac{1}{z - z'} \langle M| \Big\langle \Big(\big[z - \hat{H}\big]^{-1} - \big[z' - \hat{H}\big]^{-1} \Big) \Big\rangle_c |M\rangle \end{aligned} \tag{3.3.9}$$

$$\Leftrightarrow \sum_{M'} \chi_{M',M}(z,z') = -\frac{P_M(z) - P_M(z')}{z - z'} \equiv S_M(z,z') \quad . \tag{3.3.10}$$

Taking the sum over the second index instead of the first to produce the equivalent of equation (3.3.7) yields

$$\sum_{M} \chi_{M',M}(z,z') = \sum_{M} \langle M| \Big\langle \big[z - \hat{H}\big]^{-1} \hat{X}_{M'M'} \big[z' - \hat{H}\big]^{-1} \Big\rangle_c |M\rangle \equiv \tilde{S}_{M'}(z,z') \quad . \tag{3.3.11}$$

The appearance of the projection operator $\hat{X}_{M'M'}$ between the two resolvent operators prohibits the expansion into partial fractions as in the calculation of equation (3.3.9). The sum over M combined with the c-band average in equation (3.3.11) looks like a trace operation where the cyclic property could be used to derive the same result as in (3.3.10). But this is not the case, since the perturbation expansion (3.2.10) has already been performed, the approximation is already made and only some diagrammatic contributions retained. By defining the functions $\chi_{M,M'}(z,z')$ as in equation (3.3.4), the projections of the operator $\hat{X}_{M'M'}$ have already been carried out and the local ionic averages have already been performed fixating the sequence of ionic states. So in each term of the expansion, the c-band averages have been evaluated, which in general produces shifts of frequency arguments in the appearing ionic propagators. So the formulation (3.3.11) of the sum rule (3.3.7) does not provide a usable check for the $\chi_{M,M'}(z,z')$ as no explicit analytic expression for the functions $\tilde{S}_M(z,z')$ could be deduced.

Generally, it can only be remarked that the $\tilde{S}_M(z, z + i\nu_n)$, as well as the $S_M(z, z + i\nu_n)$, produce a non-vanishing term in the contour integration only for $i\nu_n = 0$, i.e.

$$\begin{aligned} -\frac{1}{Z_f} \oint_{\mathcal{C}} \frac{dz}{2\pi i} e^{-\beta z} S_M(z, z + i\nu_n) &= \langle \hat{X}_{M,M} \rangle \, \delta_{i\nu_n,0} \\ -\frac{1}{Z_f} \oint_{\mathcal{C}} \frac{dz}{2\pi i} e^{-\beta z} \tilde{S}_M(z, z + i\nu_n) &= \langle \hat{X}_{M,M} \rangle \, \delta_{i\nu_n,0} \quad . \end{aligned} \tag{3.3.12}$$

Notice, that (3.3.11) just represents a rotated version of (3.3.9) and thus it is an example of the difference mentioned above between integrands of rotated diagrams.

Additionally, the functions $\chi_{M,M'}(z,z')$ obey the symmetry relations

$$\chi_{M,M'}(z^*, z'^*) = \chi_{M,M'}(z,z')^* \tag{3.3.13}$$

and

$$\chi_{M,M'}(z,z') = \chi_{M,M'}(z',z) \quad , \tag{3.3.14}$$

which are revealed by inspection of the perturbation expansion.

After these general considerations, the approximation schemes of the FNCA and ENCA are applied to the Green functions $\chi_{M,M'}(z,z')$. Formulating the skeleton-expansions for these sixteen functions within the FNCA yields, that for each fixed M only the four functions $\chi_{M,0}(z,z')$, $\chi_{M,\sigma}(z,z')$ and $\chi_{M,2}(z,z')$ are coupled to each other. Therefore there exist four separate sets of integral equations, which are shown in figure 3.5. The analytical expressions for these are rather lengthy and given in appendix C. As already mentioned these equations constitute a conserving approximation, as they can be derived from a Luttinger-Ward functional.

Additionally, the symmetry properties (3.3.13) and (3.3.14) can be explicitly verified in equations (C.1)-(C.3).

To prove the fulfillment of the sum rule (3.3.10) by the $\chi_{M',M}$ within the FNCA, is somewhat harder to accomplish. It can be done by explicitly deriving the system of integral equations satisfied by the four functions $S_M(z,z')$. These turn out to be exactly the ones valid for the $\sum_{M'} \chi_{M',M}(z,z')$, which are obtained from summing each of the integral equations (C.1) to (C.3) with respect to M'.

The starting point of the derivation of the equations for the S_M is to re-write S_M as

$$S_M(z,z') = P_M(z)P_M(z')\left(1 - \frac{\Sigma_M(z) - \Sigma_M(z')}{z - z'}\right) \quad . \tag{3.3.15}$$

and then using the equations for the ionic self-energies (3.2.11).

Equation (3.3.15) makes it obvious, that the sum rule (3.3.10) reflects the thermodynamic consistency of this theory, i.e. that the equations for the one- and two-particle quantities can be derived from *one* generating functional Φ: a sum of two-particle quantities results in a function entirely determined through the ionic self-energies, i.e. a one-particle quantity.

All above statements and the equations in appendix C are formulated for two distinct and independent complex energy variables z and z'. However, for physical susceptibility functions $z' = z + i\nu_n$ is always implied.

In the ENCA, only the lowest order vertex corrections are accounted for, which implies that there occurs only one crossing of band electron lines in the skeleton expansion of the ionic self-energies and propagators. In order to consistently calculate susceptibilities, the number of crossings of band electrons lines must be preserved. Discarding all terms with more than one crossing directly leads to the ENCA versions, which are explicitly shown in figure 3.6. The analytic versions are again deferred to equations (C.8)-(C.10) in appendix C.

The even simpler approximation is given by the SNCA, where all terms with crossing band electron lines are neglected. The system of integral equations then reduces to the finite-U generalization of the one already stated in [Kur83].

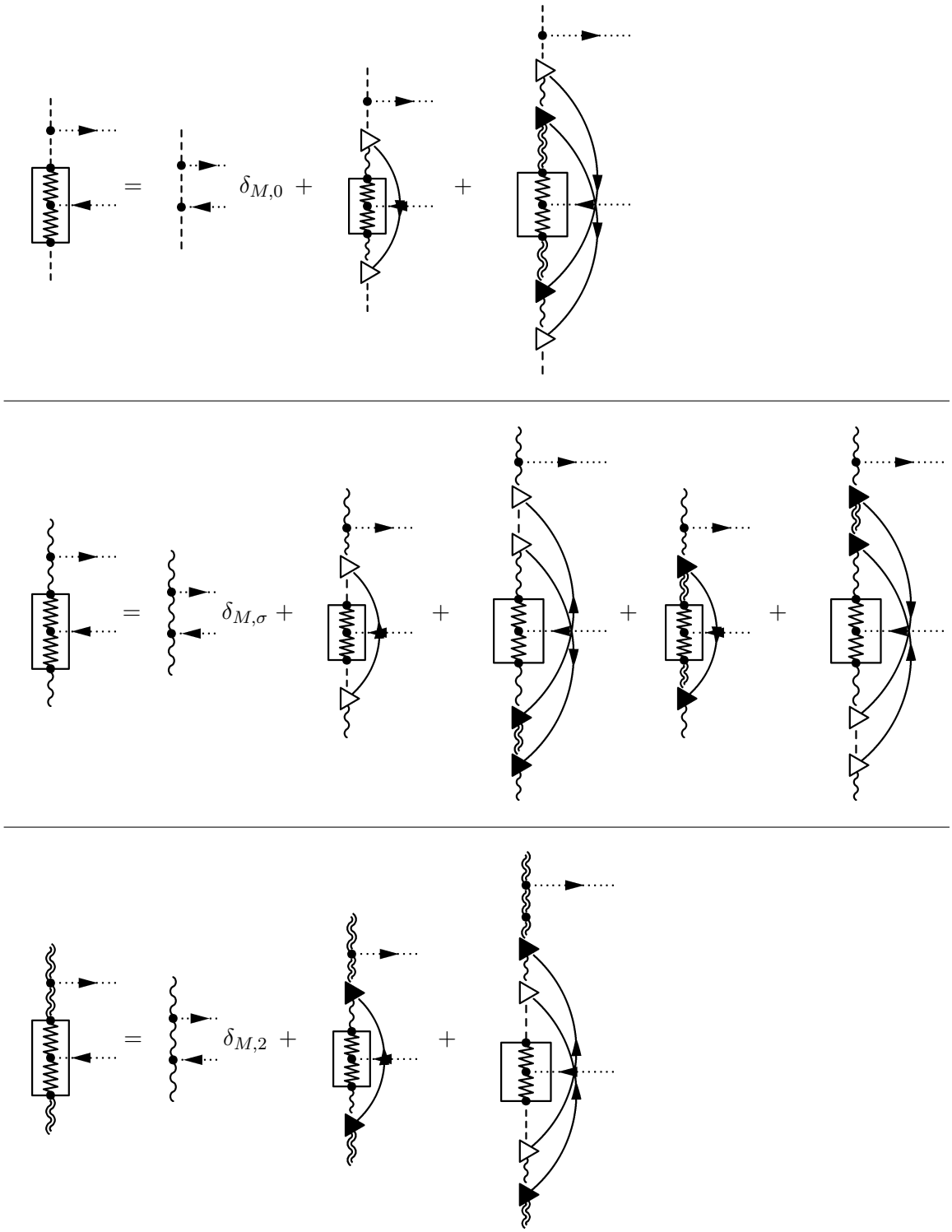

Figure 3.5: System of integral equations for $\chi_{M,0}(z,z')$, $\chi_{M,\sigma}(z,z')$, and $\chi_{M,2}(z,z')$ within the FNCA. The zig-zag line represents the ionic state M, which can either be empty (dashed), singly occupied (wiggly) or doubly occupied (double wiggly).

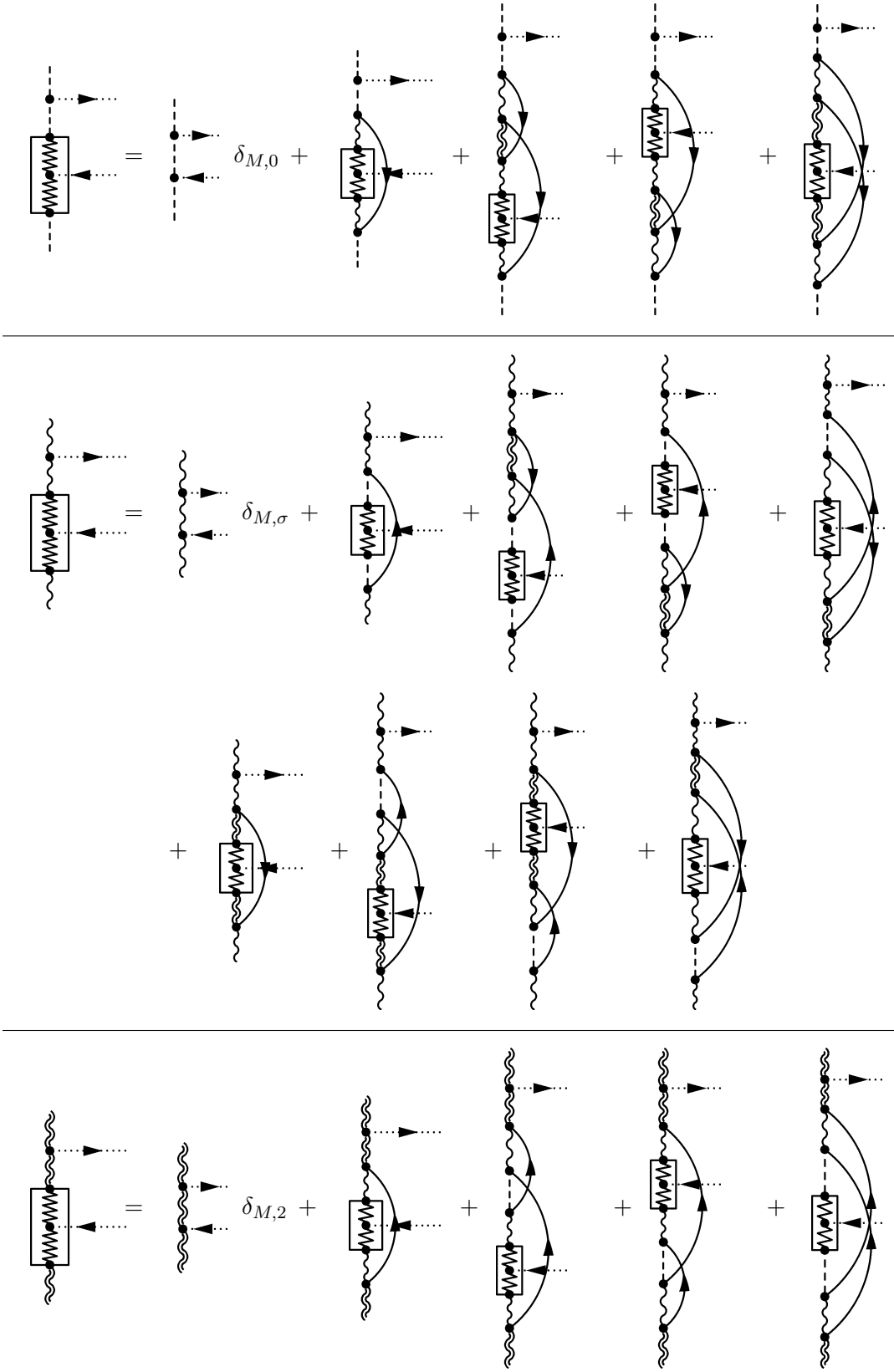

Figure 3.6: System of integral equations for $\chi_{M,0}(z,z')$, $\chi_{M,\sigma}(z,z')$, and $\chi_{M,2}(z,z')$ within the ENCA.

To obtain the physical susceptibility the contour integration of equation (3.3.3) still has to be performed,

$$\begin{aligned}\chi_{M,M'}(i\nu_n) &= -\frac{1}{Z_f}\oint_{\mathcal{C}}\frac{dz}{2\pi i}\,e^{-\beta z}\,\chi_{M,M'}(z,z+i\nu_n) \qquad (3.3.16)\\ &= \frac{1}{Z_f}\int_{-\infty}^{\infty}\frac{d\omega}{2\pi i}\,e^{-\beta\omega}\lim_{\delta\to 0}\Big[\chi_{M,M'}(\omega+i\delta,\omega+i\nu_n)-\chi_{M,M'}(\omega-i\delta,\omega+i\nu_n)\\ &\qquad +\chi_{M,M'}(\omega-i\nu_n,\omega+i\delta)-\chi_{M,M'}(\omega-i\nu_n,\omega-i\delta)\Big]\quad,\end{aligned}$$

with $\delta > 0$ an infinitesimal number. The analytic continuation of the complex variable $z \to \lim_{\delta\to 0}(\omega \pm i\delta)$ to the real axis is done using a non-zero Bose frequency $i\nu_n$ and therefore the necessary integrations along the two *different* branch-cuts ($\mathrm{Re}[z] = 0$ and $\mathrm{Re}[z + i\nu_n] = 0$) of the function $\chi_{M,M'}(z, z + i\nu_n)$ are performed properly. After this, the resulting expression (3.3.16) can be analytical continued with respect to the Bose frequency, $i\nu_n \to \lim_{\delta\to 0}(\nu + i\delta)$,

$$\begin{aligned}\chi_{M,M'}(\nu+i\delta) &= \frac{1}{Z_f}\int_{-\infty}^{\infty}\frac{d\omega}{2\pi i}\,e^{-\beta\omega}\Big[\chi_{M,M'}(\omega+i\delta,\omega+\nu+i\delta)-\chi_{M,M'}(\omega-i\delta,\omega+\nu+i\delta)\\ &\qquad +\chi_{M,M'}(\omega-\nu-i\delta,\omega+i\delta)-\chi_{M,M'}(\omega-\nu-i\delta,\omega-i\delta)\Big]\\ &= \frac{1}{Z_f}\int_{-\infty}^{\infty}\frac{d\omega}{2\pi i}\,e^{-\beta\omega}\Big[\chi_{M,M'}(\omega+i\delta,\omega+\nu+i\delta)-\chi_{M,M'}(\omega-i\delta,\omega+\nu+i\delta)\\ &\qquad -\big(\chi_{M,M'}(\omega+i\delta,\omega-\nu+i\delta)-\chi_{M,M'}(\omega-i\delta,\omega-\nu+i\delta)\big)^*\Big]\\ &\equiv \int_{-\infty}^{\infty}\frac{d\omega}{2\pi i}\Big[Y_{M,M'}(\omega,\omega+\nu)-Y_{M,M'}(\omega,\omega-\nu)^*\Big]\quad, \qquad (3.3.17)\end{aligned}$$

where the symmetry relations (3.3.13) were used and the *defect* quantities

$$Y_{M,M'}(x,y) = \frac{e^{-\beta x}}{Z_f}\Big[\chi_{M,M'}(x+i\delta,y+i\delta)-\chi_{M,M'}(x-i\delta,y+i\delta)\Big] \qquad (3.3.18)$$

introduced.

In general the two analytic continuations of the complex variables z and $i\nu_n$ do not commute. This is due to the well-known fact, that for bosonic Green functions the Fourier components for a vanishing Matsubara frequency $i\nu_n = 0$ has to be considered separately. The procedure from above applies to Fourier coefficients for the general case of a non-vanishing external frequency, i.e. $i\nu \neq 0$, but the analytical continued result yields the correct values even for the static susceptibility functions.

Due to the appearance of the exponential factor, a direct numerical evaluation of the defect quantities given the $\chi_{M,M'}$ is not possible. As for the one-particle quantities, separate

sets of equations have to be derived for the defect quantities. This is done by analytically continuing the complex variable z to the real axis, i.e. $z \to \omega \pm i\delta$, then to write down the equations for the quantities $\chi_{M,M'}(x+i\delta, y+i\delta)$ and $\chi_{M,M'}(x-i\delta, y+i\delta)$, and finally build the $Y_{M,M'}$ along the lines of their definition (3.3.18).

The deviation and the resulting equations are again deferred to appendix C due to their length.

The sum rule (3.3.10) transforms into

$$\sum_{M'} Y_{M',M}(\omega, \omega+\nu) = -2\pi i \, \frac{\xi_M(\omega)}{\nu + i\delta} \quad . \tag{3.3.19}$$

when adapted for the defect quantities.

In the following, only spin-symmetric situations are considered. The spin indices σ of every function will be specified as $\uparrow$ or $\downarrow$ and only one representative of every function will be kept, i.e.

$$\begin{aligned} &P_\sigma = P_{\bar{\sigma}} \equiv P_\uparrow \\ &\chi_{\sigma,\alpha} = \chi_{\bar{\sigma},\alpha} \equiv \chi_{\uparrow,\alpha} \quad , \qquad \alpha = \{0, 2\} \\ &\chi_{\bar{\sigma},\bar{\sigma}} = \chi_{\sigma,\sigma} \equiv \chi_{\uparrow,\uparrow} \\ &\chi_{\bar{\sigma},\sigma} = \chi_{\sigma,\bar{\sigma}} \equiv \chi_{\uparrow,\downarrow} \\ &\ldots \quad . \end{aligned} \tag{3.3.20}$$

3.3.1 Magnetic susceptibilities

The relevant quantity for the magnetic susceptibility is the auto-correlation function of the z-component of the spin operator $\hat{S}^z \sim \hat{n}_\uparrow - \hat{n}_\downarrow = \hat{X}_{\uparrow,\uparrow} - \hat{X}_{\downarrow,\downarrow}$. This translates into the linear combination

$$\chi_{mag}(z, z') = \chi_{\uparrow,\uparrow}(z, z') - \chi_{\uparrow,\downarrow}(z, z') \quad , \tag{3.3.21}$$

which needs to be determined. Setting up the equations for this linear combination using the explicit equations (C.1)- (C.3) (or (C.8)- (C.10)) all spin-symmetric terms cancel. This leads to the decoupling of the function $\chi_{mag}(z, z')$ from the $\chi_{0,M}(z, z')$ and $\chi_{2,M}(z, z')$. As a result, only one integral equation for $\chi_{mag}(z, z')$ remains

$$\begin{aligned} \chi_{mag}(z, z') &= \chi_{\uparrow,\uparrow}(z, z') - \chi_{\uparrow,\downarrow}(z, z') \\ &= \Pi_\uparrow(z, z') \Bigg\{ 1 - \int dx dy \Delta^+(x) \Delta^-(y) \Big[P_2(z'+x) \, P_0(z-y) \\ &\qquad + P_0(z'-y) \, P_2(z+x) \Big] \, \chi_{mag}(z+x-y, z'+x-y) \Bigg\} \quad . \end{aligned} \tag{3.3.22}$$

The corresponding defect equation is

$$\begin{aligned} Y_{mag}(\omega,\omega{+}\nu) = Y_1^0(\omega,\omega{+}\nu)\Big\{1 - \int dxdy\Delta^+(x)\Delta^-(y)\Big[P_2(\omega{+}x^+)\,P_0(\omega{-}y{+}\nu^+) \\ + P_0(\omega{-}y^+)\,P_2(\omega{+}x{+}\nu^+)\Big]\,\chi_{mag}(\omega{+}x{-}y^+,\omega{+}\nu{+}x{-}y^+)\Big\} \\ + 2\pi i\,\Pi_\uparrow(\omega^-,\omega{+}\nu^+)\int dxdy\Big[\Delta^-(x)\Delta^-(y)\xi_2(\omega{+}x)\,P_0(\omega{-}y{+}\nu^+) \\ + \Delta^+(x)\Delta^+(y)\xi_0(\omega{-}y)\,P_2(\omega{+}x{+}\nu^+)\Big]\,\chi_{mag}(\omega{+}x{-}y^+,\omega{+}\nu{+}x{-}y^+) \\ - \Pi_\uparrow(\omega^-,\omega{+}\nu^+)\int dxdy\Delta^-(x)\Delta^+(y)\Big[P_2(\omega{+}x^-)\,P_0(\omega{-}y{+}\nu^+) \\ + P_0(\omega{-}y^-)\,P_2(\omega{+}x{+}\nu^+)\Big]\,Y_{mag}(\omega{+}x{-}y,\omega{+}\nu{+}x{-}y) \quad . \end{aligned} \tag{3.3.23}$$

For abbreviations and definitions of occuring functions see appendix C.

The final form for the dynamic magnetic susceptibility thus reads

$$\chi_{mag}(\nu+i\delta) = \int_{-\infty}^{\infty}\frac{d\omega}{2\pi i}\Big[Y_{mag}(\omega,\omega{+}\nu) - Y_{mag}(\omega,\omega{-}\nu)^*\Big] \quad . \tag{3.3.24}$$

3.3.2 Charge susceptibilities

For the charge susceptibility the relevant quantity is the auto-correlation function of the charge operator $\hat{n} = \hat{n}_\uparrow + \hat{n}_\downarrow = \hat{X}_{\uparrow,\uparrow} + \hat{X}_{\downarrow,\downarrow} + 2\hat{X}_{2,2}$, whereas the hole susceptibility is the equivalent function for the hole operator $\hat{h} = 2 - \hat{n} = 2\hat{X}_{0,0} + \hat{X}_{\uparrow,\uparrow} + \hat{X}_{\downarrow,\downarrow}$,

$$\chi_{charge}(\tau) = \langle \mathcal{T}\,\hat{n}(\tau)\hat{n}\rangle \quad , \tag{3.3.25}$$

$$\begin{aligned} \chi_{hole}(\tau) &= \langle \mathcal{T}\,\hat{h}(\tau)\hat{h}\rangle \\ &= 4(1-\langle\hat{n}\rangle) + \chi_{charge}(\tau) \quad . \end{aligned} \tag{3.3.26}$$

As it can be seen, both susceptibilities differ only by a constant, which implies the equality of the frequency dependent functions,

$$\chi_{hole}(i\nu_n) = \chi_{charge}(i\nu_n) + 4(1-\langle\hat{n}\rangle)\delta_{i\nu_n,0} \quad . \tag{3.3.27}$$

For the functions $\chi_{M,M'}(z,z')$, the relevant quantities are (dropping an overall factor of 2)

$$\begin{aligned} \chi_{charge}(z,z') =& \chi_{\uparrow,\uparrow}(z,z') + \chi_{\uparrow,\downarrow}(z,z') + 2\Big(\chi_{2,2}(z,z') + \chi_{2,\uparrow}(z,z') + \chi_{\uparrow,2}(z,z')\Big) \\ =& \chi_{2,2}(z,z') - \chi_{0,2}(z,z') + \chi_{0,0}(z,z') - \chi_{2,0}(z,z') \\ &+ S_\uparrow(z,z') + S_2(z,z') + \frac{1}{2}\Big(\tilde{S}_2(z,z') - \tilde{S}_0(z,z')\Big) \end{aligned} \tag{3.3.28}$$

and

$$\begin{aligned} \chi_{hole}(z,z') =& \chi_{2,2}(z,z') - \chi_{0,2}(z,z') + \chi_{0,0}(z,z') - \chi_{2,0}(z,z') \\ &+ S_0(z,z') + S_\uparrow(z,z') + \frac{1}{2}\Big(\tilde{S}_0(z,z') - \tilde{S}_2(z,z')\Big) \\ =& \chi_{charge}(z,z') + S_0(z,z') + \tilde{S}_0(z,z') - S_2(z,z') - \tilde{S}_2(z,z') \quad . \end{aligned} \tag{3.3.29}$$

The equality of the hole and charge susceptibility is guaranteed by the identities (3.3.10) and (3.3.11), which are used in the derivation above and account for the appearance of the functions $S_M(z,z')$ and $\tilde{S}_M(z,z')$. As it is evident from equation (3.3.29) and (3.3.12), the latter just produce the constant difference between charge and spin susceptibility,

$$\begin{aligned} 2(1-\langle\hat{n}\rangle)\delta_{i\nu_n,0} &= 2(\langle\hat{X}_{0,0}\rangle - \langle\hat{X}_{2,2}\rangle)\delta_{i\nu_n,0} \\ &= -\frac{1}{Z_f}\oint\frac{dz}{2\pi i}e^{-\beta z}\Big(S_0(z,z+i\nu_n)+\tilde{S}_0(z,z+i\nu_n) \\ &\qquad -S_2(z,z+i\nu_n)-\tilde{S}_2(z,z+i\nu_n)\Big) \quad , \end{aligned} \tag{3.3.30}$$

once the contour integration is performed.

It can be seen from equations (3.3.28) and (C.8) that the linear combinations $c_{0,0} \equiv \chi_{0,0}-\chi_{2,0}$, $c_{0,\uparrow} \equiv \chi_{0,\uparrow}-\chi_{2,\uparrow}$, and $c_{0,2} \equiv \chi_{0,2}-\chi_{2,2}$ obey one set of equations,

$$\begin{aligned} c_{0,0}(z,z') = \Pi_0(z,z')\Big\{1 &+ 2\int dx\Delta^+(x)\left[\Lambda_{0,\uparrow}(z',x)+\Lambda_{0,\uparrow}(z,x)-1\right]c_{0,\uparrow}(z{+}x,z'{+}x) \\ &+ 2\int dx\,dy\Delta^+(x)\Delta^+(y)\,P_\uparrow(z'{+}x)\,P_\uparrow(z{+}y)\,c_{0,2}(z{+}x{+}y,z'{+}x{+}y)\Big\} \end{aligned} \tag{3.3.31}$$

$$\begin{aligned} c_{0,\uparrow}(z,z') = \Pi_\sigma(z,z')\Big\{ &\int dx\Delta^-(x)\big[\Lambda_{0,\uparrow}(z'{-}x,x)+\Lambda_{0,\uparrow}(z{-}x,x)-1\big]\,c_{0,0}(z{-}x,z'{-}x) \\ &+\int dx\Delta^+(x)\big[\Lambda_{2,\uparrow}(z'{+}x,x)+\Lambda_{2,\uparrow}(z{+}x,x)-1\big]\,c_{0,2}(z{+}x,z'{+}x) \\ +\int dxdy\Delta^+(x)\Delta^-(y)\Big[&P_2(z'{+}x)\,P_0(z{-}y)+P_0(z'{-}y)\,P_2(z{+}x)\Big]\,c_{0,\uparrow}(z{+}x{-}y,z'{+}x{-}y)\Big\} \end{aligned} \tag{3.3.32}$$

$$\begin{aligned} c_{0,2}(z,z') = \Pi_2(z,z')\Big\{ &-1+2\int dx\Delta^-(x)\big[\Lambda_{2,\uparrow}(z',x)+\Lambda_{2,\uparrow}(z,x)-1\big]\,c_{0,\uparrow}(z{-}x,z'{-}x) \\ &+2\int dxdy\Delta^-(x)\Delta^-(y)\,P_\uparrow(z'{-}x)\,P_\uparrow(z{-}y)\,c_{0,0}(z{-}x{-}y,z'{-}x{-}y)\Big\} \end{aligned} \tag{3.3.33}$$

which, in combination with the respective defect equations for $y_{0,0} \equiv Y_{0,0}-Y_{2,0}$, $y_{0,\uparrow} \equiv Y_{0,\uparrow}-Y_{2,\uparrow}$, and $y_{0,2} \equiv Y_{0,2}-Y_{2,2}$,

$$\begin{aligned} y_{0,0}(\omega,\omega{+}\nu) = I_{0,0}(\omega,\omega{+}\nu) - I_{2,0}(\omega,\omega{+}\nu) + \Pi_0(\omega^-,\omega{+}\nu^+)\Big\{ \\ 2\int dx\Delta^-(x)\left[\Lambda_{0,\uparrow}(\omega{+}\nu^+,x)+\Lambda_{0,\uparrow}(\omega^-,x)-1\right]y_{0,\uparrow}(\omega{+}x,\omega{+}\nu{+}x) \\ +2\int dx\,dy\Delta^-(x)\Delta^-(y)\,P_\uparrow(\omega{+}\nu{+}x^+)\,P_\uparrow(\omega{+}y^-)\,y_{0,2}(\omega{+}x{+}y,\omega{+}\nu{+}x{+}y)\Big\} \end{aligned} \tag{3.3.34}$$

$$y_{0,\sigma}(\omega,\omega{+}\nu) = I_{0,\sigma}(\omega,\omega{+}\nu) - I_{2,\sigma}(\omega,\omega{+}\nu) + \Pi_\uparrow(\omega^-,\omega{+}\nu^+)\Big\{ \int dx\Delta^+(x)\big[\Lambda_{0,\uparrow}(\omega{+}\nu{-}x^+,x) + \Lambda_{0,\uparrow}(\omega{-}x^-,x) - 1\big]\, y_{0,0}(\omega{-}x,\omega{+}\nu{-}x) + \int dx\Delta^-(x)\big[\Lambda_{2,\uparrow}(\omega{+}\nu{+}x^+,x) + \Lambda_{2,\uparrow}(\omega{+}x^-,x) - 1\big]\, y_{0,2}(\omega{+}x^+,\omega{+}\nu{+}x^+) + \int dxdy\Delta^-(x)\Delta^+(y)\Big[P_2(\omega{+}\nu{+}x^+)P_0(\omega{-}y^-){+}P_0(\omega{+}\nu{-}y^+)P_2(\omega{+}x^-)\Big] y_{0,\uparrow}(\omega{+}x{-}y,\omega{+}\nu{+}x{-}y)\Big\} \tag{3.3.35}$$

$$y_{0,2}(\omega,\omega{+}\nu) = I_{0,2}(\omega,\omega{+}\nu) - I_{2,2}(\omega,\omega{+}\nu) + \Pi_2(\omega^-,\omega{+}\nu^+)\Big\{ 2\int dx\Delta^+(x)\big[\Lambda_{2,\uparrow}(\omega{+}\nu^+,x) + \Lambda_{2,\uparrow}(\omega^-,x) - 1\big]\, y_{0,\uparrow}(\omega{-}x,\omega{+}\nu{-}x) + 2\int dxdy\Delta^+(x)\Delta^+(y)\, P_\uparrow(\omega{+}\nu{-}x^+)\, P_\uparrow(\omega{-}y^-)\, y_{0,0}(\omega{-}x{-}y,\omega{+}\nu{-}x{-}y)\Big\} \quad . \tag{3.3.36}$$

are sufficient to calculate the charge susceptibility as

$$\chi_{charge}(\nu+i\delta) = \int_{-\infty}^{\infty} \frac{d\omega}{2\pi i}\Big[y_{0,0}(\omega,\omega{+}\nu) - y_{0,0}(\omega,\omega{-}\nu)^* - y_{0,2}(\omega,\omega{+}\nu) + y_{0,2}(\omega,\omega{-}\nu)^*\Big] \equiv \int_{-\infty}^{\infty} \frac{d\omega}{2\pi i} y_{charge}(\omega,\nu) \quad . \tag{3.3.37}$$

The abbreviation $y_{charge}(\omega,\nu)$ as the relevant function is introduced and terms containing S_M and $\tilde{S}_M$, which contribute only in the limit $\nu \to 0$, are dropped.

3.3.3 Numerical evaluation

The practical procedure to calculate a susceptibility is as follows:

1. iterate the one-particle equations to obtain the ionic and defect propagators.
2. solve the system(s) of integral equations to obtain the functions $\chi_{M,M'}$ or appropriate linear combinations thereof.
3. calculate the inhomogeneities I_M by use of (C.18)-(C.19).
4. iterate the defect quantities $Y_{M,M'}$, Y_{mag} or $y_{M,0}$.
5. obtain the susceptibilities along the lines of equations (3.3.17), (3.3.24) or (3.3.37).

Unfortunately, the systems of integral equations for the defect quantities $Y_{M,M'}$, (C.18)-(C.19), become singular in the limit of a vanishing external frequency $\nu \to 0$. This can be anticipated by observing the sum rule (3.3.19). To fulfill the sum rule, the imaginary parts of $Y_{M,M'}$ must have the order of magnitude $\mathcal{O}(1/\nu)$, which diverges for $\nu \to 0$. In contrast, the inhomogeneities and all other functions entering the calculation stay of the order $\mathcal{O}(1)$. Put another way, when the $Y_{M,M'}$ are rescaled to $\mathcal{O}(1)$, i.e. $\nu \cdot Y_{M,M'}$, the inhomogeneities

are effectively scaled to zero, leading to singular systems. Thus, for small values of ν the system is nearly singular, which leads to very bad convergence properties of the employed iterative solution schemes.

These bad convergence properties become plausible by looking at a linear system

$$(1 - L)f = g \quad , \tag{3.3.38}$$

with the non-singular linear operator L and the inhomogeneity g, which can be solved with so-called Krylov subspace methods (see e.g. [Saa00] and [Gou96] and references therein). These methods represent the solution as a linear combination of the vectors $L^n c$, with $n = 0, 1, \ldots, M$ ($M \leq \dim(L) - 1$) and c an arbitrary non-vanishing vector. The space spanned by the M vectors $L^n c$ is the so-called Krylov subspace $\mathcal{K}_M(L, c)$, i.e.

$$\mathcal{K}_M(L, c) = \mathrm{span}\{c, Lc, L^2c, \ldots, L^{M-1}c\} \qquad , \quad M \leq \dim(L) \quad . \tag{3.3.39}$$

Iterating the linear system with the inhomogeneity g as the starting vector is a simple Krylov method, as in each iteration step m the solution is approximated by a vector $f_m \in \mathcal{K}_m(L, g)$. Since the solution must lie in $\mathcal{K}_{\dim(L)}(L, g)$ one is at least after $\dim(L)$ iteration in the position to state the solution, but especially for large systems (such as integral equations) the hope is, that this procedure converges fast and a satisfactory solution is obtained after few iterations much less than $\dim(L)$. For non-singular systems this is indeed usually the case.

The iteration procedure amounts to expanding the inverse operator in the formally exact solutions

$$f = (1 - L)^{-1} g = \sum_{n=0}^{\infty} L^n g \tag{3.3.40}$$

and approximating f by a truncated sum up to some small order m,

$$f \approx f_m = \sum_{n=0}^{m} L^n g = g + L f_{m-1} \quad . \tag{3.3.41}$$

For a nearly singular system the highest eigenvalue of L is close to one and the higher order terms omitted in (3.3.41) are not small, leading to bad convergence properties and the eventual breakdown of the whole iterative scheme.

More generally put, for nearly singular systems the contraction properties of the linear map $L + g1$ are not very pronounced. As a consequence, the convergence towards the fixed point, i.e. the solution $f = (L + g1)f$, whose existence is provided by the Banach fixed point theorem, does happen only very slowly.

As already mentioned above, the system (C.15) to (C.17) becomes nearly singular for the case of small external frequencies ν, leading to drastic consequences regarding the extraction of converged approximate solutions.

These are illustrated in the following example, where the one-particle quantities (i.e. the ionic self-energies (3.2.11)) are obtained within two different approximation schemes: The SNCA, where all vertex functions are taken to be one ($\Lambda_{M,M'}(z, z') = 1$) and in the ENCA,

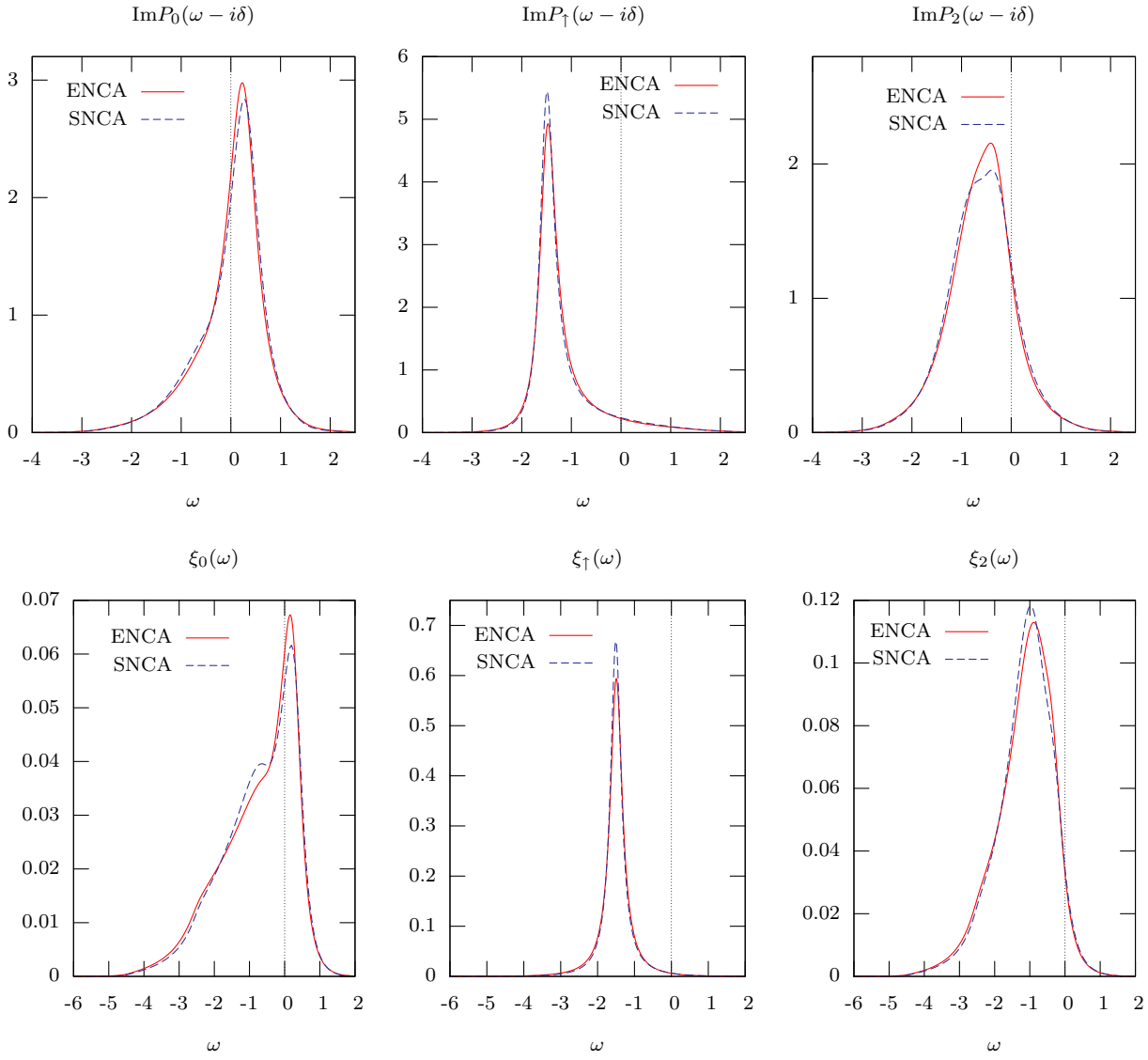

Figure 3.7: Ionic propagators $P_0(\omega - i\delta)$, $P_\uparrow(\omega - i\delta)$, and $P_2(\omega - i\delta)$ (upper, from left to right) and defect propagators $\xi_0(\omega)$, $\xi_\uparrow(\omega)$, and $\xi_2(\omega)$ (lower, from left to right) calculated with the ENCA (full) and the SNCA (dashed). Notice the different scales on the y-axis. The calculations are done for an impurity embedded in a three-dimensional simple cubic tight binding lattice with the hybridization $V = 0.7$, $\epsilon = -1.2$, $U = 1.8$ and temperature $T = 1$.

where additionally (3.2.16) is taken into account. With these at hand, the same sets of integral equations (3.3.31)-(3.3.33) and (3.3.34)-(3.3.36) for the charge susceptibility are iterated. For the sake of simplicity, diagrams containing crossing lines of band electrons are neglected and only the SNCA-versions of these two-particle equations are used. To make it clear again, the same sets of equations are iterated in both cases, differing only in the one-particle functions $P_M(\omega + i\delta)$ and $\xi_M(\omega)$. The motivation to solve the SNCA-versions of the two-particle equations with ENCA one-particle functions lies in the numerical effort to solve the ENCA-versions and by doing so, pre-iterating the SNCA versions is a promising strategy.

The imaginary part of the ionic propagators and the defect propagators are shown in figure 3.7. The calculations are done for a three dimensional tight-binding band with the half bandwidth $W = 3$, a hybridization strength of $V = 0.7$ (leading to an Anderson width $\Delta_A = \pi V^2 \rho_c(0) \approx 0.44$), the position of the unperturbed local level at $\epsilon = -1.2$, a local Coulomb interaction of $U = 1.8$ and temperature $T = 1$. The differences between SNCA and ENCA seem quite small, which could lead to the conclusion, the behavior of the integral equations for the two-particle susceptibility functions is similar, since they are solely determined by these quantities (along with the hybridization function $\Delta(\omega)$ which is the same for each approximation scheme). For the non-singular equations (3.3.31) to (3.3.33) the convergence properties are indeed similar for both input functions and the equations usually converge within 3-5 iterations. The situation is drastically altered for (3.3.34) to (3.3.36).

In figure 3.8 the functions $y_{0,2}(\omega, \omega+\nu)$ and $y_{0,0}(\omega, \omega+\nu)$ are shown after 1, 500, 1000 and 1400 iterations with the external frequency set to $\nu = 10^{-5}$. While the functions $y_{0,M}^{ENCA}$ (upper row), obtained using the ENCA approximations for the one-particle functions, converge into a fixed-point, the SNCA solutions $y_{0,M}^{SNCA}$ (lower row) do not show any signs of convergence. This is confirmed by looking at a measure for convergence in figure 3.9, which shows the mean deviation of successive iterations as a function of the iteration number i,

$$\sigma(i) = \sum_M \int d\omega \left| y_{0,M}^{i}(\omega, \omega+\nu) - y_{0,M}^{i-1}(\omega, \omega+\nu) \right| \quad . \tag{3.3.42}$$

Compared to the functions $\chi_{M,M'}$, or compared to situations with larger values of ν, the convergence of the defect functions $y_{0,M}^{ENCA}$ is very slow, but still exponential in σ. For the case of the SNCA functions $y_{0,M}^{SNCA}$ the solutions do not converge at all and the mean deviation seems to decline only linear with the number of iterations i. In the latter case, the real part acquires its shape within some 10-100 iterations, but then keeps growing. All curves can be collapsed onto one curve, if scaled with a factor inversely proportional to the number of iterations, i.e.

$$\frac{\mathrm{Re}\, y_{0,M}^{SNCA;i}}{i} = \frac{\mathrm{Re}\, y_{0,M}^{SNCA;j}}{j} \tag{3.3.43}$$

for all i and j sufficiently large.

The imaginary parts of the $y_{0,M}^{SNCA}$ shown in the inset of the lower graphs in figure 3.8 seem to behave even worse than the real parts: their form keeps changing with i and they even change sign in some parts of the frequency range. Astonishingly, when linear combined to the function y_{charge} (see (3.3.37)) most of the parts changing with i cancel and a relatively constant function remains. This is also true for the drift in real parts, as can

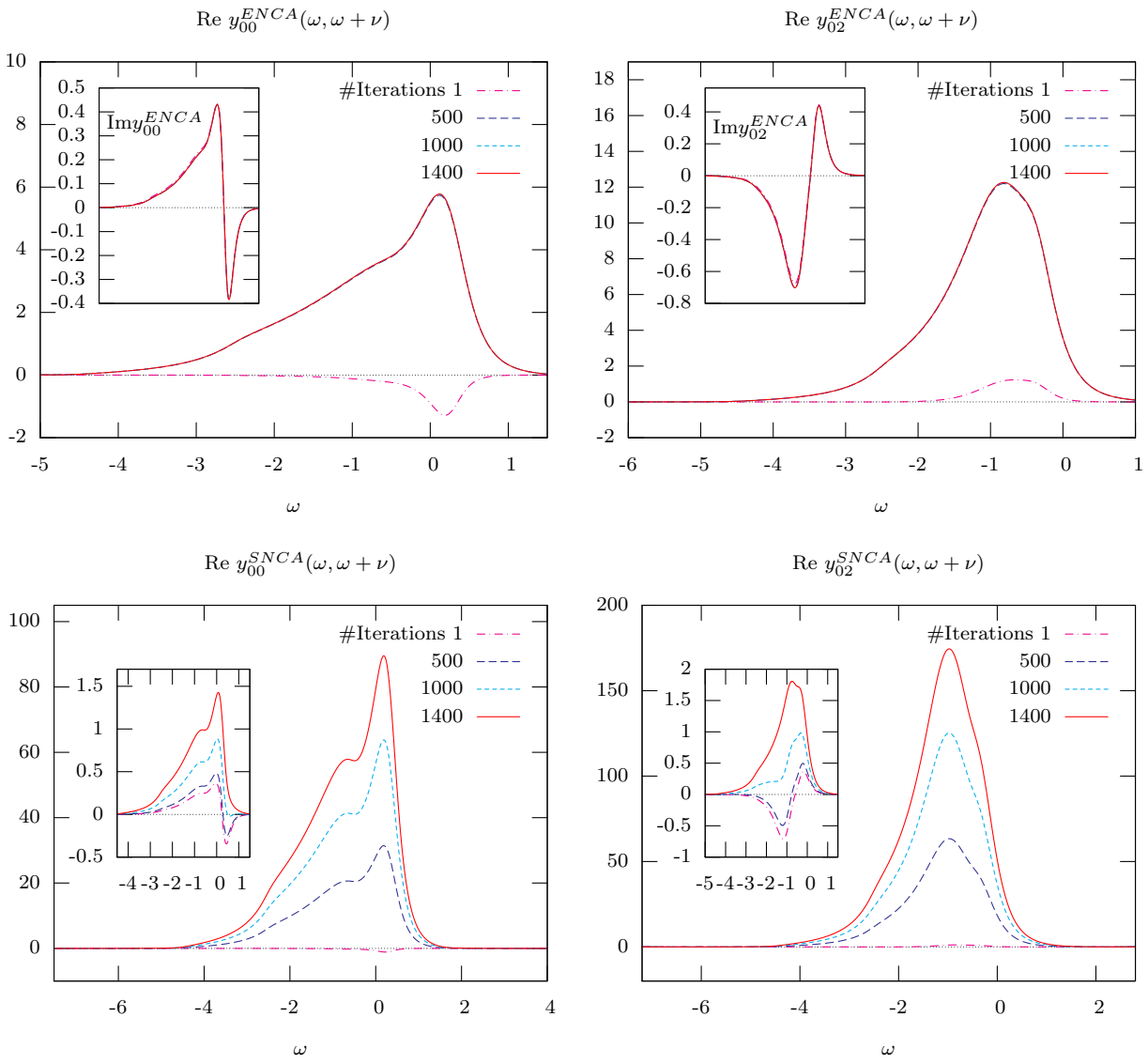

Figure 3.8: The real and imaginary parts (insets) of the two defect functions $y_{0,0}(\omega,\omega+\nu)$ (left) and $y_{0,2}(\omega,\omega+\nu)$ (right) calculated for $\nu = 10^{-5}$ after 1, 500, 1000 and 1400 iterations. The curves are obtained from the simplified SNCA-versions of the two-particle integral equations, but with the ENCA-solutions (upper row) or the SNCA-solutions (lower row) for the one-particle functions as seen in figure 3.7. For the ENCA case (upper row) the curves for 500, 1000 and 1400 iterations cannot be distinguished.

be seen in the left panel of figure 3.10. Notice the scale of the functions: The real parts of $y_{0,M}$ are of the order of 100 and the linear combination y_{charge} only of the order of 10^{-3}! It is worthwhile to note, that due to the prefactor of $1/(2\pi i)$ in equation (3.3.37) the real parts of the previously considered functions determine the imaginary part of the physical susceptibility (which vanishes proportional to ν) and vice versa. It is a very remarkable feature of the equations, that these large valued functions determine a value, which turns out to be very small.

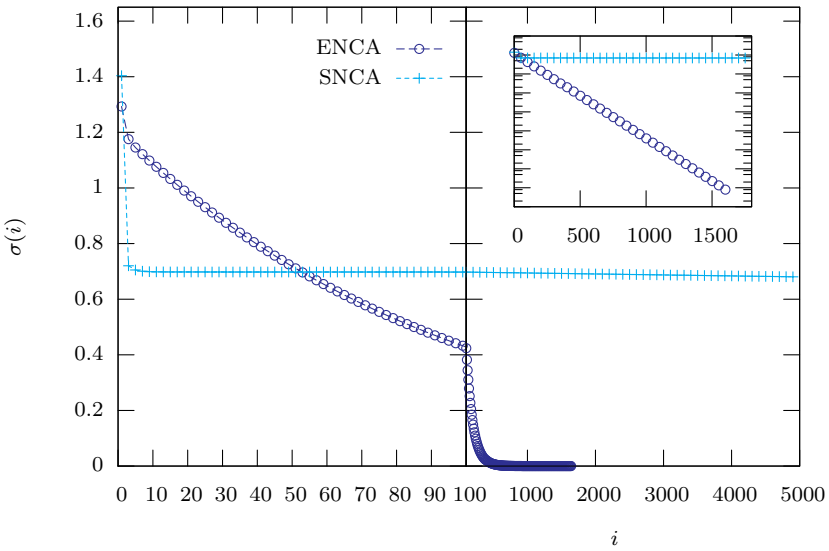

Figure 3.9: The mean deviation $\sigma(i)$ of two successive iterations as a function of the iteration number i. Circles are for the ENCA while crosses denote the SNCA. The inset reveals in a logarithmic plot the exponential convergence of the ENCA.

The question of the origin of these drifts remain unclear so far: at the one hand the functions $y_{0,M}$ contain linear combinations of the S_M and $\tilde{S}_M$, so the drift could be an actual effect building up the necessary order of magnitude. Notice however, the sum rule (3.3.19) does not give any insight here, since, for one thing it would suggest the growing of the imaginary and not the real part, for another the sum rule of the linear combinations y_{0M} yields

$$\sum_{M'} y_{M',M}(\omega, \omega+\nu) = 0 \quad . \tag{3.3.44}$$

On the other hand, the drift of the $y_{0,M}^{SNCA}$ and, more important, the physical susceptibility $\chi_{charge}^{SNCA}(10^{-5})$ as depicted in figure 3.10 depends on the numerical accuracy. For more sampling points used, the picture stays qualitatively the same but the increase of the physical susceptibility with the number of iterations is not as pronounced (see figure 3.10). Especially this point, in combination with the observed drastic sensitivity of the equations to small changes in the one-particle input functions (ENCA $\leftrightarrow$ SNCA), suggest that at least the drift in the susceptibility is unphysical and owes to numerical deficiencies and the near-singularity of the integral equations. The curves of the actual solutions should probably look like the $y_{0,M}^{ENCA}$ shown in the upper row of figure 3.8, which are also obtained for the $y_{0,M}^{SNCA}$ after some 50-100 iterations but then numerical errors keep accumulating and cause the observed drifts. It is a very remarkably fact, that despite the lack of numerical convergence for the solutions, a detailed balance is kept in the equations and errors are accumulated only in such a way, as to influence the resulting linear combination y_{charge} very little. This is especially true for the real and imaginary parts of the solutions, since their magnitudes differ considerably. The conclusion drawn thereof is that even while the actual integral equations are nearly singular and numerically ill-behaved, however, the physical quantity calculated in the end is very insensitive to these circumstances.

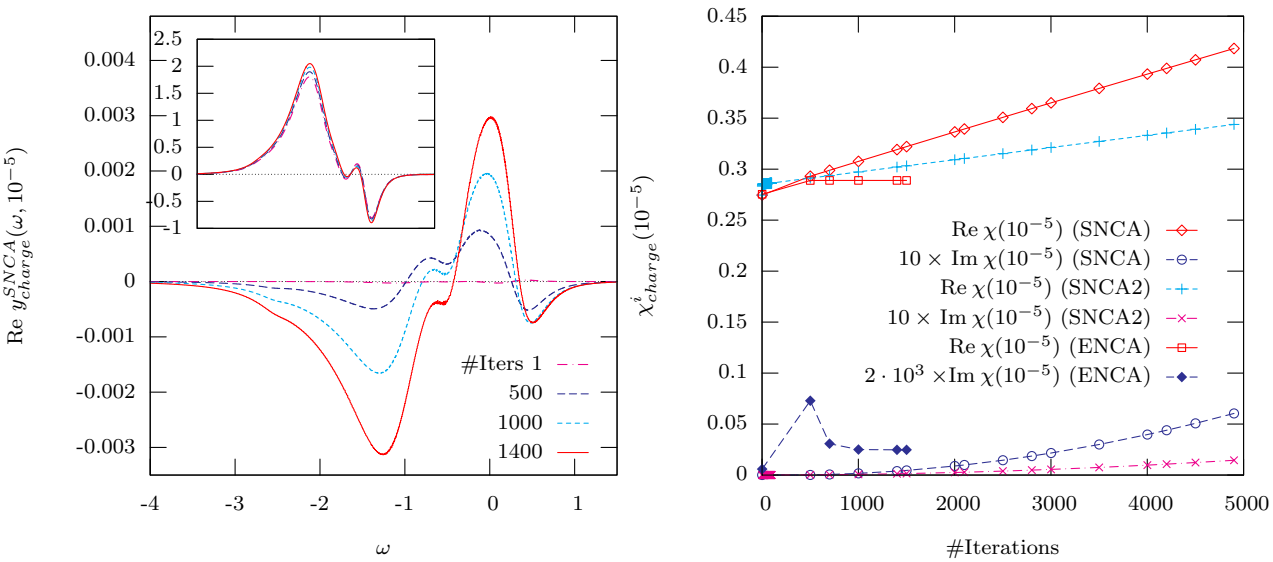

Figure 3.10: Left panel: the real and imaginary part (inset) of the relevant function $y^{SNCA}_{charge}(\omega, \nu)$ of equation (3.3.37) for the SNCA approximation scheme calculated for $\nu = 10^{-5}$ after $1, 500, 1000$ and 1400 iterations.
Right panel: the physical charge susceptibility for $\nu = 10^{-5}$ as a function of the number of iterations. The curves denoted with SNCA2 are obtained with more sample points than the others.

Iterating the full ENCA-versions of the two-particle equations as stated in (3.3.34)-(3.3.36) reveals that the tendencies described above towards drifting and accumulating errors are also present. Figure 3.11 shows the dependency of the dynamic charge susceptibility on the number of iterations. T_K refers to the low energy scale of the SIAM as it will be defined in equation (3.4.3). For high frequencies $\omega/T_K \gtrsim 1$ all different iteration parameter sets yield the same results and the curves coincide. By an inspection of low frequencies, $\omega/T_K \lesssim 1$ in the graphs, the drifting of the susceptibility values is clearly visible. The results get worse with higher number of ENCA iterations, eventually even resulting in negative values for the imaginary part, as in the high temperature calculation shown in the left graph of figure 3.11.

The conclusion, that these drifts are unphysical and only connected to the afore mentioned issues, is drawn due to two reasons: (a) the drifts are dependent on the numerical accuracy used. Points with higher numerical accuracy always are closer to the continuous reference curve in figure 3.11. (b) the scale of the absolute values of the variations is constant for different temperatures. It seems evident to assume, that the absolute value of the calculated susceptibility should influence the value of these drifts, if these were physical. Consequently, the value of the drifts should be larger for the low temperature calculation (right panel). But this is not the case and the errors are of the same magnitude as for high temperatures. This is understandable if they are determined by the numerical accuracy, which is the same for different parameter sets. Compared to the pure SNCA iterations of the previous paragraph, these drifts are a lot more pronounced for the ENCA. The scale of the accumulated error in the pure SNCA-case is of the order of $\sim 10^{-5}$/Iteration (see figure 3.10), while for the ENCA this value is as high as $\sim 10^{-3}$/Iteration. This is due to the limited numerical accuracy while handling the vertex corrections and their convolutions in the ENCA.

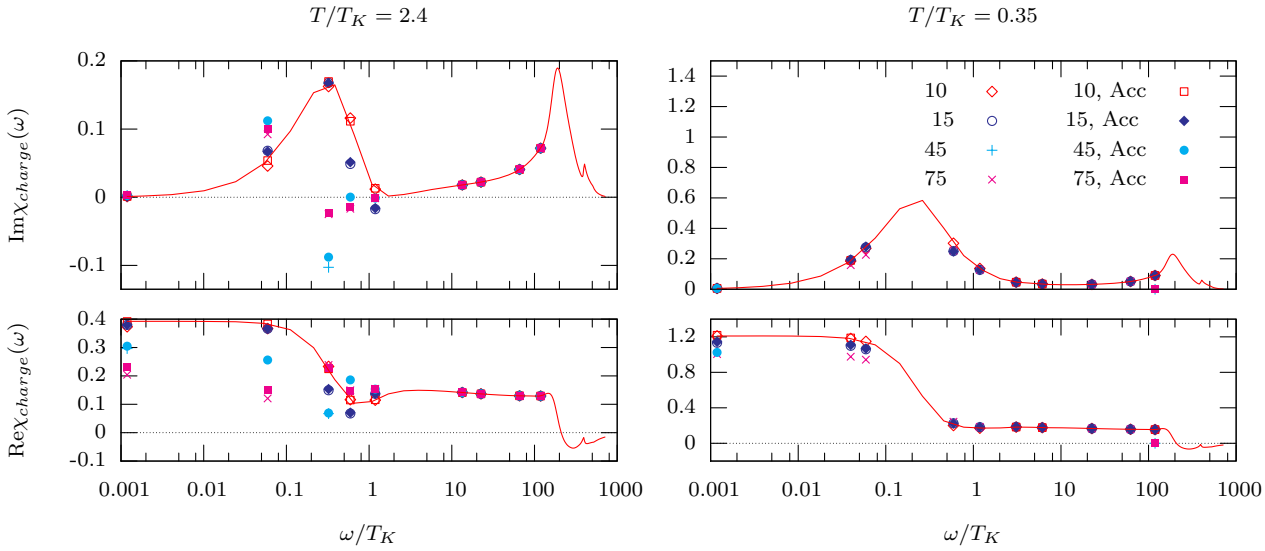

Figure 3.11: Imaginary (upper panels) and real (lower panels) parts of the dynamic charge susceptibility in a logarithmic plot for various iterations parameters. The left figure shows the results for a relatively high temperature $T/T_K \approx 2.4$, while for the right plot the temperature is $T/T_K \approx 0.35$. T_K represents the low energy scale (Kondo temperature) of the model (see equation (3.4.3) in the next section). The unlabeled continuous red graph represents the reference calculation with 250 SNCA pre-iterations and 10 ENCA iterations. The data points were obtained for 10, 15, 45 and 75 ENCA iterations and the curves additionally marked with an "Acc" are evaluated with higher numerical accuracy. The number of SNCA pre-iterations is 75 for these points. The color coding of the data points of hight temperature calculation (left graph) is the same as for the low temperature plot (right). The model parameters are $\epsilon = -1$, $U = 4$, $W = 3$ and $\Delta_A = 0.3$

The role of the SNCA pre-iterations is to set the overall scale of the functions $y_{M',M}$ and achieve the balance between their imaginary and real parts. The actual number of pre-iterations is not critical, as long as these two goals are reached, e.g. for pre-iteration numbers greater than ~ 50. Higher values do not change the results, as it can be seen by comparing the reference curve in figure 3.11, which is calculated with 250 pre-iterations (unlabeled continuous line) to the one with only 75; the number of ENCA iterations is the same (10) for both cases. The strategy to obtain reasonable estimates for the charge susceptibility is to iterate the ENCA about 10-20 times, to avoid a large accumulated error.

In that sense, the quantitative value of the susceptibility is somewhat disputable, but the hope is, that at least the qualitative features are captured. Especially trends in the dependence on external parameters, such as temperature, Coulomb repulsion or hybridization strength, should be correct, since solutions obtained for other values for the parameters T, U, V and ϵ^f share the same numerical behavior.

Generally it can be stated, that the calculation of the magnetic susceptibility is a straight forward task without any complications, and no convergence problems at all are encountered in any cases considered. However, the charge susceptibility is a very delicate matter. First of all it is of paramount importance to choose the "right" linear combination of the defect quantities $Y_{M,M'}$. The above considered linear combinations $y_{0,M}$ seem to be a good choice,

since any other combinations tried by the author gave very poor estimates, in most cases none at all. The described drifts are worse and the very subtle balance between $y_{0,M}(\omega, \omega + \nu)$ and $y_{0,M}(\omega, \omega - \nu)$ is destroyed.

Second, the equations are programmed as they are, i.e. no relaxation, mixing, or rescaling of functions during the iterations is done. The equations are particular sensitive to these kinds of manipulations: when trying to accelerate the convergence by scaling the functions (or their real or imaginary part separately) to the right order of magnitude, or oscillatory behavior is suppressed via relaxation, the above mentioned balance was destroyed, resulting in even worse convergence properties. However, this does by no means imply the non-existence of such a proper scaling. Especially the lack of the analytic expression for the functions $\tilde{S}_M$ of sum rule (3.3.11) prevented progress in this direction. With $\tilde{S}_M$ at hand, one function of the $y_{0,M}$ could be eliminated from the integral equations and the singular character of these redeemed.

It is left as a future task to investigate the mathematical and numerical properties of these equations more thoroughly.

3.4 Physical properties of the SIAM

After having explored the numerical properties of the impurity solver it is necessary to gain insights on its physical behavior. This is necessary, since the solution of the impurity model lies at the heart of locally complete approximation and possible shortcomings of the impurity solver are expected to have a significant influence on the solution of lattice system.

The SIAM has been widely and extensively studied with various methods, as already mentioned in section 3.1. Historically, the focus of the direct perturbation theory was laid on the $U = \infty$ version of SIAM [Gre83, Koj84, Bic87, And95, Kro97, Kro05]. But with the development of the DMFT (i.e. locally complete approximation) the interest in accurate and manageable impurity solvers has revived. Especially versions capable of handling a finite Coulomb repulsion $U < \infty$ are of interest [Pru89, Sak88, Kei90, Sas92, Kan96, Hau01, Sak05, Ots06a, Gre08]. Even though the one-particle equations for the ENCA approximation were already published in 1989 [Pru89], a thoroughly study of one- and especially two-particle properties within this approximation for a larger region in parameter space is still lacking in the literature. For an thorough analysis of the threshold behavior of the ionic propagators within this approximation and a comparison to other approximation schemes of direct perturbation theory the reader is referred to [Gre08].

3.4.1 One-particle properties

Figure 3.12 shows the local f-electron density of states (DOS, frequently called spectrum as well),

$$\rho_f(\omega) = -\frac{1}{\pi} \mathrm{Im}\, G_f^{(loc)}(\omega + i\delta) \quad , \tag{3.4.1}$$

and the total self-energy as defined in (2.2.23) and (2.2.24) for the symmetric SIAM ($2\epsilon^f + U = 0$) and various temperatures, whereas figures 3.13 and 3.14 show asymmetric cases. The calculations are done for a three dimensional simple-cubic (`3d-SC`) tight-binding band of c-electrons with the hopping matrix element $t = 0.5$, i.e. the half bandwidth $W = 2t\,d = 3$.

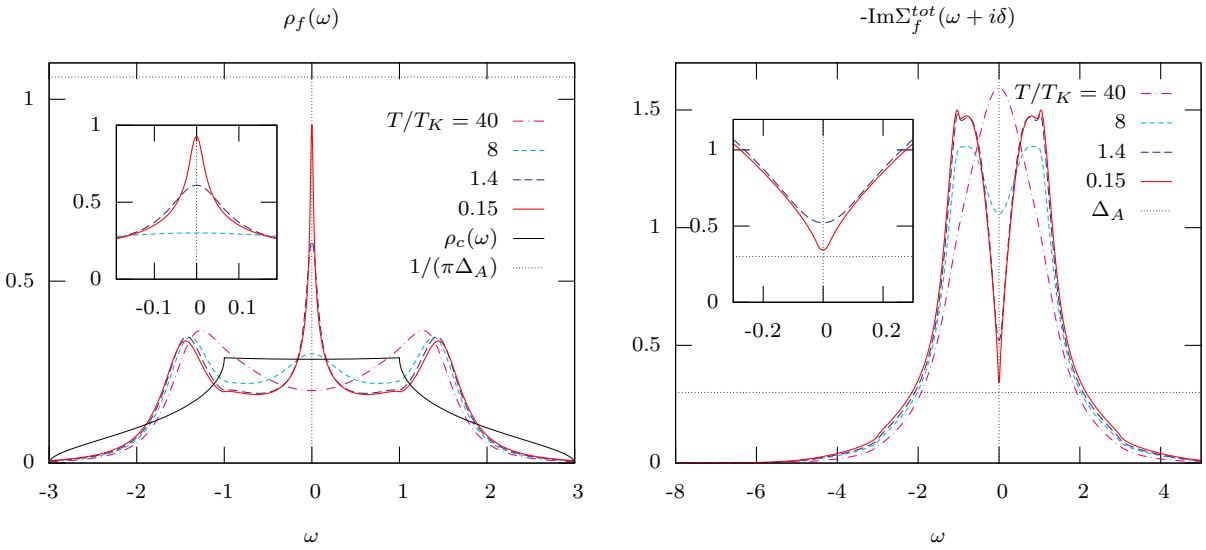

Figure 3.12: Left panel: the f-electron spectral function $\rho_f(\omega)$ calculated for the symmetric case, i.e. Coulomb repulsion $U = 2$ and $\epsilon^f = -1$ and an Anderson width of $\Delta_A = 0.3$ for various temperatures. The temperatures are measured in units of the Kondo temperature $T_K = 0.0255$ (see (3.4.3)). The c-electrons DOS $\rho_c(\omega)$ is that of a three dimensional simple-cubic tight binding band (`3d-SC`) with the half bandwidth $W = 3$, which is shown as well. The dashed line in the upper part of the figure represents the exact value of $1/(\pi\Delta_A)$ for the peak height of the Kondo resonance at $T = 0$. The inset shows the region around the Fermi level $\omega = 0$.
Right panel: negative imaginary part of the total f-electron self-energy for the same parameter values. The $T = 0$ limit of Δ_A is shown as a straight line as well. The inset shows the quadratic minimum formed at low temperatures at the Fermi level.

The free tight binding DOS of the c-electrons is shown in figure 3.12 as well, where the van Hove singularities at energies $\omega = \pm 1$ are clearly visible as cusps (for details on the lattice structure see appendix D). These van Hove singularities leave their traces in the spectra and self-energies and their visibility constitutes a test for the numerical procedures used.

In all spectra, the two high energy Hubbard peaks are visible. The position of these are roughly at the values of the levels of the isolated ion, i.e. ϵ^f and $\epsilon^f + U$. The levels are considerably broadened by hybridization processes and the maximum positions of the Hubbard peaks are renormalized away from the Fermi level $\omega = 0$. This shifts are stronger, the stronger the effective coupling to the c-electrons are, e.g. for larger values of the Anderson width

$$\Delta_A = \pi\rho_c(0)V^2 \quad , \tag{3.4.2}$$

where $\rho_c(0)$ is the c-band density of states at the Fermi level ($\omega = 0$). For Coulomb repulsions $U \geq 4 = W - \epsilon^f$, i.e. the upper level is moved out of the c-band, the peak gets sharp and eventually transforms into a δ-peak with a fractional spectral weight.

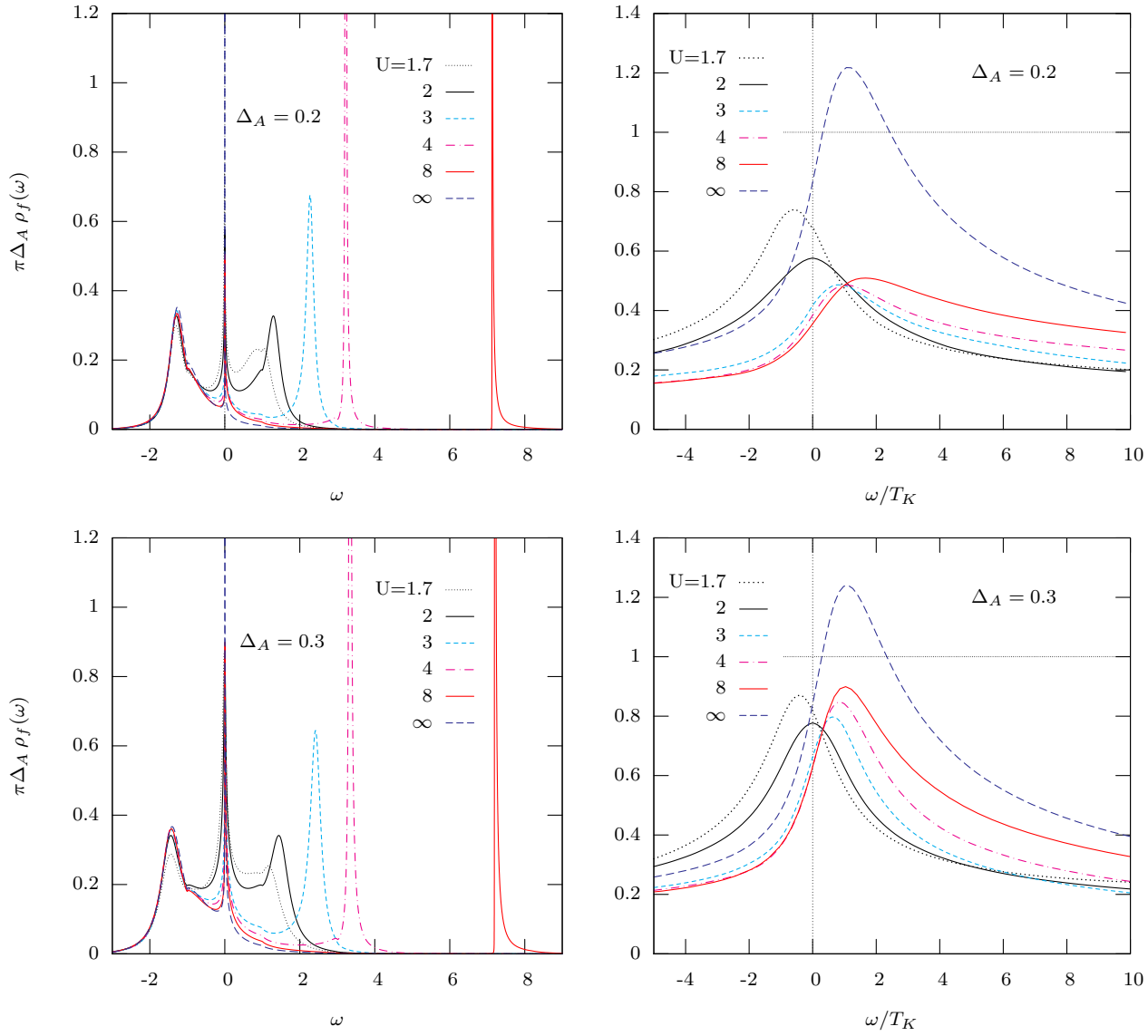

Figure 3.13: Rescaled f-electron spectra $\pi\Delta_A\,\rho_f(\omega)$ for the asymmetric case for two choices of the Anderson width $\Delta_A = 0.2$ (upper row) and $\Delta_A = 0.3$ (lower row) for varying values of U. The temperatures are chosen to be about half the Kondo temperature for each value of U, i.e. $T = T_K/2$ with T_K calculated via equation (3.4.3). The right panels show the low energy interval around the Fermi level with the frequency ω measured in units of the respective Kondo temperature. The horizontal line indicates the limiting value $\pi\Delta_A\,\rho_f(\omega) = 1$. Other parameters are the same as in figure 3.12. The f-occupation numbers are, for $\Delta_A = 0.2$ (upper row) $n_\sigma^f(U=1.7) = 0.52$, $n_\sigma^f(U=2) = 0.5$, $n_\sigma^f(U=3) = 0.477$, $n_\sigma^f(U=4) = 0.468$, $n_\sigma^f(U=8) = 0.458$ and $n_\sigma^f(U=\infty) = 0.472$ and for $\Delta_A = 0.3$ (lower row) $n_\sigma^f(U=1.7) = 0.529$, $n_\sigma^f(U=2) = 0.5$, $n_\sigma^f(U=3) = 0.467$, $n_\sigma^f(U=4) = 0.457$, $n_\sigma^f(U=8) = 0.446$ and $n_\sigma^f(U=\infty) = 0.451$.

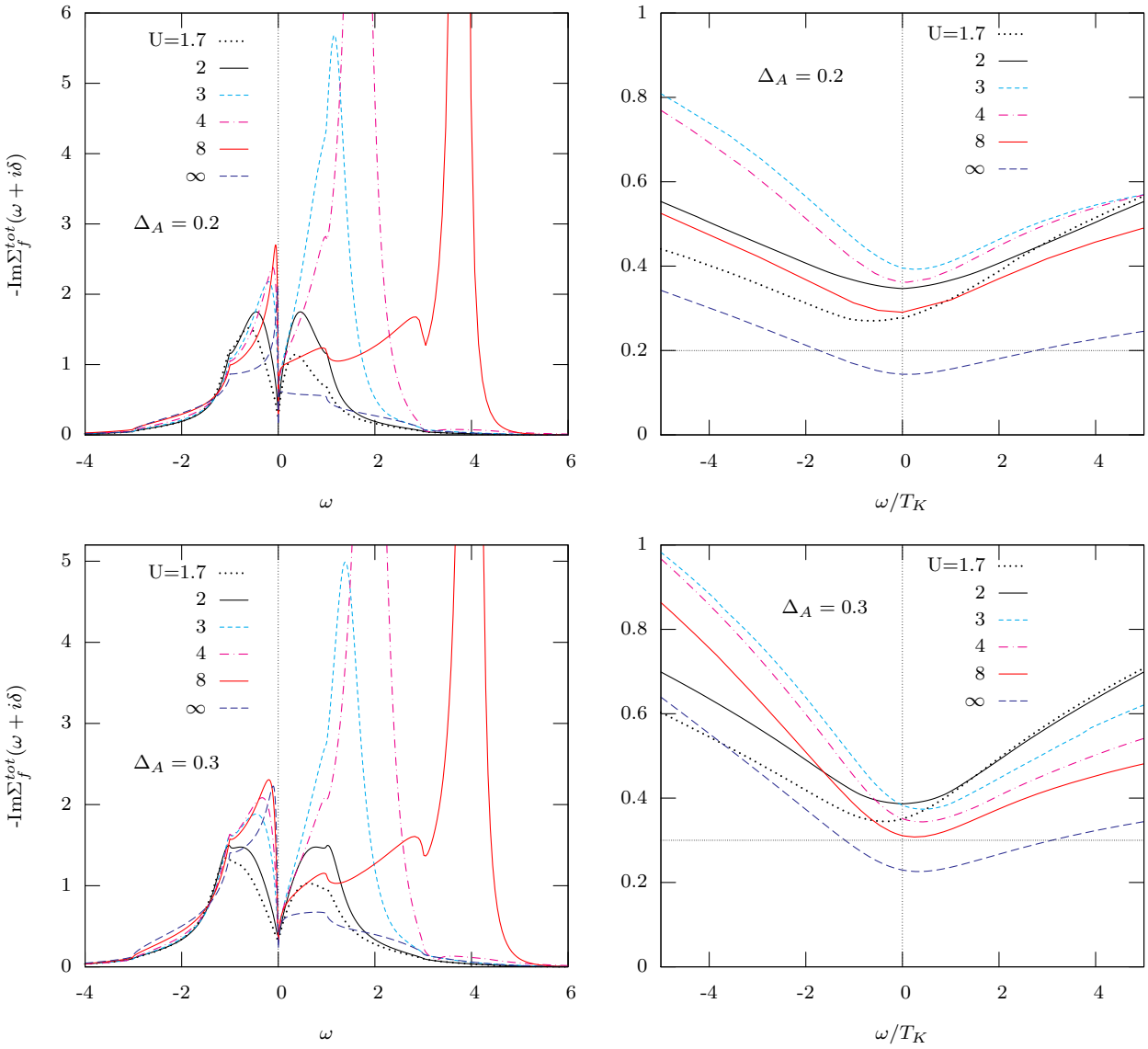

Figure 3.14: Negative imaginary parts of the total self-energy for an Anderson width $\Delta_A = 0.2$ (upper row) and $\Delta_A = 0.3$ (lower row) for different values of U. For the low energy plot (right panel) the horizontal line shows the $T = 0$ limiting value with the energy variable measured in units of the corresponding Kondo temperature T_K. Parameter values are the same as in figure 3.13.

For low temperatures a qualitatively new feature emerges at the Fermi level, the so-called Kondo peak or Abrikosov-Suhl resonance (ASR). This is one manifestation of the Kondo effect and is associated with a low-energy scale, the Kondo temperature T_K [Pru89]

$$T_K = \frac{\min(W,U)}{2\pi}\sqrt{J}\, e^{-\pi/J} \quad , \qquad J = -\frac{2U\Delta_A}{\epsilon^f(\epsilon^f+U)} \quad . \tag{3.4.3}$$

From the non-analytic exponential dependence on the effective coupling J it is apparent that T_K represents a non-perturbative energy scale and thus classifies the Kondo effect as a genuine many-body effect.

The physics of the Kondo effect is well understood and can be characterized as the formation of a dynamic singlet between the localized spin of the f-system and the itinerant c-electrons. Due to hybridization the band electrons are coupled antiferromagnetically ($J > 0$ in (3.4.3)) to the localized f-electrons and build up a screening cloud around the impurity, eventually completely compensating the local moment and thereby forming the dynamic singlet. The singlet is called dynamic, since the participating conduction-electron spin is composed of many delocalized c-electrons and thus the singlet is not attributed to a bound pair of electrons. Sloppy speaking, the band electrons adjust their spin and participate in the singlet, whenever they "fly" by the impurity.

This scenario is strictly valid only in the Kondo regime with $U = -2\epsilon^f = \infty$ and a finite J, where the Kondo-model is obtained as the asymptotic form of the SIAM. In this situation charge fluctuations of the impurity are completely suppressed ($n^f = 1$) and the local f-spin represents the only dynamic variable, which is coupled antiferromagnetically to the conduction electron spin.

Even though all parameter values chosen in this work are not close to the Kondo limit and charge fluctuations play an important role, the scenario of the Kondo screening still is in effect and the Kondo temperature will be used as the relevant low energy scale. The thing to bear in mind is the influence of the valence fluctuations present in all situations and the modifications induced by those.

The ASR at the Fermi level in the f-electron DOS at low temperatures is due to the possibility of spin-flip processes in the dynamic singlet with vanishing excitation energy. For excitation energies larger than the binding energy of the dynamic singlet, which is of the order of the Kondo temperature T_K, the singlet is destroyed and the DOS reduced. As a consequence, the width of the ASR is of the order T_K as well, but with additional broadening due to the influence of valence fluctuations and intermediate valence phenomena, especially for large Δ_A or small $|\epsilon^f|$, U.

At higher temperatures, the thermal energies are larger than the binding energy and the singlet formation is thermally suppressed, leading to the disappearance of the ASR.

The physical state at very low temperatures $T \ll T_K$ can be characterized as a local Fermi liquid [Noz75, Hew93]. This can be observed in the negative imaginary part of the total self-energy, shown in the figures 3.12 and 3.14. For low temperatures it develops a quadratic minimum, which is characteristic for a Fermi liquid state and indicates the vanishing of scattering due to the Coulomb interaction. The residual $T = 0$ limiting value of Δ_A for the imaginary part of the total self-energy is a pure one-body effect and comes from potential scattering due to the hybridization. The question whether this limit is reproduced or violated, allows one to judge the low temperature behavior of the approximation. As it

can be seen in the right graphs of figure 3.14, only the $U = \infty$ curves with vertex corrections discarded (NCA, cf. section 3.2) do violate this limit.

The value of the DOS at the Fermi level can serve as a benchmark for the impurity solver as well. At zero temperature it is determined by the exact Friedel sum rule for the Fermi liquid [Lan66, Hew93],

$$\rho_f(0) = \frac{\sin^2(\pi n_\sigma^f)}{\pi \Delta_A} \quad , \tag{3.4.4}$$

where n_σ^f is the occupation number of the impurity per spin, which is just half the total f-occupation $n_\sigma^f = \frac{1}{2} n^f$. For the symmetric case where $n_\sigma^f = \frac{1}{2}$ this evaluates to $\rho_f(0) = 1/(\pi\Delta_A)$.

Even though the ENCA calculations are not done for zero temperature, the trend given by the Friedel sum rule should be present in the Fermi liquid phase, i.e. for low and comparable temperatures such as half the Kondo temperature $T = T_K/2$. As it can be seen from figure 3.13, the value of the DOS at the Fermi level is indeed reduced for fillings away from half filling (i.e. $U \neq 2$), except for $U = \infty$ and $U = 1.7$. The increase for $U = 1.7$ ($n_\sigma^f = 0.521$ for $\Delta_A = 0.2$ and $n_\sigma^f = 0.529$ for $\Delta_A = 0.3$) contrary to the expectation, could be a finite temperature effect, which diminishes for smaller T. But since the increase is considerable, this might as well hint at a deficiency of the ENCA.

For $\Delta_A = 0.3$ (lower row in figure 3.13) the qualitative features are similar to the $\Delta_A = 0.2$ case. The DOS at the Fermi level still decreases for fillings smaller than half filling and $U < \infty$, but the trend is less pronounced. The graphs for $U = 4$ ($n_\sigma^f = 0.457$) and $U = 8$ ($n_\sigma^f = 0.446$) even have almost identical values for $\rho_f(0)$.

For both hybridization strength, the spectra for $U = \infty$ (NCA), where vertex corrections are discarded altogether, has the strongest increase in the DOS at the Fermi level. This points at the known deficiency of the NCA for low temperatures and in the valence fluctuation regime. Since the ENCA curves do not show this increase as strong, it is justified to assume that it performs better in these situations.

For dynamic quantities and finite temperature calculations not only the values of the spectra at the Fermi level are important, but the ASR as a whole as well. For the symmetric situation (i.e. half filling with $n_\sigma^f = 1/2$ and $2\epsilon^f + U = 0$) the shape of the ASR is symmetric around the Fermi level. Away from half filling it becomes asymmetric and the maximum is shifted away from $\omega = 0$ (cf. figure 3.14). For $U > 2$ the maximum is shifted towards energies above the Fermi level and for $U < 2$ to lower energies. The maximum peak height does not show an uniform trend and either increases or decreases when compared with the symmetric case, depending and the hybridization strength and the Coulomb repulsion.

For the smaller value of the hybridization ($\Delta_A = 0.2$, upper row in figure 3.13) the maximum height of the ASR first decreases with growing U but eventually starting to increase around $U = 8$. The $U = \infty$ value of the peak height is considerably larger and exceeds the $T = 0$ limiting value $1/(\pi\Delta_A)$. For the larger hybridization strength $\Delta_A = 0.3$, the heights of the ASR for $U \neq 2$ are always larger than the one for half filling, but still do not exceed the limit of $1/(\pi\Delta_A)$ for finite $U < \infty$. This hints at the possible tendency of the ENCA to overestimate the height of the Kondo resonance for very low temperatures.

It is well known, that the (S)NCA overestimates the height of the Kondo resonance and violates Fermi liquid properties for too low temperatures. This pathology is strongest for

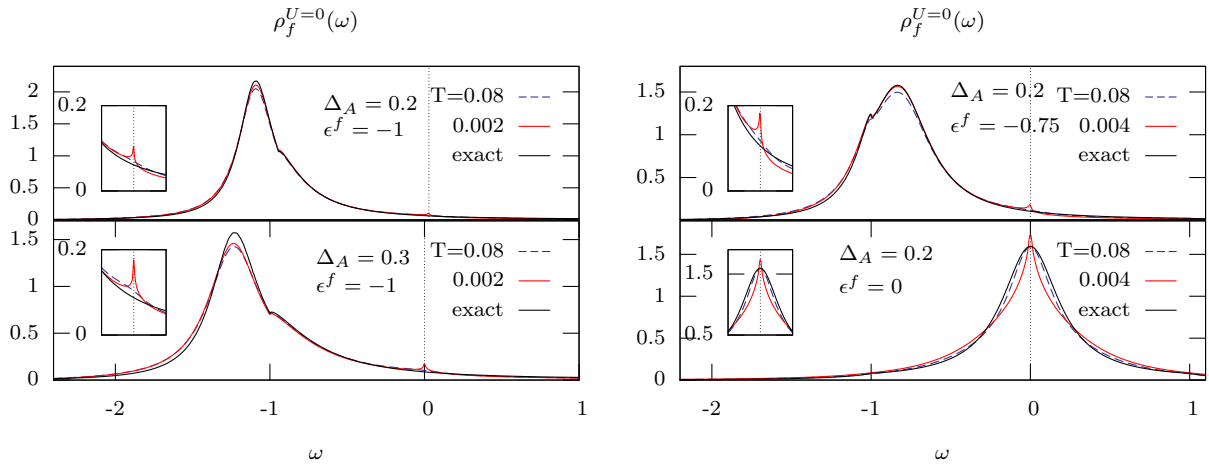

Figure 3.15: Comparison of the spectra of the exact solution (3.4.5) for the non-interacting limit ($U = 0$) with the ENCA solution for two temperatures and two hybridization strength $\Delta_A = 0.2$, 0.3 and various impurity level positions $\epsilon^f = -1$, -0.75 and 0 as indicated in the graphs. The insets show enlargements of the low energy region around the Fermi level $-0.3 \leq \omega \leq 0.3$.

the case considered here, where the orbital degeneracy is $N = 2$ (spin only), and is less pronounced for larger values of N. The pathology is associated with a pathology temperature T_p, which is much smaller than the Kondo temperature in the Kondo regime [Kur85c, Bic87]. The reason, that the $U = \infty$ spectra do severely overestimate the ASR and violate Fermi liquid relations already for $T = T_K/2$, lies in the fact that with the choice of the parameter values $\epsilon^f = -1$ and $\Delta_A = 0.2, 0.3$ the systems are still considerably away from the Kondo regime and the pathology is more pronounced [Gre83, Kur84].

In contrast to the (S)NCA, the ENCA does not overestimate the height of the Kondo peak or violate the Fermi liquid property of the total self-energy for the symmetric case down to temperatures of the order of one tenth of the Kondo temperature. In the asymmetric case this is still true for temperatures as low as half the Kondo temperature. The fact that the ENCA performs better than the (S)NCA for the same parameter values of ϵ^f and Δ_A is remarkable, especially since it reduces to the latter for large U. This leads to the conclusion, that the ENCA apparently incorporates a more favorable balance between different kinds of perturbational processes, which is of a particular importance and has been pointed out repeatedly [Gre08, Kei85, Kei90].

The pathology in the (S)NCA lies at least partly in the failure to describe strong valence fluctuations for low temperatures around the Fermi level correctly. This can be observed by studying non-interacting $U = 0$ limit [Gre83]. The exact solution of the f-Green function in that case is given by

$$F_\sigma^{U=0}(z) = \frac{1}{z - \epsilon^f - \frac{1}{N_0}\sum_{\underline{k}} \frac{V_{\underline{k}}^2}{z - \epsilon_{\underline{k}}^c}} \quad . \tag{3.4.5}$$

To get an insight, if and how the pathology becomes noticeable in the ENCA, it is worthwhile to compare the exact solution (3.4.5) with the ENCA, which is done in figure 3.15. The calculations are for different hybridization strength Δ_A and positions of the local level ϵ^f. For the ENCA calculations additionally two different temperatures are chosen. For the higher temperature the curves closely resemble the exact solution but for the lower temperature deviations emerge. Of special interest is the growing unphysical spike at the Fermi level $\omega = 0$. For the same ionic level position, it is more pronounced for a larger hybridization strength (left graphs in figure 3.15) and for constant hybridization it grows with a increasing ϵ^f. These trends confirm the expectation that the ENCA has difficulties describing valence fluctuations at very low temperatures.

3.4.2 Two-particle properties

Besides the signature of the Kondo effect via the many-body resonance at the Fermi level in the one-body Green function, the magnetic screening can be directly observed in the static magnetic susceptibility or equivalently, in the screened magnetic moment of the f-electrons,

$$\mu_{eff}(T) = \frac{1}{(g\mu_B)^2} T\chi_{mag}(0) \quad . \tag{3.4.6}$$

This is shown in the upper row of figure 3.16 as a function of temperature for various Anderson widths and Coulomb repulsions U.

For all cases considered, the local f moment tends to zero for low temperatures. The general shape of the curves resembles the exact solutions known from the literature [Km80a, Km80b, Oki83a] and the different asymptotic regimes are clearly visible. At high temperatures the impurity is effectively non-interacting and the susceptibility behaves as $1/(8T)$ resulting from the induced moment only (free orbital regime, $\mu_{eff} = 1/8$). For lower temperatures the effect of the Coulomb repulsion becomes noticeable and leads to a depopulation of empty and doubly occupied f-states, which results in a forming local f-spin along with an increased effective moment (local moment regime, $\mu_{eff} = 1/4$). As the temperature is still lowered, Kondo physics comes into play and the local f-spin is increasingly screened eventually leading to a vanishing effective moment (strong coupling regime, $\mu_{eff} = 0$). In the asymmetric case, a valence fluctuation regime with $\mu_{eff} = 1/6$ can be traversed between the free orbital and the local moment regime, depending on the detailed choice of the parameters.

The tendencies of the graphs to show the characteristic features of a physical regime depends on the specific choice of the parameter values. For large Coulomb repulsions $U + \epsilon^f > W$, where the upper Hubbard peak lies outside the c-band, e.g. $U = 4$, 8 in figure 3.16, the tendency to form a local f-moment is stronger, since direct hybridization processes involving doubly occupied f-states are strongly suppressed. Smaller Anderson width also result in a larger local moment for the obvious reason of reduced hybridization. Additionally, the screening sets in at a lower temperature due to a reduced Kondo scale T_K. For the cases of $U = 4$ and $U = 8$, the graphs bear stronger resemblance to the universal curve of the spin-$\frac{1}{2}$ Kondo model [Wil75, Km80a], since the influence of valence fluctuations, causing deviations thereof, is reduced.

The valence fluctuation regime is not directly visible for small Coulomb repulsions and can only be guessed for $U = 8$ and $U = \infty$, where the upper Hubbard peak is irrelevant

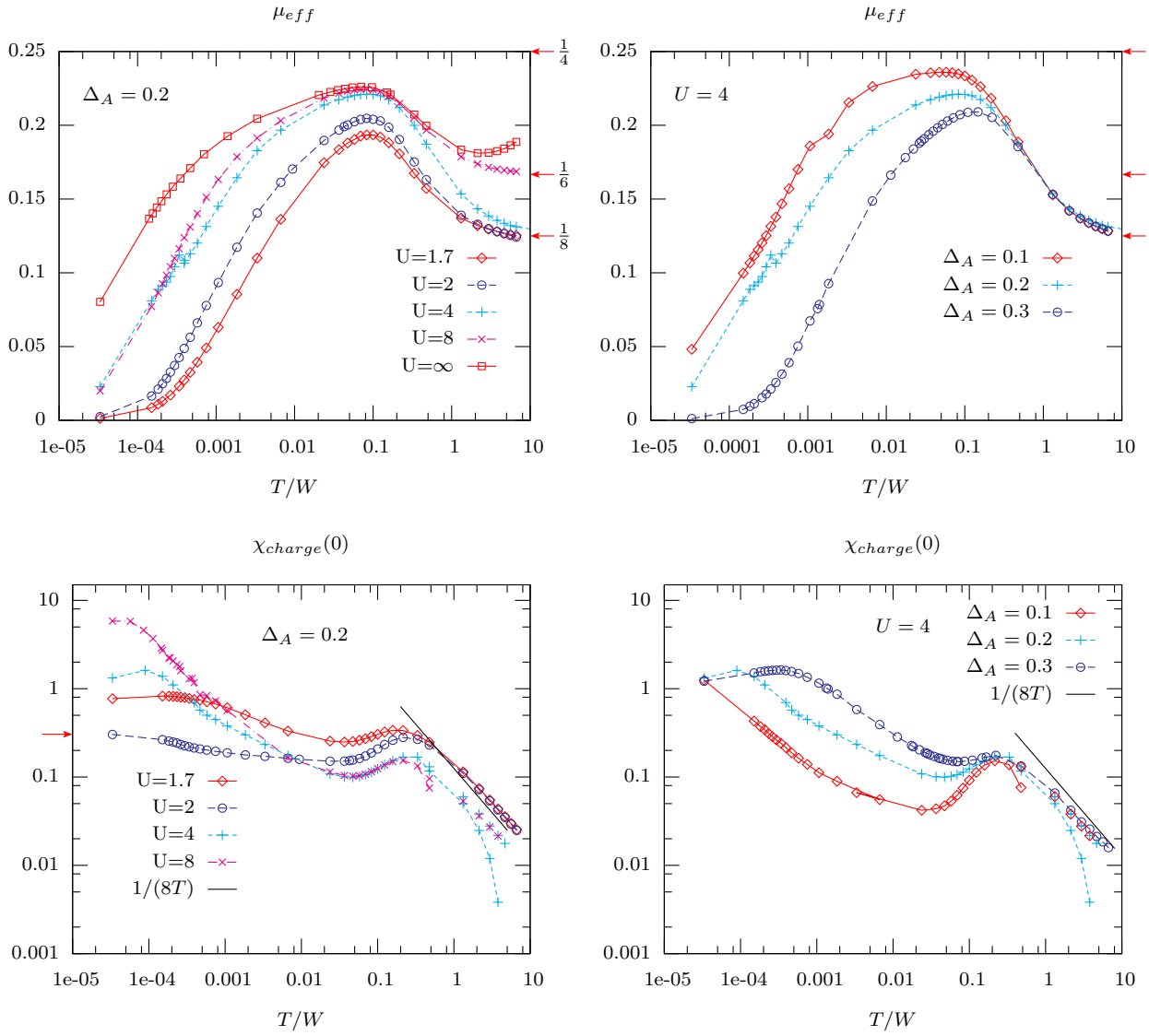

Figure 3.16: Temperature dependent screened local moment $\mu_{eff} = T\chi_{mag}(0)/(g\mu_B)^2$ (upper row) and static charge susceptibility $\chi_{charge}(0)$ (lower row). The left panels show the dependence on the local Coulomb repulsion U for a fixed Anderson width of $\Delta_A = 0.2$. For the curves in the right panels the Coulomb repulsion is fixed at $U = 4$, while the Anderson width varies as indicated. The arrows on the right border of the graphs for the screened magnetic moment (upper row) denote the values for the effective moment in the free orbital (1/8), valence fluctuation (1/6) and local moment (1/4) limit. The arrow an the left border of the charge susceptibility shows the exact $T = 0$ limit for the charge susceptibility in the symmetric case $U = 2$. For the charge susceptibility the high temperature asymptotic value $1/(8T)$ for a non-interacting impurity is shown as well (thick line). The colored dots, which are not connected by a line, denote the asymptotic charge susceptibilities calculated without any two-particle interactions. Other parameters are the same as in figure 3.12.

due to the lack of hybridization processes, even at high temperatures. Indirectly the valence fluctuations are observable through the faster reduction of the local moments with temperature and deviations from the universal Kondo curve.

The upturn in the $U = \infty$ moment around $T/W \geq 2$, which corresponds to a saturating magnetic susceptibility, is due to numerical deficiencies and should no be taken as a physical tendency.

The temperature dependent static charge susceptibility is shown in the lower row of figure 3.16 for the same parameter sets as the effective moment above it in the same figure. For high temperatures and $U < 4$ the static susceptibility behaves effectively non-interacting with $\chi_{charge} = 1/(8T)$ as expected. For $U = 4$ and $\Delta_A = 0.2$ the susceptibility still has the characteristic $1/T$ dependence for high T, but with a reduced prefactor. This can be understood as for this situations the upper Hubbard peak, incorporating half the spectral weight, is energetically just above the upper band edge of the c-band, effectively reducing the accessible spectral weight for two-particle excitations. The turquoise dots without joining lines show the high temperature susceptibility for $U = 4$ and $\Delta_A = 0.2$ calculated without two-particle interactions, i.e. only the local particle-hole propagator (2.3.44), but the full interacting one-particle Green is function used therein. It is clearly a good approximation for the high temperature behavior, confirming the assumption of an essential non-interacting impurity. The downturn in the ENCA susceptibility for $T/W > 1$ is due to numerical inaccuracies, which arise from the finite and asymmetric frequency intervals in the calculations.

For $U = 8$, $\Delta_A = 0.2$ and $U = 4$, $\Delta_A = 0.1$ the high temperature behavior is similar to the case described above ($U = 4$, $\Delta_A = 0.2$), but the numerical inaccuracies extend to lower temperatures, concealing the high temperature asymptotics which are again shown as the colored dots without a joining line.

For lower temperatures the susceptibility starts to saturate, develops a maximum and even declines again for $T/W \leq 0.2$ for all shown parameter values. As it can be seen by comparing the graphs for the charge susceptibilities and the effective magnetic moments, this behavior occurs as the formation of the local magnetic moment takes place. At these temperatures the electrons become more and more correlated and empty and doubly occupied f-states become energetically unfavorable, leading to the suppression of charge excitations and to a reduced susceptibility. Consequently, the decline in the charge susceptibility is stronger, the larger the tendency to form a magnetic moment is pronounced, that is for smaller hybridization strength and larger Coulomb repulsions.

For even lower temperatures ($T/W \leq 0.05$ in the figures) the magnetic moments become increasingly screened and the local Fermi liquid starts to form. This goes along with an enhancement in the charge susceptibility due to the formation of long-lived renormalized quasiparticles. To put it technically, the Fermi liquid quasiparticles lead to a charge susceptibility proportional to the DOS at the Fermi level. And as long as the Kondo screening is not complete, $\rho_f(0)$ keeps growing and so does the susceptibility. For $T \ll T_K$ the strong coupling fixed point is eventually reached, i.e. the system is a strongly renormalized Fermi liquid, and both quantities saturate.

For the symmetric case ($U = -2\epsilon^f = 2$) the charge susceptibility calculated within the ENCA quite accurately reproduces the exact zero temperature limit known from the Bethe

ansatz solution of the SIAM, which is indicated by an arrow on the left border of the figure 3.16.

The drastic increase of the static charge susceptibilities for $U = 4$ and $U = 8$ ($\Delta_A = 0.2$) towards lower temperatures is counterintuitive as the charge fluctuations should be suppressed for larger U. The reason for this could be either due to the failure of the ENCA equations for the charge susceptibility for too low temperatures, or some reminiscence of the valence fluctuation regime: in that regime, the impurity orbital energy ϵ^f has to be replaced with the renormalized, temperature dependent level position [Km80b]

$$E^f(T) = \epsilon^f + \frac{\Delta_A}{\pi} \ln \frac{U}{T} \quad , \tag{3.4.7}$$

which is an increasing function for decreasing T. The increase in $\chi_{charge}(T)$ is observed when the local magnetic moment becomes increasingly reduced, which is at first sight the point when the strong coupling is approached and not the valence fluctuation fixed-point. But since the situations considered have $\epsilon^f = -1$, they are not really close to the Kondo limit and valence fluctuations play a considerable role. Especially the temperature dependent level $E^f(T)$ determines the effective ionic position $\tilde{\epsilon}^f$ and temperature $\tilde{T}$ at which the local moment formation and screening takes place and which is relevant in the low temperature phase, e.g. $\tilde{T} \stackrel{!}{=} E^f(\tilde{T}) \equiv \tilde{\epsilon}^f$. Thus, for larger U values the effective f-level $\tilde{\epsilon}^f$ lies energetically closer to the Fermi level, which implies even stronger charge fluctuations.

The at first sight counterintuitive tendency, that for a given level position ϵ^f the charge susceptibility increases as U is increased away from half filling is known from perturbation theory and the exact Bethe ansatz solution of the SIAM [Sch83, Hor85b]. Consequently, the general trend of the charge susceptibility shown in figure 3.16 seems reliable and only the question remains, whether the increase is as strong as it is calculated within the ENCA.

The charge susceptibility for the asymmetric case with $U = \infty$ and relatively large orbital degeneracy of about $N = 6 - 20$ is found to have a pronounced maximum for temperatures of about some tenth of the Kondo temperature [Bru97]. This leads to the expectation that the charge susceptibilities for finite U and an orbital degeneracy of only $N = 2$ (e.g. the curves for $U = 4, 8$ in figure 3.16) might also have a maximum and possibly decreases again for temperatures $T \ll T_K$, which are not accessible within this method.

The quantitative behavior of thermodynamic quantities calculated with the ENCA can be checked against the exact solution known from the Bethe ansatz for the SIAM [Kaw81, Wie83, Tsv83b, Kaw83, Oki83a]. The static susceptibilities at $T = 0$ for the symmetric case ($U = -2\epsilon^f$) with a constant c-band DOS can even be obtained in a closed form (cf. [Oki83a, Hor85a])

$$\chi_{mag}^{exact}(T=0) = \frac{(g\mu_B)^2}{4\,T_L} \left(1 + \frac{1}{\sqrt{\pi}} \int_0^{\frac{\pi\Delta_A}{2U}} dx \, \frac{\exp\left\{x - \frac{\pi^2}{16x}\right\}}{\sqrt{x}} \right) \tag{3.4.8}$$

with

$$T_L = U \sqrt{\frac{\Delta_A}{2U}} \, \exp\left\{ -\frac{\pi U}{8\Delta_A} + \frac{\pi\Delta_A}{2U} \right\} \tag{3.4.9}$$

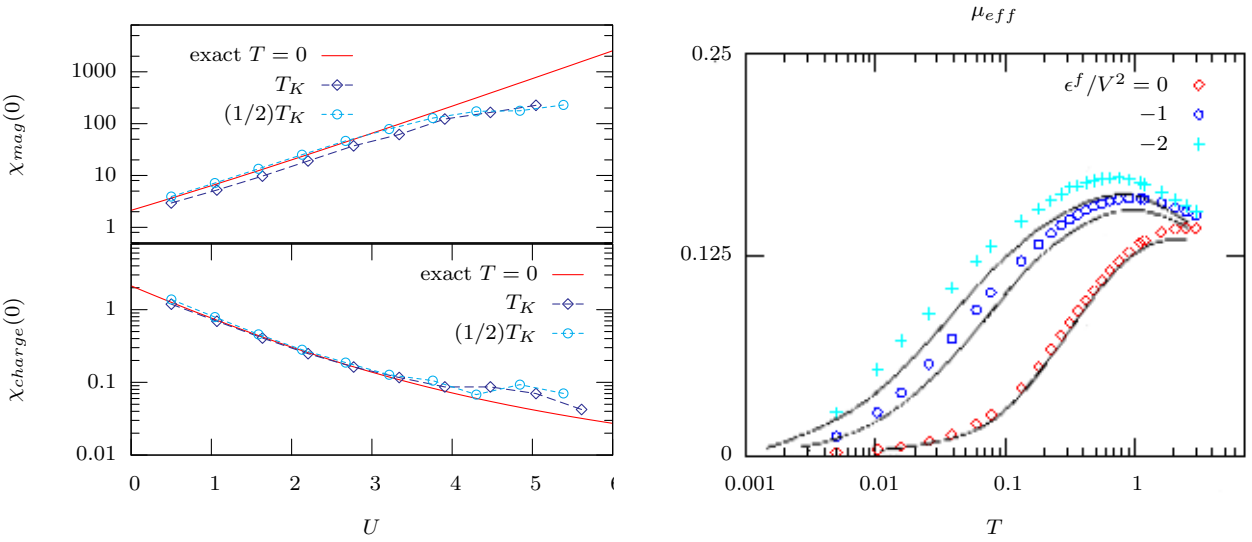

Figure 3.17: Static magnetic (upper left) and charge (lower left) susceptibility for the symmetric case $\epsilon^f = -U/2$ as a function of U for finite temperatures T_K and $T_K/2$ in comparison with the exact $T = 0$ results of equations (3.4.8) and (3.4.10). The right figure shows the temperature dependent effective magnetic moment (colored dots) for a fixed Coulomb repulsion $U = 4V^2$ and three different f-level positions $\epsilon^f = 0, -V^2, -2V^2$. The solid grey curves are the exact Bethe ansatz results for the same parameter values (after [Oki83b]). For all cases, the calculations were done for a constant c-electron DOS with half bandwidth $W = 10$. For the plots on the left an Anderson width $\Delta_A = 0.3$ was used while for the right plot $\Delta_A = 0.167$ ($V = 0.578$).

and

$$\chi^{exact}_{charge}(T=0) = \frac{1}{\pi}\sqrt{\frac{2}{U\Delta_A}}\int_{-\infty}^{\infty} dx\, \frac{e^{-\frac{\pi\Delta_A}{2U}x^2}}{1+\left(\frac{U}{2\Delta_A}+x\right)^2} \quad . \tag{3.4.10}$$

Apart from a prefactor, T_L represents the Kondo temperature of the system, but with an additional correction term for small coupling $\sim \Delta_A/U$ in the exponent. From these formulas the asymptotic values for the magnetic susceptibility in the Kondo regime ($U \to \infty$) $\chi^{exact}_{mag} = \frac{(g\mu_B)^2}{4T_K}$ and the charge susceptibility $\chi^{exact}_{charge} = 0$ can be easily deduced.

The left graphs in figure 3.17 show the exact zero temperature magnetic (upper) and charge (lower) susceptibility calculated with equations (3.4.8) and (3.4.10) for $\epsilon^f = -U/2$ as a function of U (solid red lines). For comparison, the ENCA susceptibilities are plotted for the two characteristic temperatures T_K and $T_K/2$ as well. For the magnetic susceptibility the characteristic exponential U dependence is essentially the same as for the exact Bethe ansatz result, but the absolute height is somewhat different. For $T = T_K$, the magnetic susceptibility is slightly reduced, which is certainly expected as the finite temperature ENCA susceptibility has not reached its saturation value yet. At half the Kondo temperature the agreement is generally quite good and the saturation value of the susceptibility is only slightly overestimated.

The deviations for $U > 4$ are due to the numerical method used to calculate the static susceptibilities. The static limit is obtained with the equations of section 3.3 for the dynamic magnetic susceptibility, but where the external frequency is set to a very small value,

in this case $\nu = 10^{-5}$. Since the ENCA represents a conserving approximation the results obtained with this method are the same, as if the static susceptibility was directly calculated as a derivative of a thermodynamic potential, or if separate equations for the static quantities were derived as in [Ots06b]. This reasoning is valid, as long as the minimal frequency is negligible compared to the lowest energy scale in the model. But since the Kondo temperature for $U = 4$ is already of the order of 10^{-4}, this is not ensured and the static ENCA susceptibility is decreased.

The charge susceptibility (lower left graph in 3.17) shows no significant temperature dependence for such low temperatures (see also figure 3.16) and lies right on top of the exact $T = 0$ result. The deviations for $U \geq 4$ are for the same reason, as for the magnetic susceptibility described above. The larger the Coulomb interaction, the stronger is the charge susceptibility suppressed and even vanishes in the Kondo (strong coupling) limit $U = -2\epsilon^f = \infty$.

An equally remarkable agreement is obtained for the temperature dependent calculation of the effective moment for fixed U and various ϵ^f as shown in the right graph of figure 3.17. The exact Bethe ansatz solution were taken from [Oki83b] and are shown as the solid grey lines, while the colored points are ENCA calculations for exactly the same parameter values. The overall trend of the ENCA is to slightly overestimate the effective moment but all characteristic features are essentially the same as for the Bethe ansatz. Especially the shape and the relative height of the curves is in remarkable agreement: when rescaling all ENCA calculations with one factor, all three curves can be simultaneously brought to lie right on top of the exact Bethe ansatz results. This indicates that the ENCA produces a slightly modified Kondo scale, but otherwise describes the static magnetic properties almost exactly.

Plots of the static susceptibilities for a fixed finite temperature $T = 0.05$ as a function of the Coulomb interaction are shown in figure 3.18. The left figure compares the static magnetic (red dots) and charge (blue dots) susceptibilities for the symmetric situation with the exact $T = 0$ results. Also shown is the local particle-hole propagator calculated with the full ENCA one-particle Green function (pink dots), which represents the susceptibility without explicit two-particle interactions. As it can be seen, for vanishing Coulomb repulsion the correct non-interacting limit is reproduced by all curves. The slight deviation for the particle-hole propagator is due to the wrongly calculated one-particle Green function (cf. figure 3.15).

The charge susceptibility is a monotonic decreasing function with increasing Coulomb repulsion as it is expected. The qualitative behavior is like the particle-hole propagator but the actual size is considerably reduced due to correlations. The agreement with the exact zero temperature susceptibility is pretty good, which again confirms the weak temperature dependence of it at low temperatures.

The magnetic susceptibility (red dots) does agree with the exact $T = 0$ solution for low Coulomb repulsions but deviates for $U/(1 + U) \gtrsim 1/3$ ($U \gtrsim 1/2$). This is a finite temperature effect, since the Kondo temperature decreases for larger values of U and at $U = 1/2$ it is already as small as $T_K \approx 0.05$. So for larger U, $T = 0.05$ does not represent a low temperature $< T_K$ and the susceptibility is certainly not well described by its $T = 0$ value. The susceptibility then has only a very weak U dependence and asymptotically

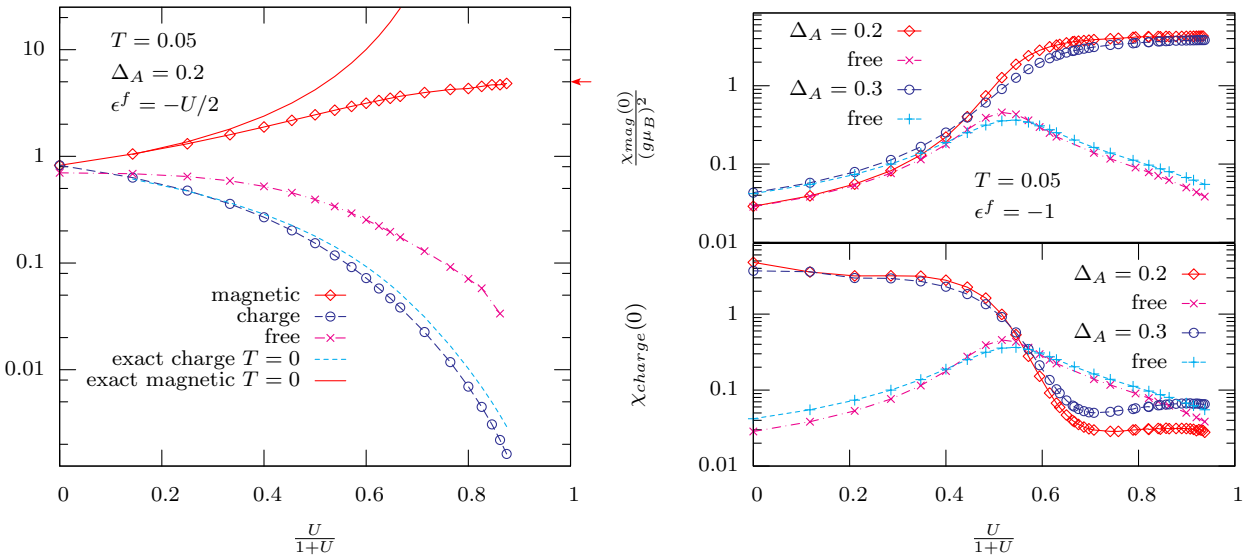

Figure 3.18: Magnetic and charge susceptibilities as functions of the Coulomb interaction U at a fixed temperature $T = 0.05$ for the symmetric situation (left graph) and a fixed ionic level position $\epsilon^f = -1$ (right). Notice, the x-axis is scaled as $U/(1+U)$, so that $U = \infty$ corresponds to $U/(1+U) = 1$. The curves labels with "free" are calculated without two-particle interaction, i.e. with the particle-hole propagator (2.3.44), but with the full one-particle Green functions used therein. The calculations were done with a 3d-SC band DOS and Anderson widths as indicated in the figures.

approaches the value of the Curie susceptibility of a free spin $\chi_{mag} = 1/(4T) = 5$, which is indicated by an arrow on the right border of the graph.

The situation is more complex for the asymmetric case with a fixed $\epsilon^f = -1$, as it is shown in the right part of figure 3.18 for two different hybridization strength. The magnetic susceptibility (upper graph) increases monotonically with increasing U since the moment formations is supported and stabilized by a larger Coulomb interaction U due to the suppression of excitation involving doubly occupied f-states, i.e. the upper Hubbard peak. For low values of $U \lesssim 2/3$ the magnetic susceptibility exactly follows the non-interacting particle-hole propagator (labeled "free"), because the system is in the low temperature Fermi liquid state and essentially non-interacting. For large U the magnetic moment and susceptibility saturate since the impurity is close to be singly occupied ($n^f(\Delta_A = 0.2) = 0.95$ and $n^f(\Delta_A = 0.3) = 0.92$) and the Kondo screening has not taken place yet as the Kondo temperature is smaller than the temperature at which the calculation is performed, e.g. $T_K \approx 0.05$ for $U = 1.3$ and $T_K(U = \infty) = 1.2 \times 10^{-4}$.

The global dependence on the hybridization strength is as expected: the magnetic susceptibility decreases with increasing Δ_A for large U, since hybridization processes destabilize the magnetic moment. At small U the Δ_A-dependence is inverted and the magnetic susceptibility correctly approaches the particle-hole propagator, where a larger hybridization induces a larger fluctuations and susceptibility.

For the charge susceptibility (lower right graph) the trend of the hybridization dependence for large U is opposite to the magnetic susceptibility, since a larger hybridization induces more charge fluctuations and thus leads to an increased susceptibility.

As a function of the Coulomb repulsion the charge susceptibility shows a sharp decrease at around $U \approx 1$. In order to understand this drop, notice that for this value of U the unperturbed doubly occupied f-state has the energy $E_2 = 2\epsilon^f + U = -1 = \epsilon^f$. Excitations from the singly to the doubly occupied state have vanishing energy and in the one-particle spectrum the upper Hubbard peak lies right around the Fermi level. So the system is in a intermediate valence state with large valence fluctuations between the singly and doubly occupied state, and a large charge susceptibility is expected. Increasing U from there, the doubly occupied state becomes more and more unfavorable, the upper Hubbard peak moves further away from the Fermi level and the susceptibility drops to smaller values and eventually saturates. The remaining structures, e.g. the slight upturn and possible downturn for very large U, results from the details of the Kondo and intermediate valence physics taking place. Since the calculations are done for a fixed temperature and the Kondo temperature decreases with increasing U, the system effectively finds itself in a higher temperature regime for larger U. And depending on how far the formation and screening of the local moment has got, the charge susceptibility might increase or decrease with U (cf. figure 3.16).

For lower Coulomb repulsions the susceptibility seems to saturate at an unexpected high value. This points at a failure of the ENCA, because for $U = 0$ the non-interacting curve (labeled as "free") should be approached but this is not the case. When lowering the value of the Coulomb repulsion from $U = 1$ the upper Hubbard peak moves to more negative energies towards the lower Hubbard peak. Correlations become more and more negligible and as the DOS at the Fermi level decreases, the susceptibility should decrease as well. This can be observed in the "free" particle-hole propagator, whereas the ENCA fails to reproduce this downturn. This confirms the already mentioned fact, that ENCA overestimates valence fluctuations in the charge susceptibility and has problems describing the charge fluctuations of non-interacting particles.

The upper left graph in figure 3.19 shows the charge susceptibility for fixed T and Δ_A and the three local ionic level positions $\epsilon^f = -1, -0.2, -0.005$ as function of $U/(1+U)$. The first thing to notice is the increase of the susceptibility when U becomes lower than ϵ^f as discussed in the paragraphs above. For $\epsilon^f = -0.005$ this cannot be observed for the obvious reason of a too small value of ϵ^f. The most remarkable thing about the dependence on ϵ^f is that it is maximal for $\epsilon^f = -1$ and then decrease for the level positions closer to the Fermi level, e.g. $\chi_{charge}[\epsilon^f = -1] > \chi_{charge}[\epsilon^f = -0.2] > \chi_{charge}[\epsilon^f = -0.005]$. This contradicts the intuition, that a larger DOS at the Fermi level, which is obtained for ϵ^f closer to the Fermi level, should result in a larger susceptibility, especially for small or vanishing U, as it is observed in the non-interacting susceptibilities, which are also shown in the figure as lines without dots.

For small U, the values of the interacting ENCA susceptibility are closer to their asymptotic values of the particle-hole propagator for ϵ^f smaller. Thus, one is lead to the conclusion the ENCA works better for these situations. But this contradicts the conclusion drawn from earlier findings that the ENCA generally performs worse in situations with more valence fluctuations. The refined insight gained from this is that the asymmetry plays a crucial role as well. This can already be anticipated by the excellent but unexpected agreement of the ENCA charge susceptibility with the exact Bethe ansatz for the symmetric situation in figure 3.17 for very small ϵ^f and U where valence fluctuations are especially strong.

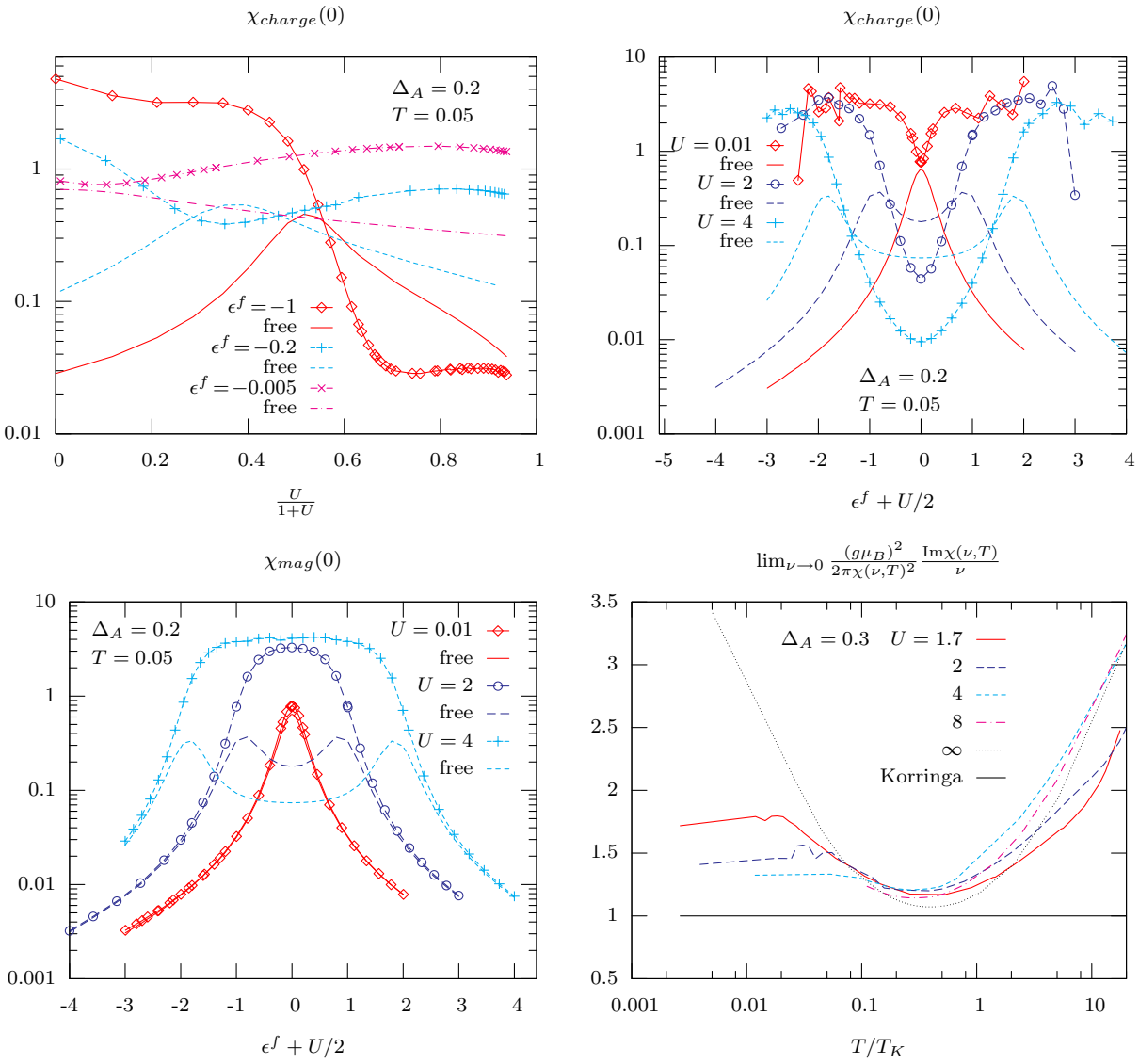

Figure 3.19: Upper left graph: static charge susceptibility for fixed temperature $T = 0.05$ and Anderson width $\Delta_A = 0.2$ for different values of the ionic level position ϵ^f as a function of U. The curves without dots represent the free charge susceptibilities, i.e. only the particle-hole propagator. Upper right and lower left graph: static charge and magnetic susceptibility for fixed $T = 0.05$ and $\Delta_A = 0.2$ as functions of the ionic level position ϵ^f relative to the half-filling value $-U/2$ for various values of U. Curves without dots indicate the particle-hole propagators.
Lower right: the function $\lim_{\nu\to 0} \frac{(g\mu_B)^2}{2\pi\chi_{mag}(\nu,T)^2} \frac{\mathrm{Im}\chi_{mag}(\nu,T)}{\nu}$ evaluated as a function of temperature and various Coulomb repulsions within the ENCA. For comparison the $U = \infty$-NCA curve is shown as well.
The first three graphs are done for an infinitely wide flat conduction band DOS, while the lower right graph is done for a 3d-SC band DOS.

In order to examine the dependency of the charge susceptibility on the asymmetry and level position the susceptibility is calculated for the case of an infinitely wide constant band DOS and fixed values of temperature $T = 0.05$ and Anderson width $\Delta_A = 0.2$ for various Coulomb repulsions and as a function of the level position relative to the symmetric case $\epsilon^f + \frac{1}{2}U$, which is shown in the upper right graph of figure 3.19. Also shown is the particle-hole propagator for each case (lines without dots), which shows a double peak structure with the peaks situated at $\epsilon^f + \frac{1}{2}U \approx \pm\frac{1}{2}U$ as it is expected, since the particle hole-propagator is roughly proportional to the f-electron DOS at the Fermi level.

The first thing to notice is that all curves are symmetric around $\epsilon^f + \frac{1}{2}U = 0$, which just reflects the particle-hole symmetry of the model.

Furthermore, the ENCA susceptibility is always minimal for half filling ($\epsilon^f + U/2 = 0$) and increases away from the symmetric case. The absolute value of the charge susceptibility in the symmetric situation is drastically reduced compared to corresponding particle-hole propagator. This indicates, that the explicit two-particle interactions strongly suppresses charge fluctuations. The susceptibility cannot be accurately described with the one-particle DOS, representing the strongly renormalized quasiparticles, but explicit two-particle correlations have to be taken into account.

On the logarithmic scale, the increase with growing distance relative to zero can be nicely fit with a parabola centered at zero, which corresponds to an exponential increase of the susceptibility,

$$\chi_{charge} \sim e^{\alpha(\epsilon^f + U/2)^2} \quad , \quad \alpha > 0 \quad . \tag{3.4.11}$$

This confirms the strong influence of the asymmetry and the presence of the valence fluctuation fixed point and intermediate valence phenomena on the charge fluctuations. However, this increase is even observed for the almost non-interacting case of $U = 0.01$, where it is not expected and can only be attributed to a failure of the ENCA since the curve should rather resemble the particle-hole propagator.

For $\epsilon^f + \frac{1}{2}U \approx \pm\frac{1}{2}U$, $\chi_{charge}(0)$ starts to saturate and then should decrease again (cf. [Hor85b]), which can only be guessed from the graphs, as for these parameter values the numerics for the charge susceptibility becomes unstable and thus does not produce reliable results. The parameter values at which the downturn in the susceptibility should occur and the ENCA fails to do so, corresponds to situations, when both Hubbard peaks in the one-particle spectrum (very roughly at ϵ^f and $\epsilon^f + U$) are either below or above the Fermi level. Physically this corresponds to the empty- and fully occupied impurity regimes, where the lowest valence state of the impurity is not dominated by the singly occupied states, but by the empty or doubly occupied ones. Considering the aim of the derivation of the ENCA – to describe an *magnetic* impurity, which has an singly occupied unperturbed ($\Delta_A = 0$) ground state – this makes some sense: the diagrams selected for this approximation were chosen in order describe spin flip scattering and the magnetic exchange coupling correctly, not charge fluctuations. Apparently, in situations were the unperturbed ground state is the singly occupied valence state, the diagrams describing magnetic excitations still approximate those for charge fluctuations, which is why the ENCA constitutes a good approximation for the charge susceptibility in these situations as well, even when U is very small. In the other situations, where the unperturbed ground state is either the empty or doubly occupied ionic state, crossing diagrams neglected in the ENCA are vital to describe charge fluctuations accurately and consequently the approximation breaks down.

This conclusion is further substantiated by the magnetic susceptibility shown in the lower left graph of figure 3.19, which is calculated for the same parameters as the charge susceptibility in the upper right graph. The particle-hole propagators are shown as well in the figure. Around the symmetric case the magnetic susceptibility is largest since the magnetic moment is most developed. For larger U the moment is stabilized further which results in a larger magnetic susceptibility. As long as either Hubbard peaks are not near the Fermi level the moment is almost the same which leads to the very weak ϵ^f-dependence and explains the plateau around zero. But as soon as one of the Hubbard peaks extends over the Fermi level, i.e. $\epsilon^f + U/2 \approx \pm U/2$, the moment is destabilized and the susceptibility drastically reduced. The curve then rapidly approaches the particle-hole propagator, indicating that the explicit two-particle interactions are unimportant for the magnetic excitations of the empty or doubly occupied ionic f-shell.

The fact, that the ENCA adequately describes the magnetic properties of the impurity for these cases, especially for the almost non-interacting case with $U = 0.01$ which can be hardly distinguished from the particle-hole propagator in the figure, but fails to describe the charge excitations for these situations, confirms the insight of the previous paragraph: The diagrams of the ENCA very accurately describe the magnetic excitations of the impurity, even in the empty and doubly occupied regimes, but produces good results for the charge susceptibility only as long as the singly occupied ionic configuration represents the unperturbed ($\Delta_A = 0$) ground state and no intermediate valence phenomena come into play.

As it was mentioned earlier in this chapter, the NCA does violate Fermi liquid properties. A more drastic misbehavior than the underestimation of the imaginary part of the total self energy at the Fermi level -Im$\Sigma(0 + i\delta) < \Delta_A$ (see discussion of figures 3.12 and 3.14) is related to zero frequency limit of the imaginary part of the dynamic susceptibility. For the Fermi liquid at $T = 0$ it has to obey the so called Korringa-Shiba relation [Shi75]

$$\lim_{\nu \to 0} \frac{(g\mu_B)^2}{2\pi \chi_{mag}(\nu)^2} \frac{\mathrm{Im}\chi_{mag}(\nu)}{\nu} = 1 \quad , \tag{3.4.12}$$

which is shown in the lower right graph of figure 3.19 for various values of U. For the NCA the quantity $\lim_{\nu \to 0} \mathrm{Im}\chi_{mag}(\nu)/\nu$ is known to diverge at $T = 0$ [MH84], which is reproduced by the $U = \infty$ curve in figure. As it can be seen in the same figure, the ENCA (finite U values) performs considerably better than the NCA ($U = \infty$ curve). Although the curves still fall short of reproducing the exact limit and even start to increase again for temperatures $T \lessapprox T_K/2$, they eventually saturate at a finite value and do not diverge. This represents a considerable improvement of the qualitative behavior of the ENCA over the NCA.

The dynamic magnetic susceptibility is shown in figure 3.20 for two different values of U and temperature. As it can be seen the Kondo effect strongly influences the low energy behavior of the magnetic excitations and the general temperature and parameter dependence is consistent with that known from perturbation theory [Shi76]. For energies lower than the Kondo temperature the magnetic response is strongly enhanced as a multitude of spin-flip excitations are possible without destroying the Kondo screening cloud. The imaginary part is shown in the right panel of the figure and shows the corresponding magnetic excitation

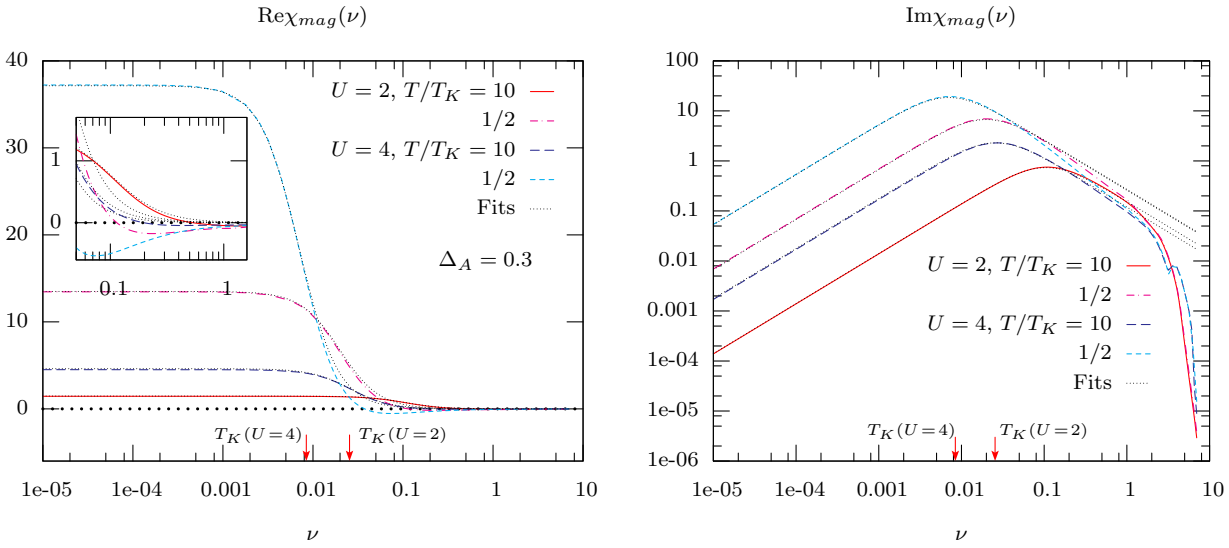

Figure 3.20: The dynamic magnetic susceptibility for $\epsilon^f = -1$ and in the symmetric $U = 2$ and the asymmetric $U = 4$ case for an Anderson width $\Delta_A = 0.3$ and two characteristic temperatures $T = 10T_K$ and $T = T_K/2$. The left graphs show the real part in a logarithmic plot and the inset shows the high energy region. The right graphs shows the imaginary part in a double-logarithmic plot. The corresponding Kondo temperatures are indicated as arrows on the frequency axis.

spectra with a peak situated roughly at the Kondo temperature and with the same width T_K for low temperatures. The high energy excitation spectra show a sudden drop for $\nu > 1$, which is due to the fast decrease of the band DOS above frequencies larger than that (cf. figure 3.12). The spectra for $U = 4$ show a very slight peak at around $\nu \approx 3$, which comes from magnetic excitations involving the upper Hubbard peak.

As shown in the graphs of figure 3.20, the susceptibility can be nicely fit with the form

$$\chi^{fit}_{mag}(\nu) = \frac{\chi_0}{1 - i\nu/\Gamma} \quad , \quad \nu \in \mathbb{R} \quad , \tag{3.4.13}$$

where the parameter Γ represents the line width for the Lorentzian and is directly proportional to the NMR impurity nuclear spin-lattice relaxation rate $1/T_1$, i.e.

$$\frac{1}{T_1\,T} = A \lim_{\nu\to 0} \frac{\mathrm{Im}\chi_{mag}(\nu)}{\nu} = A\frac{\chi_0}{\Gamma} \tag{3.4.14}$$

with A a constant involving the nuclear Bohr magneton, the g factor of the impurity nucleus and the coupling between nuclear spin and f-electron spin [Shi75]. The form (3.4.13) for the magnetic susceptibility corresponds to an exponential relaxation with relaxation time $1/\Gamma$ characteristic for weakly interacting spins.

The relaxation rate Γ for two values of the Coulomb repulsion as functions of temperature can be obtained from fits to the dynamic susceptibilities and are shown in the left graph of figure 3.21. Also shown is the same quantity calculated directly from the quotient $10^{-5}\ \chi_{mag}(10^{-5})/\mathrm{Im}\chi_{mag}(10^{-5})$, which is labeled as "static" in the figure. The agreement between these two curves is almost perfect, only at too low temperatures slight discrepancies occur.

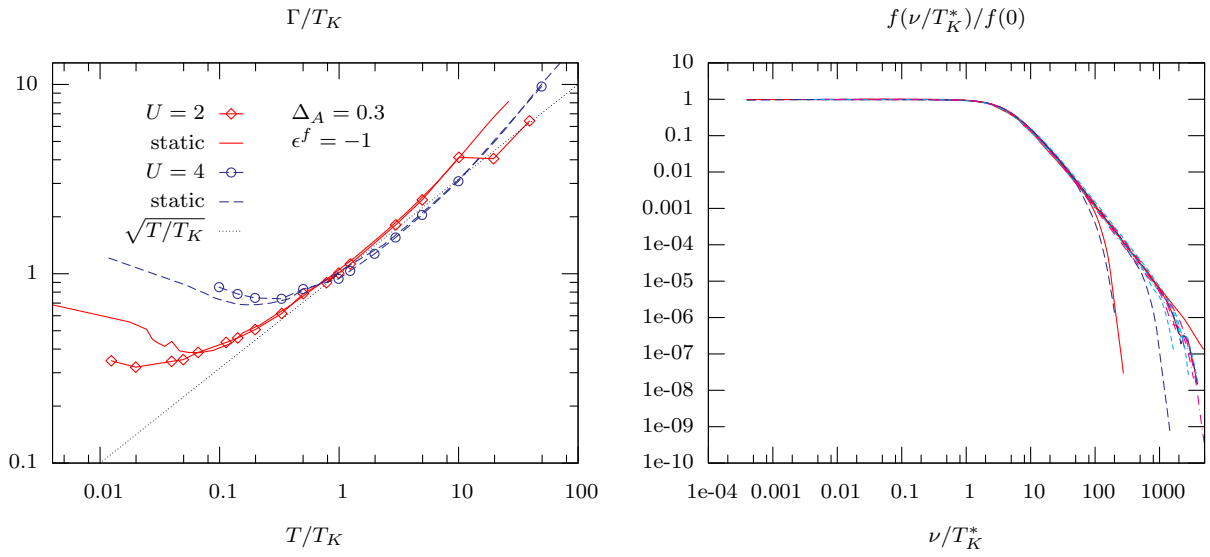

Figure 3.21: Left graph: relaxation rate Γ/T_K as a function of temperature for two different Coulomb repulsions $U = 2, 4$, $\Delta_A = -0.3$ and $\epsilon^f = -1$. The curves labeled as "static"represent the values calculated directly from the quotient $10^{-5}\ \chi_{mag}(10^{-5})/\mathrm{Im}\chi_{mag}(10^{-5})$, whereas the doted curves are obtained by fitting the form (3.4.13) to the dynamic susceptibilities.
Right graph: scaling function $f(\nu/T_K^*)/f(0)$ from equation (3.4.15) for the following parameter sets: $(\epsilon^f = -0.5; U = 1; T/T_K = 10, 1)$, $(\epsilon^f = -1; U = 2; T/T_K = 1)$, $(\epsilon^f = -1.5; U = 3; T/T_K = 1)$, $(\epsilon^f = -2; U = 4; T/T_K = 1)$, $(\epsilon^f = -1; U = 3; T/T_K = 1)$, $(\epsilon^f = -1; U = 4; T/T_K = 1, 1/2, 1/3, 1/5, 1/7, 1/10)$ and $(\epsilon^f = -1; U = 8; T/T_K = 1)$. All curves are calculated for $\Delta_A = 0.3$ and a 3d-SC band DOS.

For large temperatures Γ/T_K roughly follows a $\sqrt{T/T_K}$-law as it was already found by Jarrell and coworkers [Jar91b]. For temperatures as low as the Kondo temperature, the relaxation rate starts to saturate and takes on a value of the order of the Kondo temperature itself. This can be understood as for temperatures lower than the Kondo temperature the local Fermi liquid state is approached in which the local spin is screened and coupled to a screening cloud with a "binding energy" of about T_K.

Comparison of the absolute value for the relaxation rate of figure 3.21 with the known $T = 0$ limiting value for the symmetric case of $\Gamma = \frac{\pi}{2} T_K$ [Jar91b] yields that the calculated curve underestimates the limiting value. The reason for this probably lies in a wrong estimate for the Kondo temperature T_K used for the plot. The T_K are calculated through equation (3.4.3) and thus do not represent the exact physical low energy scale of the problem, but only an order of magnitude estimate. In order to extract the numerical value of the "real" Kondo temperature one either would have to fit the susceptibility to the universal curve of as described in [Jar91a], or at least include some small-U correction terms in (3.4.3).

In [Jar91b] it was found, that the function

$$f(\nu) = \frac{\pi T_K}{2\chi_{mag}(0)} \frac{\mathrm{Im}\chi_{mag}(\nu)}{\nu} \tag{3.4.15}$$

shows universality and depends only on T/T_K. The right graph of figure 3.21 shows this function normalized to its zero frequency value for various parameter sets. All graphs can be collapsed onto one single curve showing the universal shape of the function f. To

achieve this, the frequency argument had to be rescaled with a guess for the actual Kondo temperature T_K^*, slightly differing from the ones calculated with equation (3.4.3). The rapid decrease of some curves in the figure for frequencies of $\nu/T_K^* \gtrapprox 100$ stems from the finite width of the 3d-SC conduction band used for these calculations.

The dynamic charge susceptibilities for two different Coulomb repulsions and characteristic temperatures, calculated with a 3d-SC band DOS, are shown in figure 3.22. In the spectra the pronounced features from the excitations involving the upper and lower Hubbard peaks at energies around $|\epsilon^f|$ and $\epsilon^f + U$ are clearly visible. The height of the peak at $\nu \approx |\epsilon^f|$ for the symmetric case is about twice as high as for the asymmetric case, since in the former case $\epsilon^f + U = |\epsilon^f|$ leading to a twice as large phase space for charge excitations with that energy as for the asymmetric case, where the upper Hubbard peak is moved to higher energies.

The most prominent difference between the particle-hole propagators (labeled as "free") and the fully interacting susceptibility is the strongly suppressed high energy response of the latter: of the broad excitation continuum in the particle-hole propagator for the asymmetric case between $3 \lessapprox \nu \lessapprox 5$ only a very small peak at $\nu \approx 3$ remains. The large spectral weight in the particle-hole propagator is a direct consequence of the convolution of two one-particle DOS. P is just a measure for the phase space volume for statistical independent excitations having an energy difference ν. But for charge excitations including two-particle interactions, the one-particle DOS is not sufficient for the description of particle-hole excitations. For example the large DOS of the Kondo peak at the Fermi level is build up by the correlated quasiparticles and any high energy particle-hole excitation involving such a quasiparticle or -hole underlies severe phase space restrictions due to correlations. Put another way, for high excitation energies the quasiparticles are not stable due to their "binding" energy of only T_K and are thus do not contribute to such particle-hole excitations.

The most remarkable aspect of the charge susceptibilities are their prominent low energy features. Already the particle-hole propagators show some increased response for energies smaller than T_K, which stems from the Kondo peak around zero frequency. It is slightly temperature dependent and minimally grows with lowering T, since the Kondo peak keeps developing until $T \lessapprox T_K$ and thus the weight for particle-hole excitations increases.

In the fully interacting susceptibilities of the symmetric case these low energy excitations are suppressed due to correlations and only a very slight increase is visible for $T = T_K/2$.

For the asymmetric case, however, the low energy increase is drastic and already for $T = 10T_K$ the peak is quite pronounced. For half the Kondo temperature $T = T_K/2$ it is larger by a factor of about 100 and the absolute hight even exceeds the high energy feature at ϵ^f. Due to its very small width $\sim T_K$ the peak is visible only in the logarithmic plot of the insets.

This very pronounced low energy response is produced by particle-hole excitations of the quasiparticles, which are formed in the local Fermi liquid phase at low temperatures. The lower the temperature becomes, the more these quasiparticles are stabilized and can be excited with energies lower than T_K. The temperature dependence of the charge excitations spectrum is shown in figure 3.23. The build-up of spectral weight in the low energy region upon lowering the temperature and the following saturation for $T \lessapprox T_K/10$ can be seen. In the saturation, the low energy excitation peak is broader and extends to higher energies than for larger temperatures. This indicates, that for lower temperatures the quasiparticles

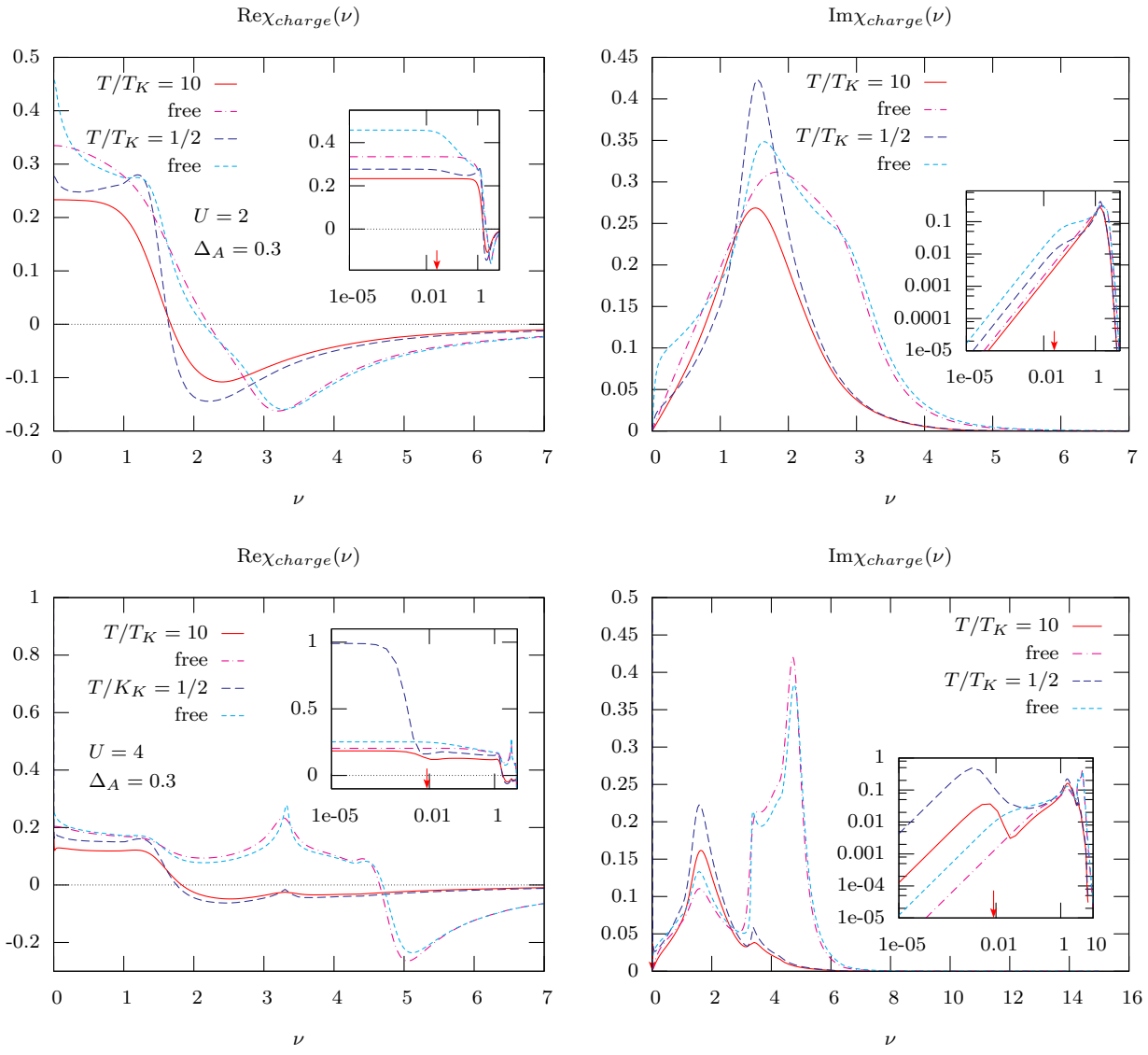

Figure 3.22: Real (left) and imaginary (right) part of the dynamic charge susceptibilities for the symmetric ($\epsilon^f = -1$, $U = 2$, upper row) and asymmetric ($\epsilon^f = -1$, $U = 4$, lower row) case for a 3d-SC band DOS, an Anderson width $\Delta_A = 0.3$ and two characteristic temperatures $T = 10T_K$ and $T = T_K/2$. The curves for the particle-hole propagators ("free") are shown as well. The insets show the corresponding low energy region on a (double-) logarithmic scale. The Kondo temperature for each case is indicated by the red arrow on the frequency axis in the low energy insets.

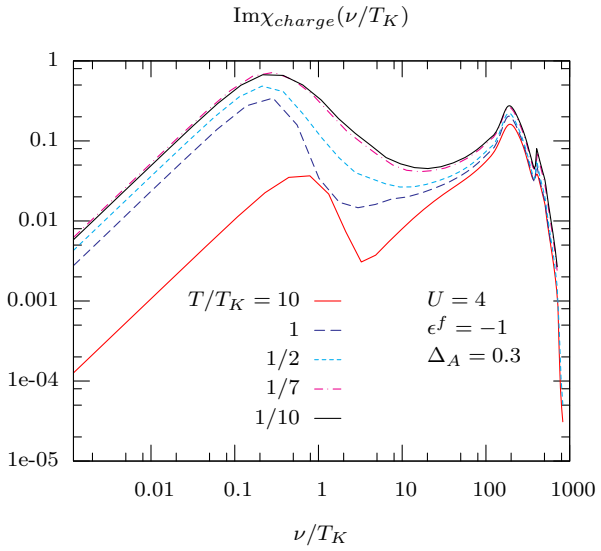

Figure 3.23: Imaginary part of the dynamic charge susceptibility for the asymmetric case $\epsilon^f = -1$, $U = 4$ for decreasing temperatures $T/T_K = 10$, 1, $\frac{1}{2}$, $\frac{1}{7}$ and $\frac{1}{10}$. The curves are calculated for $\Delta_A = 0.3$ and a 3d-SC simple cubic band DOS.

are more stable and can sustain particle-hole excitations with higher energies due to the reduced thermal fluctuations.

The fact that these excitations are strongly enhanced in the asymmetric case compared to the symmetric situation is associated with the presence of the valence fluctuation fixed point in the former case, as it was already argued for the static susceptibility on page 70. A similar but not as strong temperature dependent increase in the dynamic susceptibility for temperatures of the order of the Kondo temperature was already found for larger orbital degeneracy and $U = \infty$ with the NCA [Bru97].

Inspection of the low energy part of the many-body spectrum obtained with the NRG method [And04] indeed suggests the possibility of an enhanced charge response for the asymmetric situation compared to the symmetric case. However, such a low energy peak was not reported in other NRG calculations of the charge susceptibility as [Sak89] or [Fro91].

In summary it can be stated that the ENCA constitutes an excellent approximation for both, the one- and two-particle properties of the SIAM for temperatures down to some tenth of the Kondo temperature. The description of magnetic excitations is very good for all parameter values considered, while charge excitations are described accurately only for situations, where the singly occupied impurity valence state represents the unperturbed ($\Delta_A = 0$) ground state. This leads to an accurate description of the one-particle Green functions, including both charge and magnetic excitations, for not too low temperatures and not too large hybridization strengths Δ_A. Exact zero temperature Fermi liquid relations are slightly violated, but not as bad as in the (S)NCA.

The static magnetic quantities like susceptibility and screened moment almost perfectly agree with the exact Bethe ansatz results for all parameter values considered, even in the non-interacting or valence fluctuation regimes, which could not be expected. The dynamic magnetic susceptibilities correctly reproduce the temperature and parameter dependence of the magnetic excitations and even the scaling found earlier is obtained. Only the Korringa-

Shiba relation is not accurately reproduced for very low temperatures, but the improvement of the ENCA over the NCA is considerable.

4 The Hubbard model

In 1963 the Hubbard model was proposed independently by Hubbard [Hub63], Gutzwiller [Gut63] and Kanamori [Kan63] in order to describe metallic ferromagnetism. Even though the description of ferromagnetism within this model turns out to be a very delicate task, the model has been established as the simplest model for the description of correlated electrons on a lattice.

Despite its simplicity the Hubbard model is not exactly solvable and poses a highly non-trivial problem for the theoretic description. Only in one dimension the exact solution for thermodynamic quantities was obtained by means of the Bethe ansatz technique [Lie68, Lie03]. For higher dimensions only few exact statements exist (cf. [Bae95, Tas98b] and references therein).

The physical phenomena found to be described by the model include correlated paramagnetic metals and fluids, the Mott-Hubbard metal-to-insulator transition (MIT), ferromagnetism (FM), antiferromagnetism (AFM) and spin-density wave (SDW) phases and also various sorts of superconductivity, possibly relevant for the high-temperature superconductors (High-T_C). For reviews and introductory texts see for example [Pru95, Geb97, Faz99, Man04] and references therein.

After the introduction of the Hamiltonian in the first section of this chapter, the generic properties of the Hubbard will be reviewed in section 4.2. Of special interest are the implications of the strong correlations present in the model and the physical picture of the generic Fermi liquid phase encountered at low temperatures will be presented. In section 4.3, a new route to the breakdown of this Fermi liquid phase will be discussed. Section 4.4 focusses on the static and dynamic two-particle quantities in the light of the development of the previous sections. For the dynamic magnetic susceptibility phenomenological forms are introduced and their applicability is discussed. As a last application of the approximations made in the previous chapters, the magnetic phase diagram of the Hubbard model on various lattices and the influence of frustration is discussed.

4.1 Hamiltonian

In metals the long-ranged Coulomb interaction is usually screened and only short-range components have to be considered. In the Hubbard model only the on-site Coulomb U repulsion is retained. For the sake of simplicity the orbital structure of the ions is assumed to be a simple s-shell with spin degeneracy only. Additionally, the electrons can transfer between sites i and j with an amplitude t_{ij}, which accounts for the itinerancy and band formation of the electrons. Thus the Hamiltonian is given by

$$\hat{H} = \sum_{ij,\sigma} t_{ij} \hat{c}^\dagger_{i\sigma} \hat{c}_{j\sigma} + \sum_{i\,\sigma} \epsilon_\sigma \, \hat{c}^\dagger_{i\sigma} \hat{c}_{i\sigma} + U \sum_i \hat{n}_{i\uparrow} \hat{n}_{i\downarrow} \quad , \tag{4.1.1}$$

where the operator $\hat{c}_{i\sigma}$ ($\hat{c}^\dagger_{i\sigma}$) annihilates (creates) an electron in a localized Wannier orbital at lattice site i with spin σ, $\hat{n}_{i\sigma} = \hat{c}^\dagger_{i\sigma}\hat{c}_{i\sigma}$ represents the number operator for electrons with spin σ at site i and ϵ_σ is the ionic level position, which is assumed to be the same at each site. Note that all information of the lattice is encoded into to one-particle hopping amplitude t_{ij}.

In the following only spin-symmetric, i.e. paramagnetic situations are considered and the ionic energies are taken to be spin independent, $\epsilon_\uparrow = \epsilon_\downarrow \equiv \epsilon$. The orbital matrix-structures of chapter 2 can therefore be ignored and all formulas reduce to scalar equations.

4.2 Lattice Kondo effect in the Hubbard model

The local DOS of the Hubbard model calculated within the locally complete approximation and the ENCA as the impurity solver for various temperatures on a three dimensional simple cubic (3d-SC) lattice with nearest neighbor transfer is shown in the upper graph of figure 4.1 for the symmetric case (half filling, $n_\sigma = 0.5$) and for the asymmetric situation in figures 4.2 and 4.3.

The calculations are done for a hopping amplitude $t = 0.5$, which leads to a half bandwidth for the non-interacting DOS of $W = 2dt = 3$. The Coulomb repulsion is taken to be $U = 4.5$ for the symmetric and $U = 6$ and $U = 10$ for the asymmetric cases, the average particle number per lattice site and spin (filling) is $n_\sigma = 0.5$ (symmetric), $n_\sigma = 0.48$ and $n_\sigma = 0.485$ (asymmetric), respectively. Also shown are the spectral function obtained within the free theory 2.2.4 ("free").

In all spectra the lower and upper Hubbard band around the positions of the ionic excitation energies, $\epsilon < 0$ and $\epsilon + U > 0$, respectively, are clearly visible. For the free theory the form of the spectral intensities for each Hubbard band closely resembles the non-interacting DOS with its van Hove singularities. These sub-bands arise due to the transfers of electrons between neighboring sites. Since each local ion supports two excitations with approximately half the spectral weight and these couple independently to the neighbors, one can think of each of the levels ϵ and $\epsilon + U$ forming its own tight-binding band. Consequently, the width of the sub-bands is approximately half the total non-interacting bandwidth, in this case $W_{sub} \approx 1.5$.

In the spectral functions of the locally complete approximation the Hubbard bands are broadened by thermal fluctuations as well as by the interaction. The width of the sub-bands is somewhat broadened and the height reduced. The van Hove singularities of the free theory DOS are completely smeared out and only very broad maxima remain.

Around the Fermi level $\omega = 0$ a very strong temperature dependent feature emerges at low temperatures. This feature signals the formation of low energy effective quasiparticles and is intimately connected to the Kondo effect, which was already discussed in section 3.4.

The conceptual difference between this lattice version of the Kondo effect and the SIAM is, that in the former there is no distinction between a local interacting f-electron system and a non-interacting conduction band, but only one species of particles exists. The same electrons are subjected to the Coulomb interaction on every lattice site, tend to become localized by it, form magnetic moments and support cascades of particle-hole excitations, which screen these forming local moments eventually forming a dynamic singlet as in the impurity model. Similar to the SIAM, the dynamic low energy singlet allows a multitude

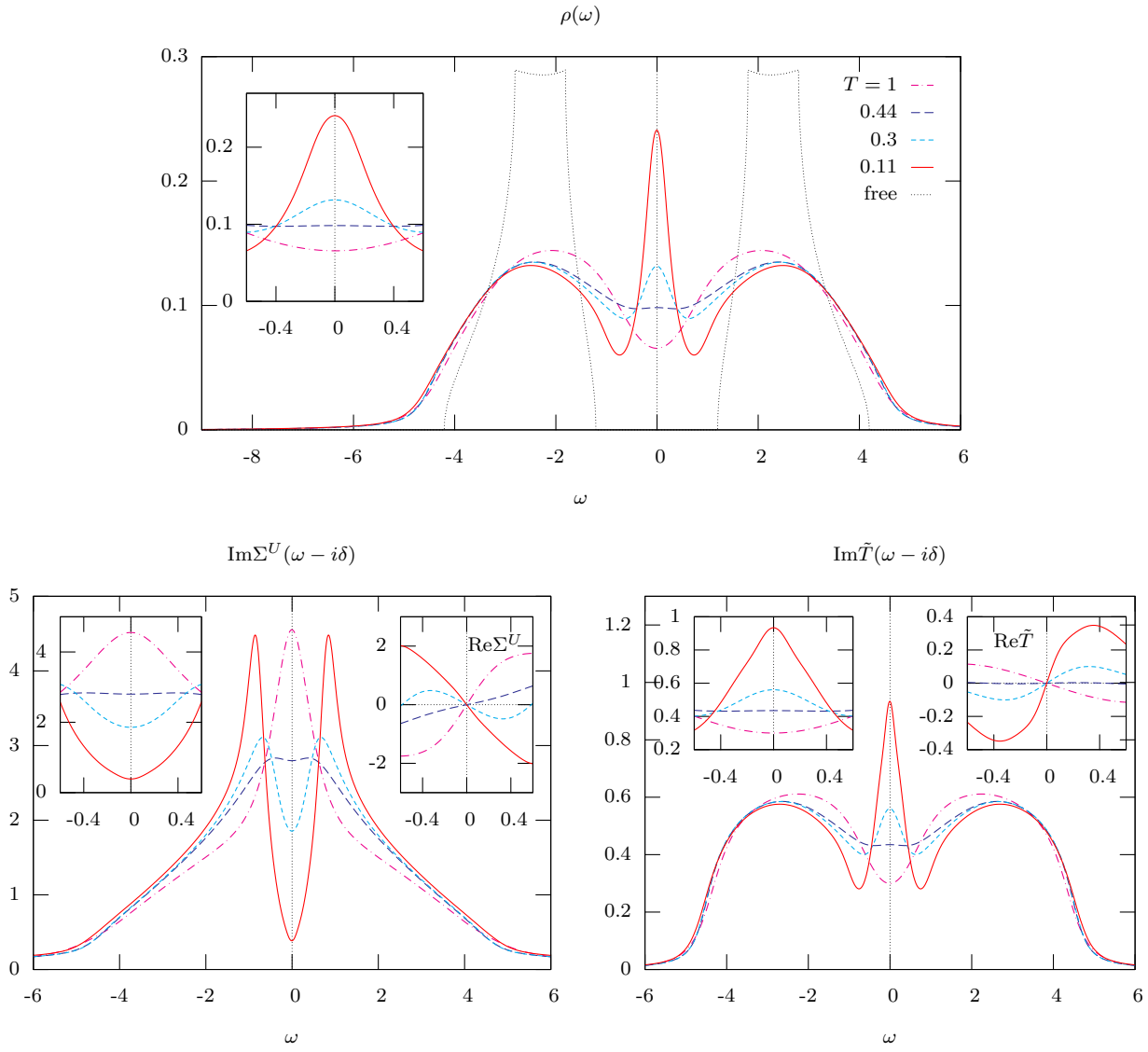

Figure 4.1: Local spectral function ρ (upper graph), correlation self-energy Σ^U (lower left) and effective medium $\tilde{T}$ (lower right) for the symmetric (half filled) Hubbard model on a 3d-SC lattice for Coulomb repulsion $U = 4.5$ ($\epsilon = -2.25$, $n_\sigma = 0.5$), half bandwidth $W = 3$ ($t = 0.5$) and various temperatures ($T = 1, 0.44, 0.4, 0.11$) and as functions of frequency within the locally complete approximation (colored curves). The grey dashed curve in the upper graph represents the free theory ("free") DOS. The insets show the low energy regions around the Fermi level.

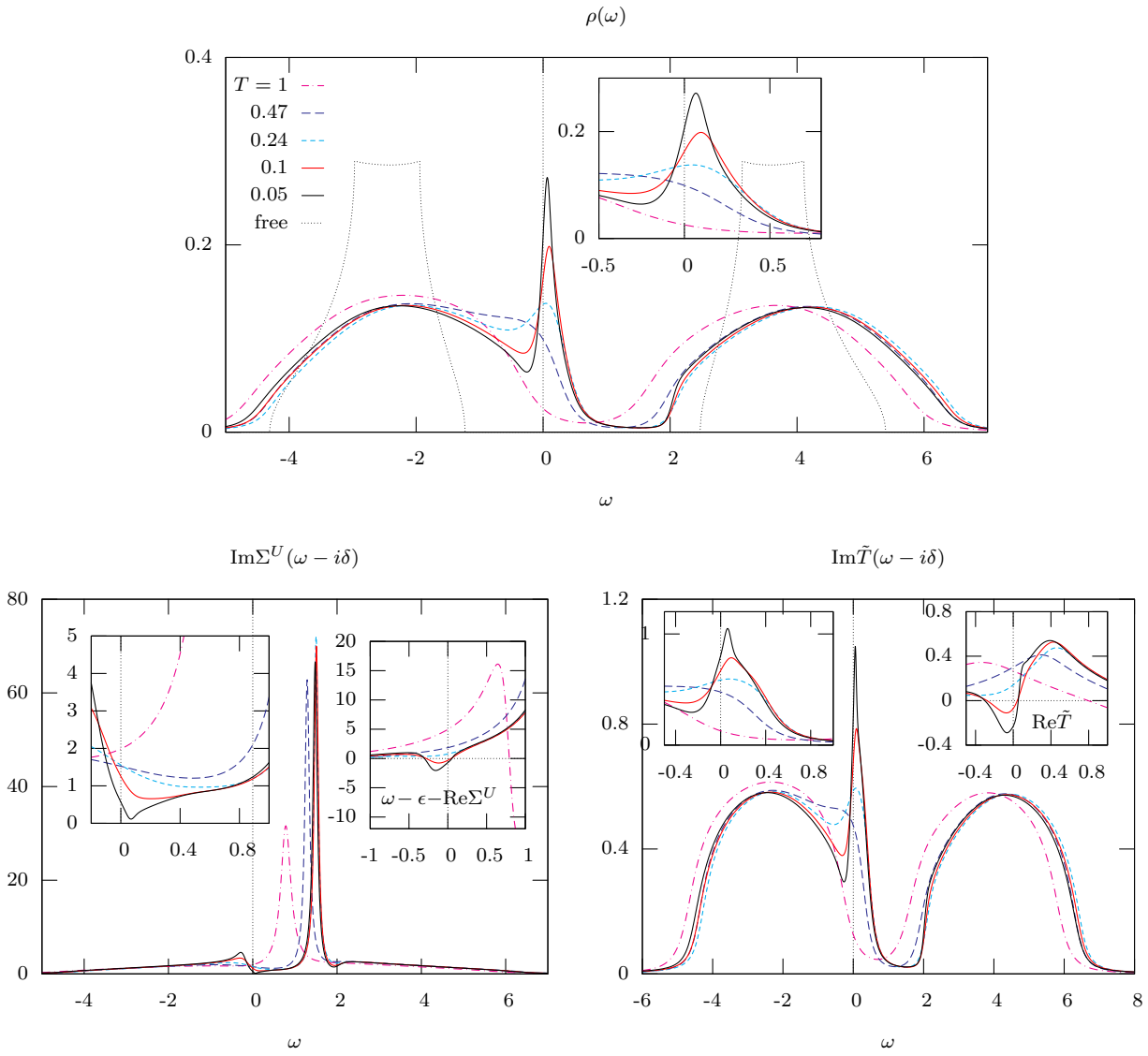

Figure 4.2: Local spectral function ρ (upper graph), correlation self-energy Σ^U (lower left) and effective medium $\tilde{T}$ (lower right) for the asymmetric Hubbard model on a 3d-SC lattice for Coulomb repulsion $U = 6$, filling $n_\sigma = n/2 = 0.48$, half bandwidth $W = 3$ ($t = 0.5$) and various temperatures ($T = 1, 0.47, 0.24, 0.1, 0.05$) and as functions of frequency within the locally complete approximation. The grey dashed curve in the upper graph represents the free theory ("free") DOS. The insets show the low energy regions around the Fermi level.

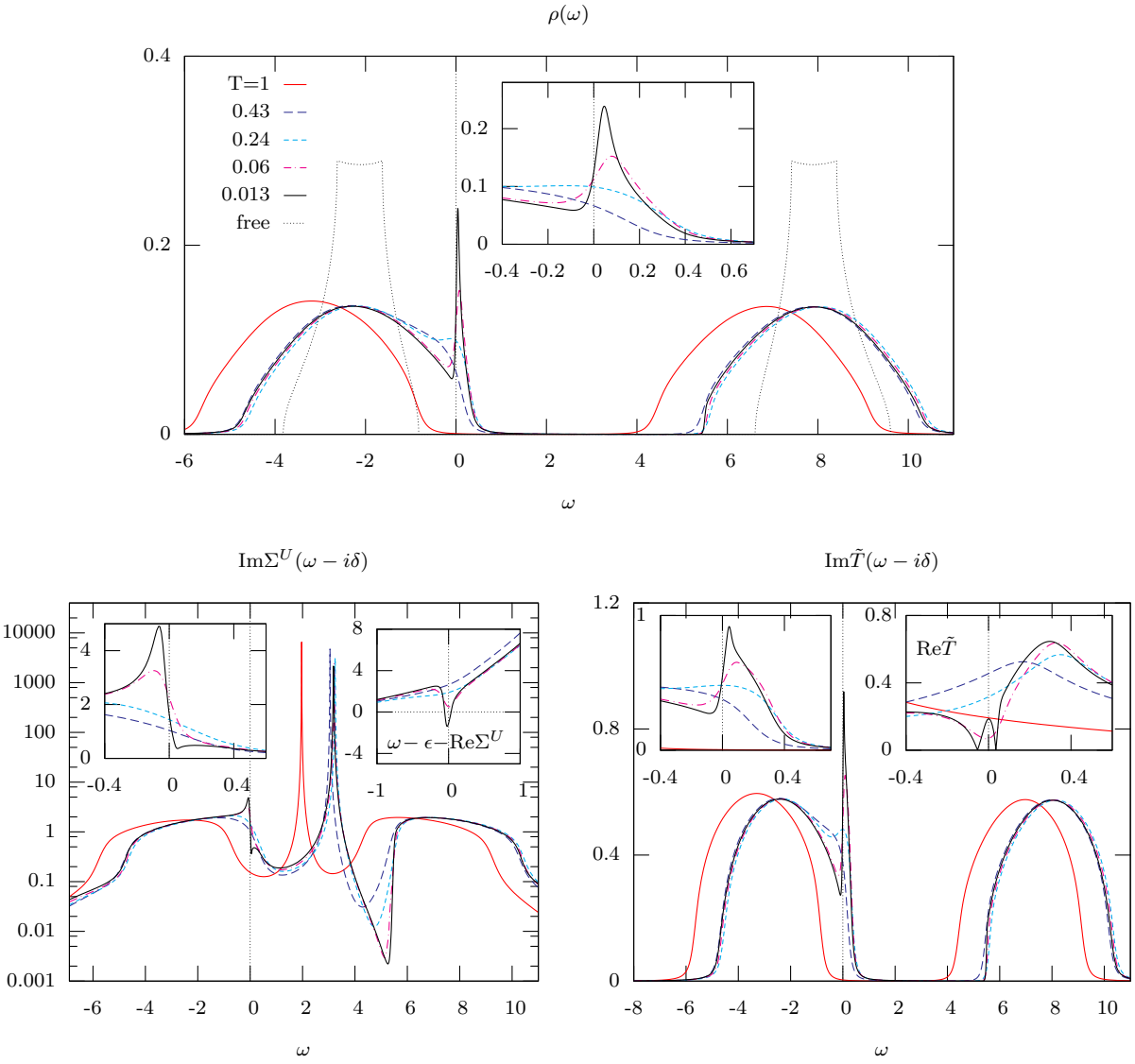

Figure 4.3: Local spectral function ρ (upper graph), correlation self-energy Σ^U (lower left) and effective medium $\tilde{T}$ (lower right) for the asymmetric Hubbard model on a 3d-SC lattice for Coulomb repulsion $U = 10$, filling $n_\sigma = n/2 = 0.485$, half bandwidth $W = 3$ ($t = 0.5$) and various temperatures ($T = 1, 0.42, 0.24, 0.06, 0.025$) and as functions of frequency within the locally complete approximation. The grey dashed curve in the upper graph represents the free theory ("free") DOS. The insets show the low energy regions around the Fermi level.

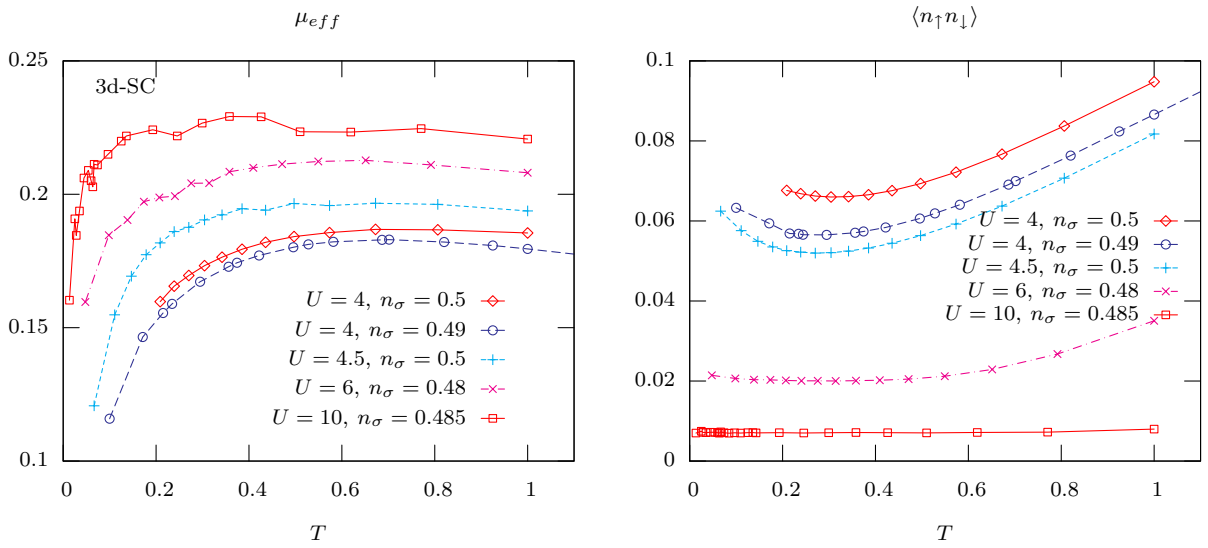

Figure 4.4: Effective local magnetic moment $\mu_{eff}^{(loc)}$ (left graph) and double occupancy $\langle n_\uparrow n_\downarrow \rangle$ (right graph) of the Hubbard model on the 3d-SC lattice as a function of temperature for various parameter values as indicated.

of spin flip excitations which give rise to the formation of the low energy quasiparticles and lead to the many-body resonance at the Fermi level. The energy associated with the dynamic singlet is denoted by T^* and represents the low energy scale of the problem.

The screening can explicitly be observed in the right graph of figure 4.4, where the effective local magnetic moment

$$\mu_{eff}^{(loc)} = T\chi_{mag}^{(loc)}(0) \tag{4.2.1}$$

is shown as a function of temperature for various Coulomb repulsions and fillings. Generally, the effective local moments are larger and closer to the maximum value of 1/4 for higher values of the local Coulomb repulsion, since double occupation is reduced and the local occupation is closer to one. Away from half filling $n_\sigma < 0.5$, the local moments become destabilized by the presence of holes in the system. Upon lowering the temperatures all shown effective moments decrease. For one thing, this is a consequence of increased itinerancy of the electrons due to the growing spectral density at the Fermi level. For another thing, at very low temperatures the decrease is attributed dynamical screening.

Also shown in the figures 4.1, 4.2 and 4.3 are the correlation self-energy Σ^U and the effective medium $\tilde{T}$ (lower rows) for the same parameter values as the spectra ρ. In the imaginary parts of the self-energies, the maxima indicate strong scattering and lead to minima in the DOS. This can be observed most dramatically in the asymmetric cases, where the sharp peaks at energies $\omega \approx 1$ and $\omega \approx 3$ produce the band gap between the lower and upper Hubbard bands.

The self-energies clearly support the notion of a low temperature Fermi liquid, since they develop a quadratic minimum in $\mathrm{Im}\Sigma^U(\omega - i\delta)$ at the Fermi level (see insets). This signals the vanishing of the scattering amplitude for the quasiparticles at the Fermi level and their increased lifetime. For the asymmetric case this minimum is slightly shifted to

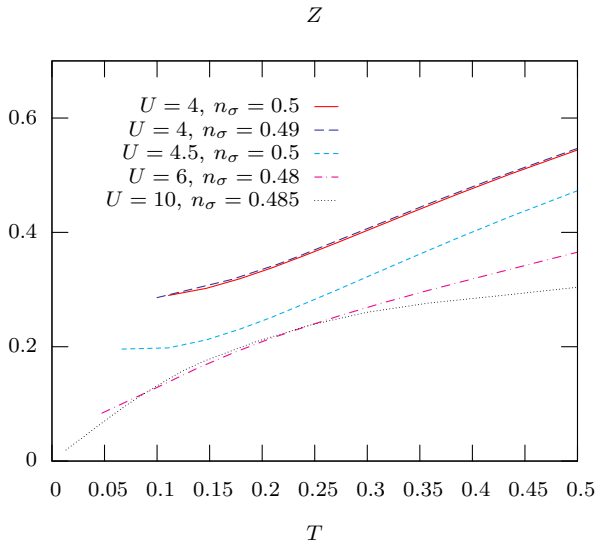

Figure 4.5: The function $Z(T)$ for the Hubbard model on the 3d-SC lattice for various parameter values calculated with equation (4.2.3). The physical quasiparticle weight is given by the $T = 0$ extrapolation of the shown curves.

higher energies in accord with the shift in the many-body resonance in the one-particle DOS.

The quasiparticle weight, representing the spectral weight for the renormalized quasiparticle-excitations, can be deduced from the derivative of the real part of the correlations self-energy at the Fermi level

$$Z = \frac{1}{1 - \frac{\partial \mathrm{Re}\Sigma^U}{\partial \omega}(0)} \qquad (T = 0) \qquad (4.2.2)$$

$$= \left[1 - \int \frac{d\omega}{\pi} \frac{\mathrm{Im}\Sigma^U(\omega + i\delta)}{\omega^2 + (\pi T)^2}\right]^{-1} \qquad (T \geq 0) \quad . \qquad (4.2.3)$$

In the second line a finite temperature extension is used, which is obtained via the Kramers-Kronig relation [Ser91]. Both definitions coincide for low temperatures and yield the same $T = 0$ extrapolation which is strictly speaking the only point, where the quasiparticle weight is defined. For high temperatures the Fermi liquid definition (4.2.2) correctly breaks down since the derivative changes sign, while the finite temperature extension (4.2.3) yields finite values.

The function $Z(T)$ calculated with equation (4.2.3) is shown in figure 4.5 as a function of temperature and various values for U and n_σ. The physically relevant data are the extrapolations to zero temperature $T \to 0$ of the shown curves. It can be guessed from the figure, that the $T = 0$ extrapolated values for the quasiparticle weight strongly depends on the Coulomb matrix element and is drastically reduced for larger U, while the filling dependency is rather weak. This is expected since large correlations lead to a stronger renormalization of the original electrons and therefore considerably reduce Z. But variations in the filling do not influence the quasiparticle formation equally strong, since the occupation numbers of the different valence states are changed only slightly.

A more physical intuitive quantity connected with the quasiparticle weight is the effective mass enhancement of the actual thermally relevant quasiparticles compared to the original (non-interacting) electrons,

$$\frac{m^*}{m} = \frac{1}{Z} \quad . \tag{4.2.4}$$

The larger the Coulomb repulsion is, the larger is the effective mass m^* of the quasiparticles. This is intuitive, since larger correlations imply less mobile excitations, as the particles feel the presence of the surroundings and become less inclined to transfer to neighboring sites, which in turn implies a larger effective mass. As it can be seen from the $U = 10$ graph in figure 4.5, these enhancement factors can be as large as 100-1000, in which situations one speaks of Heavy-Fermion materials (cf. [Col07, Hew93, Gre91]).

The effective media $\tilde{T}$ are shown in the right graph of the lower rows in figures 4.1, 4.2 and 4.3. Their overall form strongly resembles that of the spectral functions including lower and upper Hubbard bands and the feature at the Fermi level. The distribution of spectral weight in $\mathrm{Im}\tilde{T}$ is intuitively understandable, since it is the hybridization function for the effective impurity and thus represents a measure for the intensity of nearest neighbor transfers to and from that local site. A large value of $\mathrm{Im}\tilde{T}$ indicates a strong hybridization with the neighboring sites. Since the low energy spectral weight for hybridization processes at the Fermi level is considerable, the itinerant nature of the low energy quasiparticles is confirmed directly. The real parts (insets) are only shown for completeness.

The itinerant character of the quasiparticles can also be observed in the $\underline{k}$-resolved spectral densities as shown in the lower rows of figures 4.6, 4.7 and 4.8. The low energy excitations around the Fermi level, which sum up to the many-body resonance in the local spectrum, form a band and show a significant dispersion, which has the same momentum dependence as non-interacting electrons, i.e. $\sim t_{\underline{k}}$.

The band formation of the weakly interacting quasiparticles can also be observed indirectly in the double occupancy $\langle n_\uparrow n_\downarrow \rangle$[1]. For non-interacting particles, the double occupancy is given by its statistical weight $\langle n_\uparrow n_\downarrow \rangle^{U=0} = \langle n_\sigma \rangle^2$, while the local Coulomb repulsion tends to suppress it. This can be seen in the right graph of figure 4.4, where the overall scale of the curves is considerably smaller for larger values of U. The double occupancy is also reduced for decreasing temperature since the doubly occupied valence states are thermally depopulated. But at some temperature, the quasiparticles start to form the low energy band structure. The formation of an increasing fraction of itinerant particles at lower temperatures leads to an increase in the double occupancy, because they necessarily have

[1] The double occupancy can be either calculated from the one-particle Green function and self-energy as [Geo93, Vil97]

$$\langle n_\uparrow n_\downarrow \rangle = -\frac{1}{\pi U} \mathrm{Im} \int d\omega \, f(\omega) \Sigma^U(\omega + i\delta) G^{loc}(\omega + i\delta) \tag{4.2.5}$$

or directly from the dynamic susceptibilities,

$$\langle n_\uparrow n_\downarrow \rangle = \frac{1}{\pi} \int d\nu \left(\frac{1}{2} + g(\nu) \right) \left[\mathrm{Im}\chi^{loc}_{charge}(\nu + i\delta) - \mathrm{Im}\chi^{loc}_{mag}(\nu + i\delta) \right] \quad , \tag{4.2.6}$$

where $f(\omega)$ and $g(\nu)$ represent the Fermi and Bose function, respectively. The results obtained with both methods agree very well, but since the dynamic susceptibilities involve considerably more numerical effort, the presented data are calculated with equation (4.2.5).

admixtures of the latter to ensure the itinerancy. Thus, the low temperature increase of the double occupancy can be viewed as an indication for a band formation. Alternative but equivalent explanations use the entropy gain from itinerant particles in contrast to the loss of interaction energy following the increased double occupancy [Geo93].

Due to the itinerant quasiparticles in the lattice version of the Kondo effect, the dynamic low energy singlet extends over the whole lattice. At very low temperatures the quasiparticles establish coherence over the whole lattice and the Fermi liquid state forms. This implies long-lived quasiparticles, which can be best seen in the $\underline{k}$-resolved spectra for the asymmetric cases, figures 4.7 and 4.8, where at lowest temperatures a very sharp peak emerges out of the quasiparticle band structure around the Fermi level. The lattice coherence of the quasiparticle in the Fermi liquid state is essential, since local excitations at every lattice site must be mixed with the appropriate phase factors in order to provide the screening of all local magnetic moments.

In effect, the Kondo temperature of the SIAM is replaced by the low energy scale of the model T^*, at which coherence over the whole lattice starts to build up. An estimation of this coherence temperature is not as easy as in the SIAM, but it is of the order of the width of the low energy excitations at the Fermi surface in the k-resolved spectra, since it also represents the "binding energy" of the dynamic singlet. As already mentioned, one difference of the Hubbard model to the SIAM is the difficulty to distinguish between "those electrons" forming the local moments, and "the others" screening them. Another point is, that in metallic situations of the Hubbard model, the excitations near the Fermi level are always of an itinerant nature and thus – from a local impurity perspective – valence fluctuations will always be influential.

In contrast to the free theory, where in the symmetric situation with $U = 4.5$ and $n_\sigma = 0.5$, the DOS at the Fermi level vanishes and consequently the system described would be a correlation-driven Mott insulator, the locally complete solution predicts a metallic situation, as it would have been guessed from Luttinger's theorem. As it can be seen in the band structure $\rho(\underline{k}, \omega)$ of figures 4.6, 4.7 and 4.8, the sharpest peaks occur whenever the crystal momentum equals the Fermi momentum of the unperturbed Fermi surface, $\underline{k} = \underline{k}_F$, as it is characteristic for the infinite lifetime of the developing low temperature Fermi liquid. The formation of the quasiparticles at low temperatures and the concurrent establishment of a Fermi surface thus represents a rather intriguing fulfillment of Luttinger's theorem.

A correlation-driven Mott-Hubbard metal-insulator transition (MIT) is expected in the Hubbard model and found within the locally complete approximation with critical values of U of the order of the bandwidth [Pru93, Bul99, Bul01, Kar05]. At finite, but low temperatures the transition is of first order with hysteresis effects, while for zero temperature the transition is continuous, but with a finite excitation gap in the one-particle DOS right at the transition.

The basic ingredients necessary to establish this correlated coherent low temperature state, namely moment formation and antiferromagnetic exchange interactions in order to screen magnetic moments, can be explicitly observed in the large U limit of the Hubbard model. For very large Coulomb interactions U, doubly occupied states are effectively removed from the dynamics and are only accounted for in virtual excitations producing the

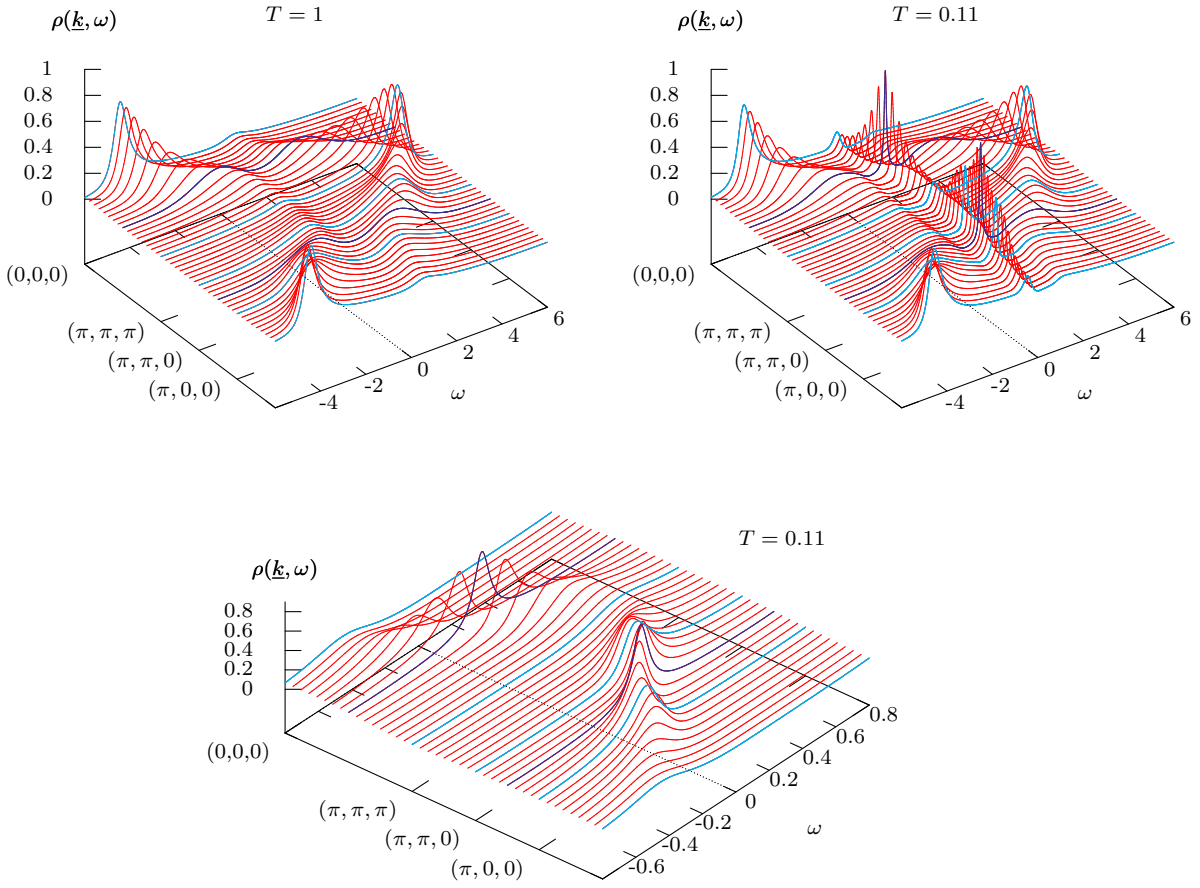

Figure 4.6: $\underline{k}$-resolved spectral function (band structure) for the symmetric (half filled) Hubbard model, $U = 4.5$, $n_\sigma = 0.5$ and a 3d-SC lattice for two different temperatures $T = 1$ and $T = 0.11$. The graph in the lower row shows the low energy region around the Fermi level for $T = 0.11$. The turquoise lines mark the special $\underline{k}$ vectors as indicated on the axis, while the blue lines mark the approximate position of the Fermi wave-vectors $\underline{k}_F$.

effective couplings. An unitary transform of the Hubbard Hamiltonian (4.1.1) can then be performed to yield the so-called tJ-model [Aue98, Faz99],

$$\hat{H}_{eff} = \sum_{i\,\sigma} \epsilon_\sigma \, \hat{\tilde{c}}^\dagger_{i\sigma} \hat{\tilde{c}}_{i\sigma} + \sum_{ij,\sigma} t_{ij} \hat{\tilde{c}}^\dagger_{i\sigma} \hat{\tilde{c}}_{j\sigma} + \frac{1}{2} \sum_{ij} J_{ij} \left(\underline{\hat{S}}_i \cdot \underline{\hat{S}}_j - \frac{1}{4} \hat{n}_i \cdot \hat{n}_j \right) + \hat{I} \quad , \tag{4.2.7}$$

where the operators $\hat{\tilde{c}}^\dagger_{i\sigma} = (1 - \hat{n}_{i\bar{\sigma}})\, \hat{c}^\dagger_{i\sigma}$ are restricted to act only on empty and singly occupied states, $\underline{\hat{S}}_i$ represents the total spin operator at site i, $\hat{n}_i = \sum_\sigma \hat{n}_{i\sigma}$ the number operators and the exchange coupling J_{ij} is given by

$$J_{ij} = \frac{4t_{ij}^2}{U} > 0 \quad . \tag{4.2.8}$$

The term $\hat{I}$ in (4.2.7) is also of order $\mathcal{O}(t^2/U)$ but involves three-site hopping processes and is usually omitted in the literature.

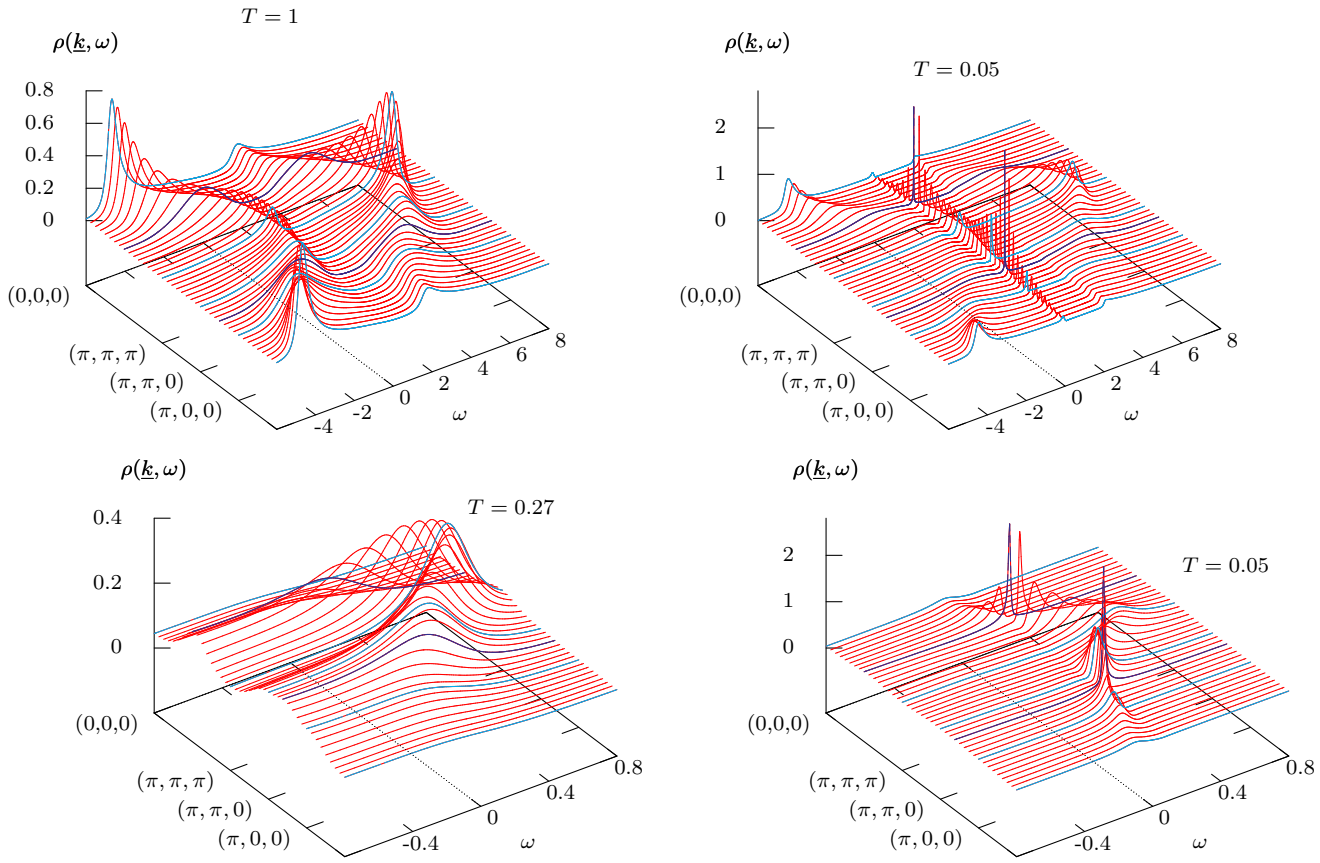

Figure 4.7: $\underline{k}$-resolved spectral function (band structure) for the asymmetric Hubbard model, $U = 6$, $n_\sigma = 0.48$ and a 3d-SC lattice for temperatures $T = 1, 0.05$. The graphs in the lower row show the low energy region around the Fermi level for $T = 0.27$ and $T = 0.05$. The turquoise lines mark the special $\underline{k}$ vectors as indicated on the axis, while the blue lines mark the approximate position of the Fermi wave-vectors $\underline{k}_F$.

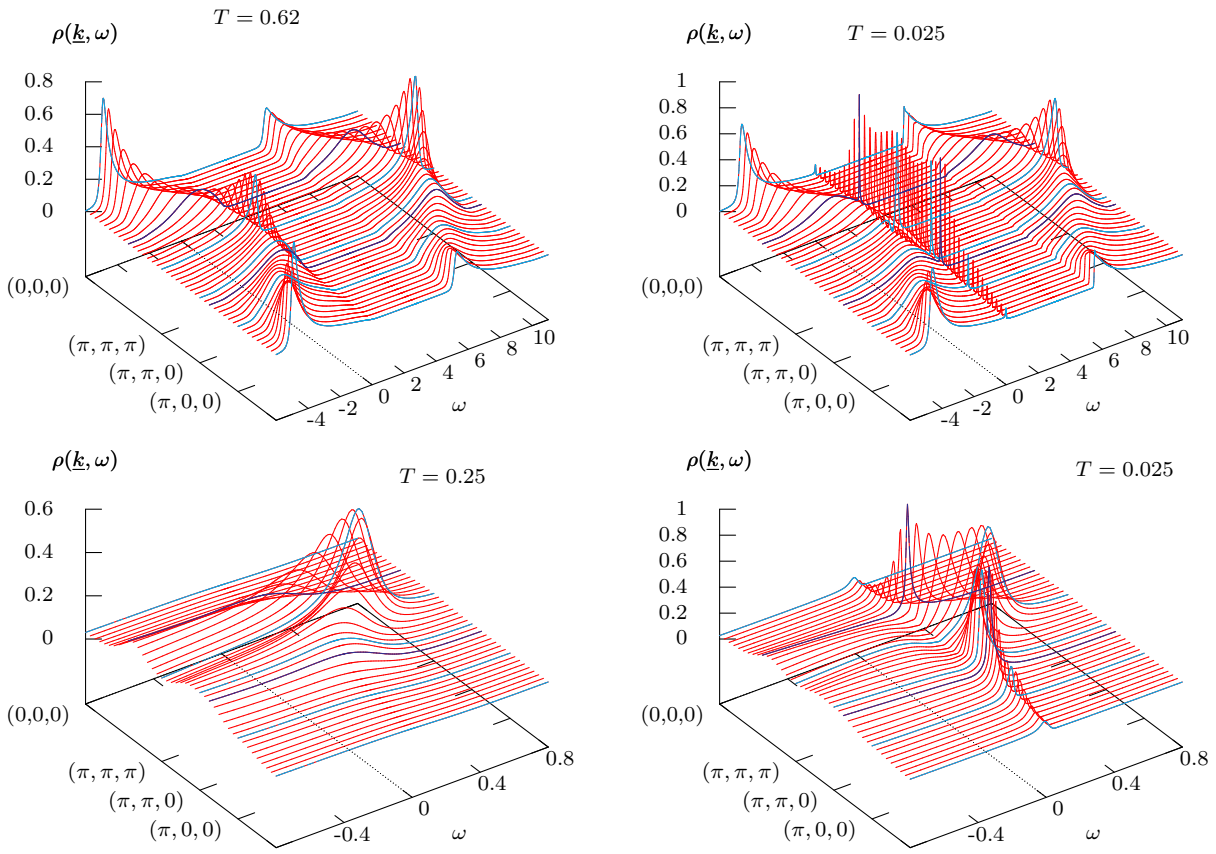

Figure 4.8: $\underline{k}$-resolved spectral function (band structure) for the asymmetric Hubbard model, $U = 10$, $n_\sigma = 0.485$ and a 3d-SC lattice for temperatures $T = 1, 0.05$. The graphs in the lower row show the low energy region around the Fermi level for $T = 0.25$ and $T = 0.05$. The turquoise lines mark the special $\underline{k}$ vectors as indicated on the axis, while the blue lines mark the approximate position of the Fermi wave-vectors $\underline{k}_F$.

The tendency of a large Coulomb interaction to localize the electrons and form local magnetic moments, e.g. local spins, can clearly be seen in the interaction term of (4.2.7). The effective coupling J_{ij} is generated by virtual excitations of an electron from site i onto an already occupied (neighboring) site j and is positive, as it can be seen from (4.2.8). Thus, spin degrees of freedom in the tJ-model and the large U Hubbard model are coupled antiferromagnetically.

Note, that the one-body and three-site terms in the tJ-model vanish for half filling and reduce the Hamiltonian to the Heisenberg model of antiferromagnetically coupled quantum mechanical spins.

4.3 Breakdown of the Fermi liquid

The question whether a lattice model forms a Fermi liquid state at low temperatures or rather transforms into something commonly referred to as non-Fermi liquid or singular Fermi liquid is a very delicate one[2]. For the one-dimensional interacting Fermi gas, including the Hubbard model, the ground state is not a Fermi liquid but rather a so-called *Luttinger* liquid, or at least a state closely related to it, due to a singular scattering amplitude at the Fermi level (for reviews see [Voi95], [Ste01] or [Var02]). The singular scattering amplitude arises from perfect nesting, i.e. parallel parts of the Fermi surface with the appropriate particle- or hole-like character, which is alway fulfilled in one dimension for particles at the Fermi level.

Within the locally complete approximation for the Hubbard model, where only local correlations are included, the expected generic low energy state is indeed the Fermi liquid described in the previous section. This is apparent as the crucial step in the solution of the lattice problem is the effective impurity model with a self-consistently determined effective medium $\tilde{T}$. As demonstrated in section 3.4, the low temperature phase of the spin-$\frac{1}{2}$ SIAM is a local Fermi liquid under the assumption of a "well behaved" medium. Since the correlation self-energy of the SIAM directly enters the lattice theory and represents the self-energy for lattice excitations as well, cf. (2.2.20), this naturally leads to a Fermi liquid state of the lattice model for low temperatures.

The question arises, under which circumstances the Fermi liquid state might be replaced by alternative non-Fermi liquid phases. One possible route is to extend the locally complete approximation to include nonlocal correlations, which may lead to a pseudogap formation (see for example [Vil97, Hus01, Jar01, Sad05, Mai05] and references therein).

For an impurity model, multi-channel generalizations with additional electronic conduction bands may lead to an overcompensation of the impurity spin and non-Fermi liquid behavior as well (for a review see for example [Cox98]).

In an even simpler approach, the medium for the spin-$\frac{1}{2}$ SIAM is assumed to have a pseudogap, i.e. it vanishes as a power-law at the Fermi level $\omega = 0$,

$$\Delta(\omega) \sim |\omega|^r \qquad , \quad r \geq 0 \quad . \tag{4.3.1}$$

For values of the exponent $r > \frac{1}{2}$ a transition to a local moment phase with an underscreened impurity spin and non-Fermi liquid properties is found [Bul97, Kol05].

[2] The possibility of thermodynamic phase transitions to ordered phases such as superconductivity or magnetism is ignored for the moment.

Non-Fermi liquid behavior is also known to occur in situations with nested Fermi surfaces [Lee87, Vir90, Sch05]. Due to the nesting property of the Fermi surface, the susceptibility is strongly enhanced and consequently the quasiparticle scattering amplitude is unusual high and shows a linear T-dependence, instead of the quadratic Fermi liquid form.

At the heart of a general microscopic argumentation towards the establishment of a Fermi liquid lie assumptions regarding the analyticity of the irreducible interaction vertex (cf. [Voi95, Var02]). Within an impurity model, and equally so for the locally complete approximation, the relevant interaction vertex is just the sum of the correlation self-energy and the (effective) medium. From that point of view, the breakdown of the Fermi liquid state for the pseudogap medium (4.3.1) is no surprise, since the medium has a non-analyticity at $\omega = 0$.

In the locally complete theory, the medium for the impurity model cannot be chosen arbitrarily, but is determined through the lattice self-consistency and one therefore cannot introduce non-analyticities in a manner directly analogous to the pseudogap model. However, the point where this seems possible, is by means of the non-interaction DOS which enters the theory through the lattice sums, see e.g. equation (2.2.10).

The first candidate of such a non-analytic non-interacting DOS which comes to mind is the two dimensional simple cubic (2d-SC) lattice with its logarithmic divergence in the band center (see appendix D).

The results of a locally complete calculation for the 2d-SC lattice in the symmetric case for $U = 4$ ($\epsilon = -2$) are shown in figures 4.9 (DOS $\rho(\omega)$, correlation self-energy $\Sigma^U(\omega - i\delta)$ and effective medium $\tilde{T}(\omega - i\delta)$) and 4.10 (band structure $\rho(\underline{k}, \omega)$). Also shown in figure 4.9 is the free theory DOS, which displays the logarithmic divergence in the band centers roughly at ϵ and $\epsilon + U$. For the locally complete solution the logarithmic divergences of the free theory DOS are completely smeared out and only very flat maxima remain. Apart from the slightly changed shapes and widths, the curves look similar to the three-dimensional ones shown in figures 4.1 and 4.6. But a major difference concerning the signatures of a Fermi liquid occur at low temperatures. Even though the quadratic minimum starts to form in $\mathrm{Im}\Sigma^U$ around the Fermi level, it eventually halts and the trend is reversed, resulting in a maximum at $\omega \approx 0$. This low temperature state is certainly not a usual Fermi liquid anymore. Accompanying the formation of the maximum in the self-energy, a dip develops at $\omega \approx 0$ in $\mathrm{Im}\tilde{T}$.

In order to rule out any numerical misbehavior or ENCA deficiency as the origin for these structures, plots for the self-energy and the effective medium obtained with the NRG used as an impurity solver[3] are shown in figure 4.11. There, the same characteristics as in the ENCA calculation are found, confirming their correctness and physical origin.

4.3.1 Simple model density of states

Since the 2d-SC lattice shows perfect nesting at half-filling, the destruction of the Fermi liquid state could be a mere consequence of that instead of the non-analyticity of the non-interacting DOS. In order to decide the question whether the system is a realization of

[3] The algorithm used for the NRG is the one described in [Pet06] and the numerical DMFT(NRG) code for this calculation was provided by F.B. Anders, for which the author is very grateful.

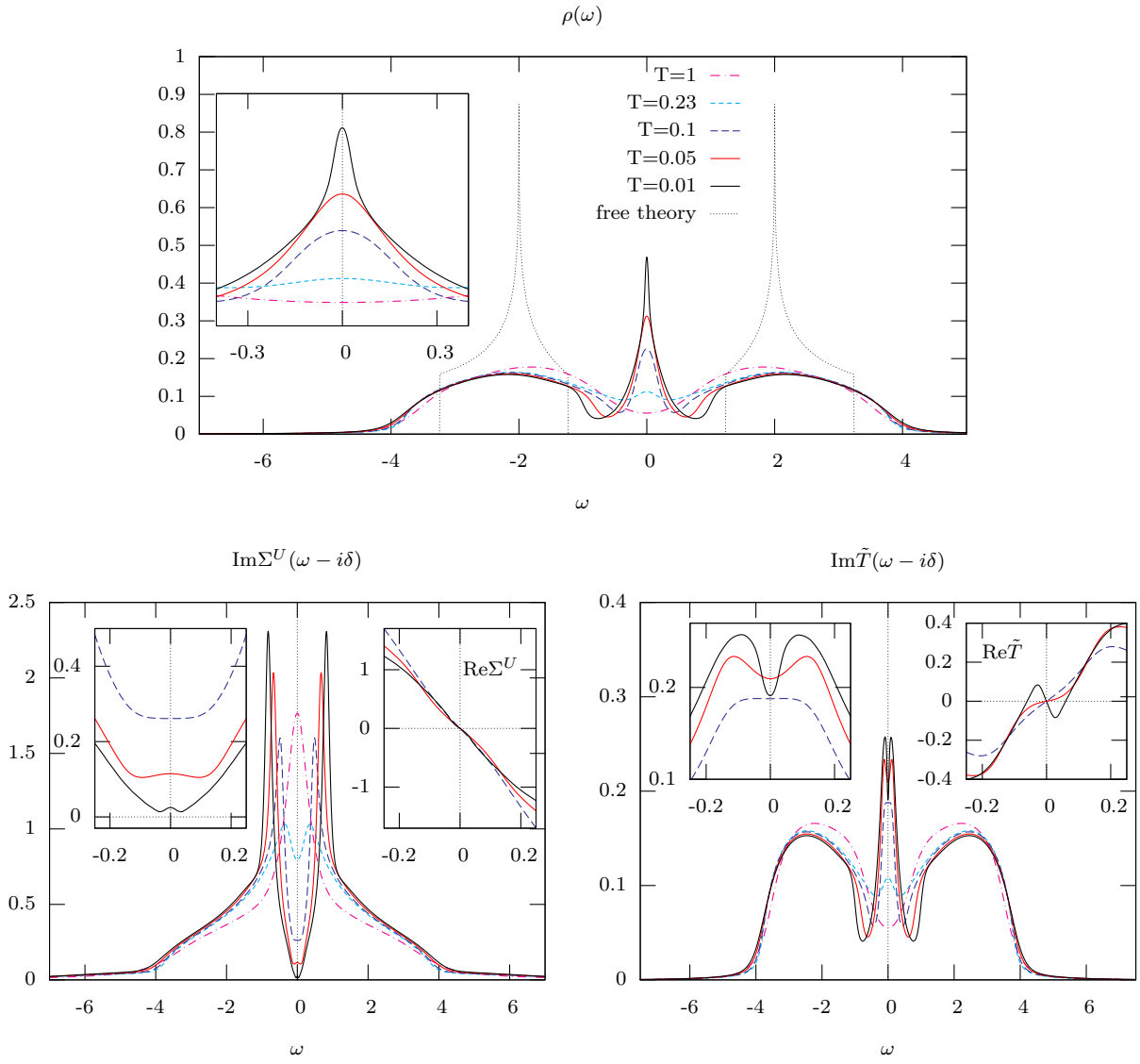

Figure 4.9: Local spectral function ρ (upper graph), correlation self-energy Σ^U (lower left) and effective medium $\tilde{T}$ (lower right) for the symmetric Hubbard model in two dimensions for Coulomb repulsion $U = 4$ ($\epsilon = -2$), half bandwidth $W = 2$ ($t = 0.5$) and various temperatures and as functions of frequency within the locally complete approximation (colored curves). The grey dashed curve represents the free theory (Hubbard-I) DOS.

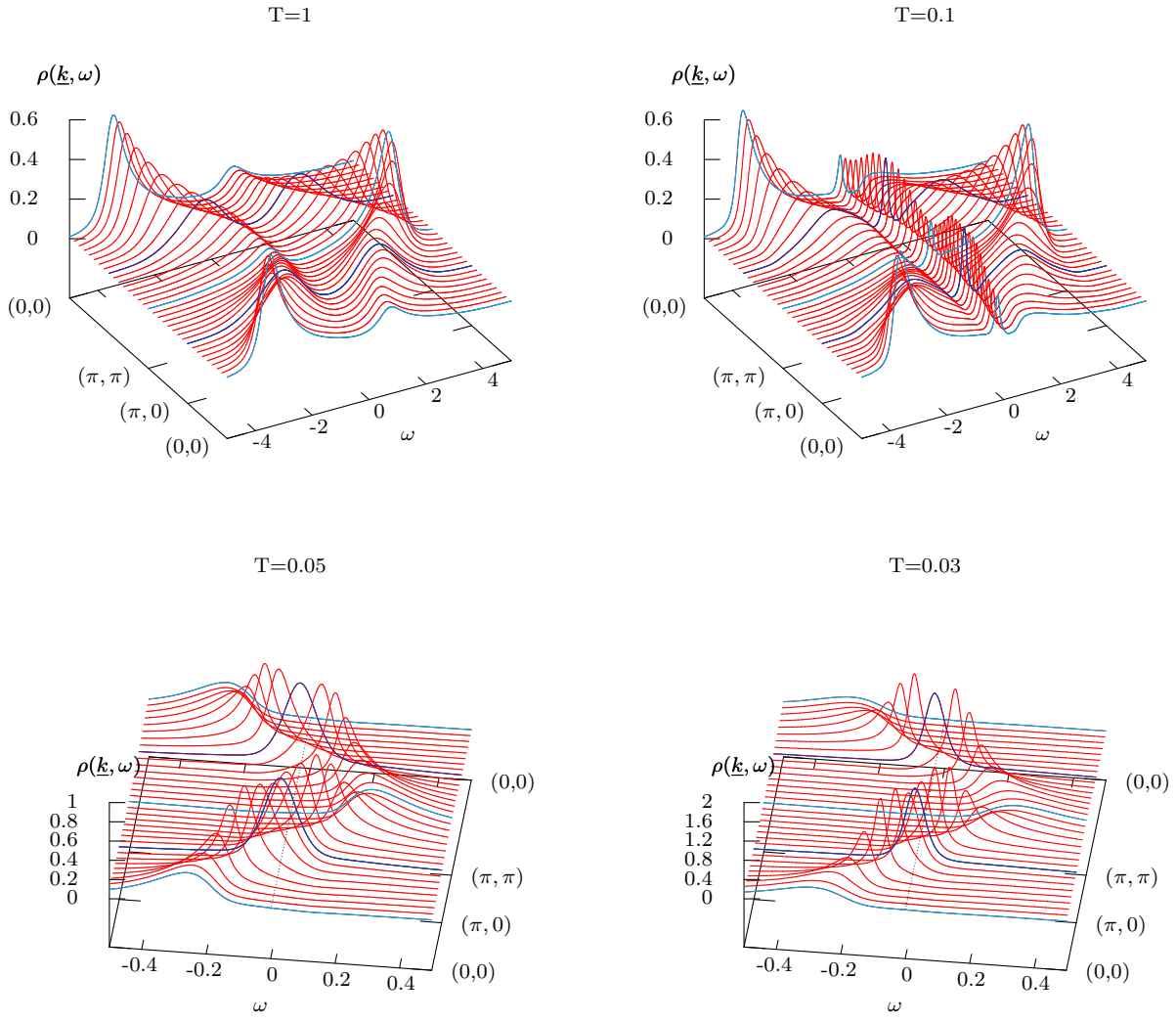

Figure 4.10: $\underline{k}$-resolved spectral function $\rho(\underline{k},\omega)$ for the symmetric Hubbard model, $U = -2\epsilon = 4$, in two dimensions for two different temperatures $T = 1, 0.1$ (upper row). The graphs in the lower row show the low energy region around the Fermi level for two even lower temperatures $T = 0.05, 0.03$. The turquoise lines mark the special $\underline{k}$ vectors as indicated on the axis, while the blue lines mark the approximate position of the Fermi wave-vectors $\underline{k}_F$.

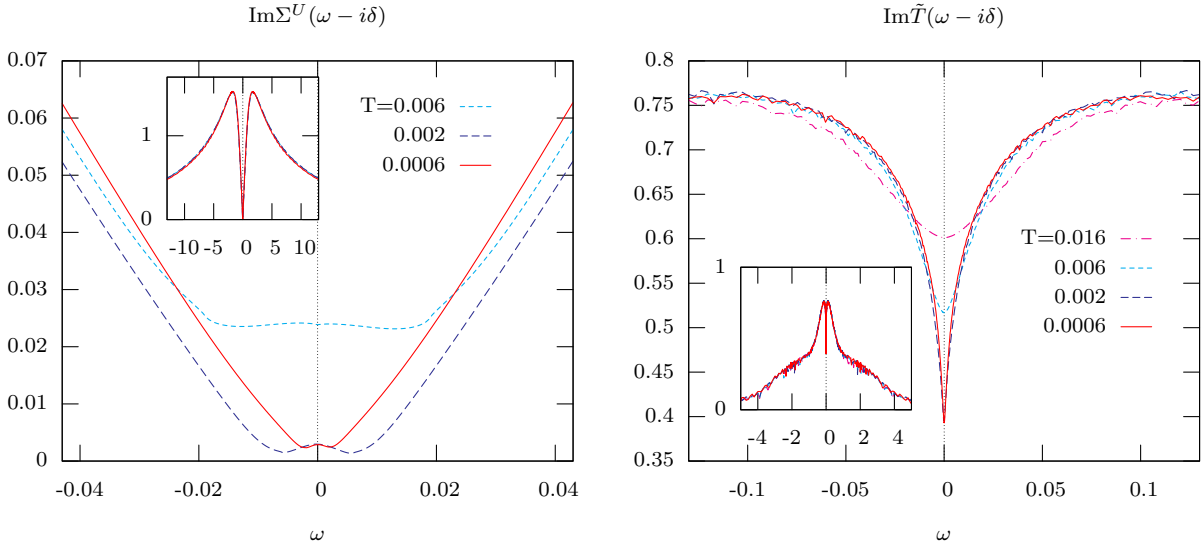

Figure 4.11: Imaginary parts of the self-energy (left) and the effective medium (right) of the symmetric Hubbard model in a 2d-SC lattice for low energies calculated with the NRG method as the impurity solver for $U = 4$ ($\epsilon = -2$,$n = 1$) and various temperatures as indicated. The insets show a larger region of excitations energies.

a so-called "nested Fermi liquid" [Vir90] or the unusual behavior is solely caused by the non-analyticity, it is worthwhile to consider a simplified model DOS of the following form:

$$\rho_\alpha^{cusp}(\omega) = \begin{cases} \frac{1+\alpha}{2\alpha W}\left(1 - \left(\frac{|\omega|}{W}\right)^\alpha\right) & , \quad \alpha > 0 \\ \frac{1}{2W}\ln\left(\frac{W}{|\omega|}\right) & , \quad \alpha = 0 \end{cases} , \tag{4.3.2}$$

where $-W \leq \omega \leq W$. For $\alpha < 2$ this DOS possesses a cusp at $\omega = 0$, which transforms into a logarithmic divergence for $\alpha \to 0$. Since no reference to any Fermi surface is made, the nesting properties of these model DOS are utterly unimportant and only the non-analyticity at $\omega = 0$ is incorporated.

For a given correlation self-energy Σ^U, or equivalently $\tilde{G}(z) = \frac{1}{z - \Sigma^U(z)}$, the scattering matrix can be calculated analytically with the help of equation (2.2.10). The result is a functional of $\tilde{G}$ and the exponent of the cusp-DOS α

$$T[\tilde{G}(z);\alpha] = \int_{-W}^{W} dx \, \frac{x^2 \rho_\alpha^{cusp}(x)}{\tilde{G}^{-1} - x} \tag{4.3.3}$$

$$\overset{\alpha>0}{=} \frac{1+\alpha}{\alpha}\frac{1}{\tilde{G}}\left[-1 + \frac{1}{\tilde{G}W}\,\mathrm{Artanh}(\tilde{G}W) - \frac{1}{3+\alpha}(\tilde{G}W)^2 \; {}_2F_1\left(1, \frac{3+\alpha}{2}; \frac{5+\alpha}{2}; (\tilde{G}W)^2\right)\right] \tag{4.3.4}$$

$$\overset{\alpha=0}{=} \frac{1}{\tilde{G}}\left[-1 + \frac{1}{2\tilde{G}W}\left(Li_2(\tilde{G}W) - Li_2(-\tilde{G}W)\right)\right] \quad , \tag{4.3.5}$$

where ${}_2F_1$ is the Gauss's hypergeometric function and Li_2 the Dilogarithm. Solving equation (2.2.11) for the effective medium yields the analytic expression in an explicit form,

$$\tilde{T}[\tilde{G};\alpha] = \frac{T(z)}{1+\tilde{G}(z)T(z)} \tag{4.3.6}$$

$$\overset{\alpha\geq 0}{=} \frac{1}{\tilde{G}} - W\frac{\alpha}{(1+\alpha)\,\mathrm{Artanh}(\tilde{G}W) - \tilde{G}W - \frac{1+\alpha}{3+\alpha}\left(\tilde{G}W\right)^3\,{}_2F_1\left(1,\frac{3+\alpha}{2};\frac{5+\alpha}{2};(W\tilde{G})^2\right)} \tag{4.3.7}$$

$$\overset{\alpha=0}{=} \frac{1}{\tilde{G}} + \frac{2W}{Li_2(-W\tilde{G}) - Li_2(W\tilde{G})} \quad . \tag{4.3.8}$$

In the following the three showcases of $\alpha = 0, 1, 2$ are considered, as they suffice to reproduce and illustrate the origin of the non-Fermi liquid behavior.

For $\alpha = 0$ equation (4.3.8) already constitutes the final formula, while for the other two cases equation (4.3.7) can be simplified:

$\underline{\alpha = 1}$: For $\alpha = 1$ the non-interacting DOS has a linear cusp at $\omega = 0$, as it can be seen in the inset of figure 4.12. The hypergeometric function reduces to an elementary function, i.e.

$${}_2F_1\left(1,2;3;z^2\right) = -\frac{2}{z^4}\left(z^2 + \ln(1-z^2)\right) \quad , \tag{4.3.9}$$

leading to the effective medium

$$\tilde{T}[\tilde{G};\alpha=1] = \frac{1}{\tilde{G}} - W\frac{1}{\frac{1}{\tilde{G}W}\ln\left(1-(\tilde{G}W)^2\right) + 2\,\mathrm{Artanh}(\tilde{G}W)} \quad . \tag{4.3.10}$$

$\underline{\alpha = 2}$: For $\alpha = 2$ the non-interacting DOS does not have a non-analyticity and is differentiable at $\omega = 0$ (see inset of figure 4.12). The hypergeometric function again reduces to an elementary function,

$${}_2F_1\left(1,\frac{5}{2};\frac{7}{2};z^2\right) = -\frac{5}{3}\frac{1}{z^5}\left(3z + z^3 - 3\,\mathrm{Artanh}(z)\right) \quad , \tag{4.3.11}$$

which results in an effective medium

$$\tilde{T}[\tilde{G};\alpha=2] = \frac{1}{\tilde{G}} - \frac{2}{3}W\frac{1}{\frac{1}{\tilde{G}W} + \left(1-\frac{1}{(\tilde{G}W)^2}\right)\,\mathrm{Artanh}(\tilde{G}W)} \quad . \tag{4.3.12}$$

The crucial difference between the three forms for the effective medium for $\alpha = 0$, 1 and 2 is the disappearance of the logarithmic terms in the denominator of (4.3.12) for the case of $\alpha = 2$.

Suppose the system is about to form a Fermi liquid state and consequently, the correlation self-energy has the corresponding form,

$$\tilde{G}(\omega - i\delta) = \frac{1}{\omega - i\delta - \Sigma^U(\omega - i\delta)} \tag{4.3.13}$$

$$\overset{FL}{=} \frac{Z}{\omega - i\Gamma((\pi T)^2 + \omega^2)} + \tilde{G}^{(inc)}(\omega - i\delta) \quad . \tag{4.3.14}$$

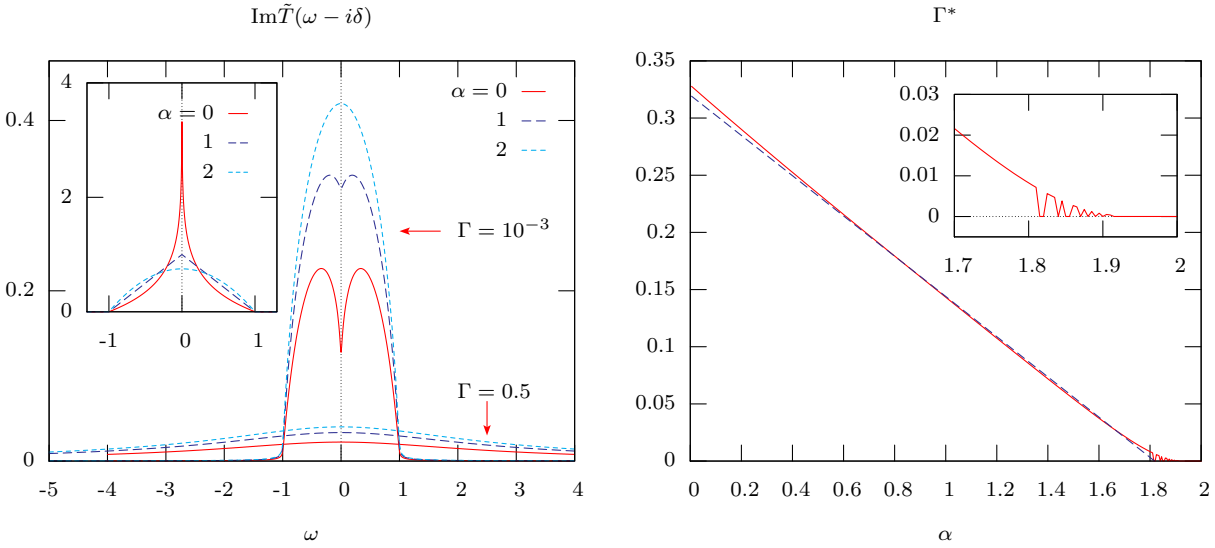

Figure 4.12: Left panel: Imaginary parts of the effective media (4.3.8), (4.3.10) and (4.3.12) as functions of ω for the showcases $\alpha = 0, 1, 2$ for two values of the imaginary part Γ. The inset shows the cusp-DOS for the three values of $\alpha = 0, 1, 2$.
Right panel: The value of the imaginary part Γ^*, where the coefficient of the quadratic term in the low frequency expansion for the effective medium vanishes, i.e. $a_2(\Gamma^*, \alpha, W, T) = 0$ plotted as a function of the exponent α of the cusp-DOS (4.3.2). The inset shows the region $1.7 \leq \alpha \leq 2$ where Γ^* goes to zero. The blue dashed line is a linear fit $\Gamma^* \approx 0.32(1 - 0.55\,\alpha)$.
In both graphs $W = T = Z = 1$ was used.

The first term in the second line constitutes the quasiparticle contribution, with the quasiparticle weight Z (cf. (4.2.2)) and an infinite lifetime for $T = 0$ at the Fermi level $\omega = 0$, and Γ is a measure for the residual interaction. The quadratic dependence of the quasiparticle damping (also called scattering amplitude) on ω as well as T, i.e. $\Gamma((\pi T)^2 + \omega^2)$, is characteristic for a Fermi liquid and deviations thereof indicate non-Fermi liquid behavior. The second term represents the incoherent backflow, which incorporates the high-energy features and can be assumed to vanish at the Fermi level, i.e. $\tilde{G}^{(inc)}(0 - i\delta) \approx 0$.

Note, that the following argument does not depend on the exact form (4.3.14) for $\tilde{G}$, as for example the scattering amplitude could be set to a constant, i.e. the quadratic dependency on ω and T could be ignored, and the results would only change quantitatively, not qualitatively.

Using the form (4.3.14) in the explicit formulas (4.3.8), (4.3.10) and (4.3.12), the imaginary parts of the effective media are plotted for different values of Γ in figure 4.12.

For the larger value of $\Gamma = 0.5$, all three cases $\alpha = 0$, 1, 2 yield a broad curve with a single maximum at $\omega = 0$. While for a small value of $\Gamma = 10^{-3}$ the effective medium for $\alpha = 2$ still has a dome-like shape with a single maximum at $\omega = 0$, the $\alpha = 0$ and 1 curves behave qualitatively different: both curves possess two maxima symmetric around $\omega = 0$ with a spiky minimum in between right at the Fermi level. Upon further decreasing Γ towards zero, the curve for $\alpha = 1$ essentially stays like it is shown, while for $\alpha = 0$ the spike keeps deepening and eventually reaches zero for $\Gamma \to 0$ (not shown in the graph).

The question arises, for which exponents α of the non-interacting DOS (4.3.2) the spiky minima at the Fermi level in the imaginary part of the effective medium can be produced. In order to find a criterion, the analytic solution for the effective medium (4.3.7) is expanded around the Fermi level[4],

$$\tilde{T}(\omega; i\Gamma; \alpha) = ia_0(\Gamma, \alpha) + a_1(\Gamma, \alpha)\,\omega + ia_2(\Gamma, \alpha)\,\omega^2 + \mathcal{O}(\omega^3) \quad . \tag{4.3.15}$$

For symmetric situations considered here, all coefficients a_n are real and lead to a purely imaginary quadratic term. A change of sign in the quadratic coefficient a_2 from negative to positive values indicates the transition from a maxima to a minima at $\omega = 0$ and thus provides the sought criterion. In the right graph of figure 4.12 that value Γ^* for the residual interaction is shown, at which the quadratic coefficient vanishes, i.e.

$$\Gamma^* : a_2(\Gamma^*, \alpha, W, T, Z) = 0 \quad . \tag{4.3.16}$$

It can be seen, that for all exponents between zero and roughly two, the quadratic coefficient vanishes for some $\Gamma^* > 0$ and consequently a minimum forms. The region of α close to two is shown in the inset and it can be seen, that for those values of α the numerical procedure to solve the transcendent equation (4.3.16) becomes unstable. Consequently the question, whether the minimum forms for all non-differentiable DOS ($\alpha < 2$) or some critical $\alpha^* < 2$ exists, cannot be answered. The functional dependence on the exponent can be roughly fit with a linear function, $\Gamma^* \approx a - b\alpha$, which indicates that the tendency to form a minimum is less pronounced for larger values of α. This seems evident from the cusps in ρ_α^{cusp}, which are also less pronounced for larger α.

So far it has been demonstrated, that under the assumption of a Fermi liquid, the cusps or logarithmic divergence at the Fermi level in the non-interacting DOS lead to a non-analytic pseudogap in the effective medium. For a non-divergent non-analytic DOS ($\alpha > 0$) the pseudogap in the effective medium is not completely formed, but only a cusp-like minimum develops. Since within the locally complete approximation, the effective medium has to be used for the effective impurity model and a SIAM with a pseudogap medium may show non-Fermi liquid behavior, the assumption of a Fermi liquid might lead to a contradiction. Therefore the influence of the self-consistency has to be examined further.

Further studies with model DOSs possessing non-analyticities at the Fermi level are shown in figure 4.13. The case indicated with (a) is the locally complete solution for the cusp-DOS with $\alpha = 1$ ($\rho_{\alpha=1}^{cusp}$) for $U = 2.5$ and at half filling $n_\sigma = 0.5$, while case (b) is for the same DOS, but different $U = 4$ and $n_\sigma = 0.485$. The cases (c) and (d) have asymmetric DOS, where the parts with negative energy $\omega < 0$ are taken to be constant and for $\omega > 0$ the DOS declines linearly (c) or like a square-root (d).

In all cases the effective medium develops a minimum for low temperatures and the correlation self-energy Σ^U concurrently shows the maximum at the same position. The spiky minima obtained in the analytic studies above are smeared out to form smooth minima due to the self-consistency. For the cases (a), (c) and (d) the structures form right at the Fermi level, thereby destroying the Fermi liquid phase. Only in case (b) the maximum in the correlations self-energy is shifted to values above the Fermi level, preserving the possibility

[4] The calculation is straightforward, but the resulting coefficients a_n are rather cumbersome and provide little insight, which is why they are not reproduced in the text.

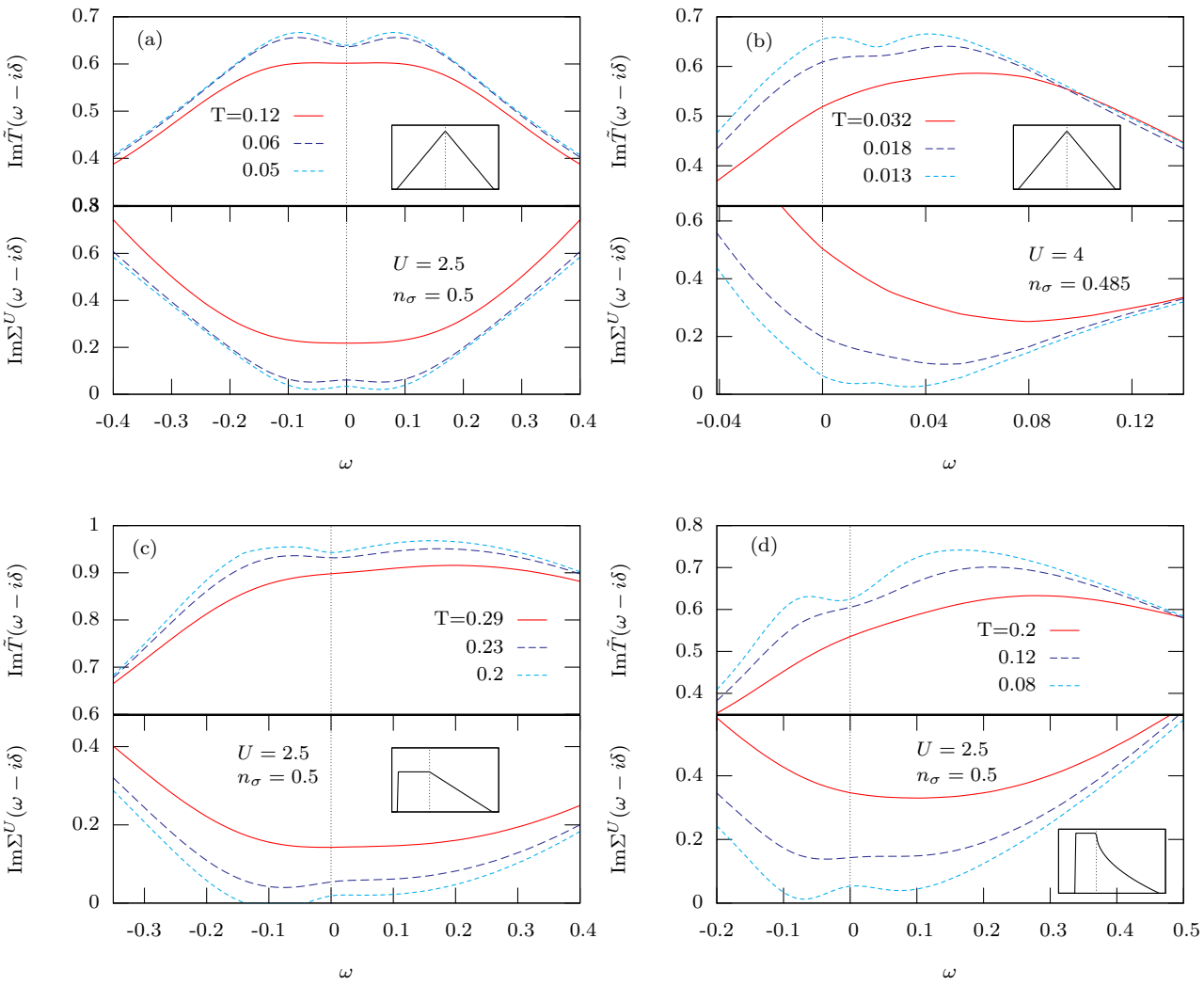

Figure 4.13: Various solutions of the Hubbard model with different model DOS as shown in the insets. The different temperatures are as indicated in the graphs and the other parameters are: (a) $U = 2.5$, $n_\sigma = 0.5$; (b) $U = 4$, $n_\sigma = 0.485$; (c) $U = 2.5$, $n_\sigma = 0.5$; (d) $U = 2.5$, $n_\sigma = 0.5$.

of a Fermi liquid formation, as the lower minimum could move to the Fermi level. But the double minimum structure would probably lead to some unusual temperature dependencies in physical quantities, depending on the height of the well between both minima.

4.3.2 Digression: pathology

In the self-energy for the lowest temperature of case (c), a pathology of the locally complete approximation with the ENCA as the impurity solver can be observed. The minimum in the imaginary part of the correlations self-energy at negative energies around $\omega \approx -0.1$ would extend to negative values of $\mathrm{Im}\Sigma^U(\omega - i\delta) < 0$. Since that would introduce numerical instabilities during the iteration procedure of the approximation, the imaginary part is set to something small but finite, e.g. 10^{-8}, leaving the flat piece from -0.15 to -0.05 observable

in the curve. Negative values of the imaginary part are certainly unphysical as this implies a violation of causality.

The reason for the pathology is found in the overestimation of the DOS at the Fermi level through the ENCA. As described in section 3.4, the ENCA fails to produce the exact zero temperature limit of the height of the Kondo resonance and exceeds the limiting value for very low temperatures. Within the locally complete approximation, this tendency can have dramatic consequences, since the correlation energy is obtained as a subtraction of the effective medium from the inverted local Green function, cf. (2.2.16)-(2.2.19) along with (2.2.21). At energies where $\mathrm{Im}\Sigma^U$ becomes small, e.g. around the Fermi level when approaching a Fermi liquid state, the subtraction can produce unphysical sign changes, whenever the Green function slightly overestimates the Kondo resonance.

As described in section 3.4, the overestimation of the height of the Kondo resonance through the ENCA is worse, in situations where the effective hybridization is large. Since in the locally complete approximation the effective medium has a shape similar to the one-particle Green function, the hybridization strength at the Fermi level is strongly dependent on the chosen parameters value. Depending on temperature T, filling n_σ, lattice type, ..., the pathology occurs sooner, whenever the self-consistently determined effective medium is larger at the Fermi level. This pathology represents the physical limit for the applicability of the ENCA impurity solver within the locally complete approximation and cannot be circumvented by other means as to extend the ENCA.

4.3.3 Cubic lattices

After having explored the non-Fermi liquid properties of some model DOS, it is interesting to study real lattices with similar features. Almost all of the cubic DOS have noticeable van Hove singularities in not too large space dimensions, typically logarithmically divergences or square-root like cusps. For an overview and examples consult appendix D.

Figure 4.14 shows the different solutions for $\tilde{T}$ (upper rows) and Σ^U (lower rows) of the Hubbard model for various cubic lattices in different space dimensions. The non-interacting DOS, which are also plotted in the insets of each graph, their parameter values and the positions of their van Hove singularities are best describe in the following list:

(a) Simple-cubic lattice with nearest neighbor hopping in two space dimensions (2d-SC). This DOS has a logarithmic divergence in the band center.

(b) Simple-cubic lattice with nearest and next-nearest neighbor hopping ($t'/t = -0.2$) in two space dimensions (2d-SCNNN). This DOS has a logarithmic divergence at $\omega = -0.4$.

(c)+(d) Body-centered cubic lattice with nearest neighbor hopping in three space dimensions (3d-BCC). This DOS has a logarithmic divergence in the band center.

(e) Face-centered cubic lattice with nearest neighbor hopping in three space dimensions (3d-FCC). This DOS has a logarithmic divergence at $\omega = -2$ and a square-root van Hove singularity at $\omega = 0$.

(f) Simple-cubic lattice with nearest and next-nearest neighbor hopping ($t'/t = -0.46$) in three space dimensions (3d-SCNNN). This DOS has square-root van Hove singularities at $\omega \approx -1$, -0.82, -0.24 and 0.08.

It can be clearly seen in the graphs, that all effective media develop the minimum in the immediate vicinity or right at the Fermi level for low temperatures, except for case (f). In case (b), where the logarithmic divergence is not situated at the Fermi level but at $\omega \approx -0.4$, the minimum in $\mathrm{Im}\tilde{T}$ is shifted to energies slightly below zero. For the three dimensional simple cubic lattice with considerable next-nearest neighbor hopping (f), the medium develops a very steep edge right at the Fermi level rather than a minimum.

All correlation self-energies show rather unusual behavior. In the cases (a), (b), (c) and (e) a maximum is developed at or near the Fermi level, as it is expected from the model-DOS studies of figure 4.13. For the asymmetric case (b), where the singularity is moved to lower energies, the maximum is also moved away from the Fermi level. For case (e), which represents also an asymmetric situation but the non-analyticity is still situated at the Fermi level, the maximum in $\mathrm{Im}\Sigma^U$ is also found at $\omega = 0$, but the two minima next to it are asymmetric. In the 3d-BCC lattice with larger Coulomb repulsion, case (d), the formation of the maximum is not clearly visible and might be suppressed in favor of a linearly rather than quadratic dependence of the imaginary part around the Fermi level. The tendency to increase linearly away from the Fermi level can also be observed for the smaller value of $U = 2.75$ in case (c). For the 3d-SCNNN shown in part (f) a quadratic minimum is found in $\mathrm{Im}\Sigma^U$ around the Fermi level, but it is formed very asymmetric and remains so to very low temperatures, as it can be seen in the upper right inset. The increase in $\mathrm{Im}\Sigma^U(\omega - i\delta)$ from $\omega = 0$ to negative energies is considerably slower and less steep than from zero to positive ω. For very low temperatures (inset) a quadratic fit to the minimum can be justified only up to energies of the size of the temperature, e.g. $|\omega - \omega_{min}| \approx T$. The question whether the quadratic dependence remains as $T \to 0$ or if it is replaced by an asymmetric functional dependence cannot be answered with this approach and thus remains unanswered.

While for the situations (a), (c) and (d) the destruction of the Fermi liquid is directly observable, Fermi liquid ground states might still be possible for cases (b), (e) and (f). However, even if the Fermi liquid turns out to be stable in the latter cases, the finite temperature behavior is nonetheless expected to be rather peculiar, e.g. non-Fermi liquid like, due to the strong renormalizations and unusual energy dependencies of $\mathrm{Im}\Sigma^U$ in the vicinity of the Fermi level.

As it should be clear from the studies shown so far, the key ingredient for the suppression of the Fermi liquid formation is the non-analyticity in the non-interacting DOS at or near the Fermi level.

In order to understand the encountered behavior, notice that the origin of the van Hove singularities are flat parts in the dispersion relation. As examples, figure 4.15 shows the dispersion relations for the 2d-SC (left graph) and the 3d-FCC (right graph) lattice. The corresponding points in the Fermi surface leading to the van Hove singularities at $\omega = 0$ for half filling are for example $\underline{k} = (0, \pm\pi)^T$ (2d-SC) and $\underline{k} = (\pm\pi/2, \pm\pi/2, 3\pi/2)^T$ (3d-FCC). As it can be seen from the figures, all these points are associated with saddle points in the dispersion.

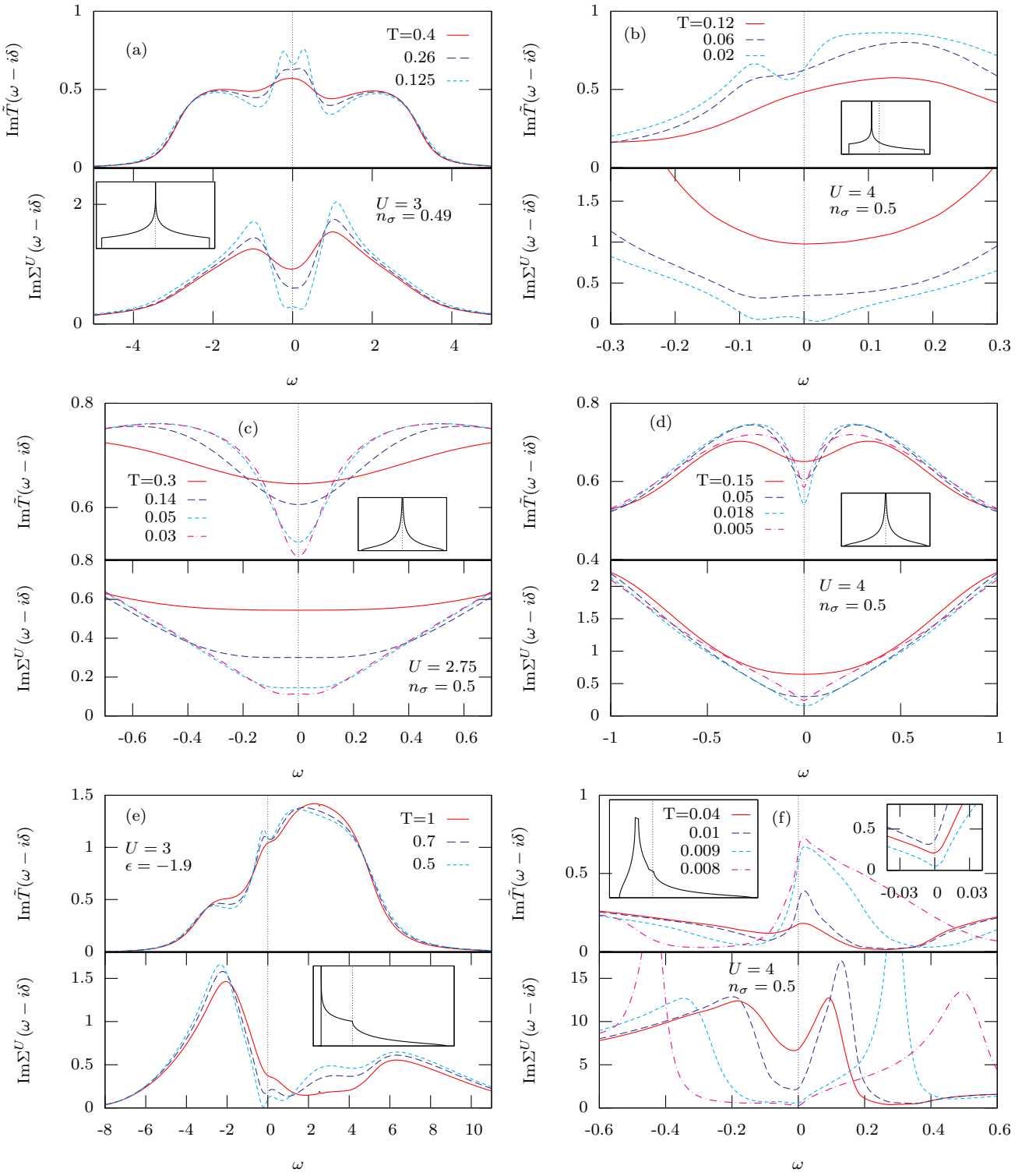

Figure 4.14: The effective medium (upper graphs) and correlation self-energy (lower graphs) of the Hubbard for different cubic lattices. The non-interacting DOS are shown in the insets. The parameter sets are: (a) 2d-SC, $U = 3$, $n_\sigma = 0.49$; (b) 2d-SCNNN $t'/t = -0.2$, $U = 4$, $n_\sigma = 0.5$; (c) 3d-BCC, $U = 2.75$, $n_\sigma = 0.5$; (d) 3d-BCC, $U = 4$, $n_\sigma = 0.5$; (e) 3d-FCC $U = 3$, $\epsilon = -1.9$; (f) 3d-SCNNN $U = 4$, $t'/t = -0.46$, $n_\sigma = 0.5$ and the temperatures as indicated. The right inset in figure (f) shows $\mathrm{Im}\Sigma^U$ in the low energy region for even lower temperatures $T = 0.007$, 0.006 and 0.004.

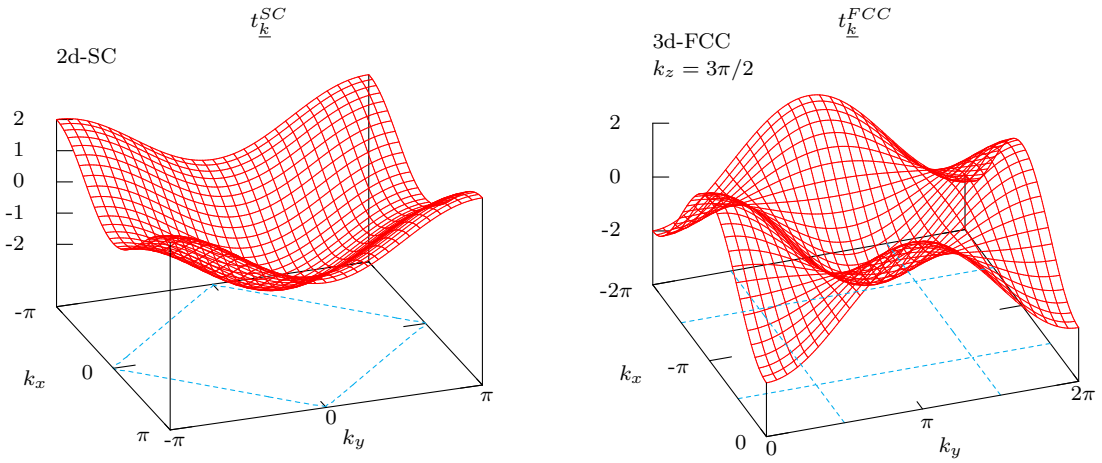

Figure 4.15: The dispersion relation for the 2d-SC (left) and 3d-FCC (right) lattice. In the latter case the z-component set to $3\pi/2$ and only one quadrant is shown for clarity. The lines on the bottom of each graph indicate the position of the Fermi surface for half filling.

If these saddle points occur right at the Fermi surface, which is the case at half filling for these two examples, the dispersion relation cannot be approximated by a linear function around the Fermi surface, i.e.

$$t_{\underline{k}} \not\approx \frac{k_F}{m^*}|\Delta\underline{k}| \quad , \tag{4.3.17}$$

with $\Delta\underline{k} = \underline{k} - \underline{k}_F$ and $\underline{k}_F$ a Fermi wave vector. The expansion around these points rather yield hyperbolic functional dependencies

$$t_{\underline{k}} \sim \begin{cases} \Delta k_x^2 - \Delta k_y^2 & 2\mathrm{d} - \mathrm{SC} \\ \Delta k_x \, \Delta k_y & 3\mathrm{d} - \mathrm{FCC} \end{cases} . \tag{4.3.18}$$

Therefore the usual argument leading to a quadratic dependence of the scattering amplitude on energy and temperature, i.e. $\mathrm{Im}\Sigma^U(\omega - i\delta) \propto \omega^2 + \pi^2 T^2$, is not applicable at these special $\underline{k}$-points. Instead the quadratic momentum dependence leads to an enhancement of low energy excitations due to the very small energy denominators, and consequently an enhanced scattering. Averaged over the whole Fermi surface in order to obtain the full (local) scattering amplitude, an energy and temperature independent additional constant contributed from these points seems possible.

The physical origin of the increased scattering could either be the removal of certain band states from the vicinity of the Fermi surface, i.e. the formation of a band gap, or a partial localization of those electrons. The difference between these two scenarios cannot be directly resolved on the basis of one-particle properties. Even though only the calculation of the conductivity or the resistivity could directly reveal the nature of the situation encountered

here, an indirect argument can be provided nonetheless. The spectral intensities of the effective media for all situations are reduced, when the increased scattering is encountered. Since the effective medium characterizes the hybridization amplitude of a local lattice site, this indicates decreased hopping to neighboring sites within this energy interval. The reason can either be a a reduced mobility of the electrons (localization) or the lack of states within that energy region at the surrounding sites (band gap). In first order, the number of states available on the surrounding sites is given by the local density of states of these sites, i.e. the local one-particle DOS. The latter function does not show any sign of a (pseudo) gap formation, which could be taken as a sign of some sort of localization taking place.

However, at this point care has to be taken, since the present approximation only accounts for momentum independent self-energies and effective media. Theses quantities represent momentum averages over iso-energy surfaces of the whole Brillouin zone. Thus details of possible band gaps developing only in some points of the Brillouin zone are averaged and maybe even smeared out. Therefore a band gap might still be there, but just not visible in the local DOS.

The physical picture of the scenario leading to the breakdown or at least strong modification of the Fermi liquid can be summarized: at high temperatures, thermal fluctuations are large and the details and flat parts of the Fermi surface are not noticeable. In that case, the system behaves regular and the tendency of the spin-$\frac{1}{2}$ SIAM to form a local Fermi liquid dominates. Lowering the temperature leads to an increased screening of the developing local moments and the band states can be mixed coherently to form the low energy Fermi liquid, i.e. the quasiparticles start to emerge. This is observed in the graphs, as the quadratic minimum in the self-energy and the new quasiparticle band around the Fermi level are formed, which both become more pronounced for lower temperatures. Since the self-energy is momentum independent, the quasiparticles attain the same Fermi surface as in the non-interacting case [MH89b]. Upon further lowering the temperature, the flat parts of the Fermi surface become influential and lead to a large scattering amplitude for the quasiparticles and the Fermi liquid formation is disturbed.

The physical origin of the increased scattering is speculated to be a consequence of a partial localization of the quasiparticles at the flat points on the Fermi surface. In order to bring more light into this subject, the calculation of the conductivity and approximations involving momentum dependent self-energies are desirable.

4.3.4 Relevance for the investigation of pseudogap behavior

The behavior encountered in the foregoing paragraphs has some bearings on the investigations of pseudogap and related phenomena in cuprate superconductors.

As already stated, the local DOS corresponding to the calculations presented in figures 4.13 and 4.14 do not show any pseudogap, i.e. a diminishing of the spectral weight in the many-body resonance at or near the Fermi level, even though they can be quite deformed. However, features similar to those encountered in pseudogap systems can be observed in the $\underline{k}$-resolved band structures (e.g. 4.10), since the quasiparticle peaks right at the Fermi surface are suppressed. Therefore it seems beneficial to study the circumstances under which such a behavior could occur.

Within the locally complete approximation, pseudogap behavior can only be introduced via Σ^U. The local Green function is given by

$$G^{(loc)}(z) = \frac{1}{N_0} \sum_{\underline{k}} \frac{1}{z - \Sigma^U(z) - t_{\underline{k}}} = \int dx \, \frac{\rho^0(x)}{z - \Sigma^U(z) - x} \tag{4.3.19}$$

$$= G^{U=0}(z - \Sigma^U(z)) \tag{4.3.20}$$

and is thus completely determined by the functional form of the non-interacting Green function, but evaluated for arguments in the complex plane at $\xi = z - \Sigma^U(z)$. This implies for a Fermi liquid at $T = 0$, where the imaginary part of the self-energy vanishes at the Fermi level $\mathrm{Im}\xi = 0$, that the interacting DOS at $\omega = 0$ is given by the value of the non-interacting one[5]. From this it is obvious, that a maximum growing in an otherwise small $\mathrm{Im}\Sigma^U$ at the Fermi level indeed indicates a tendency to produce a pseudogap in the local DOS.

Pseudogap behavior is found and studied in the two dimensional Hubbard and tJ models. The key ingredient to capture these effects is believed to be the inclusion of non-local correlations into the approximation. Therefore these models are usually studied with the help of more advanced techniques, such as cluster extensions of the locally complete approximation [Mai05, Mac06b] or by explicitly accounting for non-local fluctuations [Vil97, Hau03, Sad05]. The occurrence of pseudogaps and the suppression of coherent quasiparticle formation for some parts of the Fermi surface, both effects are found within these calculations, are attributed to the presence of strong antiferromagnetic spin fluctuations. The self-energy, which is momentum dependent in these approximations, indicates a strongly enhanced scattering for some wave vectors, due to the presence of spin fluctuations.

It is very tempting to view the findings described in this study as precursors to the characteristic spin-fluctuation induced pseudogap behavior. One could argue, that due to the assumption of a local self-energy in the locally complete approximation, the non-local spin fluctuations are included only in a mean-field manner and the details of the $\underline{k}$-dependence of the self-energy are averaged to yield a mean effect. The remnants of the pseudogap physics is then only seen in the slight maximum of $\mathrm{Im}\Sigma^U$, which results from the average over the whole Fermi surface, but the effects are too much smeared out and less pronounced to leave any trace in the local DOS.

However, this is not in accord with the explanation presented here. The argument for the increased scattering rate of the quasiparticles did solely rely on the non-analytic structure of the non-interacting DOS and the concomitant flat parts of the Fermi surface! This is sufficient to violate some basic assumptions of a Fermi liquid description, leading to an increased scattering amplitude at some points in the Brillouin zone.

It could be certainly suspected, that both scenarios might be connected, since the flat parts of the Fermi surface in the 2d-SC and 3d-BCC lattice, which are responsible for the van Hove singularities, also cause a strongly enhanced AFM magnetic susceptibility, indicating the presence of strong AFM fluctuations. But the enhanced magnetic susceptibility in both these lattices results from (perfect) nesting with an antiferromagnetic nesting vector.

[5] Notice, this would imply a diverging DOS for the Fermi liquid state at half-filling in the 2d-SC and 3d-BCC lattices! Since this contradicts the assumption of analyticity of the Fermi liquid, the breakdown of the latter can already be anticipated.

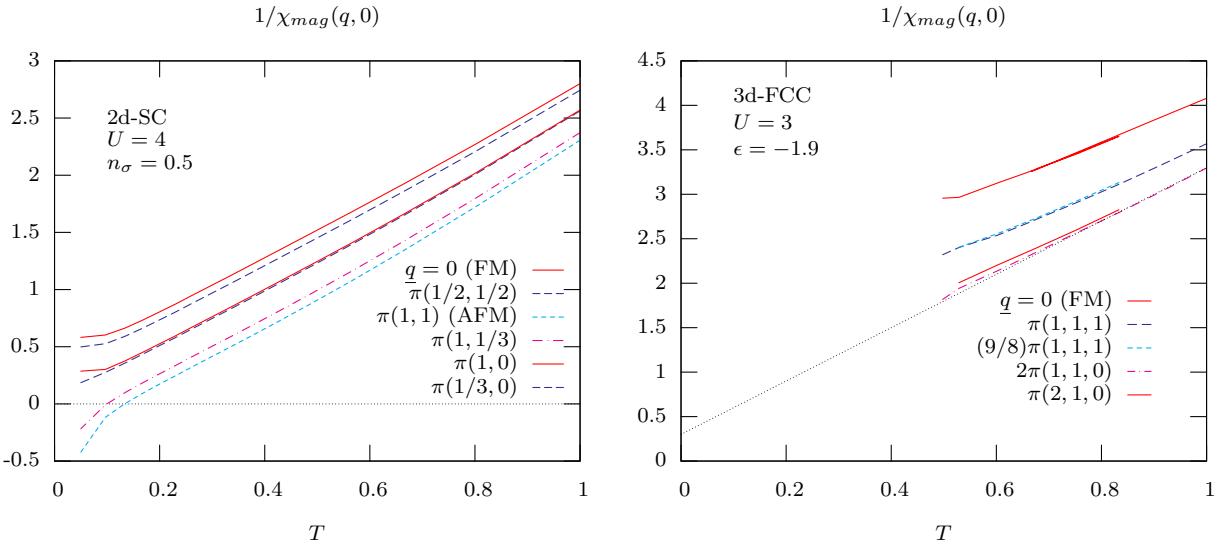

Figure 4.16: The inverse static magnetic susceptibility for the 2d-SC lattice for $U = 4$, $n_\sigma = 0.5$ (left graph) and the 3d-FCC lattice for $U = 3$, $\epsilon = -1.9$ (right graph) as functions of temperature. The different curves correspond to various $\underline{q}$-modes as indicated. The dashed grey line in the right graph is the linear extrapolation $3(T + 0.1)$.

Such nesting is for example lacking in the 3d-FCC lattices and the presence of strong spin fluctuations is therefore questionable in this case.

To examine this issue, the magnetic susceptibility is calculated and shown in figure 4.16. The graphs show the temperature dependency of the inverse susceptibility $\frac{1}{\chi_{mag}(\underline{q},0)}$ for some selected wave vectors on the 2d-SC (left graph) and 3d-FCC (right graph) lattice. Lowering the temperature indeed strongly enhances the susceptibility in the 2d-SC case and even leads to a phase transition at $T \approx 0.14$. The $\underline{q} = (\pi,\pi)^T$-component of the susceptibility is always largest, and thus diverges at the highest temperature, indicating the AFM instability. In this case, enhanced AFM fluctuations are indeed present in the system and might play a role in the destruction of the Fermi liquid. However, even though the magnetic susceptibility of the 3d-FCC lattice is also increasing with lower temperatures, the absolute value is by far lower than in the 2d-SC case. The extrapolation[6] of the curves to lower temperatures even indicates the absence of a transition to an ordered state, since the critical temperature for the transition comes out to be below zero (dashed grey line). Consequently, the magnetic fluctuations are considerably less and cannot be the cause of the observed strong anomalies, especially at the temperatures where the latter occur.

An argument usually presented in favor of a AFM spin-fluctuation driven pseudogap is, that introducing geometric frustration into the system by means of next-nearest neighbor hopping, suppresses AFM fluctuations and consequently leads to a vanishing of the pseudogap, which is indeed observed. However, the effects described above may lead to the same qualitative behavior: frustration changes the non-interacting DOS ρ^0 and moves the non-analyticity in ρ^0 away from the Fermi level (either to higher or lower energies, depending

[6] Data points below temperatures of about $T \leq 0.5$ could not be obtained due to the pathology described in section 4.3.2.

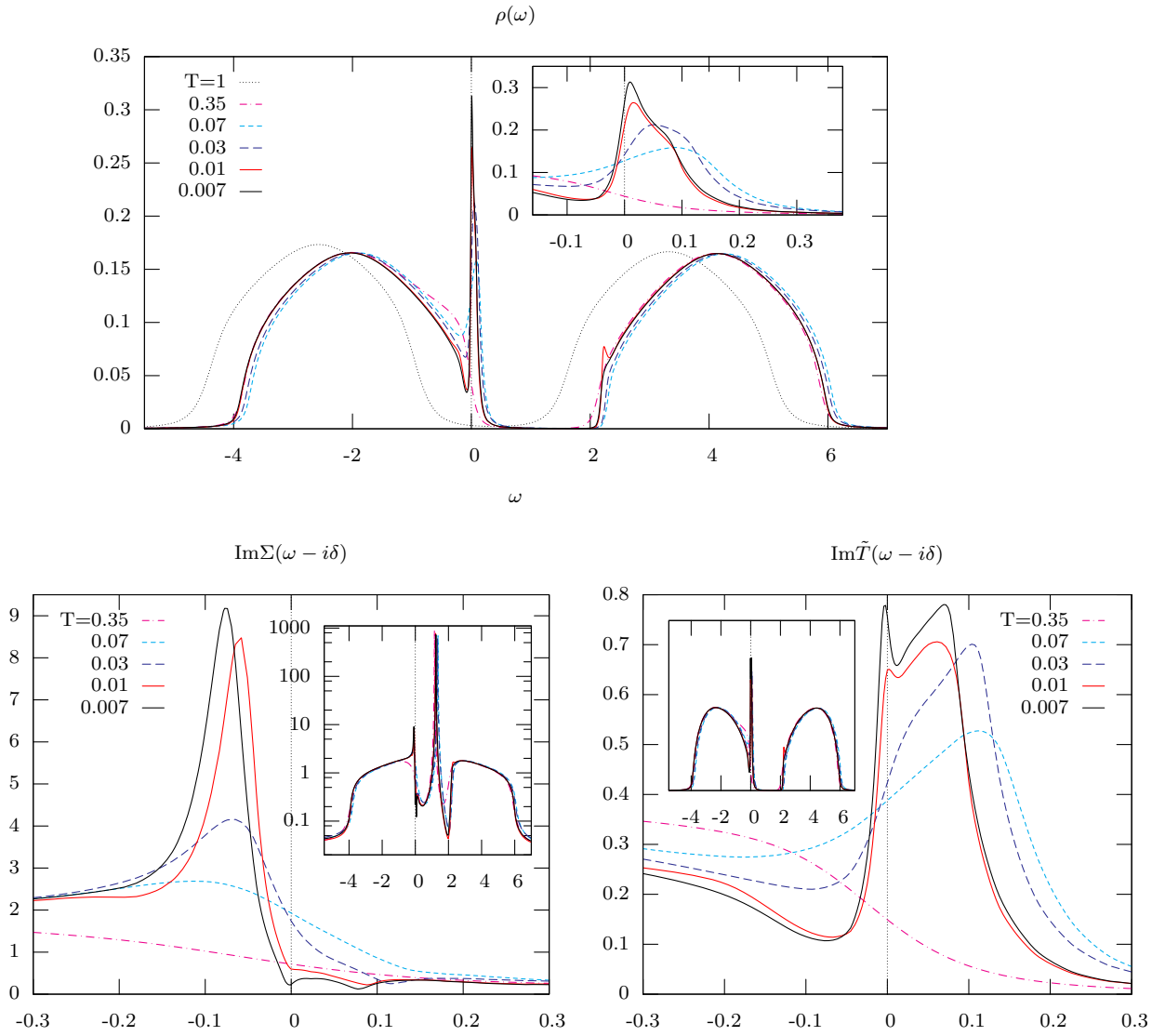

Figure 4.17: Local DOS (upper graph), correlation self-energy (lower left) and effective medium (lower tight) for the asymmetric Hubbard model on a 2d-SC lattice with $U = 6$ and filling $n_\sigma = 0.49$ for various temperatures. The insets show the low energy (local DOS) and high energy (self-energy and medium) region.

on the sign of the next-nearest neighbor matrix element), as it can be seen in graph (b) of 4.14 or in appendix D. Consequently, the quasiparticle band structure is now disturbed at energies off the Fermi surface and the maximum in $\mathrm{Im}\Sigma^U$ is shifted to finite energies. The low energy excitations at the Fermi level do not have to respond to non-analyticities at low temperatures and thus, with increased frustration, the Fermi liquid ground state becomes stable again.

The same characteristic behavior can also be observed, if the unfrustrated lattice is doped away from half filling. There, the same reasoning applies as in the frustrated case. The flat parts of the iso-energy surface are shifted away from zero energy and consequently, the Fermi

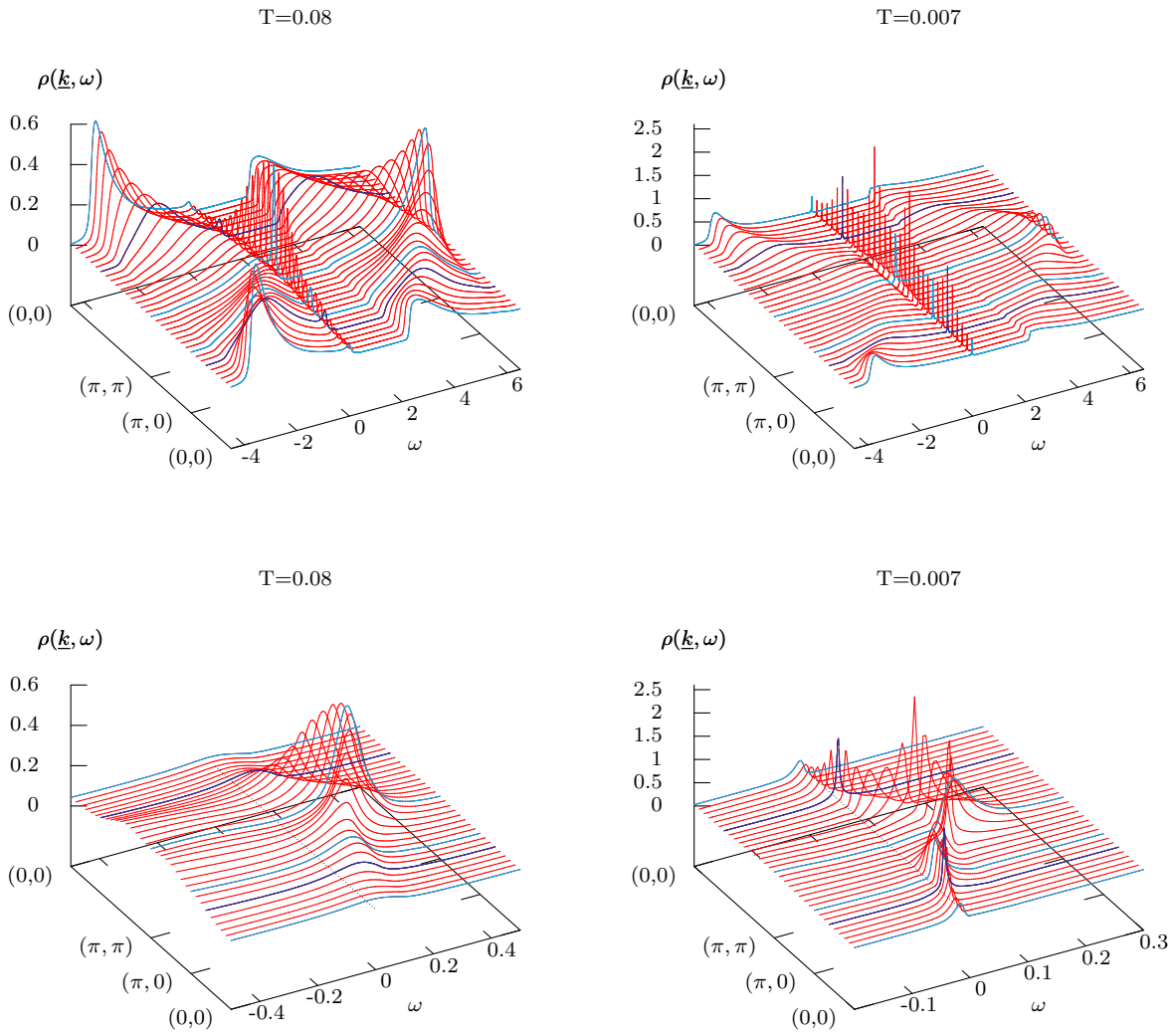

Figure 4.18: Band structure for the asymmetric Hubbard model on a 2d-SC lattice with $U = 6$ and filling $n_\sigma = 0.49$ for two low temperatures. The upper row shows the complete energy region, while the lower row show the low energy region around the Fermi level. The turquoise lines mark the special $\underline{k}$ vectors as indicated on the axis, while the blue lines mark the approximate position of the Fermi wave-vectors $\underline{k}_F$.

surface becomes regular. The van Hove singularity, and correspondingly the maximum in $\mathrm{Im}\Sigma^U$ is also shifted to finite energy and the formation of a Fermi liquid becomes possible again. This is the case for the 2d-SC lattice at filling $n_\sigma = 0.49$ and $U = 6$ as it is shown in figure 4.17. The upper graph of figure 4.17 shows the local spectral function with the lower and upper Hubbard bands[7] and the many-body resonance at the Fermi level. The inset shows the latter for an enlarged interval around $\omega = 0$. In can be seen, that while

[7] The origin of the sharp spike in the local DOS at the lower edge of the upper Hubbard band for $T = 0.1$ is not clear yet. Within the numerical simulations, it behaves in a meta-stable manner, as it is not consistently observed for lower temperatures. It has been speculated, that it results from a bound state

lowering the temperature the resonance becomes more pronounced, at $T \approx 0.03$ starts to deform indicating the disruption of the Fermi liquid formation and then a new low energy peak emerges right above the Fermi level due to the recurring formation of the Fermi liquid. The resulting form of the resonance is quite asymmetric with a hunch at $\omega \leq 0.1$.

The imaginary part of the self-energy is shown in the lower left graph of the figure. The Fermi liquid minimum at the Fermi level and the increased scattering amplitude around $\omega \approx 0.03$ can be clearly seen. The accompanying minimum in the effective medium shows right above the Fermi level and for both quantities, the insets show the high energy interval for completeness.

The scenario is further supported by the band structure $\rho(\underline{k}, \omega)$ shown in figure 4.18. For the higher temperature $T = 0.08$ the system looks like a developing Fermi liquid with the quasiparticle band forming slightly above the Fermi surface (left column). But at the lower temperature $T = 0.007$, the quasiparticles at the flat parts of the Fermi surface $\omega \approx 0.03$ are suppressed, while at the Fermi level the formation goes undisturbed, which is best seen in the low energy section shown in the lower row.

The finite temperature properties of this situation are expected to be rather unusual due to the pronounce asymmetry in the self-energy and the second minimum at finite energies.

Undoubtfully, non-local correlations do play an important role in the physics of the two dimensional Hubbard model and for the understanding of materials showing unconventional superconductivity, such as the cuprates. But the scenario described in this work certainly opens an additional route to the destruction of the Fermi liquid ground state and the unusual finite temperature properties, such as a linear temperature dependence of the resistivity. The origin of this behavior is similar to the anomalies found in nested Fermi liquid systems [Vir90, Sch99b, Sch05]. But the major difference is, that no nesting properties of the Fermi surface are necessary and only flat parts, i.e. van Hove singularities, need to exist to lead to a possible breakdown of the Fermi liquid description.

Certainly, in the situations of lattices with nesting considered here, such as the SC and BCC lattices at half-filling, the enhanced fluctuations support the effect and both scenarios mix. But since in the locally complete approximation the detailed momentum dependence of the fluctuations are not respected and only treated in a mean-field manner, the effect of fluctuations, and especially their momentum dependence, is averaged and not as strong.

In order to discriminate more clearly between the effects of non-local fluctuations and pure Fermi surface effects proposed in this work, approximation schemes which respect the $\underline{k}$ dependence of the self-energy would be helpful. The average over the Fermi surface would be circumvented and the regions of the Fermi surface could be studied in detail in lattices with both nesting and only flat parts at the Fermi surface.

4.4 Susceptibilities and magnetism in the Hubbard model

4.4.1 Sketch of the phase diagram

Before explicit calculations for the magnetic properties of the Hubbard model are presented, it is instructive to get an overview on the expected and already encountered phases.

of a quasiparticle and an immobile collective mode, possibly of polaronic nature [Kar05, Kar08], but will not be discussed further in this work.

Magnetism depends strongly on the lattice structure and the number of electrons per lattice site (filling). For instance, in theories for the magnetism of localized magnetic moments, such as the Heisenberg model, the arrangement and coupling of the spins on some lattice is essential and geometric frustration has the effect of suppressing order. On the other hand, for metals the geometry of the hopping matrix elements t_{ij}, i.e. the resulting band structure $t_{\underline{k}} = \frac{1}{N_0} \sum_{ij} e^{i\underline{k}(\underline{R}_i - \underline{R}_j)} t_{ij}$, and the Fermi surface play a crucial role.

If large, almost parallel regions of the Fermi surface with the appropriate electron- and hole-like character exist, a very large phase space volume for magnetic scattering processes at the Fermi surface results and an enhanced magnetic susceptibility is the consequence. This is known as *(perfect) nesting* and the finite wave vector $\underline{q}_0$ for which it occurs is known as the *nesting vector*, i.e.

$$t_{\underline{k}+\underline{q}_0} \approx t_{\underline{k}} \tag{4.4.1}$$

for many $\underline{k}$ on the Fermi surface. This is the case for the simple cubic and body centered cubic lattices with nearest neighbor hopping at half filling[8].

As another point, the interplay and competition between strong correlations and the kinetic energy are believed to be the causes for itinerant ferromagnetism (FM) in transition metals. FM is thus very sensitive to the filling and the lattice structure, i.e. the distribution of spectral weight in non-interacting DOS.

As a starting point for the investigation, it is worthwhile to consider the Hubbard model on the three dimensional simple cubic (3d-SC) lattice. The SC lattice exhibits perfect nesting in any space dimension d for the antiferromagnetic (AFM) nesting vector, $\underline{q}_{AFM} = \pi(1,1,1)^T$ for $d = 3$, which leads to the presence of strong AFM spin fluctuations. Within a weak coupling ($U/t \ll 1$) Stoner (RPA) treatment a diverging static susceptibility for the AFM wave vector $\underline{q}_{AFM}$ and thus a AFM phase transition is found with the critical Néel temperature at half filling (cf. [Pen66, Hir87, Faz99])

$$T_N^{RPA} = 1.13 W e^{-\frac{1}{\rho^0(0)\,U}} \quad , \tag{4.4.2}$$

where $\rho^0(0)$ is the non-interacting tight-binding DOS at the Fermi level and $W = 2dt = 3$ the half bandwidth. The characteristic t[9] and U dependence of this result remains true for the SC lattice in any spacial dimension except for $d = 2$ where the logarithmic divergence of the non-interacting DOS at the Fermi level leads to a additional square root in the exponent[10], i.e.

$$T_N^{RPA}(d=2) \sim W e^{-\sqrt{\frac{t}{U}}}. \tag{4.4.3}$$

The AFM transition occurs at half-filling for any non-zero value of the Coulomb repulsion $U > 0$, which is a drastic consequence of the perfect nesting property of the SC lattices.

The AFM phase transition is also present for fillings away from half filling $n_\sigma \neq \frac{1}{2}$ up to a critical value of doping which at zero temperature $T = 0$ can be deduced within the weak coupling approximation

$$\delta_C^{RPA} = 1 - 2n_\sigma \sim \frac{1}{U}\, e^{-\frac{1}{\rho^0(0)\,U}} \quad . \tag{4.4.4}$$

[8] For details on some lattice structures see appendix D.
[9] Remember $\rho^0(0) \sim 1/t$.
[10] The same is true for the three dimensional body centered cubic lattice.

In the opposite strong coupling limit ($U/t \gg 1$) and for half filling $\delta = 0$, the critical Néel temperature can be calculated from the high-temperature expansion for the antiferromagnetic Heisenberg model [Rus74] with the appropriate coupling (see (4.2.7) and (4.2.8)),

$$T_N^{strong} = 3.83 \, \frac{t^2}{U} \quad . \tag{4.4.5}$$

As it can be already anticipated by the presence of an AFM exchange coupling for the large U limit in (4.2.7), AFM is expected to be a robust phenomenon for the Hubbard model. In situations, where additional next-nearest neighbor hopping amplitudes t' are introduced, the perfect nesting property of the SC lattice is lost and the AFM region is expected to shrink [San93, Ari00, Zit04b, Pru05]. Only in situations, where t' is very large or on lattices with geometric frustration and without any sort of nesting, AFM is expected to vanish [Ulm98, Mer06, Kyu07].

At intermediate to large U ferromagnetism is expected away from half filling[Pen66, Bul90, Her97, Faz99]. In contrast to the robust occurrence of AFM, ferromagnetism is a very subtle phenomenon in the Hubbard model. A rigorous proof for fully polarized FM in the Hubbard model at $U = \infty$ for various cubic lattices and a filling of one electron plus or minus half filling was presented by Nagaoka [Nag65, Nag66] (for a more general treatment see [Faz99, Han96, Han97]). The necessary restrictions on the lattice structure, signs of the hopping matrix elements and doping already suggests that FM is found in the Hubbard model only for very specific situations.

Quite generally, the conditions favoring FM in single-band Hubbard models include low densities [MH95, Pie96], situations where the Fermi level lies inside a flat part of a band or generally a flat band near one band edge resulting in a sharp structure in the non-interacting DOS [Tas92, Mie93, Obe97, Wah98, Ulm98, Vol99, Faz99, Ari00, Mer06, Pan07].

The common feature of all these scenarios is that the kinetic energy and especially its balance with the interaction energy is the key quantity deciding whether a tendency towards FM is developed or not. For certain band structures it could be beneficial to put electrons with the minority spin in higher energy band states and thereby avoid interactions in the majority band through the symmetry correlations, leading to a FM ground state with an essential weakly interacting band of majority spins. Or the quantum mechanical interference of hopping processes for electrons or holes on certain paths through the lattice produce effectively exchange interactions favoring FM, as it is found for the Nagaoka-type FM and e.g. three-site ring exchange processes on some special non-bipartite lattices [Pen96, Tas98a].

For intermediate values of the Coulomb repulsion U a transition from the antiferromagnetism of a weakly interacting electronic band to the phase of localized spins is expected at half filling. The transition temperature is thus an interpolation between the asymptotic forms (4.4.3) and (4.4.5) [Jar93, Dar00]. For systems off half filling antiferromagnetism is expected to extend to some value of doping, maybe transforming into some sort of incommensurate (IC) magnetism before disappearing altogether [Pen66, Fre95, TZ97]. This is expected since for increasing doping $\delta \neq 0$, the system is always metallic and particle-hole excitations are gradually suppressed due to the deviation from perfect nesting of the Fermi surface, but possibly other approximate nesting vectors appear. Additionally, several forms of a phase separated ground state are expected for large U and away from half filling [Vis74, Eme90, Zit02, Pru03, Mac06a]

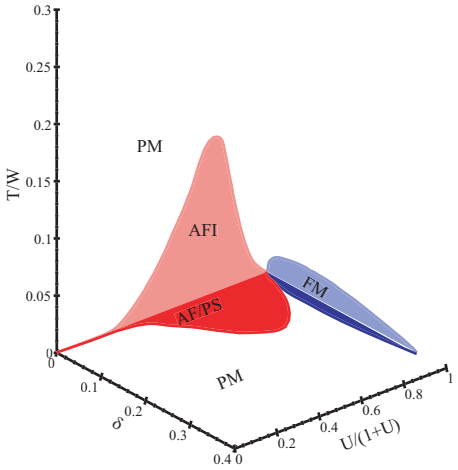

Figure 4.19: Schematic phase diagram of the single band Hubbard model on the simple cubic lattice with nearest neighbor hopping within the locally complete approximation taken from [Pru03]. PM denotes the paramagnetic metal, AFI the antiferromagnetic insulator, AF/PS the phase-separated antiferromagnetism and FM ferromagnetism. Note that in this picture W is chosen as the full bandwidth, while in the present work it is defined as the half bandwidth.

As a summary of the above remarks, a schematic phase diagram is shown in figure 4.19. The diagram portrays the situation for the Hubbard model on the simple cubic lattice. As argued, at the edges of the AF/PS phase incommensurate magnetism is generally expected. The regions of the various phases are enlarged or shrunk depending on the specific lattice structure and frustration.

Of special importance for the latter considerations is the different nature of the magnetism in various parts of the phase diagram. As it was already mentioned, at small Coulomb interactions the itinerant Stoner-type magnetism is encountered. Magnetic ordering is produced by an enlarged scattering for particle-hole pairs at the Fermi surface. At large U and at (or very close to) half filling large local magnetic moments are present and the electrons are almost localized. The systems thus consists of localized spins and Heisenberg-type local moment magnetism is encountered. In situations with intermediate interaction strength and close to half filling or for very large U and off half filling, considerable magnetic moments are formed, but the system is still metallic. These cases correspond to a correlated metal where both of the above archetypes mix and the details of the lattice might be essential.

4.4.2 Magnetic excitations in the Hubbard model

Results for the inverse static susceptibility calculated according to equation (2.3.42) are shown for three different sets of parameters in figure 4.20. The left graphs show some selected $\underline{q}$ modes as functions of temperature, while the right graphs show the $\underline{q}$ dependence for several temperatures and the wave vectors chosen as indicated.

In the situations shown in the upper two rows of figure 4.20 with $U = 4.5$, $n_\sigma = 0.5$ and $U = 6$, $n_\sigma = 0.48$ the temperature dependent susceptibilities follow an approximately linear curve, i.e. $\chi_{mag} \sim \frac{1}{(T - T_C(\underline{q}))^\gamma}$ with $\gamma = 1$. The $\underline{q}$ dependent critical temperature $T_C(\underline{q})$ is highest for the AFM wave vector $\underline{q}_{AFM}$, so that the system undergoes a second order phase transition to an antiferromagnetically ordered state. For the third case shown with

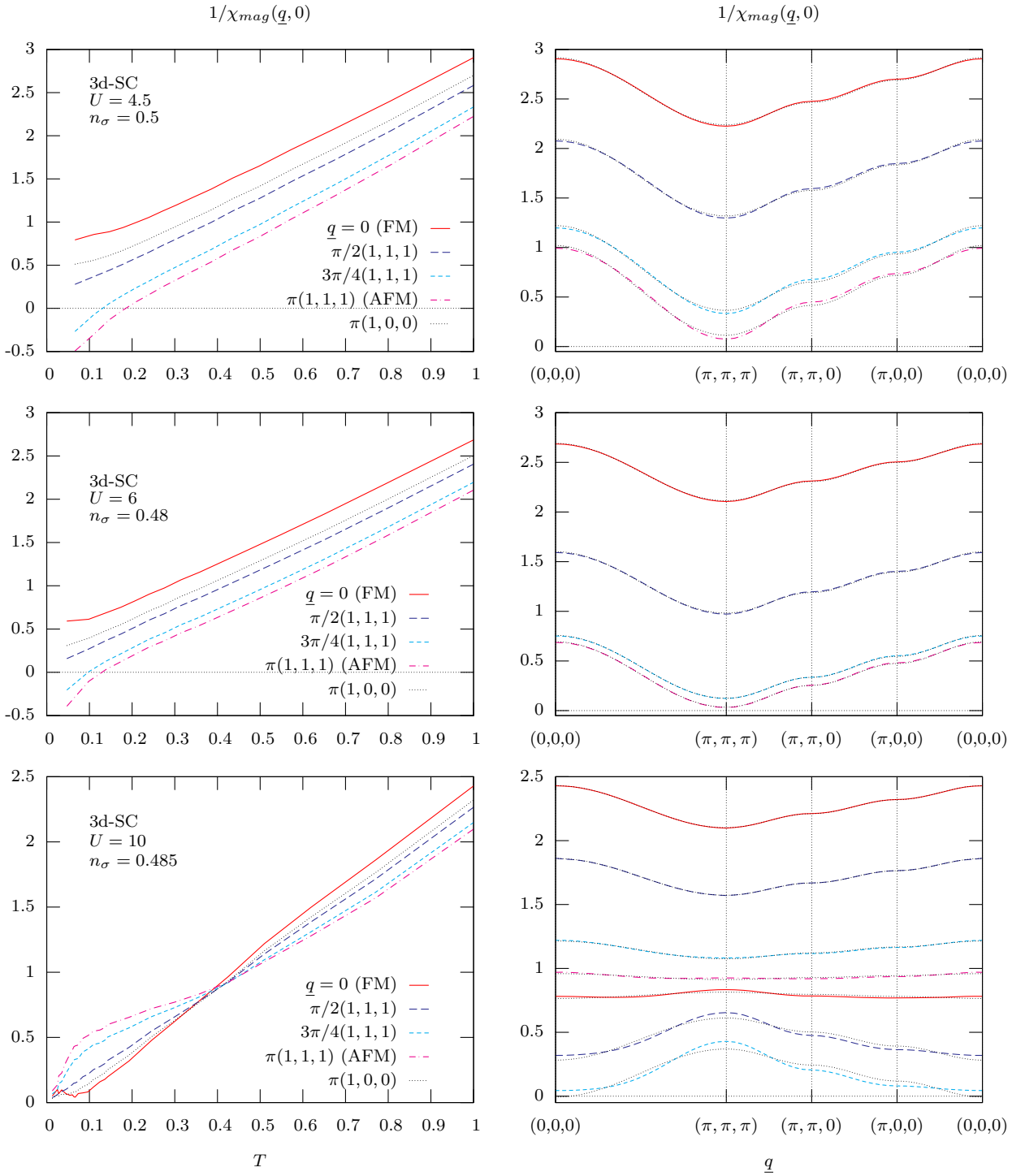

Figure 4.20: Inverse static magnetic susceptibility for the Hubbard model on a 3d-SC lattice for $U = 4.5$ and $n_\sigma = 0.5$ (upper row), $U = 6$ and $n_\sigma = 0.48$ (middle row), and $U = 10$ and $n\_s = 0.485$ (lower row). The left graphs show it as function of temperature and for some selected $\underline{q}$-modes, while the right graphs show a $\underline{q}$-loop as indicated and curves for some selected temperatures, which decrease top to bottom. The grey dashed curves in the right graphs represent fits with a function $a + b\langle tt\rangle_{\underline{q}}$ (see equation (4.4.11)).

$U = 10$ and $n_\sigma = 0.485$ the linear temperature dependency of the inverse static magnetic susceptibility is seen only for high temperatures $T \geq 0.4$. Upon lowering the temperature the different $\underline{q}$-modes start to behave differently and cross each other, leading to an enhanced FM ($\underline{q} = 0$) and a suppressed AFM susceptibility.

Before the temperature dependency of the susceptibilities is discussed, an understanding of its variation with the external wave vector $\underline{q}$ is desirable. Therefore, it is necessary to consider the particle-hole propagator, since it is the only explicitly wave-vector dependent quantity in this approximation. To get a rough estimate, the momentum and frequency sums of equation (2.3.15) and (2.3.16) can be decoupled in an RPA-like manner, $\frac{1}{N_0}\sum_{\underline{k}} t_{\underline{k}} t_{\underline{k}+\underline{q}} G(\underline{k}, i\omega_n) G(\underline{k}+\underline{q}, i\omega_n) \approx (\frac{1}{N_0}\sum_{\underline{k}} t_{\underline{k}} t_{\underline{k}+\underline{q}}) \frac{1}{N_0}\sum_{\underline{k}} G(\underline{k}, i\omega_n) G(\underline{k}+\underline{q}, i\omega_n)$. Solving equation (2.3.15) for the particle-hole propagator then yields

$$P(\underline{q}, \nu)|^{(decoupled)} = \left[\frac{1}{\langle \tilde{G}\tilde{G}\Lambda \rangle(\nu)} - \frac{\langle \tilde{G}\tilde{G} \rangle(\nu)}{\langle \tilde{G}\tilde{G}\Lambda \rangle(\nu)} \langle tt \rangle_{\underline{q}} \right]^{-1} \tag{4.4.6}$$

$$\approx \left[\frac{1}{\langle \tilde{G}\tilde{G}\Lambda \rangle(\nu)} - b \, \langle tt \rangle_{\underline{q}} \right]^{-1} \quad , \tag{4.4.7}$$

where in the second line, the fact was used that – to a first approximation – the prefactor of the elementary two-particle hopping is a frequency independent constant b, due to cancellation effects in the fraction. The brackets indicate the appropriate momentum or frequency average, i.e.

$$\langle tt \rangle_{\underline{q}} = \frac{1}{N_0} \sum_{\underline{k}} t_{\underline{k}} t_{\underline{k}+\underline{q}} \tag{4.4.8}$$

$$\langle A \rangle(\nu) = \Big(\frac{1}{\beta} \sum_{i\omega_n} A(i\nu_n | i\omega_n) \Big) \Big|_{i\nu_n \to \nu + i\delta} \quad . \tag{4.4.9}$$

The elementary two-particle hopping amplitude $\langle tt \rangle_{\underline{q}}$ of equation (4.4.8) can be explicitly calculated for all cubic lattices considered in this work. It turns out, that it is just given by the negative single particle dispersion relation where the hopping matrix elements are replaced by their squares, i.e.

$$\langle tt \rangle_{\underline{q}} = - \, t_{\underline{q}} \big|_{t \to t^2; t' \to t'^2} \quad . \tag{4.4.10}$$

For all three cubic lattices without next-nearest neighbor hopping ($t' = 0$) this implies the equality of the two-particle hopping and the one-particle dispersion, apart from the different prefactor. For lattices with next-nearest hopping ($t' \neq 0$), the relative sign between the two terms in $\langle tt \rangle_{\underline{q}}$ is changed with respect to the dispersion $t_{\underline{q}}$ and an qualitatively different wave vector dependency may result.

Inserting the estimate for P into (2.3.42) or (2.3.42a) equation (2.3.48) yields the approximative form of the susceptibility

$$\chi(\underline{q}, \nu)|^{(decoupled)} = \left[\frac{1}{\chi^{(loc)}(\nu)} + \frac{1}{P^{(loc)}(\nu)} - \frac{1}{\langle \tilde{G}\tilde{G}\Lambda \rangle(\nu)} + b \, \langle tt \rangle_{\underline{q}} \right]^{-1} \tag{4.4.11}$$

$$\equiv \frac{1}{a(\nu) + b \, \langle tt \rangle_{\underline{q}}} \quad . \tag{4.4.12}$$

From the form of equation (4.4.11) the elementary two-particle hopping $\langle tt \rangle_{\underline{q}}$ can directly be identified with the paramagnon dispersion relation for magnetic excitation modes.

For the static susceptibility this form is also shown as the dashed curves in the figure 4.20, with the parameters $a(0)$ and b extract from a numerical fit. As it can be seen for the situations with $U = 4.5$, $n_\sigma = 0.5$ and $U = 6$, $n_\sigma = 0.48$ the decoupled approximations agree very well with the actual susceptibility, which is calculated with the non-decoupled particle-hole propagator (2.3.45). This implies, that a tight-binding treatment of the particle-hole excitation (and with this the susceptibilities) is sufficient to describe two-particle propagations in these situations accurately. Quantum mechanical coherence of a propagating particle-hole pair, which is destroyed by the RPA-like decoupling, needs to be preserved in the treatment only for processes with very few hoppings. This is in accord with the observation, that the dominant momentum component is the antiferromagnetic $\underline{q} = (\pi, \pi\,\pi)^T$-mode, where nearest neighbor processes play the major role.

For the case in which $U = 10$, $n_\sigma = 0.485$ agreement is found only for high temperatures $T \geq 0.4$ while below that, the different $\underline{q}$-modes deviate from this simple form. Some are enhanced over the value given by (4.4.12), while other are suppressed. This indicates the increased importance of quantum mechanical interference, i.e. the information on the relative phases, over the whole propagation process of a particle-hole excitation along its path.

The fact that this breakdown of the tight-binding treatment goes along with a change in the nature of the dominant magnetic excitation mode seems very plausible from the general expectations formulated in the previous section 4.4.1: at large U and away from half filling the detailed balance between correlation and kinetic energy dominates the response and might lead to an enhancement of ferromagnetic ($\underline{q} = 0$) or incommensurate ($0 \neq \underline{q} \neq (\pi, \pi, \pi)^T$) components of the susceptibility.

Returning to the temperature dependency of the susceptibilities, the two cases with $U = 4.5$, $n_\sigma = 0.5$ and $U = 6$, $n_\sigma = 0.48$ will be brought into focus first. The linear variation of all curves in the upper two graphs of figure 4.20 seems plausible, since the locally complete approximation treats the spatial correlations in a mean-field manner and thus a critical exponent of $\gamma = 1$ is expected. However, that this dependency extends over the whole temperature range from the transition up to $T = 1$ is somewhat remarkable. Even though the system is highly correlated at all temperatures due to the large value of U (the upper Hubbard band is alway clearly separated from the lower) the temperature dependent transformation from the original electrons to the low energy quasiparticles constitutes a strong renormalization of the thermally relevant excitations. Therefore traces of the formation of the low energy quasiparticles would be expected.

At high temperatures, the behavior is easily understood by reconsidering the local magnetic moments for these situations shown in figure 4.4: due to the large value of U and the fixed local occupation number, these are for one thing large and for another thing almost temperature independent before the screening sets in at low temperatures. This can be anticipated, since the lower Hubbard band is almost completely below the Fermi level, the local occupancy almost one electron per site and charge fluctuation into the upper Hubbard band involving doubly occupied sites are strongly suppressed due to the large U (cf. figures 4.1, 4.2, 4.3 and 4.4). The system behaves essentially as a spin system at high temperatures, for which a Curie-like linearly varying inverse susceptibility is reasonable,

especially in a mean-field treatment. But since itinerant excitations are present after all, the local magnetic moments are not independent but interact via a effective $\underline{q}$-dependent exchange couplings.

This scenario is the adaption of the interpretation of equation (2.3.42a) in section 2.3.2 and the couplings $J(\underline{q}, 0)$ are explicitly known through equation (2.3.48). To explicitly confirm this picture, the couplings are shown in the right graphs of figure 4.21. As it can be seen, they are almost constant for high temperatures and the absolute values are of the order of $J_0 = 4t^2/U$.

As a direct consequence of the approximative form (2.3.42a), the dependency on the external wave vector $\underline{q}$ of J is the same as for the full inverse magnetic susceptibility, which is shown in the right graphs of figure 4.20. Consequently the antiferromagnetic coupling is positive and maximal, while all other components are smaller, even negative, and minimal for the FM one and this order is preserved for all temperatures.

Upon lowering the temperature, Kondo physics comes into play and the low energy quasiparticles start to form. This induces a reduction of the local magnetic moments (cf. figure 4.4) due to an increased itinerancy as a consequence of the formation of the low energy band structure around the Fermi level. Additionally, Kondo-like screening diminishes the local moments as well. Smaller moments would lead to a demagnetizing of the system and the magnetic susceptibility would be expected to drop. On the other hand, the increase of spectral weight at the Fermi level produces an enhanced particle-hole propagator and the effective coupling, mediated through these particle-hole excitations, grows in magnitude, which would in turn increase the magnetic susceptibility. Both trends can be clearly seen in the magnetic moments shown in figure 4.4 and the particle-hole propagator and effective couplings of figure 4.21 (left and right graphs, respectively).

These opposite trends almost exactly cancel each other and the linear temperature dependency persist down to the transition. The quasiparticle band structure which leads to a reduction of the local magnetic moments just provides the extra spectral weight at the Fermi level to increase the coupling.

While the argument for high temperatures utilized the local moment picture of magnetism, the low temperature situation is more adequately described as the Stoner-type response of itinerant quasiparticles. The magnetic particle-hole excitations supported by the quasiparticles are enhanced through the nesting property of the Fermi surface. The effective vertex $\Gamma_{mag}(0)$ represents the interaction for magnetic excitations and is of the order of the bare Coulomb interaction U (see figure 4.22). Even the transition temperature for $U = 4.5$, $T_N \approx 0.19$, is very close to the value obtained from a modified Stoner criterion, $1 \stackrel{!}{=} \Gamma_{mag}(0)\rho(0)$, which yields $T_N^{Stoner} \approx 0.2$.

In this case, the picture in which the magnetism can be understood transforms from the local moments magnetism at high temperature to an itinerant picture at lower temperatures.

The situation for $U = 6$, $n_\sigma = 0.48$ is not as clear. Even though the high temperature description as local moments magnetism is very well applicable, at lower temperatures the itinerant picture is not as well justified. While the particle-hole propagator does indeed show the enhanced behavior due to the itinerant quasiparticle and nesting, the effective interaction is considerably too large. The modified Stoner criterion yields a transition temperature of $T_N^{Stoner} \approx 0.27$, which is more than twice the actual value $T_N \approx 0.13$.

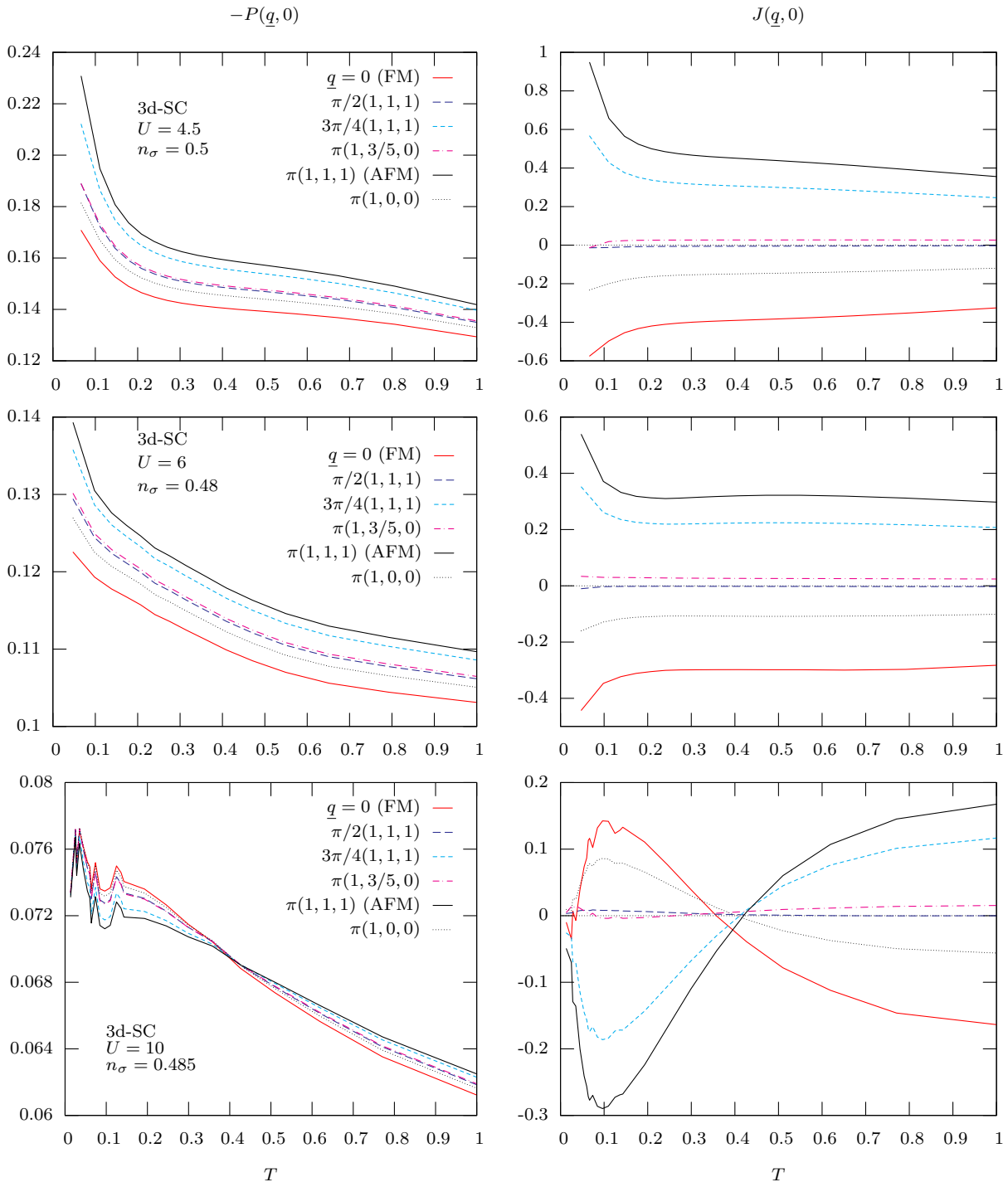

Figure 4.21: Negative static particle-hole propagator (left graphs) and effective coupling of local moments $J(\underline{q},0)$ (right graphs, see equation (2.3.48)) for the Hubbard model on a 3d-SC lattice for $U = 4.5$, $n_\sigma = 0.5$ (upper row), $U = 6$, $n_\sigma = 0.48$ (middle row) and $U = 10$, $n_\sigma = 0.485$ (lower row) for selected values of the external wave vector q and as a functions of temperature T. The legends and coloring of the left graphs is also valid for the right ones. The noisy oscillations of the particle-hole propagator at temperatures below $T \leq 0.12$ are due to the difficulty to fix the electronic filling at exactly the desired value and the large influence of very small variations thereof.

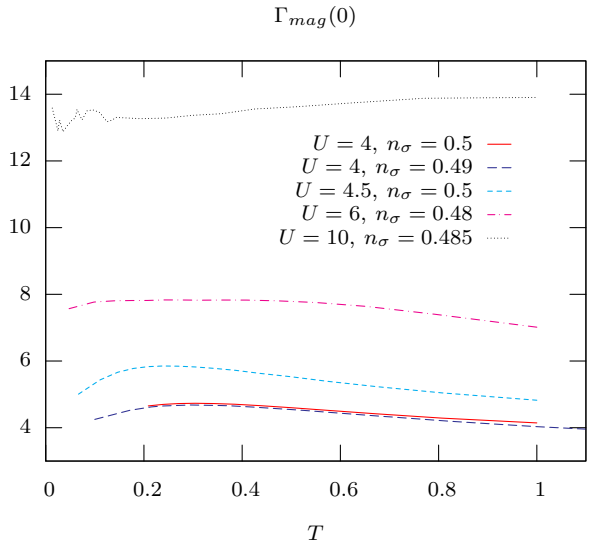

Figure 4.22: Static magnetic two-particle vertex $\Gamma_{mag}(0)$ for the Hubbard model on a 3d-SC lattice for various parameter values as a function of the temperature T.

The two archetypical pictures of magnetism are thus only approximately valid for the presented cases. This is of course no surprise since the situation for these intermediate to large values of U corresponds to the strongly correlated metal, where large local moments, as well as itinerant quasiparticles are present. Both pictures mix and no clear distinction is generally possible.

The third situation shown in the figures 4.20 and 4.21 for $U = 10$, $n_\sigma = 0.485$ shows a qualitatively different behavior. As already stated, the linear temperature dependency of the inverse static magnetic susceptibility is seen only for very high temperatures $T \geq 0.4$.

The overall magnitude of the particle-hole propagator is reduced compared to the cases with $U = 4.5$ and 6. The reason for this lies in the removal of spectral weight from the vicinity of the Fermi surface. For one thing, the upper Hubbard band in the one-particle DOS for $U = 10$ is shifted to higher energies. The energy region between the Fermi level and the upper Hubbard band is now best characterized as an actual band gap, instead of a region with increased scattering due to the interaction (see figures 4.1, 4.2 and 4.3). This leads to an suppressed phase space for the excitation of positive energy particles or holes. Additionally, at low temperatures spectral weight is removed from the vicinity of the Fermi level, since the quasiparticle weight and the line width of the many-body resonance is reduced due to the decreasing characteristic energy scale with increasing U.

At temperatures $T \leq 0.4$, where the deviations from the linear inverse susceptibility start to show and the characteristic $\underline{q}$ dependence of the coupling $J(\underline{q}, 0)$ changes, the lower Hubbard band in the one-particle spectrum moves towards the Fermi level. The structures emerging at the Fermi level are very sharp, especially at low temperatures, where the many-body scale T^* sets the order of magnitude for the width and variation of these structures. The consequence is an increased influence of the detailed distribution of spectral weight near the Fermi surface. For some $\underline{q}$-modes the quantum mechanical superpositions of propagating particles and holes summed in the particle-hole propagator interfere in a

destructive manner, while others are increasingly favored like the ferromagnetic $\underline{q} = 0$-mode. As a consequence the coupling function shown in the lower right graph of figure 4.21 does change its characteristic wave vector dependence and the antiferromagnetic component becomes energetically unfavorable, while the ferromagnetic one becomes largest.

This is exactly the situation characterized in the introductory section 4.4.1 of a strongly correlated metal with large local magnetic moments where the detailed competition between kinetic and interaction energy comes into play.

But at even lower temperatures $T \leq 0.1$, which is of the order of the low energy scale T^*, the qualitative behavior of the effective coupling strength $J(\underline{q}, 0)$ changes again, as the absolute value rapidly decreases. This is a consequence of the onset of lattice coherence amongst the quasiparticles, where the local moments become increasingly screened due to the dynamic Kondo singlet forming at each site. Correlations are built into the quasiparticle band structure and thus particle-hole excitations sustaining the effective exchange coupling between the moments are suppressed.

Dynamic response

The dynamic magnetic lattice susceptibilities for the two cases $U = 6$, $n_\sigma = 0.48$ and $U = 10$, $n_\sigma = 0.485$ are shown in the figures 4.23 and 4.24, respectively.

For small to medium Coulomb repulsions, e.g. $U = 6$, every $\underline{q}$-mode shows a typical spin relaxation with a relaxation rate of the order of the low energy scale. This is expected, since the magnetic properties are dominated by the dynamical screening of local moment. The coupling of these local moments leads to the enhancement of the antiferromagnetic component.

In the plots of the imaginary parts of the lattice susceptibility shown in figure 4.23 the paramagnon dispersion $\langle tt \rangle_{\underline{q}}$ can be observed as the position of the maximum of the paramagnon peak. In accord with the expected scenario for a continuous phase transition this position approaches zero upon reducing the temperature, which indicates the softening of the critical mode, in this case $\underline{q}_{crit} = \underline{q}_{AFM}$.

Before proceeding, a further exploration of the decoupled analytical form for the susceptibility is beneficial. In order to do so, an assumption for the function $a(\nu)$ of equation (4.4.12) has to be made. Inspired by the plots of figure 4.23 it is chosen to describe a usual spin relaxation, i.e.

$$a(\nu) = -i\nu/\gamma + c \quad . \tag{4.4.13}$$

This is especially justified by reconsidering the characteristic form for the dynamic local susceptibility $\chi^{(loc)}_{mag}(\nu)$ from the SIAM (3.4.13). Thus the final simple approximation for the dynamic response within a tight-binding treatment has the form

$$\chi(\underline{q}, \nu)|^{(decoupled)}_{mag} = \frac{1}{-i\nu/\gamma + c + b \langle tt \rangle_{\underline{q}}} \quad . \tag{4.4.14}$$

This approximative form is also shown as the grey curve in the graphs of figures 4.23 and 4.24. The agreement with the calculated functions is excellent, since both curves are almost indistinguishable in the graphs.

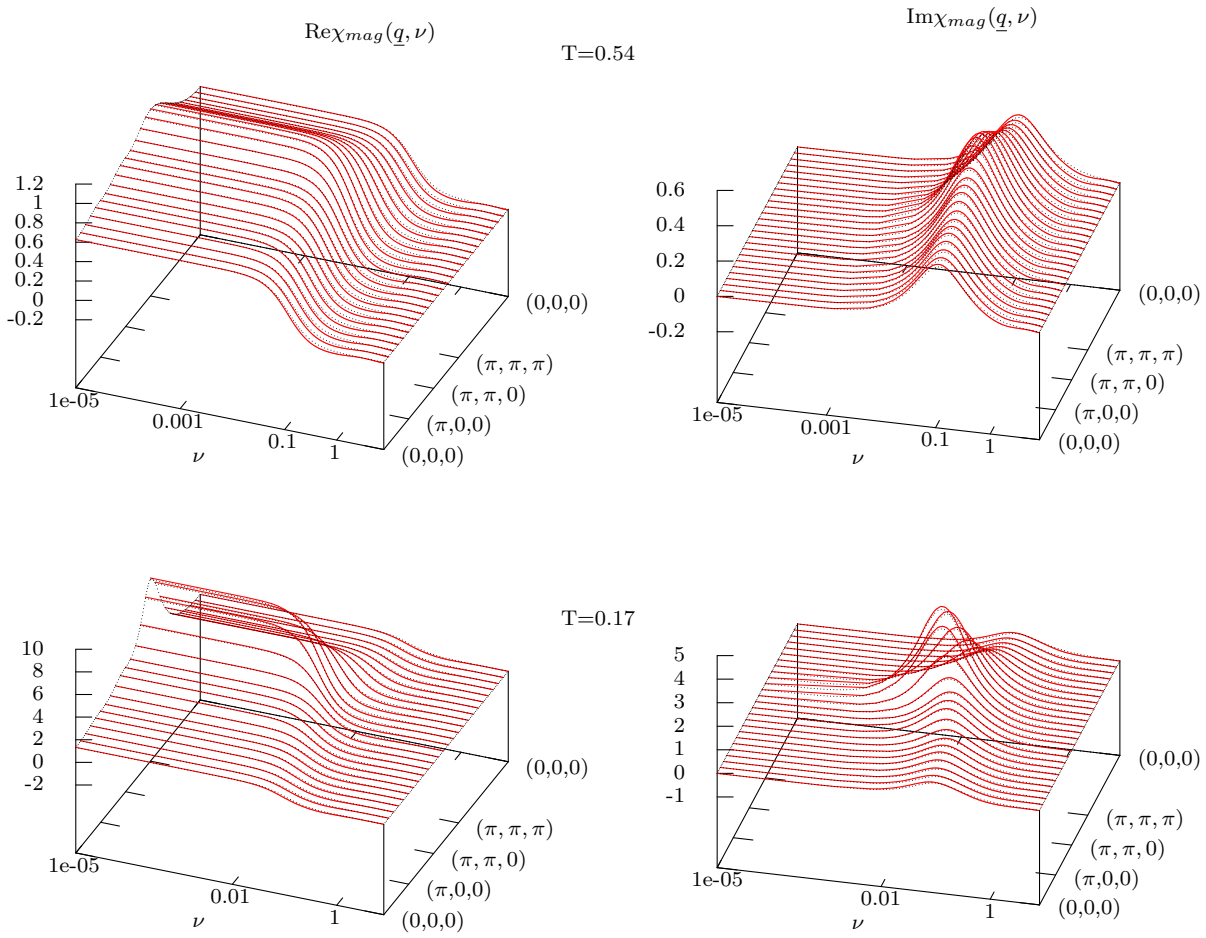

Figure 4.23: Real (left) and imaginary part (right) of the dynamic magnetic susceptibility for $U = 6$ and $n_\sigma = 0.48$ for two different temperatures $T = 0.54$ (upper) and $T = 0.17$ (lower). Notice the different scales on the z-axes.

In order to make the connection to a more commonly known form and to further elucidate the physical implications of the approximation (4.4.14), the two-particle hopping $\langle tt \rangle_{\underline{q}}$ in the denominator of (4.4.14) can be expanded around the critical wave vector $\underline{q}_{crit}$, and the result for the susceptibility is

$$\chi(\underline{q},\nu)|^{(decoupled)} \approx \frac{C}{(\underline{q}-\underline{q}_{crit})^2 + \xi^{-2} - i\nu/D} \qquad |(\underline{q}-\underline{q}_{crit})| \ll \pi \quad , \tag{4.4.15}$$

where C is some dimensional constant. The quantity D represents a microscopic diffusion constant, which accounts for the characteristic timescale for the spin relaxation and ξ represents the correlation length, which governs the exponential decay of the correlations.

The latter is explicitly revealed by a Fourier transform of the static ($\nu = 0$) susceptibility to coordinate space, which yields a typical Ornstein-Zernicke form for large $|\underline{r}|/\xi$

$$\chi(\underline{r},0)|^{(decoupled)} \sim |\underline{r}|^{-\frac{(d-2)}{2}}\, e^{-\frac{|\underline{r}|}{\xi}} \left(1-(d-3)\frac{\xi}{|\underline{r}|}\right) \overset{d=3}{=} |\underline{r}|^{-\frac{1}{2}}\, e^{-\frac{|\underline{r}|}{\xi}} \quad . \tag{4.4.16}$$

The temperature dependency of the correlation length ξ can be extracted from fits to the calculated susceptibility (not shown) and yields a inverse square-root dependency, i.e.

$$\xi(T) \sim \frac{1}{\sqrt{T}} \quad . \tag{4.4.17}$$

The square-root is just the consequence of the mean-field treatment of the spatial correlations within the present approach. Thus, the result represents just another viewpoint on the statement made above, when discussing the linear temperature dependency of the inverse magnetic susceptibility of figure 4.20.

The situation is quite different for the case with large $U = 10$, as it can be seen in figure 4.24, where the imaginary parts of the dynamic susceptibilities are shown for four temperatures. At high temperatures the paramagnon peak with a maximum at the antiferromagnetic wave vector $\underline{q}_{AFM}$ is clearly visible. The approximate form (4.4.14) still describes the dynamic response quite accurately. At the temperature $T = 0.06$ the ferromagnetic response is already enhanced (upper right graph) and the decoupled form cannot describe the susceptibility sufficiently. The form of each wave vector component is still in accord with a common relaxation ansatz, but the relative height of the different modes and the peak-positions cannot be described with such a simple form. As already stated, this is due to the failure of the tight-binding treatment of particle-hole excitations and the importance of the information about the relative phases for those excitations.

At an even lower temperature of $T = 0.02$ (lower left graph of figure 4.24) incommensurate $\underline{q}$-modes start to dominate and even the form for a single $\underline{q}$-mode is not approximated by (4.4.14), since an additional structure emerges at energies right above the paramagnon peak. This is best seen in the ferromagnetic $\underline{q} = 0$-mode and for $T = 0.013$, where the side peak develops at $\nu \approx 0.04$. It appears to be present in every wave vector component but is absorbed into the paramagnon peak away from $\underline{q} = 0$. Furthermore the emerging feature does not show any sign of dispersion and thus indicates some localized collective mode.

In order to shed more light on the origin of this localized collective mode, the imaginary part of the particle-hole propagator is shown in the left graph of figure 4.25. The prominent peak at energies $1 \lesssim \nu \lesssim 4$ stems from excitations involving particles (or holes) in the lower Hubbard band and the quasiparticle band structure. The inset shows the very pronounced high energy peak involving the upper Hubbard band around $\nu \approx 10$. The small humps in the low energy tails for $\nu \lesssim 0.2$ are the contributions from pure quasiparticle-quasihole excitations. At higher temperatures up to $T \lesssim 0.4$, $P(\underline{q},\nu)$ has an unchanged form and only minor modifications occur. No significant changes in the qualitative behavior of the particle-hole excitations are detected at the temperatures where the collective mode emerges, and therefore they cannot be the sole cause for the new feature in $\chi_{mag}(\underline{q},\nu)$.

The right graph of figure 4.24 shows the imaginary part of the effective magnetic two-particle interaction $\Gamma_{mag}(\nu)$ (see equations (2.3.42) and (2.3.43)). The dramatic increase of

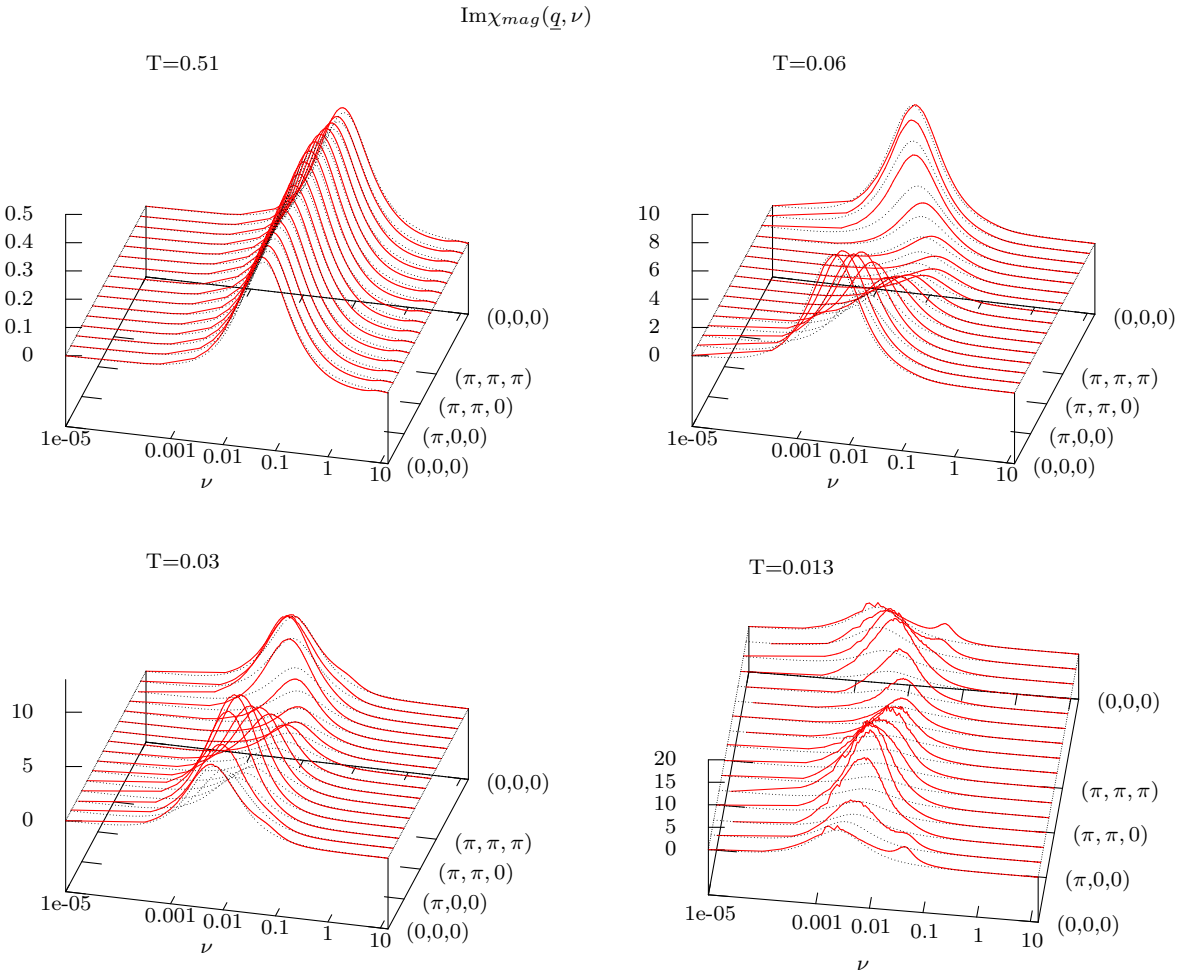

Figure 4.24: Imaginary part of the dynamic magnetic lattice susceptibility $\chi_{mag}(\underline{q},\nu)$ for $U = 10$ and $n_\sigma = 0.485$ for various temperatures as indicated. Notice the different scales on the z-axes.

Im$\Gamma_{mag}(\nu)$ at high energies indicates very high magnetic scattering and strong renormalizations of quasi-free propagating modes described by $P(\underline{q},\nu)$ due to the dominating nature of the large local magnetic moments.

But more remarkable is the qualitative change in Im$\Gamma_{mag}(\nu)$ which occurs as the new feature emerges in the magnetic lattice susceptibility: at temperatures below $T \lesssim 0.06$ the imaginary part Im$\Gamma_{mag}(\nu)$ changes sign for small energies $\nu < 0.1$ and develops a new minimum at $\nu \approx 0.04$. This is the exact energetic position of the feature in $\chi_{mag}(\underline{q},\nu)$. The local susceptibility, which is shown in the upper inset of the graph, increases for lower temperatures, whereas the (negative) local particle-hole propagator is almost temperature independent (lower inset). Since the effective two-particle vertex is given by the sum of both inverted functions, $\Gamma_{mag} = {\chi^{(loc)}_{mag}}^{-1} + {P^{(loc)}}^{-1}$, this eventually leads to the observed change of sign and, as a consequence, the appearance of the collective mode. This nicely confirms the local nature of the latter.

The question, whether this collective mode is of pure magnetic nature or involves charge excitations as well can be answered by investigating the two-particle charge excitations of

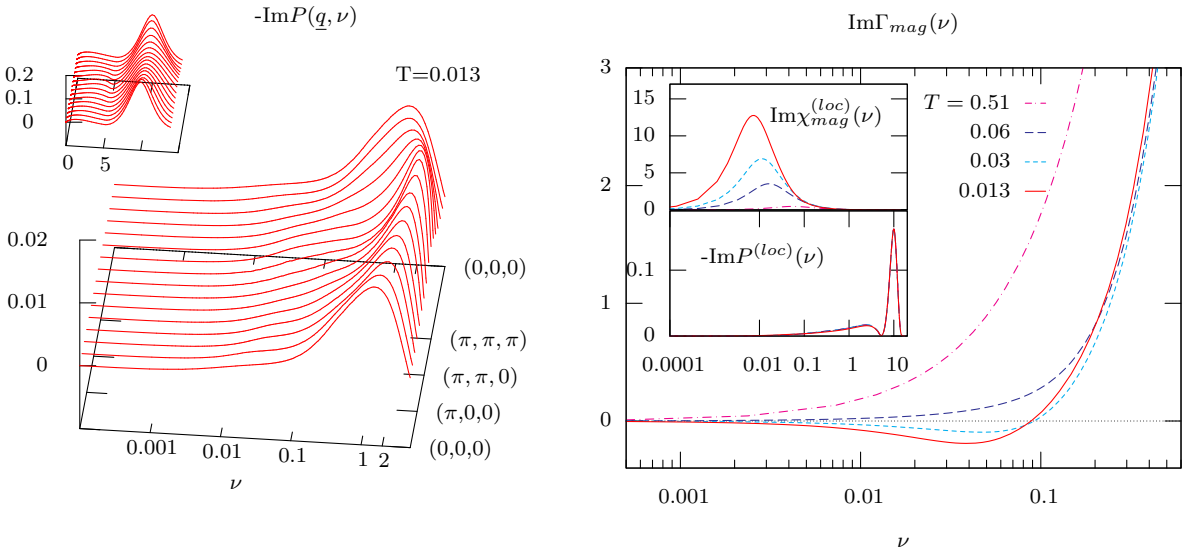

Figure 4.25: Left graph: negative imaginary part of the dynamic particle-hole propagator for $U = 10$, $n_\sigma = 0.48$ and $T = 0.013$ for low energies an a logarithmic frequency axis. The inset shows the whole frequency range on a non-logarithmic scale.
Right graph: imaginary part of the effective magnetic two-particle interaction $\Gamma_{mag}(\nu)$ for $U = 10$, $n_\sigma = 0.48$ and various temperatures. The insets shows the imaginary part of the local susceptibility (upper) and local particle-hole propagator as functions of frequency.

the system. The temperature dependent static lattice and local susceptibilities are shown in figure 4.26, while the dynamic lattice charge susceptibility is shown in figure 4.27 for various parameters sets.

A first thing to notice is the reduced absolute value of χ_{charge}, when compared to magnetic excitations. This is a consequence of the large Coulomb interaction strongly suppressing charge fluctuations, even though the systems are metallic, i.e. have considerable spectral weight at the Fermi level. The two-particle excitations have to respect the correlations built into the low energy quasiparticles.

The second thing to recognize is the very weak dependence on the external wave vector $\underline{q}$, which is especially true for larger Coulomb U.

For $U = 4.5$, $n_\sigma = 0.5$ and $U = 6$, $n_\sigma = 0.48$ the one-particle DOS have a broad distribution of spectral weight around the Fermi level (cf. figures 4.1 and 4.2). As a consequence static charge susceptibilities are thermally enhanced for very high temperatures. Upon lowering the temperature, the states above the Fermi level become depopulated and the static charge susceptibilities decline (see figure 4.26). Additionally the correlations effects become increasingly noticeable at lower temperatures leading to an additional suppression of charge fluctuations. An opposing trend towards an increase in the susceptibility is given by the increase of spectral weight of the DOS at the Fermi level with decreasing temperature. This eventually leads to a minimum of the charge susceptibility followed by a rise towards lower T in $\chi_{charge}(\underline{q}, 0)$.

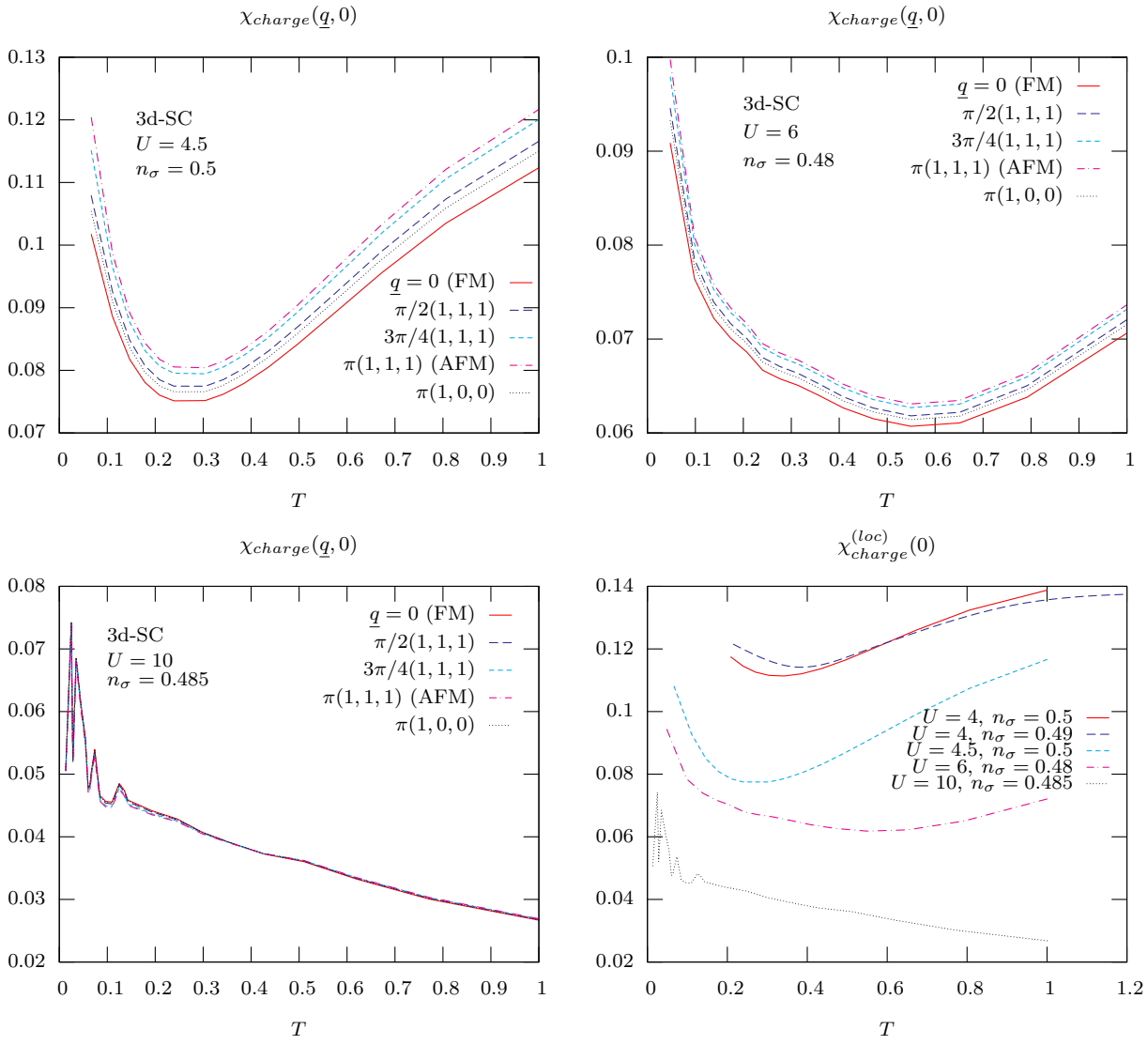

Figure 4.26: Temperature dependence of the static charge susceptibility $\chi_{charge}(\underline{q},0)$ for $U = 4.5$, $n_\sigma = 0.5$ (upper left graph), $U = 6$ and $n_\sigma = 0.48$ (upper right graph), $U = 10$ and $n_\sigma = 0.485$ (lower left graph) and the local static charge susceptibility $\chi^{(loc)}_{charge}(0)$ for various parameters as indicated (lower right graph). Some selected $\underline{q}$-modes are shown for the lattice susceptibilities as indicated in the key. The noisy fluctuations in the $U = 10$-curves for low temperatures are again due to the difficulty to fix the desired filling very accurately and the strong influence of variations in n_σ.

For very high Coulomb repulsions, e.g. the graph for $U = 10$ and $n_\sigma = 0.485$ in figure 4.26, the thermally enhanced charge susceptibility is moved to very large temperatures not shown in the figure, so that the decrease upon lowering the temperature does not occur and only the increase due to the growing spectral weight at the Fermi level becomes visible in the curves.

At temperatures in the range of the many body scale an additional enhancement of the susceptibilities occurs. The low energy quasiparticles start to form and charge fluctuations are enhanced. In comparison to the SIAM, the overall low temperature increase and especially the difference between half filling and away from it is not as pronounced in the lattice model (see section 3.4.2). This leads to the conclusion, that due to the self-consistency of the lattice the influence of the valence fluctuations encountered in the effective impurity model (see discussion for the SIAM on page 70) is strongly reduced. The medium $\tilde{T}$ for the effective impurity model embedded in the lattice already incorporates correlations, as it represents hoppings to the likewise correlated surrounding sites. This is in contrast to the SIAM, where the hybridization function does not include any sort of interactions. Valence fluctuations of a given site in the lattice are thus generally suppressed, since they would necessarily involve transfer processes to neighboring sites, where they are also subjected to correlations.

The local charge susceptibilities (lower right graph in figure 4.26) have the same characteristic temperature dependence and magnitude as their lattice counterparts, which indicates the domination of localized two-particle charge excitations in the lattice model. The strong dependency on the Coulomb repulsion signals the increasing suppression of charge excitations with larger U as it is expected.

Now the focus is brought back to the dynamic lattice charge susceptibility $\chi_{charge}(\underline{q}, \nu)$ shown in figure 4.27. In all the graphs, the broad peaks stemming from the high energy excitations at $\nu \approx |\epsilon|$ and $\nu \approx \epsilon + U$ are clearly visible. Apart from a slight thermal broadening at higher temperatures, these are essentially temperature independent. A remarkable thing is the almost total lack of dispersion in these peaks, which explicitly confirms the localized character of the excitations. The strong correlations essentially prohibit a two-particle charge excitation to propagate through the lattice, once created at a lattice site. Due to the large Coulomb energies involved, but even more important through the disregard of spin correlations in charge excitations, the particle-hole pair is energetically very unfavorable and immediately recombines again at that same lattice site.

At very low temperatures, low energy two-particle charge excitations are encountered in an impurity model, as it was demonstrated in section 3.4.2 for the SIAM. Due to the local nature of the charge excitations in the lattice model, these low energy features directly translate themselves into the lattice charge susceptibility. Analog to the SIAM, they occur as a consequence of fluctuations due to the proximity of an intermediate valence regime, and are thus absent in the symmetric situation with $U = 4$ and $n_\sigma = 0.5$, but develop in the low energy region for the asymmetric cases (see figure 4.27).

The charge susceptibility does not show any unexpected behavior and thus can be discarded in the question concerning the origin of the collective mode visible in the magnetic susceptibility. For $U = 10$, $n_\sigma = 0.485$ the low energy feature seems to be more pronounced than for $U = 6$, $n_\sigma = 0.4$. But most of this can be attributed to the different scale on the z-axis of the corresponding plots and the actual slight difference in height is caused

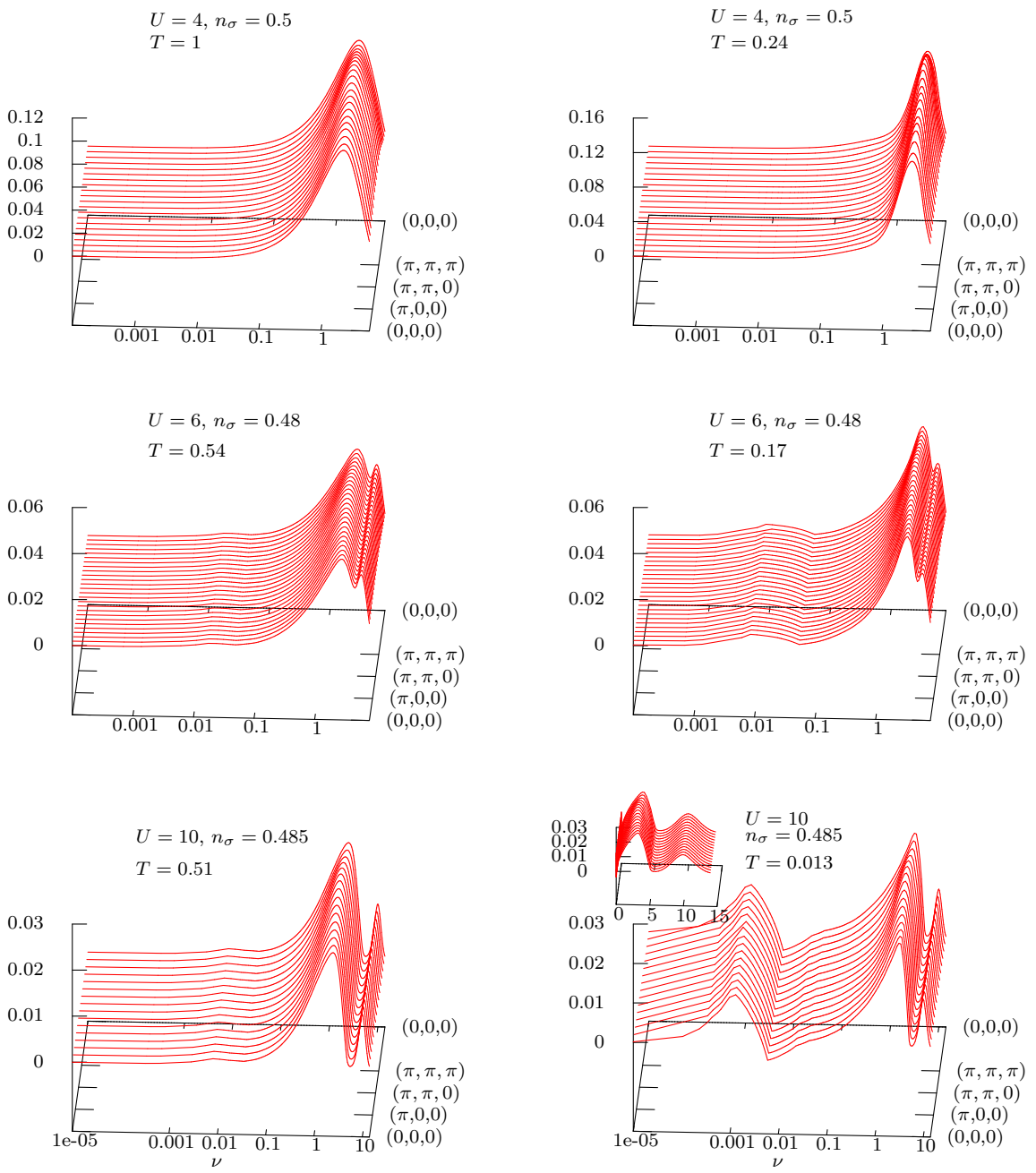

Figure 4.27: Imaginary parts of the dynamic charge lattice susceptibility $\chi_{charge}(\underline{q}, \nu)$ for $U = 4$, $n_\sigma = 0.5$ (upper row), $U = 6$, $n_\sigma = 0.48$ (middle row) and $U = 10$, $n_\sigma = 0.485$ (lower row) for the temperatures as indicated. The inset of the last graph shows the high energy region in a non-logarithmic plot.

by the higher temperature and smaller U in the later case, and as such totally expected. Consequently the collective mode is of pure magnetic origin.

The proposed physical picture behind the collective mode is that of a singlet-triplet excitation of a Kondo singlet associated with a (partially) screened localized moment. The finite energy of such a local excitation is just given by the energy necessary to break that singlet, i.e. its "binding energy". The situation is quite analog to the SIAM: at very low temperatures $T \leq T_K$ the static magnetic response saturates at a value $\sim \frac{1}{T_K}$ and the imaginary part of the dynamic susceptibility exhibits a peak at a finite energy $\sim T_K$ indicating the breakup of the singlet. In the lattice model, the Kondo temperature is replaced by the low energy scale T^*, and in situations, where Kondo-screening of local moments occurs, these singlets can be broken up and the excitation is observable. This picture is substantiated by observing that the energetic position of the collective mode $\omega_{coll} \approx 0.04$ is approximately equal to the width of the many-body resonance in the band structure at the Fermi level (≈ 0.02), which is a measure for the low energy scale T^*.

However, due to the incomplete screening in the lattice system the situation is more complicated than for the SIAM. The dispersive peaks also seen in the spectrum of figure 4.24 corresponds to the spin-response of the still itinerant part of the correlated quasiparticles. Since not all local moments are screened there exist still "unbound" electronic states. Magnetic excitations within these states feel the full correlations built into the quasiparticles and the interference effects of particle-hole pairs. Therefore a considerable dispersion results and the relative intensities of those modes is determined by the subtle competition of correlations and kinetic energy.

This argumentation certainly should not be taken too literally, since a strict distinction between localized moments, excitations of Kondo-singlets and other itinerant excitations cannot be made. There is only one species of electrons which provide the local moments along with the heavy quasiparticles and the Kondo-screening at very low temperatures. But in a pictorial sense, the argumentation is applicable and the basic mechanism explaining the localized spin excitation in the dynamic susceptibility is justified.

Consequence of the RPA-decoupling

At this point, a note is in place concerning the physical implications of the RPA-like decoupling of the frequency sums in the Bethe-Salpeter equations of section 2.3.2 (see equation (2.3.41)). The local two-particle interaction vertices, originally depending on three frequency arguments, are accounted for only as averages over two internal frequencies and the information about the energetics and phases of the participants of a particle-hole excitations is thus lost. Only the relative energy of the particle-hole pair is kept as a dynamic variable and their phase informations retained.

As long as antiferromagnetic or generally short ranged correlations dominate the situation, this decoupling constitutes a minor approximation. Extended excitations visiting many sites and their detailed energetics at each local site do not play an important role there. But in situations, where quantum mechanical interference and the detailed phases-information of excitations propagating through the whole lattice, and especially their interactions at lattice sites in between, becomes important, the RPA-like character of the approximation becomes apparent. This is the case in situations where strong incommen-

surate or ferromagnetic fluctuations become important, as for very large U and away from half filling in the Hubbard model.

In spite of this statement, qualitative features should still be faithfully reproduced within this decoupling and only the quantitative values should change, when compared to an non-decoupled calculation. But this certainly can have dramatic consequences for the calculation of phase diagrams and transition temperatures, since a quantitative change of, say, a ferromagnetic transition temperature from a finite value to zero is more likely a qualitative change. However, the presence of enhanced ferromagnetic fluctuations is the same qualitative behavior, regardless whether the actual transition occurs or not and in that sense the qualitative features should be properly described.

Especially the occurrence of the collective mode should be observable with other, more elaborate and accurate methods, since its cause is a qualitative change in the dynamic local two-particle vertex $\Gamma_{mag}(\nu)$, which is independent of the decoupling.

4.4.3 Critical temperatures and the influence of the lattice

Up to now several aspects concerning the typical behavior and physical mechanisms in the Hubbard model have been discussed. Now, the question arises which phase transitions do occur for what parameter values. In section 4.4.2 expectations concerning this issue were already formulated. Additionally, for the two cases of $U = 4.5$, $n_\sigma = 0.5$ and $U = 6$, $n_\sigma = 0.48$ transitions to antiferromagnetically ordered states were indeed found in the previous section. Performing calculations for various values for U, n_σ and on different lattices, estimates for transitions temperatures and the nature of the transitions can be obtained.

Results for transition temperatures from such parameter scans are shown in figure 4.28 for the three dimensional simple cubic lattice without (upper left graph) and with next-nearest neighbor hopping (upper right), $t'/t = 0$ (3d-SC) and $t'/t = -0.2$ (3d-SCNNN) respectively. The lower left graph shows the antiferromagnetic Néel temperature as a function of doping for the two cases of the SC and the body-centered cubic (BCC) lattice. The lower right graph shows the effective local magnetic moment as a function of the local level position (inset: local occupation number) for the SC lattice with a fixed temperature $T = 1/3$ for three different values of U.

The qualitative features of the upper two plots for the simple cubic lattice are as expected: extending from small values for the Coulomb interaction up to to intermediate values of the order of the bandwidth $U \approx 2W = 6$[11] antiferromagnetism is found for all fillings considered (red squares). As a function of the Coulomb repulsion U the Néel temperature T_N of the antiferromagnetic transition has a maximum for values around $U \approx 3.5 \approx 1.15W$. The existence of this maximum is certainly expected from the two asymptotic curves for small and large U, equations (4.4.2) and (4.4.5), respectively. The absolute height of the transition temperature at half filling is in complete agreement with the findings of earlier studies [Jar93, Fre95, TZ97, Dar00].

[11] For the lattices with a non-vanishing next-nearest neighbor hopping $t' \neq 0$ the half bandwidth W generally differs from its $t' = 0$ value. But since the size of the half bandwidth W is only utilized as an order of magnitude estimation, these differences are ignored. For all the SC lattices a value of $W = 3$ is used, while for the BCC and FCC lattices $W = 4$, resulting from a hopping matrix element of $|t| = 0.5$ for all cases.

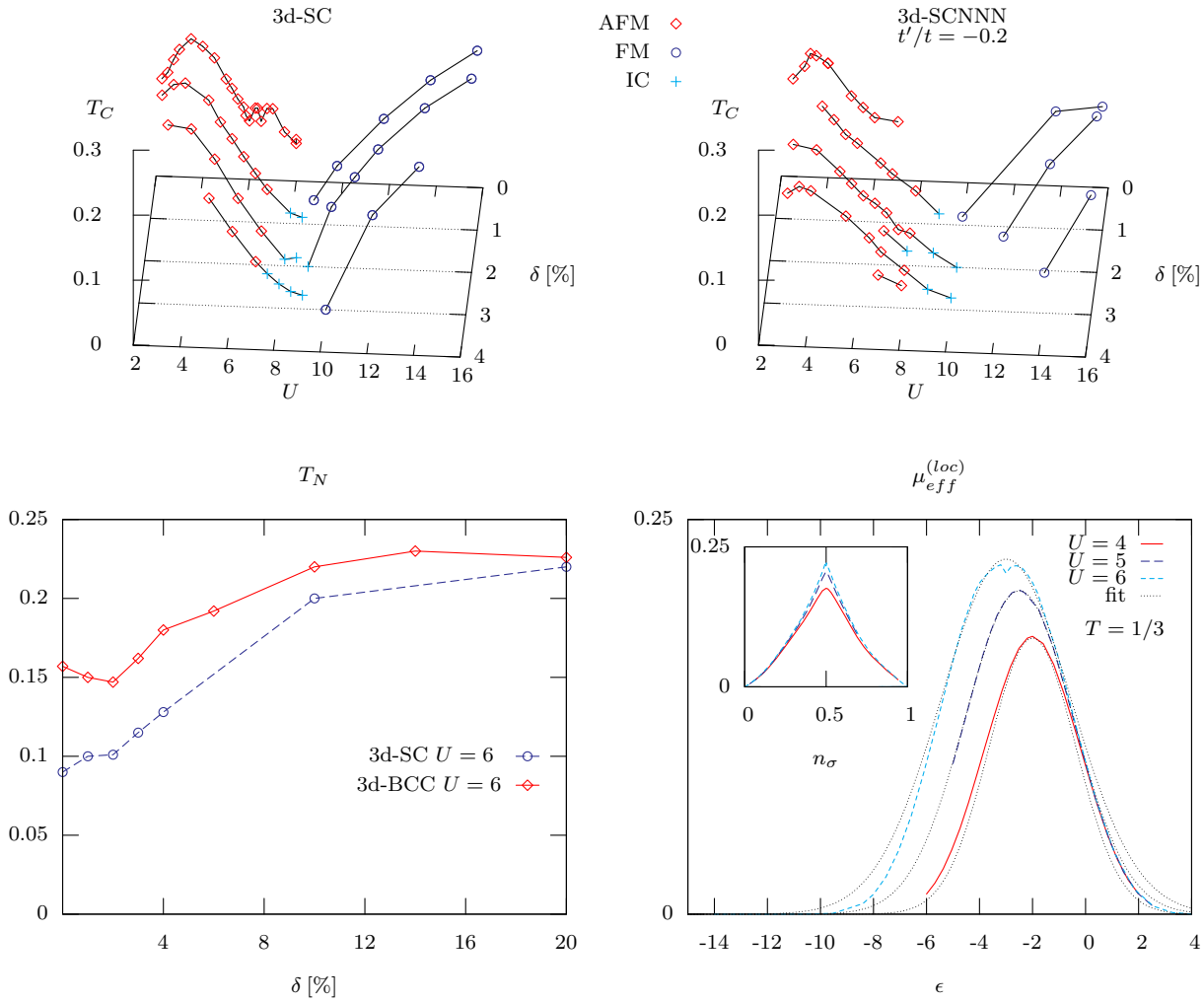

Figure 4.28: Upper graphs: critical temperatures for magnetic phase transitions in the Hubbard model on the 3d-SC (left) and the 3d-SCNNN (right) lattice as function of the Coulomb interaction U and doping $\delta = 1-2n_\sigma$ (measured in percent). "AFM", "FM" and "IC" stand for antiferromagnetic, ferromagnetic and incommensurate transitions, respectively.
Lower left graph: Néel temperature for the SC and BCC lattice as a function of doping for $U = 6$.
Lower right graph: effective local moment for the SC lattice at a fixed temperature $T = 1/3$ and as a function of the local level position ϵ or the occupation number n_σ (inset). The thin grey curves show fits with a Gaussian function $A \exp\big(-(\epsilon + U/2)^2/T^2\big)$.

For the case of the SC lattice and around $U \approx 6 = 2W$ the transitions temperature at half filling ($\delta = 0$) shows some peculiar oscillations. These are due to difficulties obtaining a converged solution of the self-consistency cycle of the locally complete approximation for low temperatures. This is in part due to the Mott-Hubbard metal-insulator transition (MIT) taking place in that region, where the first order nature of the transition with its hysteresis effects leads to numerical instabilities. Additionally, far above the MIT, e.g. $U \gg 2W$, stable solutions for the effective impurity model within the ENCA could not be obtained due to the vanishing DOS around the Fermi level, prohibiting the calculation of transition temperatures in these situations.

Concerning the dependence on doping δ, the Néel temperature T_N does not behave as expected and as found in other, equivalent studies [Jar93, TZ97]. Instead of rapidly decreasing with increasing doping and becoming zero for at a critical doping δ_c, which is maximal $\delta_c \approx 15 - 20\%$ for $U \approx W$, the present approach yields a almost constant, sometimes even increasing critical temperature. This can be explicitly seen in the lower left graph of figure 4.28, where T_N is shown for fixed value of $U = 6$ and for the SC and BCC lattice as a function of doping. Both curves grow for increasing doping and seem to saturate for $\delta \approx 16\%$. For larger values of doping, no results could be extracted due to the pathology described in section 4.3.2.

The combination of the reason underlying the pathology with the RPA decoupling is responsible for the wrong doping dependence of the Néel temperature. Upon increasing the doping, the center of the lower Hubbard band moves closer to the Fermi level resulting in a stronger overestimation of the height of the one-particle DOS due to the self-consistency. Consequently, the local particle-hole propagator $P^{(loc)}$ is directly influenced by this effect. In the other hand, the effect on the local susceptibility is minor, since magnetic excitations are described very accurately within the ENCA (cf. section 3.4.2). This imbalance in the description of one- and two-particle quantities in combination with the very sensitive structure of the susceptibility (2.3.42a), leads to a massive overestimation of the critical temperature. Small variations of the one-particle DOS at the Fermi level of about 5% can already lead to a decrease of the critical temperatures of the order of 0.1.

This explanation is further substantiated by correlating the increase in T_N with the increase in the DOS at the Fermi level $\rho(0)$ for various lattices. For example, in the BCC lattice $\rho(0)$ grows considerably slower for increasing doping than for the SC lattice due to the larger bandwidth and the less steep behavior near the band edges. This is most easily seen in the non-interacting DOS shown in appendix D, as the same characteristics are present for the fully interacting approximations, since both Hubbard bands resemble the non-interacting DOS in their shape (see also lower graph of figure 4.31). As a consequence, T_N increases slower for the BCC than the SC lattice, as it can be seen in the lower left graph of figure 4.28.

In order to confirm the statement that the magnetic excitations are also described accurately within the locally complete approximation and the ENCA as the impurity solver and not the reason for the wrong doping dependence, the local magnetic moments are shown as a function of the ionic level position ϵ in the lower right graph of figure 4.28 (the inset shows the same quantity as a function of the filling n_σ). All calculated moments show the expected behavior of a pronounced maximum at half filling $\epsilon = -U/2$ ($n_\sigma = 0.5$) and then rapidly decreasing away from it. Notice that the moments for different Coulomb repulsions

all coincide for $\epsilon \gtrsim -1$ indicating the unimportance of correlations and interaction effects once the average ionic occupation number is drastically reduced from one, i.e. $n_\sigma \gtrapprox 0$. The same is true, when the upper Hubbard band reaches the Fermi level, that is for fillings near $n_\sigma \lessapprox 1$.

As a function of the ionic level ϵ, the local moments for the SC lattice can be nicely fit with a Gaussian function,

$$\mu_{eff}^{(loc)} = A\, e^{-(\beta(\epsilon+U/2))^2} \quad . \tag{4.4.18}$$

A plateau in $\mu_{eff}^{(loc)}$ around half filling similar to the SIAM (see figure 3.19) is expected only for larger values of U, when a true band gap appears between the lower and upper Hubbard band.

Judging from the rapid decrease in the local moment away from half filling, the expectation would obviously be a fast decline in the Néel temperature for finite doping, at least at large U, where local moments are the driving force behind the magnetic ordering. Since this is not observed in the calculation, the reason must be indeed found in the one-particle quantities entering the transition temperature, which confirms the statements made above.

For large values of U and away from half filling ferromagnetic transitions occur (blue circles in the upper two graphs of figure 4.28). The absolute height of the FM transition temperature are comparable and even larger than the Néel temperatures, suggesting a very robust tendency towards it. This contradicts the expectation that ferromagnetism is a very subtle and sensitive phenomenon, especially on the SC lattice and that it is expected and found to occur only for very large U [Obe97]. Additionally the fact that the FM region apparently shrinks with the introduction of a negative next-nearest neighbor hopping $t'/t = -0.2$ (upper right graph in figure 4.28) also contradicts the expectations concerning the stabilization of FM depending on the kinetic energy and the form of the non-interacting DOS (see section 4.4.1).

The reason for this failure is found in the RPA-like decoupling of the Matsubara sums in the Bethe-Salpeter equations and was already discussed in the last paragraphs of the previous section (cf. page 133). The weak-coupling RPA is known to drastically overestimate the tendency towards ordering and thus transitions temperatures are usually way too large. Due to the decoupling in the present approach, the approximations fails to capture those two-particle correlations essential to the description of ferromagnetism and which would lead to a strong suppression of FM. As a consequence, the presented transition temperatures more likely render those of the usual RPA, but calculated with the full correlations retained in the one-body excitations. In that sense they mimic the ones obtained from a usual modified Stoner criterion, $1 = \tilde{U}\rho(0)$.

From that point of view, the decrease of the FM region for the SCNNN lattice becomes also clear, as the DOS at the Fermi level is reduced with the introduction of $t' \neq 0$, while the effective interaction essentially stays the same.

In accord with earlier findings [Pen66, Fre95, TZ97] incommensurate transitions occur away from half filling at the edge of the AFM region, where the transition temperatures become very small (turquoise crosses in the upper two graphs of figure 4.28).

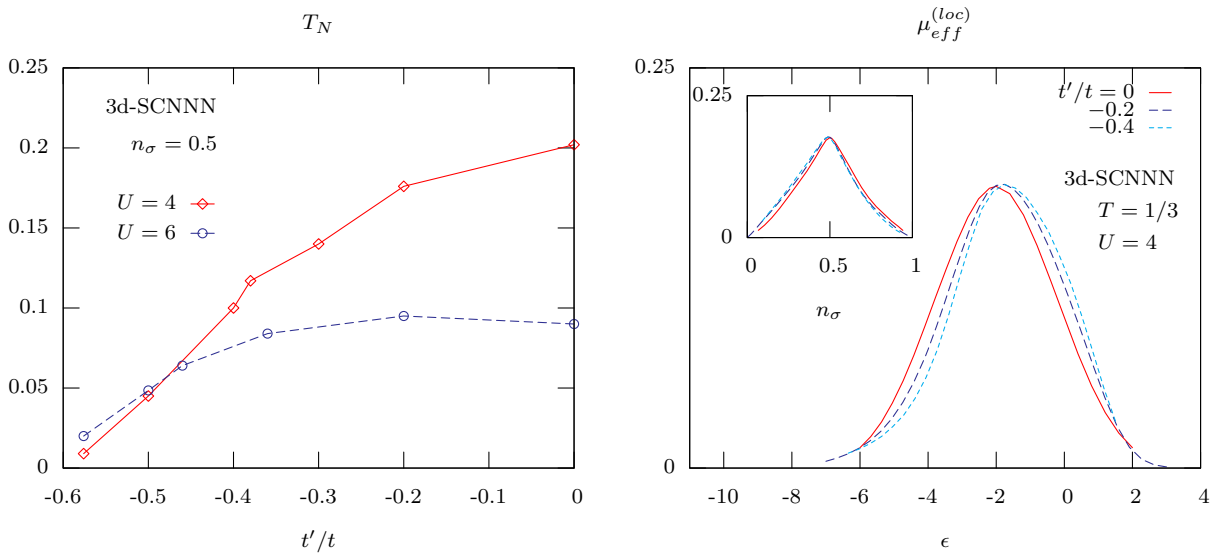

Figure 4.29: Left graph: Néel temperature for the SCNNN lattice as a function of doping of the next-nearest neighbor hopping t'/t for two values of U.
Right graph: Effective local moments in the Hubbard model for the SC (left graph) and SCNNN (right graph) lattice. The left graph shows $\mu_{eff}^{(loc)}$ for three different Coulomb repulsions along with fits of a Gaussian function $A \exp\big(-(\epsilon + U/2)^2/T^2\big)$ (grey dashes). The right graphs are done for $U = 4$ and three different next-nearest neighbor hoppings t'/t. The insets shows the same quantity as a function of the filling fraction n_σ. The temperature was chosen to be $T = 1/3$ for all curves.

Influence of frustration and the lattice structure

The influence of the lattice structure on the antiferromagnetic transition temperature at half filling is visualized in the left graph of figure 4.29, where T_N is shown as a function of the next-nearest neighbor hopping t' for the 3d-SCNNN lattice. Increasing the absolute value of t' results in a reduction of T_N eventually reaching zero for $t'/t \approx -0.6$. This is in agreement with the expectation since at low to intermediate values of U the disturbance of the nesting property of the Fermi surface (cf. figure D.2 in appendix D) due to t' reduces the phase space for magnetic scattering while at large values of U, where local moments are the driving force behind the magnetism, geometric frustration in the couplings also suppresses AFM.

However, the local moments are not influenced by the introduction of frustration, only their couplings are affected. This can be deduced from the right graph in figure 4.29, where the maximum value of $\mu_{eff}^{(loc)}$ is not reduced, even for t'/t as large as -0.4. Only the dependence on ϵ or n_σ is slightly altered and an asymmetry introduced, but the characteristic behavior remains unchanged with increasing frustration.

In order to examine the robustness of AFM in different geometries, figure 4.30 compares the Néel temperature for all three cubic lattices without and with next-nearest neighbor hopping. For the SC lattices the effect of t' is moderate, as the transition temperature resembles the $t' = 0$ curve and its value is reduced by somewhat about $10 - 20\%$.

More drastic is the influence of a non-vanishing t' in the BCC lattice. While the transition temperatures for $t' = 0$ are of the same magnitude and follow the same characteristic U-

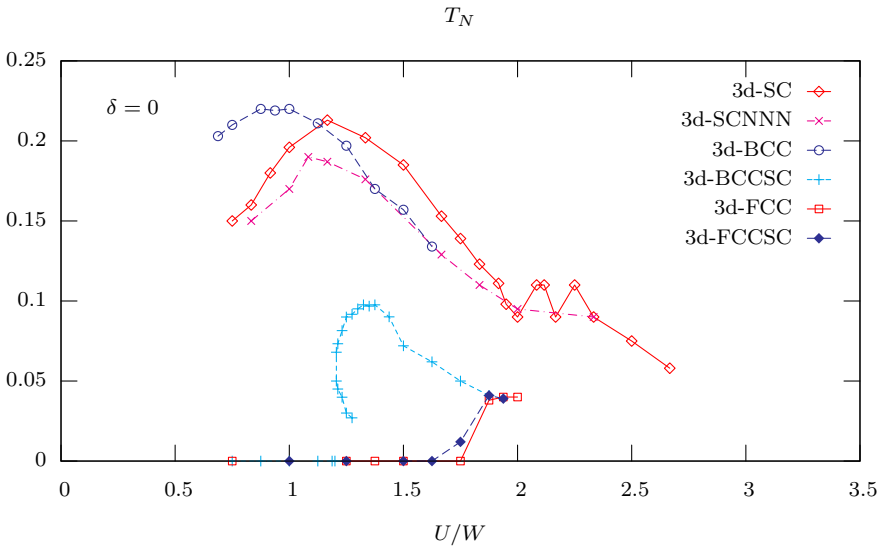

Figure 4.30: Néel temperature for the three cubic lattices without and with next-nearest neighbor hopping for half filling ($\delta = 0$) as a function of U in units of the half bandwidth W. The next-nearest neighbor hopping is $t'/t = -0.2$ for the SCNNN and BCCSC lattices, while for the FCCSC lattice it is $t'/t = 0.2$. The hopping is chosen to be $t = 0.5$ for the SC and BCC lattices and $t = -0.5$ for the FCC case. This implies a half bandwidth of $W = 3$ for the SC lattices and $W = 4$ for the BCC and the FCC lattices (see footnote 11).

dependence as in the SC lattice, the suppression of antiferromagnetism for the BCCSC lattice with $t'/t = -0.2$ is considerably stronger. For small Coulomb repulsion T_N is even reduced to zero.

The pronounced difference in the sensitivity to t' at small and large U in the BCCSC lattice demonstrates the different nature of the magnetism. At small U, magnetism is caused by an enhanced scattering amplitude for particle-hole pairs at the Fermi surface due to the nesting property. This enhancement is very sensitive to the geometry of the Fermi surface, as it can be seen in figure D.2 of appendix D. Trying to fit the AFM wave vectors ($\underline{q}_{AFM} = \pi(1,1,1)^T$ in the SC lattice and $\underline{q}_{AFM} = 2\pi(1,1,1)^T$ and $2\pi(1,0,0)^T$ in the BCC case) into the respective Fermi surfaces, thereby mimicking the phase space volume for a particle-hole excitation, the stronger influence of t' on the BCC nesting property becomes obvious: while in the SC case the corresponding parallel regions are slightly deformed, in the BCC lattice whole parts of the Fermi surface are moved to different crystal momentum vectors, thereby not only disturbing but destroying the nesting property. This leads to the vanishing of the Néel temperature for small to intermediate U in the BCCSC lattice, while for the SCNNN case the temperatures are only reduced.

On the other hand, at large U the magnetic response of the system is produced by strong local moments, which are not very sensitive to the lattice type, as shown in the right graph of figure 4.29. The elementary exchange couplings are still antiferromagnetic, as it can be guessed from the effective large U limit of the Hubbard model (4.2.7), and t' merely introduces geometric frustration. The resulting effective exchange between neighboring sites is thus reduced through the presence of t', but still of antiferromagnetic nature for not too large t'. Therefore the local moment magnetism is rather insensitive to the lattice

structure as compared to the small U Stoner magnetism dominated by the geometry of the Fermi surface.

This picture is confirmed in the face-centered cubic (FCC) lattices, with and without next-nearest neighbor hopping. Antiferromagnetism does not occur at half filling for small to intermediate U due to the complete lack of any nesting. But at large $U \gtrsim 7$ AFM starts to show, due to the presence of large local magnetic moments which still couple antiferromagnetically. This is in qualitative agreement with earlier findings [Ulm98].

The transformation between itinerant and local moment magnetism can either be smooth, as in the simple-cubic lattices or the unfrustrated body-centered cubic lattice, or quite abrupt as in the frustrated body-centered cubic case. There, the Néel temperature jumps from zero to a finite value $T_N \approx 0.09$ between $U = 4.75$ and $U = 5$.

The inverse static antiferromagnetic susceptibility $1/\chi_{mag}(\underline{q}_{AFM}, 0)$ is shown in the upper left graph of figure 4.31 for these two values of the Coulomb repulsion. At high temperatures both curves show the usual linear behavior, but at lower temperatures they saturate and even start to increase again. For $U = 4.75$ the inverse susceptibility always stays positive, i.e. $\chi_{mag}(\underline{q}_{AFM}, 0)$ is alway finite and no phase transition occurs. For $U = 5$, however, before traversing the minimum $1/\chi_{mag}(\underline{q}_{AFM}, 0)$ reaches zero, implying a diverging susceptibility and an AFM phase transition. The minimum in the inverse susceptibility, i.e. the maximum in $\chi_{mag}(\underline{q}_{AFM}, 0)$, is encountered only at unphysical temperatures below the transition.

Contrary to the case of the SC lattice with $U = 10$, $n_\sigma = 0.485$ (cf. figures 4.20 and 4.21), where the saturation in one wave vector component of the susceptibility was accompanied by an increase in another one, in this situation all $\underline{q}$-components show the qualitative same temperature dependency and the antiferromagnetic component is always the largest (not shown).

By increasing the Coulomb matrix element from $U = 4.75$ to $U = 5$, the solid red curve in the left graph of figure 4.31 transforms smoothly into the dashed blue one. Thereby the minimum in $1/\chi_{mag}(\underline{q}_{AFM}, 0)$ is continuously shifted towards the zero axis and introduces a discontinuous transition with a finite Néel temperature as soon as it reaches zero. By further increasing U from that point two zeros of $1/\chi_{mag}(\underline{q}_{AFM}, 0)$ are produced, which occur at temperatures $T_1 \approx 0.03$ and $T_2 \approx 0.09$ in the case of $U = 5$. This leaves the somewhat unusual situation, that antiferromagnetism occurs only in the finite temperature interval $[T_1, T_2]$ and the paramagnetic phase becomes stable again for very low temperatures $T < T_1$. By tuning the Coulomb repulsion in that manner, the low temperature region $T < T_1$ always has a finite susceptibility and thus no magnetic instability is produced. Therefore the branch of the susceptibilities below T_1 is taken as the physical value of the susceptibility, even though no statement could have been made for $T < T_2$, when regarding the susceptibility for a fixed U as a functions of temperature.

As a consequence the Néel temperature in figure 4.30 attains a negative slope and a reentrant behavior is predicted. Such characteristics imply the rather unusual behavior, that the system can be driven to antiferromagnetism by *increasing* the temperature, i.e. by heating.

For the Hubbard model within weak coupling treatments reentrant behavior was already found in infinite [Hal94] and two [Hon96] space dimensions. Similar reentrant behavior was found in the extended Hubbard model with an additional nearest neighbor Coulomb interaction for the charge-ordering transition [Pie99].

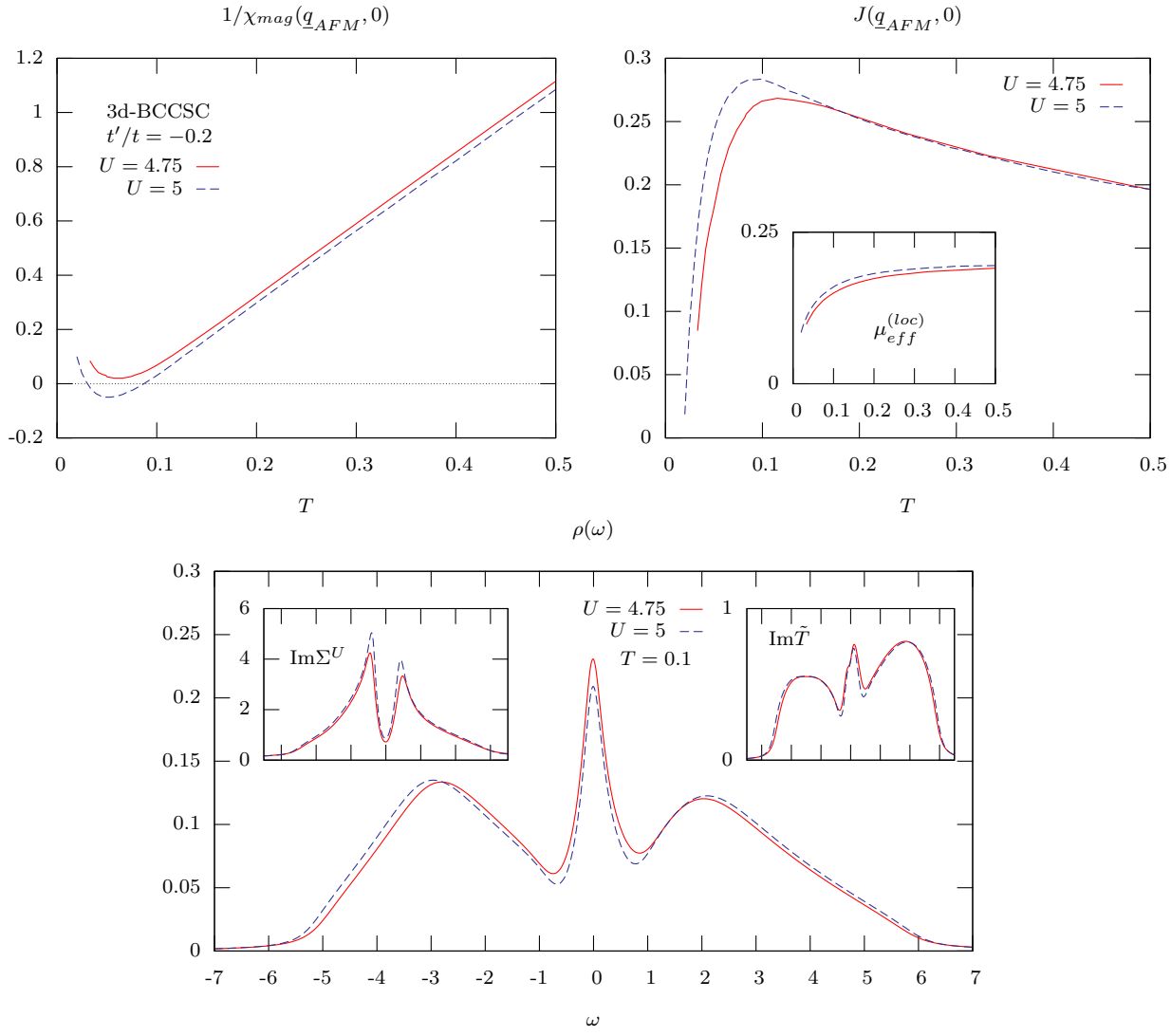

Figure 4.31: Inverse static antiferromagnetic susceptibility (upper left graph) effective antiferromagnetic coupling function (upper right graph), effective local moment (inset in upper right graph) and the one-particle DOS (lower graph) for the 3d-BCCSC ($t'/t=-0.2$) lattice at half filling for two values of the Coulomb repulsion $U=4.75$ and $U=5$. The insets in the lower graph show the imaginary part of the correlation self-energy $\mathrm{Im}\Sigma^U(\omega-i\delta)$ (left) and the effective medium $\mathrm{Im}\tilde{T}(\omega-i\delta)$ (right). The temperature for the one-particle quantities is $T=0.1$.

In order to understand this behavior figure 4.31 shows the effective antiferromagnetic exchange coupling $J(\underline{q}_{AFM}, 0)$ (upper right graph; cf. equation (2.3.48)), the local moment $\mu_{eff}^{(loc)}$ (inset; cf. equation (4.2.1)) and the one-particle quantities (lower graph). As it could already be guessed from the inverse magnetic susceptibility, all quantities displayed for the situations $U = 4.75$ and $U = 5$ show the same qualitative characteristics: both situations are metallic with a rather pronounced many-body resonance at the Fermi level in the DOS (lower graph), the correlation self-energies (left inset in the lower graph) have the characteristic quadratic Fermi liquid minimum around $\omega \approx 0$ and the effective media (right inset in the lower graph) are also very similar in both cases. The $\underline{k}$-resolved band structures (not displayed) are qualitatively the same as well.

The effective couplings (upper right graph) and the magnetic moments (inset) have the same qualitative temperature dependence and differ only slightly in their absolute values. The moments decline with decreasing temperature and are quite large before the onset of lattice coherence at very low temperatures around $T \approx 0.1$. The effective AFM coupling at first increases with decreasing temperature due to the growing many-body resonance at the Fermi level, then saturates and even declines for very low temperatures. As argued in the previous section, the drop is a consequence of the onset of lattice coherence and the overall reduction of magnetic exchange due to the correlations building up to provide the Kondo-screening.

Since the influence of frustration is larger for smaller values of U, this leads to the accelerated decline in J for $U = 4.75$ when lattice coherence sets in at $T \approx 0.1$. Additionally, coherence sets in at temperatures T a little bit higher for smaller U, due to the increase of the low temperature scale T^* with decreasing U. This is also reflected in the somewhat unexpected fact that the coupling for the larger $U = 5$ exceeds that for the lower value $U = 4.75$. From the perspective of local moment magnetism the coupling should be inversely proportional to U and when seen from the weak coupling point of view, the height of the DOS at the Fermi level should be influential. Both reasonings would suggest the coupling to be smaller for the larger $U = 5$. The observed inverse tendency could be attributed to the different nature of the processes generating the coupling: the fraction of virtual excitation is larger with larger U and the influence of three and four site processes and their quantum mechanical interference (all processes which respect the geometry of the Fermi surface) is diminished. This just again reflects the qualitative difference between the pictures of local moment and itinerant Stoner magnetism and emphasizes the different impact of frustration on both types.

However, the difference in the absolute value of the antiferromagnetic coupling is only rather small and not qualitative. But nevertheless a dramatic difference in the magnetic properties is encountered, which therefore clearly indicates a delicate competition between the ordering tendency of the local moments and the reduction of the couplings between those due to the onset of lattice coherence and screening. A slight change in the magnitude of the local moment and the effective exchange coupling as a consequence of an increased Coulomb interaction U can induce a discontinuous jump in the transition temperature from zero to a finite value.

The observed reentrant behavior is a consequence of this competition and the delicate temperature dependence of the many-body effects. Near zero temperature the local moments are screened and the effective exchange couplings are very small due to the correla-

tions built into the screening clouds. In this situation the thermodynamically relevant degrees of freedom are the quasiparticles forming the renormalized Fermi liquid. So magnetism is characterized as Stoner-type magnetism of these excitations, but due to the frustration, the ordering is suppressed. With increasing temperature the coherent quasiparticles become destabilized and the screening is suppressed, leading to growing local moments. The less coherent the quasiparticles become, the less pronounced is the influence of frustration on the quantum mechanical interference of particle-hole excitations and consequently the effective exchange coupling increase. Thus at some temperature the system behaves more like a spin-system with antiferromagnetic couplings. If at some temperature these moments and couplings are strong enough, ordering occurs. Even though the paramagnetic low temperature phase is characterized by itinerant electronic excitations, the transition is produced by local moments and Heisenberg-type magnetism. At even higher temperatures the magnetically ordered state becomes unstable again due to thermal fluctuations leading to a re-establishing of a paramagnetic state.

So within this scenario, both archetypical forms of magnetism are in direct competition and the detailed temperature dependence of the many-body effects in connection with frustration lead to this reentrant behavior. Thus, such behavior can be expected to occur on many different lattices, where itinerant Stoner magnetism is suppressed by sufficiently large frustration, but local moment magnetism is still present. As a hint in that direction, even in the simple cubic lattice the transition was shown to be of first order with an abrupt jump in the Néel temperature [Zit04a, Zit04b].

Competition between the ordering of local moments due to indirect exchange mechanisms and Kondo screening are typically encountered in the periodic Anderson model (PAM) and the Kondo lattice model (KLM). Even if the similar competition encountered above is not a generic feature of the Hubbard model and occurs only for special situations, its mere existence in this simple model is still astonishing and shows the possibility of very complex phenomena induced by strong correlations.

Concluding remarks

Antiferromagnetism is indeed a generic and very robust phenomenon for the Hubbard model near half filling, especially in the local moment regime at large U, where it even occurs for non-bipartite lattices such as the FCC lattice.

At half filling a quantitative description within the present approach is obtained. Especially the regime between pure local moment and itinerant Stoner-type magnetism is described very well. The correlation effects leading to local moment formation, screening and their delicate competition are fully incorporated.

For large U and for finite doping, the delicate balance between kinetic energy and correlation effects leads to the suppression of magnetic ordering. In these situations the Kondo-screening and establishment of lattice coherence can be observed down to very low temperatures. Consequently a local collective magnetic mode associated with the breakup of Kondo-singlets emerges in the dynamic magnetic susceptibility, in addition to the dispersive response of still itinerant excitations.

Away from half filling antiferromagnetic fluctuations are overestimated as a consequence of the tendency of the ENCA to produced too high values of the DOS at the Fermi level and the very sensitive form of the susceptibility to such, even small, errors.

The tendency towards ferromagnetism is very pronounced within the present approach, which is a consequence of the disregard of certain correlations by means of the decoupling of frequency sums in the RPA-like manner. Therefore the estimates for the transition temperatures are too high and rather mimic those of the usual RPA.

Incommensurate magnetism is also found at the edges of the antiferromagnetic phase boundary. One advantage of the approach presented here is its capability to describe arbitrary ordering wave vectors due to the direct evaluation of the particle-hole propagator. This is especially important since this is not done in a framework of well-defined infinitely long-lived effective particles, as it is usually done in slave-boson, FLEX or two-particle self-consistent approaches in these situations (cf. [Sai97, Vil97, Bic91]). The full one-particle renormalization of the locally complete approximation and the dynamic two-particle vertex are retained.

An accurate description of incommensurate fluctuations is of special interest for the anomalous normal state properties of cuprate superconductors modelled through the two dimensional Hubbard model. However, when applying the present approximation to two-dimensional systems, it turns out that their overall behavior closely resemble the findings described above. Transition temperatures, which were calculated by the author but are not shown in this work, have the same characteristic interaction and doping dependence as in the higher dimensional case shown above. Even dynamic susceptibilities are qualitatively equivalent to the description to the previous chapters. Characteristic behavior of low dimensional systems or pronounced doping and momentum dependencies of response functions expected in the 2d Hubbard model (cf. [Ere01, Ari06, Yus07, She07, She08, Li08]) are not encountered, due to the neglect of the momentum dependency in the interaction self-energy and two-particle vertex. Within the present approximation the dimensionality only enters through the non-interacting DOS and the particle-hole propagator. Both of these influences are not strong enough to introduce behavior characteristic for low dimensional systems, and the mean-field like character of the present approximation dominates.

A step towards the incorporation of such effects can be archived by avoiding the RPA-like decoupling in order to better represent the mutual influence of lattice and local dynamics.

5 Summary and outlook

In this thesis, one- and two-particle correlation functions of strongly correlated electron systems were investigated in detail. Since the exact evaluation of Green functions in interacting systems is possible only for certain models or under very specific circumstances, approximation schemes had to be employed.

In the first chapter a diagrammatic approach to correlated electrons in a crystal lattice was reviewed, and the determining equations for the relevant two-particle Green functions, the Bethe-Salpeter equations, were derived. It was argued in some detail, how the locally complete approximation for the one-particle Green function – known in the literature as the dynamical mean-field theory (DMFT) – has to be extended to yield two-particle correlation functions. It was especially discussed, under which circumstances the mapping of the lattice model onto an interacting magnetic impurity model embedded into a self-consistent non-interacting host can be sustained in the two-particle extension.

Even though a numerical solution of the resulting coupled Bethe-Salpeter equations for the corresponding two-particle Green functions is within reach by means of the Matsubara-space matrix formalism, an evaluation for real frequencies was preferred. This was done in order to avoid the non-trivial, numerical analytic continuation of complex Fourier coefficients to the real frequency axis. Therefore, the integral equations were decoupled in the energy variables in a RPA-like manner and a rather simple, but still non-trivial form for the dynamic lattice susceptibility matrix was obtained. Judging from the functional form only, the hope was formulated (and in the later chapters confirmed) that this approximation could bridge between the two archetypical pictures of magnetism, i.e. the magnetism of itinerant weakly interacting particles and completely localized magnetic moments coupled by effective exchange interactions.

The essential step of the locally complete approximation is the solution of an effective single impurity Anderson model (SIAM). This step was described in chapter 3 and the existing enhanced non-crossing approximation (ENCA) was extended to treat dynamic susceptibilities as well. The procedure and difficulties encountered during the numerical calculation of two-particle correlation functions were then described and their predictions compared with existing results.

The ENCA was shown to properly describe the static and dynamic properties of the impurity. Apart from a slight violation of Fermi liquid relations at too low temperatures, the Green functions were obtained very accurately for various values of the Coulomb matrix element and over the whole range of excitation energies. The static charge and spin susceptibility were shown to be in excellent agreement with the exact results known from Bethe ansatz solutions. Even in situations with a very small local Coulomb matrix element U and in situations with strong valence fluctuations, the approximation proved to be very accurate. Only the charge susceptibility fell short of reproducing the correct results in intermediate valence situations.

The numerical simulations necessary to solve the coupled ENCA integral equations can be performed on simple desktop computers within minutes. In contrast to other methods like QMC, NRG or exact diagonalization, the extraction of dynamical Green functions of real energy variables does not involve any free parameters or numerical arbitrariness. These, more technical but equally important points, in combination with very accurate physical description, qualify the ENCA as a very promising candidate for an impurity solver to be used in the self-consistency cycle of the locally complete approximation.

The Hubbard model, which represents the simplest model for strongly interacting electrons in a crystal lattice, was investigated within the locally complete approximation in chapter 4. A particular emphasis was laid on the complicated many-body phenomena emerging at low temperatures. Especially the physical picture behind the formation of low energy quasiparticles as a characteristic indication of the lattice Kondo effect was developed.

It was discussed, that usually the low energy quasiparticles form a Fermi liquid ground state within the locally complete approximation. As a counterexample, a new route to the breakdown of the Fermi liquid formation was proposed. In situations, where van Hove singularities in the non-interacting density of states (DOS) are encountered in the vicinity of the Fermi level, the quasiparticle scattering amplitude was shown to behave in a non-Fermi liquid manner. The effective medium was shown to develop a minimum right at or in the vicinity of the Fermi level, which in turn led to the unusual energy dependence of the correlation self-energy. The physical reason for the enhanced quasiparticle scattering was speculated to be connected to a partial localization of electronic excitations in the flat parts of the dispersion relation.

In the following sections the magnetic properties of the Hubbard model were considered. At first, the different magnetic phases to be expected in the Hubbard model were briefly reviewed. For the simple-cubic lattice with and without next-nearest neighbor hopping the phase diagram was later produced. The transition temperatures did agree quite well with the values already known from the literature. Discrepancies were encountered for the doping dependency of the antiferromagnetic Néel temperature and the absolute height of the ferromagnetic transition temperature. Both overestimations could be attributed to the RPA-like decoupling of frequency sums in the Bethe-Salpeter equations.

Concerning the physical mechanisms underlying the magnetic response, it was of special interest in which situations the basic pictures of local moment and itinerant Stoner magnetism could be used to characterize the system. For Coulomb repulsions of the order of the half bandwidth, large local moments were encountered, and at high temperatures the model could be characterized to behave like a spin system. Upon lowering the temperature the forming quasiparticles could lead to a transformation of the picture into a behavior better described as Stoner magnetism. However, in these strongly correlated metallic situations with large moments and itinerant quasiparticles, a clear distinction between either types of magnetism is somewhat artificial.

At intermediate values of the Coulomb interaction, antiferromagnetic fluctuations dominated the behavior. The dynamic susceptibility showed a typical relaxation behavior with a dispersive paramagnon peak, and could be very well approximated by a tight-binding treatment of the particle-hole excitations. The antiferromagnetic transition was signalled by a softening of the critical mode, in complete agreement with the usual scenario for a continuous phase transition.

At large interaction strength and for finite doping, the competition between correlation and kinetic energy effects led to an overall suppression of the magnetic response. The simplified tight-binding description of the particle-hole excitations failed to provide a correct description, due to the neglect of important phase-informations and quantum mechanical interference of the propagating particles. For high temperatures the very large local moments dominated the magnetic properties and resulted in an enlarged antiferromagnetic response. At lower temperatures the behavior was qualitatively changes and ferromagnetism started to be dominant. But for very low temperatures of the order of the low energy scale T^*, the effective exchange couplings were dramatically reduced as consequence of the correlations built into the quasiparticle band structure. In this situation a localized collective magnetic mode emerged. It was attributed to a breakup of Kondo-singlets associated with screened local moments and consequently had a finite excitation energy $\sim T^*$.

The remaining discussion focussed on the influence of the lattice structure and frustration on the magnetic properties. It was shown, how frustration and the lack of nesting can lead to the complete suppression of antiferromagnetic order in the domains characterized by itinerant Stoner magnetism. In contrast, situations where large local moments are the driving force behind the magnetic ordering tendencies, the sensitivity to frustration and the lattice structure is greatly diminished.

In the strongly correlated metal, the competition between both types of magnetism can lead to an intriguing reentrant behavior. This was explicitly observed in the frustrated body-centered cubic lattice with small next-nearest neighbor hopping. The paramagnetic metal was shown to be unstable towards antiferromagnetism only in a finite temperature interval $0 < T_1 \leq T \leq T_2$.

The approximations presented were shown to yield excellent results for the description of strongly correlated systems. The essential many-body effects are captured in the one- and two-particle Green functions. Strong renormalizations leading to local moment formation, large effective masses and Kondo screening are faithfully incorporated.

The approximation for the dynamic susceptibility was capable of describing the very delicate transformation from the itinerant Stoner magnetism to localized moment magnetism characteristic for Heisenberg spin-system. The theoretically hard to grasp intermediate regime can be addressed and the competition of intriguing many-body effects described.

The ability to predict the dynamic magnetic susceptibility opens a wide field of application. This key quantity in the description of solids can be directly measured in experiments like inelastic neutron scattering (INS). The results of theoretical model calculations can be compared to experimental data and relevant mechanisms identified.

Concerning the future prospects, the first thing to do is certainly to avoid the RPA-like decoupling of the frequency sums in the Bethe-Salpeter equations. This could be either done by completely avoiding any decoupling and analytically continuing the equations to real frequencies. Or a more sophisticated decoupling scheme could be used, in which averages over products of local and itinerant quantities are performed in order to capture leading effects of their mutual influence.

As it should be clear by now, the details of the lattice structure can play a very important role. The presented approach is capable of dealing with arbitrary lattice structures and physical quantities can be obtained for any wave vector, while incorporating complicated many-body effects. Therefore, it could be applied to the calculation of observable quantities

in which the lattice enters explicitly, like optical conductivities, NMR relaxation times and generally transport coefficients,

Another direction of future progress involves the application of the approximation to more complicated models, such as two- and three-band Hubbard models or the periodic Anderson model (PAM). The latter consists of an array of periodically positioned correlated Anderson impurities, each of which coupled to the same uncorrelated host. Within these models, the influence of various sorts of hybridization and hopping matrix elements could be studied. Especially their implications concerning the competition between indirect Ruderman-Kittel-Kasuya-Yosida- (RKKY) exchange and Kondo-screening is very interesting.

Due to the increased number of one- and two-particle matrix elements in multi-band models, the phase space is considerably enlarged, and the physical behavior found in such models is rather complex. Considering the already very intricate physical behavior of the comparatively simple one-band Hubbard model, the importance of a thorough and detailed understanding of correlation effects and their underlying basic mechanisms is essential. Hopefully, this thesis contributes some insight within this ambitious undertaking.

Appendix

A Details and examples to the cumulant perturbation theory

This appendix is meant as a supplement to chapter 2 and gives some details and examples to the cumulant perturbation theory and the locally complete approximation.

General setup

The excluded volume problem of the perturbation expansion as stated in equation (2.1.11), is exemplified on a typical expression contributing to the one-body Green function (2.1.14) with a fixed number of hopping terms $\hat{T}_{ij}$. For simplicity it is assumed, that $\hat{T}_{ij}$ connects only nearest neighbors and transfers an electron from site j to site i. Indicating this hopping process by a dashed arrow pointing from site j to site i, contributions included in such a term can be represented by graphs on a lattice as the ones shown in A.1. On every site j to (from) which an arrow points, the appropriate creation (annihilation) operator is implied. Since the unperturbed Hamiltonian does not mix different lattice sites, the expectation value factorizes in a product of expectation values of creation and annihilation operators on the same site, connected through hopping matrix elements. Thus for every lattice site with N arrows entering and leaving, a local N-particle Green function

$$G^N_{i\alpha_1,i\ldots,i\alpha_l;i\alpha'_l,\ldots,i\alpha'_1}(\tau^{(l_1)},\ldots,\tau^{(l_N)};\tau^{(l'_N)},\ldots,\tau^{(l'_1)})|^{(0)} = \langle\mathcal{T}\big[\hat{c}_{i\alpha_1}(\tau^{(l_1)})\ldots\hat{c}_{i\alpha_N}(\tau^{(l_N)})\,\hat{c}^\dagger_{i\alpha'_N}(\tau^{(l'_N)})\,\hat{c}^\dagger_{i\alpha'_1}(\tau^{(l'_1)})\big]\rangle_0 \tag{A.1}$$

is produced.

The lattice indices are chosen such, that only one-body Green functions appear. Such a contribution is shown in figure A.1(a). To get the complete contribution of this term, the sum over all possible lattice sites has to be performed. By doing so, all possible continuous path, connected and disconnected, are generated, which start at the site labeled with $1'$ and end at 1. These two sites represent the external operators $\hat{c}^\dagger_{j\beta}(\tau'_1)$ and $\hat{c}_{i\alpha}(\tau_1)$. Path with lines starting and ending at lattice sites other than 1 or $1'$ need not to be taken into account, since the Hamiltonian conserves the particle number. The contribution in figure A.1(a) represents a path with one additional disconnected ring. The analytic contribution is a product of eight local one-body Green functions connected with elementary transfers (representing the path from $1'$ to 1) and an additional product of four local one-body Green functions also connected with transfers but unconnected to the former path (representing the ring),

$$\Big(\underbrace{G^1_{1'}|^{(0)}\,t_{1j}G^1_j|^{(0)}\,t_{jn}G^1_j|^{(0)}\ldots t_{mk}G^1_k|^{(0)}\,t_{k1'}G^1_1|^{(0)}}_{\text{path from } 1' \text{ to} 1}\Big)\cdot\Big(\underbrace{t_{l_1l_2}\,G^1_{l_2}|^{(0)}\ldots t_{l_4l_1}G^1_{l_1}|^{(0)}}_{\text{disconnected loop}}\Big)\quad . \tag{A.2}$$

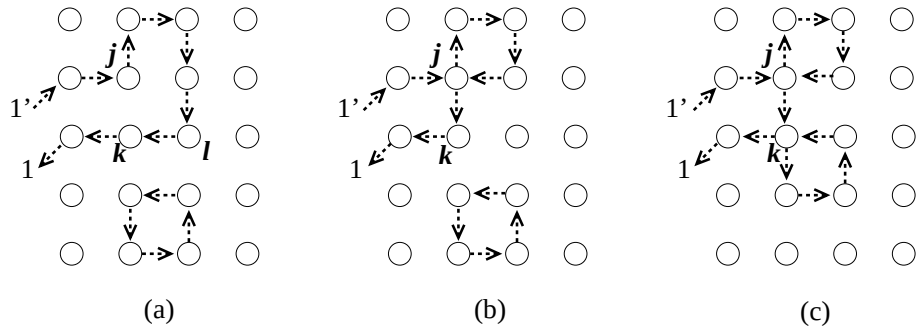

Figure A.1: Different contributions to the one-particle Green function

In equation (A.2) the time arguments and quantum numbers are omitted for brevity, but the lattice indices kept. By performing the lattice sums in (A.2), all deformed versions of the path shown in figure A.1 are created. One such deformed path is shown in the graph of figure A.1(b). There, the site labeled with the index l is moved onto the site labeled with j. Since in that case, two arrows enter and leave the site j, a two-body Green function has to be used on site j. In usual perturbation expansions, i.e. a perturbation theory with respect to the interaction, Wick's theorem would be applied to decompose this higher Green function into products of one-particle Green functions,

$$G^2(12;2'1')|^{(0)} = G^1(1;1')|^{(0)}G^1(2;2')|^{(0)} - G^1(1;2')|^{(0)}G^1(2;1')|^{(0)} \quad . \tag{A.3}$$

The then generated terms are the same as the ones obtained by just taking equation (A.2) and freely summing over all lattice indices. By using Wick's theorem consequently for every higher Green function and doing this kind of analysis thoroughly, all lattice sums could be performed freely to get the complete contribution of a term with fixed number of hoppings. Concerning the partition function, for every specific diagram connecting start- and endpoint $1'$ and 1, such as the term on the left in brackets in equation (A.2), higher order terms produce a series of closed unconnected loops which just multiply this expression. By examining these terms, it would become clear, that to every perturbational term the whole partition function is generates as a factor and thus would cancel with the explicit prefactor in equation (2.1.11). As a direct consequence of this, only connected diagrams had to be taken into account, where no factorized loops exist.

However, Wick's theorem is not applicable in the present scheme, since the unperturbed Hamiltonian $\hat{H}_0$ includes the local Coulomb interaction. To get the accurate physical contribution of a term of the type portrayed in equation (A.2), we must restrict the sum of lattice sites to those sets, not having any two or more local one-particle Green function on the same site. Alternatively stated, we have to sum all path which do not intersect each other. For example, summing the position of the loop in figure A.1(b) over the lattice sites, it eventually ends up at the position shown in figure A.1(c). The term with a product of two Green functions at the site k has to be excluded, since the right term to include has a two-particle Green function at the site k and cannot be factorized by the use of Wick's theorem.

As stated in the main text, the solution to this problem is the usage of cumulant Green functions. Roughly speaking, the N-body cumulant represents the N-body correlations

present in the N-body Green function. The N-body Green function can thus be expressed as a sum over products of cumulants as indicated in equations (2.1.17) to (2.1.19).

To understand, how the usage of cumulant averages solves the excluded volume problem, suppose the lattice sum of the graph shown in figure A.1(a) is done in an unrestricted manner. An error is made, whenever site l is equal to site j and a product of two one-body Green functions is taken into account instead of a two-body Green function. In order to correct this, the two terms involving products of two one-body Green functions at site j[1] need to be subtracted and the accurate term shown in A.1(b) added. Exactly this is done by replacing the two-body Green function at site j with the local two-body cumulant.

A in-depth analysis of symmetry factors, signs and possible paths on the lattice reveals, that using only local N-body cumulant vertices instead of local N-body Green functions, allows for the lattice summations in all diagrams to be done without restrictions. The cumulant correction terms included at every local vertex exactly cancel all unphysical terms generated through the free lattice sums. A direct consequence is the applicability of the linked cluster theorem, i.e. the factorization and thereby cancelation of the partition function for every connected diagram.

The diagrammatic rules to obtain the analytic expression for a contribution with E external creation and annihilation operators attached to a selected sites and with given times and quantum numbers are as follows:

1. Draw a connected graph composed of point vertices and directed lines connecting the point vertices. E point vertices must be situated at the positions of the external lines and each point vertex must have the equal number of entering and leaving lines attached.

2. Assign a lattice index to every point vertex.

3. Assign a time variable to every directed connection between lattice sites.

4. Assign local quantum numbers to the start- and endpoint of every connection between lattice sites and include the associated matrix element $t_{ij}^{\alpha\beta}$.

5. For every lattice site with N entering and N leaving lines, include the N-body cumulant average. The time arguments and quantum numbers have to match the ones of the attached lines.

6. Multiply by the symmetry factor and sign of the diagram

7. Sum over all lattice indices, quantum numbers and integrate all time arguments (except the ones specified for the external lines).

The diagrammatic rules for a contribution with E external operators can also be formulated in Fourier and Matsubara space:

[1] Two of these terms exist. Additionally to the shown term, there exists a term, where the direction of the ring starting and ending at j in figure A.1(b) is reversed, which is also a term produced by the free lattice sum.

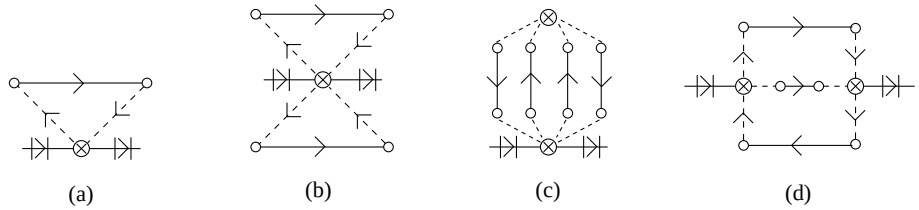

Figure A.2: Contributions to the cumulant self-energy Σ^c.

1. Draw a connected graph composed of point vertices and directed lines connecting the point vertices and with E external lines. Each point vertex must have the equal number of entering and leaving lines attached.

2. Assign a crystal momentum to every line; momentum is conserved at every point vertex.

3. Assign a Matsubara frequency to every directed connection between lattice sites.

4. Assign local quantum numbers to the start- and endpoint of every connection between lattice sites and include the associated matrix element

$$t_{\underline{k}}^{\alpha\beta} = \frac{1}{N_0} \sum_{i,j} e^{i\underline{k}(\underline{R}_i - \underline{R}_j)} \, t_{ij}^{\alpha\beta} \quad . \tag{A.4}$$

5. For every vertex with N entering and N leaving lines include the N-body cumulant average. The frequency arguments and quantum numbers have to match the ones of the attached lines.

6. Multiply by the symmetry factor and sign of the diagram

7. Sum over all crystal momentum, quantum numbers and Matsubara frequencies (except the ones specified for the external lines).

The term *diagram* in the context of the cumulant perturbation theory will always refer to a contribution generated with the above rules. Such a diagram represents one topological arrangement of cumulant vertices and their connections on the lattice, including the symmetry factors, sign factors, time integrations (frequency sums) and lattice (momentum) sums. Due to the above rules, no two or more lattice indices can be chosen to be equal for any cumulant vertices, i.e. no two cumulant vertices can occur on the same lattice site. These contributions are implicitly generated be the free lattice sums.

In order to determine a physical quantity of interest, e.g. the one-body Green function, all topological distinct diagrams contributing to this quantity have to be summed up.

Locally complete approximation

The central quantity for the determination of the one-body Green function is the cumulant self-energy $\underset{\approx}{\Sigma}^c$. As stated in the main text, it is build from all one-particle irreducible (1PI) diagrams. Some terms contributing to the cumulant self-energy are depicted in figure A.2.

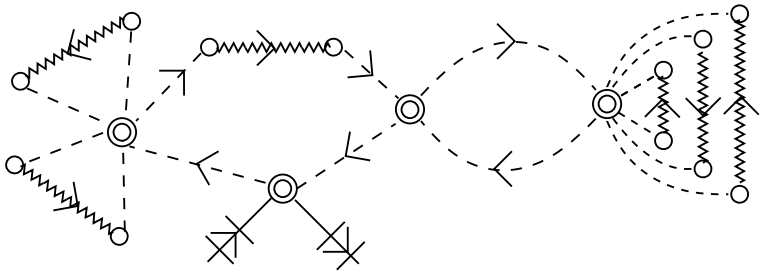

Figure A.3: Typical contribution to the local Green function the locally complete approximation when expressed in terms of effective local averages with the corresponding partition function Z_{loc} (nested circles). The zig-zag lines with attached transfers denote propagations excluding the base point of the loop.

The dashed lines denote the single-electron transfers $\underline{\underline{t_k}}$ and a crossed circle stands for a local cumulant Green function, whose number of entering and leaving lines indicate its order. Arrows enclosed in vertical bars do not represent any Green function, but merely indicate the external frequency and momentum entering and leaving the diagram. The single full line depicts the one-body Green function of the *free theory*, which is composed of atomic Green functions $\underline{\underline{G}}(i\omega_n)|^{(0)}$ and successive single-electron transfers only, without any higher order cumulants appearing.

In all terms contributing to $\underline{\underline{\Sigma}}^c$ the external lines have to be attached to a local n-body cumulant average, where necessarily $n > 2$. The inner lines have to start and end with single-electron transfers $\underline{\underline{t_k}}$ to make sure no two cumulants appear on the same lattice site, while all lattice summations are performed freely. The terms shown in figure A.2(a)-(c) contribute to the local, i.e. momentum independent, self-energy, since the external lines are attached to the same local cumulant. The term shown in A.2(d) constitutes the first non-local contribution.

For the locally complete approximation, the diagrams specified through the selection rules a) and b) in section 2.2 (see page 11) contribute to the cumulant self-energy. As argued in the main text, these rules break the scheme of the cumulant perturbation theory and do not only select whole topological diagrams. As examples for diagrams, which do not contribute as a whole, but are included only partially, consider figure A.2(c) and (d). Both diagrams are not included as long as the two explicitly shown cumulant vertices are on different lattice sites, since they are connected by more than two lines (four and three), which disobeys condition b). However, they are included if the vertices come together on the same site, which happens as the lattice sums are carried out.

The nature of the locally complete approximation is best revealed by reversing the cumulant decomposition for the local one-body Green function. By doing this, i.e. expressing all cumulant vertices in terms of physical local Green function, most of the cumulant correction terms cancel each other, so that at each local site only one physical N-body expectation value remains. The unconnected diagrams, which do appear, can all be absorbed into a effective partition function an every site, and thus define a effective local average. A typical contribution to the local Green function is indicated in figure A.3. The nested circles indicate the effective local average with the partition function Z_{loc}. The zig-zag lines with

attached transfers denote loop-propagations which do not directly visit their base site, i.e. the site where they start and end. This restriction on inner loops is a consequence of the fact that all terms incorporating a loop which did return to the base site were used to cancel cumulant correction terms on that site. As indicated in that figure, inner loops have additional nested inner loops attached, where again the base point of that nested loop must be excluded from the propagation.

The error made in the locally complete approximation can be clearly seen, as the loop-propagations attached to any inner site will for example touch the site 0 with the external lines attached. This term is unphysical and should be replaced by a term with a higher order Green function at the site with the external lines, but is not done in this approximation.

The irreducible transfer matrix $\tilde{\underset{\approx}{T}}$ is introduced as the sum of all processes starting and ending at a specific site, without returning to this site during the propagation. Inner loops starting and ending at any site during such a loop-propagation may return to the original site, but they merely represent processes dressing this irreducible propagation. So when expressing the local Green function with the fully dressed irreducible loop propagator, the diagram shown in figure A.3 is part of the first term in the schematic expansion of figure 2.3, having only one inner loop.

B Matrix notation of orbital quantum numbers

The orbital structure of physical quantities is encoded into a matrix notation. One- and two-particle quantities are indicated by a wavy and straight double underline, respectively. The matrix elements are

$$A_{\alpha\beta} = \left[\underset{\approx}{A}\right]_{\alpha\beta} \tag{B.1}$$

$$A_{\alpha\beta\gamma\delta} = \left[\underline{\underline{A}}\right]_{\alpha\beta\gamma\delta} \tag{B.2}$$

and their graphical representation is depicted in the upper part of figure B.1. The matrix multiplication of these objects is defined by

$$\left[\underset{\approx}{A}\,\underset{\approx}{B}\right]_{\alpha\beta} = \sum_{\kappa} A_{\alpha\kappa}\, B_{\kappa\beta} \tag{B.3}$$

$$\left[\underline{\underline{A}}\,\underline{\underline{B}}\right]_{\alpha\beta\gamma\delta} = \sum_{\kappa} A_{\mu\beta\gamma\kappa}\, B_{\alpha\kappa\mu\delta} \quad , \tag{B.4}$$

which is shown in the lower part of figure B.1.

The order of the creation and annihilation operators in the definition of Green functions, i.e. all creation operators are to the right of the annihilation operators, is shadowed in the order of the matrix indices. Schematically

$$A_{\alpha\beta\gamma\delta} \sim \langle \hat{c}_\alpha \hat{c}_\beta \hat{c}^\dagger_\gamma \hat{c}^\dagger_\delta \rangle \quad . \tag{B.5}$$

Combined with the definition of the matrix multiplication (B.4), this causes that the sequence of factors in a product is reversed in the graphical representations compared to its analytical counterpart.

A two-particle matrix, which is composed of the two one-particle quantities $\underset{\approx}{A}$ and $\underset{\approx}{B}$ is indicated with the notation $\underline{\underline{AB}}$ and its matrix elements follow the definition of a tensor product,

$$\begin{aligned} \left[\underline{\underline{AB}}\right]_{\alpha\beta\gamma\delta} &\equiv \left[\underset{\approx}{A} \otimes \underset{\approx}{B}\right]_{\alpha\beta\gamma\delta} \\ &= A_{\alpha\gamma}\, B_{\beta\delta} \quad , \end{aligned} \tag{B.6}$$

which can be seen on the left side in figure B.2.

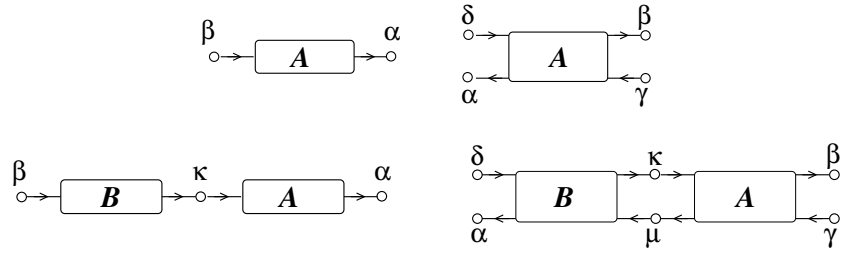

Figure B.1: Graphical representation of orbital matrices and their multiplication. On the left are the graphical representation and the definition of a multiplication for one-body matrices, on the right for two-body matrices.

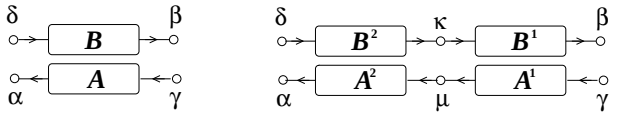

Figure B.2: Graphical representation of the composite object $\underline{\underline{\underline{AB}}}$ (left) and the multiplication $\underline{\underline{\underline{A^1B^1}}}\ \underline{\underline{\underline{A^2B^2}}}$ (right).

For the matrix product of two composite quantities the distributive law is obtained with the above definitions

$$\left[\underline{\underline{\underline{A^1B^1}}}\ \underline{\underline{\underline{A^2B^2}}}\right]_{\alpha\beta\gamma\delta} = \sum_{\kappa\mu} \left[\underset{\approx}{A}^1 \otimes \underset{\approx}{B}^1\right]_{\mu\beta\gamma\kappa} \left[\underset{\approx}{A}^2 \otimes \underset{\approx}{B}^2\right]_{\alpha\kappa\mu\delta} \tag{B.7}$$

$$= \sum_{\mu} A^1_{\mu\gamma}\, A^2_{\alpha\mu} \sum_{\kappa} B^1_{\beta\kappa}\, B^2_{\kappa\delta} \tag{B.8}$$

$$= \left[(\underset{\approx}{A}^2 \underset{\approx}{A}^1) \otimes (\underset{\approx}{B}^1 \underset{\approx}{B}^2)\right]_{\alpha\beta\gamma\delta} \tag{B.9}$$

$$= \left[\underline{\underline{\underline{(A^2A^1)(B^1B^2)}}}\right]_{\alpha\beta\gamma\delta} \quad . \tag{B.10}$$

The reverse order of the one-particle product of $\underset{\approx}{A}^1$ and $\underset{\approx}{A}^2$ stems from the fact that this part describes a hole-propagation, i.e. the arrows along the lines point in the opposite direction.

C Integral equations for general susceptibilities in the SIAM

In this appendix, the general analytic expressions for the sets of integral equations determining the susceptibility functions $\chi_{M,M'}(z,z')$ and $Y_{M,M'}(z,z')$ are explicitly stated. For the motivation and discussion of these see section 3.3.

The analytical expression for the coupled set of integral equations for the susceptibility functions $\chi_{M,M'}(z,z')$ as they are shown in figure 3.5 read within the FNCA

$$\begin{aligned}\chi_{M,0}(z,z') = \Pi_0(z,z')\Big\{&\delta_{0,M} \\ &+ \sum_\sigma \int dx \Delta^+(x)\, \Lambda_{0,\sigma}(z',x)\, \chi_{M,\sigma}(z{+}x, z'{+}x)\, \Lambda_{0,\sigma}(z,x) \\ &+ \sum_\sigma \int dx\, dy \Delta^+(x)\Delta^+(y)\, \Lambda_{0,\sigma}(z',x)\, P_\sigma(z'{+}x)\, \Lambda_{2,\sigma}(z'{+}x{+}y, y)\cdot \\ &\cdot \chi_{M,2}(z{+}x{+}y, z'{+}x{+}y) \Lambda_{2,\bar\sigma}(z{+}x{+}y, x)\, P_{\bar\sigma}(z{+}y)\, \Lambda_{0,\bar\sigma}(z,y)\Big\} \end{aligned} \tag{C.1}$$

$$\begin{aligned}\chi_{M,\sigma}(z,z') = \Pi_\sigma(z,z')\Big\{&\delta_{\sigma,M} \\ &+ \int dx \Delta^-(x)\, \Lambda_{0,\sigma}(z'{-}x, x)\, \chi_{M,0}(z{-}x, z'{-}x)\, \Lambda_{0,\sigma}(z{-}x, x) \\ &+ \int dx\, dy \Delta^-(x)\Delta^+(y)\, \Lambda_{0,\sigma}(z'{-}x, x)\, P_0(z'{-}x)\, \Lambda_{0,\bar\sigma}(z'{-}x, y)\cdot \\ &\cdot \chi_{M,\bar\sigma}(z{-}x{+}y, z'{-}x{+}y)\, \Lambda_{2,\bar\sigma}(z{+}y, x)\, P_2(z{+}y)\, \Lambda_{2,\sigma}(z{+}y, y) \\ &+ \int dx \Delta^+(x)\, \Lambda_{2,\sigma}(z'{+}x, x)\, \chi_{M,2}(z{+}x, z'{+}x)\, \Lambda_{2,\sigma}(z{+}x, x) \\ &+ \int dx\, dy \Delta^+(x)\Delta^-(y)\, \Lambda_{2,\sigma}(z'{+}x, x)\, P_2(z'{+}x)\, \Lambda_{2,\bar\sigma}(z'{+}x, y)\cdot \\ &\cdot \chi_{M,\bar\sigma}(z{+}x{-}y, z'{+}x{-}y)\, \Lambda_{0,\bar\sigma}(z{-}y, x)\, P_0(z{-}y)\, \Lambda_{0,\sigma}(z{-}y, y)\Big\} \end{aligned} \tag{C.2}$$

$$\chi_{M,2}(z,z') = \Pi_2(z,z')\Big\{\delta_{2,M} + \sum_\sigma \int dx\Delta^-(x)\,\Lambda_{2,\sigma}(z',x)\,\chi_{M,\sigma}(z-x,z'-x)\,\Lambda_{2,\sigma}(z,x) + \sum_\sigma \int dx\,dy\Delta^-(x)\Delta^-(y)\;\Lambda_{2,\sigma}(z',x)\,P_\sigma(z'-x)\,\Lambda_{0,\sigma}(z'-x-y,y)\cdot \cdot\,\chi_{M,0}(z-x-y,z'-x-y)\,\Lambda_{0,\bar\sigma}(z-x-y,x)\,P_{\bar\sigma}(z-y)\,\Lambda_{2,\bar\sigma}(z,y)\Big\} \quad \text{(C.3)}$$

where the symmetry properties of the vertex functions

$$\Lambda_{\sigma,0}(z,z') = \Lambda_{0,\sigma}(z-z',z') \quad \text{(C.4)}$$
$$\Lambda_{\sigma,2}(z,z') = \Lambda_{2,\sigma}(z+z',z') \quad \text{(C.5)}$$

were used and the short-hand notations

$$\Delta^\pm(x) \equiv \Delta(x)\,f(\pm x) \quad \text{(C.6)}$$
$$\Pi_M(z,z') \equiv P_M(z)\,P_M(z') \quad \text{(C.7)}$$

introduced. Even so the above equations are formulated with two distinct complex variables z and z', for physical susceptibility functions $z' = z + i\nu_n$ is always implied.

Approximating the full vertex functions through their ENCA expressions (3.2.16) and inserting these into (C.1)-(C.3) yields

$$\chi_{M,0}(z,z') = \Pi_0(z,z')\Big\{\delta_{0,M} + \sum_\sigma \int dx\Delta^+(x)\,\big[\Lambda_{0,\sigma}(z',x) + \Lambda_{0,\sigma}(z,x) - 1\big]\,\chi_{M,\sigma}(z+x,z'+x) + \sum_\sigma \int dx\,dy\Delta^+(x)\Delta^+(y)\,P_\sigma(z'+x)\,P_{\bar\sigma}(z+y)\,\chi_{M,2}(z+x+y,z'+x+y)\Big\} \quad \text{(C.8)}$$

$$\chi_{M,\sigma}(z,z') = \Pi_\sigma(z,z')\Big\{\delta_{\sigma,M} + \int dx\Delta^-(x)\big[\Lambda_{0,\sigma}(z'-x,x) + \Lambda_{0,\sigma}(z-x,x) - 1\big]\,\chi_{M,0}(z-x,z'-x) + \int dx\Delta^+(x)\big[\Lambda_{2,\sigma}(z'+x,x) + \Lambda_{2,\sigma}(z+x,x) - 1\big]\,\chi_{M,2}(z+x,z'+x) + \int dx\,dy\Delta^+(x)\Delta^-(y)\Big[P_2(z'+x)\,P_0(z-y) + P_0(z'-y)\,P_2(z+x)\Big]\,\chi_{M,\bar\sigma}(z+x-y,z'+x-y)\Big\} \quad \text{(C.9)}$$

$$\chi_{M,2}(z,z') = \Pi_2(z,z')\Big\{\delta_{2,M} + \sum_\sigma \int dx \Delta^-(x)\big[\Lambda_{2,\sigma}(z',x) + \Lambda_{2,\sigma}(z,x) - 1\big]\, \chi_{M,\sigma}(z-x, z'-x) + \sum_\sigma \int dx\, dy \Delta^-(x)\Delta^-(y)\, P_\sigma(z'-x)\, P_{\bar\sigma}(z-y)\, \chi_{M,0}(z-x-y, z'-x-y)\Big\} \quad \text{(C.10)}$$

which are explicitly shown in figure 3.6.

To shorten lengthy equations in the following, frequencies just above and below the real axis will be abbreviated with

$$\begin{aligned} x^+ &\equiv x + i\delta \quad , \qquad \delta > 0 \\ x^- &\equiv x - i\delta \quad . \end{aligned} \quad \text{(C.11)}$$

To derive the equations for the defect quantities $Y_{M,M'}$ the identities

$$\begin{aligned} A(\omega^+)B(\omega^+) - A(\omega^-)B(\omega^-) = {} & \big[A(\omega^+) - A(\omega^-)\big]B(\omega^+) \\ & + A(\omega^-)\big[B(\omega^+) - B(\omega^-)\big] \quad , \end{aligned} \quad \text{(C.12)}$$

$$\begin{aligned} A(\omega^+)B(\omega^+)C(\omega^+) - A(\omega^-)B(\omega^-)C(\omega^-) = {} & \big[A(\omega^+) - A(\omega^-)\big]B(\omega^+)C(\omega^+) \\ & + A(\omega^-)\big[B(\omega^+) - B(\omega^-)\big]C(\omega^+) \\ & + A(\omega^-)B(\omega^-)\big[C(\omega^+) - C(\omega^-)\big] \end{aligned} \quad \text{(C.13)}$$

and

$$\Delta^+(x)e^{\beta x} = \Delta^-(x) \quad \text{(C.14)}$$

are repeatedly used. This allows to write down the sets in a closed form,

$$Y_{M,0}(\omega,\omega{+}\nu) = I_{M,0}(\omega,\omega{+}\nu) + \Pi_0(\omega^-,\omega{+}\nu^+)\Big\{ \sum_\sigma \int dx \Delta^-(x)\, \big[\Lambda_{0,\sigma}(\omega{+}\nu^+,x) + \Lambda_{0,\sigma}(\omega^-,x) - 1\big] Y_{M,\sigma}(\omega{+}x,\omega{+}\nu{+}x) + \sum_\sigma \int dx\, dy \Delta^-(x)\Delta^-(y)\, P_\sigma(\omega{+}\nu{+}x^+)\, P_{\bar\sigma}(\omega{+}y^-)\, Y_{M,2}(\omega{+}x{+}y,\omega{+}\nu{+}x{+}y)\Big\} \quad \text{(C.15)}$$

$$\begin{aligned} Y_{M,\sigma}(\omega,\omega{+}\nu) = {} & I_{M,\sigma}(\omega,\omega{+}\nu) + \Pi_\sigma(\omega^-,\omega{+}\nu^+)\Big\{ \int dx \Delta^+(x)\big[\Lambda_{0,\sigma}(\omega{+}\nu{-}x^+,x) + \Lambda_{0,\sigma}(\omega{-}x^-,x) - 1\big]\, Y_{M,0}(\omega{-}x,\omega{+}\nu{-}x) \\ & + \int dx \Delta^-(x)\big[\Lambda_{2,\sigma}(\omega{+}\nu{+}x^+,x) + \Lambda_{2,\sigma}(\omega{+}x^-,x) - 1\big]\, Y_{M,2}(\omega{+}x^+,\omega{+}\nu{+}x^+) \\ & + \int dx\, dy \Delta^-(x)\Delta^+(y)\Big[P_2(\omega{+}\nu{+}x^+)P_0(\omega{-}y^-) + P_0(\omega{+}\nu{-}y^+)P_2(\omega{+}x^-)\Big] Y_{M,\bar\sigma}(\omega{+}x{-}y,\omega{+}\nu{+}x{-}y)\Big\} \end{aligned} \quad \text{(C.16)}$$

$$
\begin{aligned}
Y_{M,2}(\omega,\omega{+}\nu) = I_{M,2}(\omega,\omega{+}\nu) + \Pi_2(\omega^-,\omega{+}\nu^+)\Big\{ & \\
\sum_\sigma \int dx \Delta^+(x) \big[\Lambda_{2,\sigma}(\omega{+}\nu^+,x) + \Lambda_{2,\sigma}(\omega^-,x) - 1\big]\, Y_{M,\sigma}(\omega{-}x,\omega{+}\nu{-}x) & \\
+ \sum_\sigma \int dx\, dy \Delta^+(x)\Delta^+(y)\, P_\sigma(\omega{+}\nu{-}x^+)\, P_{\bar\sigma}(\omega{-}y^-)\, Y_{M,0}(\omega{-}x{-}y,\omega{+}\nu{-}x{-}y)\Big\} \quad . &
\end{aligned}
\tag{C.17}
$$

The inhomogeneities $I_{M,M'}$ are rather lengthy,

$$
\begin{aligned}
I_{M,0}(\omega,\omega{+}\nu) = Y_0^0(\omega,\omega{+}\nu)\Big\{ & \delta_{0,M} \\
& + \sum_\sigma \int dx \Delta^+(x) \left[\Lambda_{0,\sigma}(\omega{+}\nu^+,x) + \Lambda_{0,\sigma}(\omega^+,x) - 1\right] \chi_{M,\sigma}(\omega{+}x^+,\omega{+}\nu{+}x^+) \\
& + \sum_\sigma \int dx\, dy \Delta^+(x)\Delta^+(y)\, P_\sigma(\omega{+}x{+}\nu^+)\, P_{\bar\sigma}(\omega{+}y^+)\, \chi_{M,2}(\omega{+}x{+}y^+,\omega{+}x{+}y{+}\nu^+)\Big\} \\
- 2\pi i\, \Pi_0(\omega^-,\omega{+}\nu^+)\Big\{ & \\
& \sum_\sigma \int dx\, dy \Delta^+(x)\Delta^-(y)\, \xi_{\bar\sigma}(\omega{+}y)\, P_2(\omega{+}x{+}y^+)\, \chi_{M,\sigma}(\omega{+}x^+,\omega{+}\nu{+}x^+) \\
& + \sum_\sigma \int dx\, dy \Delta^-(x)\Delta^-(y)\, P_{\bar\sigma}(\omega{+}y^-)\, \xi_2(\omega{+}x{+}y)\, \chi_{M,\sigma}(\omega{+}x^+,\omega{+}\nu{+}x^+) \\
& + \sum_\sigma \int dx\, dy \Delta^+(x)\Delta^-(y)\, P_\sigma(\omega{+}\nu{+}x^+)\, \xi_{\bar\sigma}(\omega{+}y)\, \chi_{M,2}(\omega{+}x{+}y^+,\omega{+}\nu{+}x{+}y^+)\Big\}
\end{aligned}
\tag{C.18}
$$

$$
\begin{aligned}
I_{M,2}(\omega,\omega{+}\nu) = Y_2^0(\omega,\omega{+}\nu)\Big\{ & \delta_{2,M} \\
& + \sum_\sigma \int dx \Delta^-(x) \big[\Lambda_{2,\sigma}(\omega{+}\nu^+,x) + \Lambda_{2,\sigma}(\omega^+,x) - 1\big]\, \chi_{M,\sigma}(\omega{-}x^+,\omega{+}\nu{-}x^+) \\
& + \sum_\sigma \int dx\, dy \Delta^-(x)\Delta^-(y)\, P_\sigma(\omega{+}\nu{-}x^+)\, P_{\bar\sigma}(\omega{-}y^+)\, \chi_{M,0}(\omega{-}x{-}y^+,\omega{+}\nu{-}x{-}y^+)\Big\} \\
- 2\pi i\, \Pi_2(\omega^-,\omega{+}\nu^+)\Big\{ & \\
& \sum_\sigma \int dx\, dy \Delta^-(x)\Delta^+(y) \xi_{\bar\sigma}(\omega{-}y)\, P_0(\omega{-}x{-}y^+)\, \chi_{M,\sigma}(\omega{-}x^+,\omega{+}\nu{-}x^+) \\
& + \sum_\sigma \int dx\, dy \Delta^+(x)\Delta^+(y) P_{\bar\sigma}(\omega{-}y^-)\, \xi_0(\omega{-}x{-}y)\, \chi_{M,\sigma}(\omega{-}x^+,\omega{+}\nu{-}x^+) \\
& + \sum_\sigma \int dx\, dy \Delta^-(x)\Delta^+(y)\, P_\sigma(\omega{+}\nu{-}x^+)\, \xi_{\bar\sigma}(\omega{-}y)\, \chi_{M,0}(\omega{-}x{-}y^+,\omega{+}\nu{-}x{-}y^+)\Big\}
\end{aligned}
\tag{C.19}
$$

$$
\begin{aligned}
I_{M,\sigma}(\omega,\omega{+}\nu) &= Y^0_\sigma(\omega,\omega{+}\nu)\Big\{\delta_{\sigma,M} \\
&+ \int dx\Delta^-(x)\big[\Lambda_{0,\sigma}(\omega{+}\nu{-}x^+,x)+\Lambda_{0,\sigma}(\omega{-}x^+,x)-1\big]\,\chi_{M,0}(\omega{-}x^+,\omega{+}\nu{-}x^+) \\
&+ \int dx\Delta^+(x)\big[\Lambda_{2,\sigma}(\omega{+}\nu{+}x^+,x)+\Lambda_{2,\sigma}(\omega{+}x^+,x)-1\big]\,\chi_{M,2}(\omega{+}x^+,\omega{+}\nu{+}x^+) \\
&+ \int dx\,dy\Delta^+(x)\Delta^-(y)\Big[P_2(\omega{+}\nu{+}x^+)P_0(\omega{-}y^+){+}P_0(\omega{+}\nu{-}y^+)P_2(\omega{+}x)\Big]\chi_{M,\bar\sigma}(\omega{+}x{-}y^+,\omega{+}\nu{+}x{-}y^+)\Big\} \\
&- 2\pi i\,\Pi_\sigma(\omega^-,\omega{+}\nu^+)\Big\{ \\
&\qquad \int dx\,dy\Delta^+(x)\Delta^-(y)\xi_{\bar\sigma}(\omega{-}x{+}y)P_2(\omega{+}y^+)\,\chi_{M,0}(\omega{-}x^+,\omega{+}\nu{-}x^+) \\
&\qquad + \int dx\,dy\Delta^-(x)\Delta^-(y)P_{\bar\sigma}(\omega{-}x{+}y^-)\xi_2(\omega{+}y)\,\chi_{M,0}(\omega{-}x^+,\omega{+}\nu{-}x^+) \\
&\qquad + \int dx\,dy\Delta^-(x)\Delta^+(y)\xi_{\bar\sigma}(\omega{+}x{-}y)P_0(\omega{-}y^+)\,\chi_{M,2}(\omega{+}x^+,\omega{+}\nu{+}x^+) \\
&\qquad + \int dx\,dy\Delta^+(x)\Delta^+(y)P_{\bar\sigma}(\omega{+}x{-}y^-)\xi_0(\omega{-}y^+)\,\chi_{M,2}(\omega{+}x^+,\omega{+}\nu{+}x^+) \\
&\quad + \int dx\,dy\Delta^+(x)\Delta^+(y)P_2(\omega{+}\nu{+}x^+)\,\xi_0(\omega{-}y)\,\chi_{M,\bar\sigma}(\omega{+}x{-}y^+,\omega{+}\nu{+}x{-}y^+) \\
&+ \int dx\,dy\Delta^-(x)\Delta^-(y)P_0(\omega{+}\nu{-}y^+)\,\xi_2(\omega{+}x^+)\,\chi_{M,\bar\sigma}(\omega{+}x{-}y^+,\omega{+}\nu{+}x{-}y^+)\Big\}
\end{aligned}
\tag{C.20}
$$

where

$$
Y^0_M(x,y) = \frac{e^{-\beta x}}{Z_f}\big[\Pi_M(x{+}i\delta,y)-\Pi_M(x{-}i\delta,y)\big] = -2\pi i\,\xi_M(x)P_M(y) \tag{C.21}
$$

$$
\xi_M(x) = -\frac{1}{2\pi i}\frac{e^{-\beta x}}{Z_f}\big[P_M(x{+}i\delta)-P_M(x{-}i\delta)\big] = \frac{e^{-\beta x}}{Z_f}\,\rho(x) \quad , \tag{C.22}
$$

and the so-called defect propagators $\xi_M(x)$, which are real and positive semi-definite functions.

D Lattice structures and dispersion relations

Simple Cubic Lattice

The simple-cubic (SC) lattice with nearest-neighbor hopping in d dimensions is a bipartite Bravais lattice formed with the primitive vectors

$$\underline{a}_i = a\,\underline{e}_i\ , \quad i = 1, 2, \ldots, d \quad .$$

The conventional as well as the Wigner-Seitz primitive cell is a cube of side-length a shown in figure D.1 for three dimensions.

The tight-binding dispersion relation for nearest neighbor hopping only reads

$$t^{sc}_{\underline{k}} = -2t \sum_{i=1}^{d} \cos(ak_i) \quad , \qquad -\pi/a \leq k_i \leq \pi/a \quad . \tag{D.1}$$

Including a next-nearest neighbor hopping matrix element t' along the diagonals of the faces of the cube, the dispersion relation acquires an additional term,

$$t^{scnnn}_{\underline{k}} = -2t \sum_{i=1}^{d} \cos(ak_i) - 4t' \sum_{i,j=1;i<j}^{d} \cos(ak_i)\cos(ak_j) \quad , \qquad -\pi/a \leq k_i \leq \pi/a \quad . \tag{D.2}$$

The Fermi surface FS, defined through

$$FS = \{\underline{k}_F \,:\, \epsilon + t_{\underline{k}_F} \stackrel{!}{=} 0\} \quad , \tag{D.3}$$

where ϵ represents a one-particle level determined by the filling factor, is shown for two characteristic cases of (D.1) and (D.2) and $\epsilon = 0$ in figure D.2(a) (left and right graph, respectively).

The the dispersion relation, evaluated along a loop in the Brillouin zone, as well as the density of state,

$$\rho^0(\omega) = \frac{1}{N_0} \sum_{\underline{k}} \delta(\omega - t_{\underline{k}}) \tag{D.4}$$

are shown in figure D.3 for two and three dimensions.

Body-Centered Cubic Lattice

The body-centered cubic (BCC) lattice in three dimensions is a Bravais lattice formed with the primitive vectors

$$\underline{a}_1 = a\,\underline{e}_1\ , \quad \underline{a}_2 = a\,\underline{e}_2\ , \quad \underline{a}_3 = \frac{a}{2}\,(\underline{e}_1 + \underline{e}_2 + \underline{e}_3)\ .$$

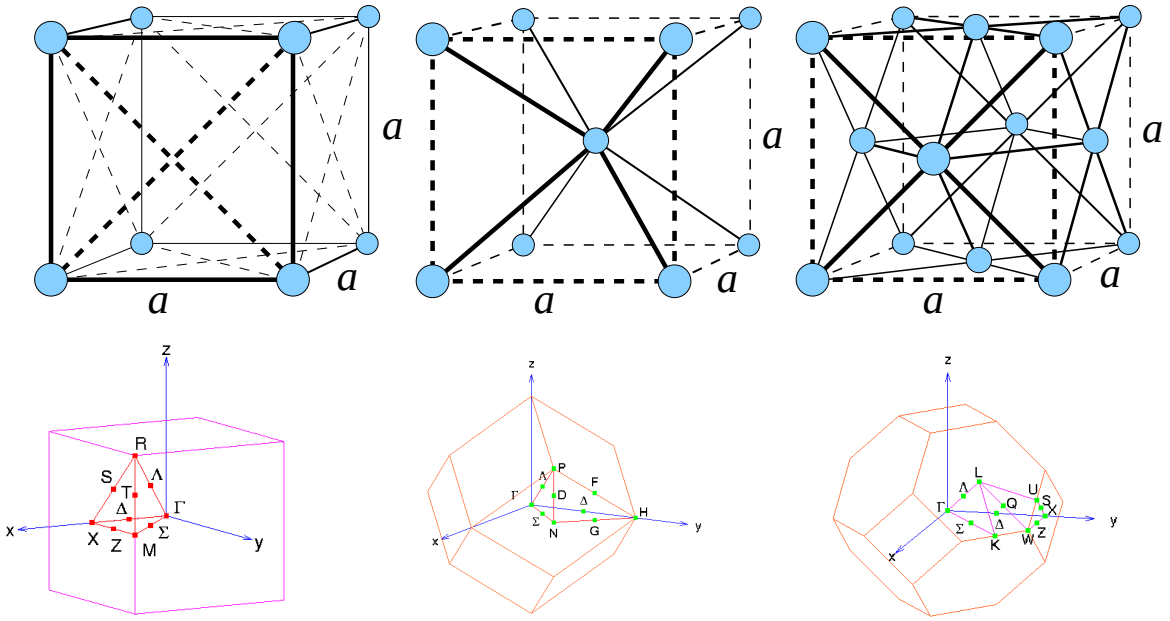

Figure D.1: Lattice structures (top row) and first Brillouin zones for the simple cubic (left), body-centered cubic (middle), and face-centered cubic (right) lattice. In the pictures for the lattice structure (top), solid lines indicate the nearest neighbor hopping matrix element t, while dashed lines indicate the next-nearest neighbor hopping matrix element t'. In the Brillouin zones symmetry points are shown as well.

Including only a nearest neighbor hopping matrix element t this lattice is bipartite and the corresponding tight-binding dispersion relation in d dimensions reads

$$t^{bcc}_{\underline{k}} = -8t \prod_{i=1}^{d} \cos(k_i a/2) \quad , \qquad -2\pi/a \leq k_i \leq 2\pi/a \quad . \tag{D.5}$$

Taking an additional next-nearest neighbor hopping t' along the edges of the cube into account, this lattice in no longer bipartite and the tight-binding dispersion relation is given by

$$t^{bccsc}_{\underline{k}} = -8t \prod_{i=1}^{d} \cos(k_i a/2) - 2t' \sum_{i=1}^{d} \cos(a k_i) \quad , \qquad -2\pi/a \leq k_i \leq 2\pi/a \quad . \tag{D.6}$$

The Fermi surfaces, tight binding DOS and dispersions are shown in figures D.2 and D.3.

Face-Centered Cubic Lattice

The face-centered cubic (FCC) lattice in three dimensions is a Bravais lattice formed with the primitive vectors

$$\underline{a}_1 = \frac{a}{2}\left(\underline{e}_1 + \underline{e}_2\right) \ , \quad \underline{a}_2 = \frac{a}{2}\left(\underline{e}_1 + \underline{e}_3\right) \ , \quad \underline{a}_3 = \frac{a}{2}\left(\underline{e}_2 + \underline{e}_3\right) \ .$$

Including only nearest neighbor hopping t, the FCC lattice is non-bipartite.

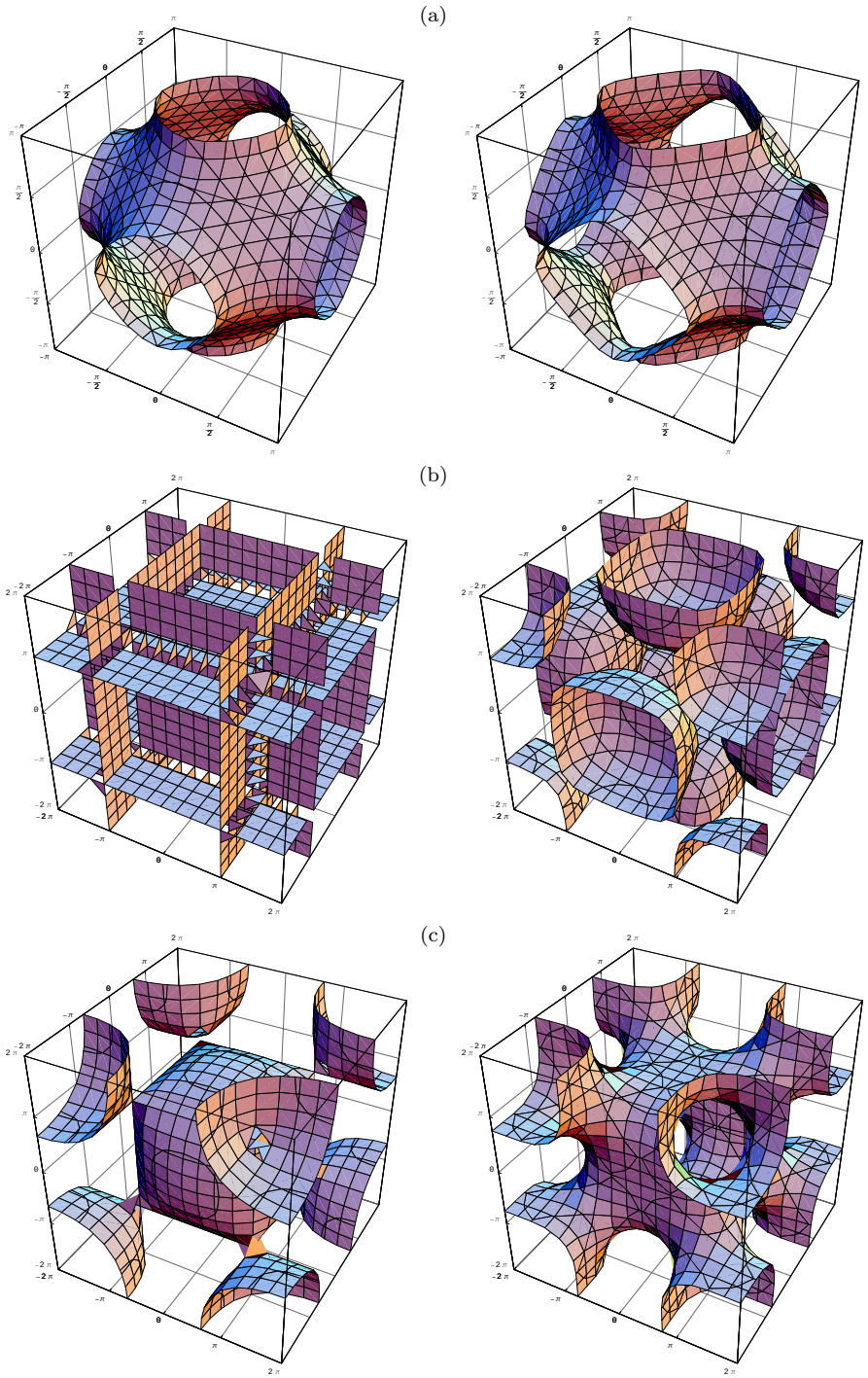

Figure D.2: Fermi surfaces for the three types of cubic lattices in three dimensions: (a) simple cubic, without (left) and with (right) next-nearest neighbor hopping $t'/t = -0.2$. (b) body centered cubic, without (left) and with (right) next-nearest neighbor hopping $t'/t = -0.2$. (c) face centered cubic, without (left) and with (right) next-nearest neighbor hopping $t'/t = 0.4$.

The tight-binding dispersion relation in d dimensions reads

$$t_{\underline{k}}^{fcc} = -4t \sum_{i,j=1;j<i}^{d} \cos(k_i a/2)\, \cos(k_j a/2) \quad , \qquad -2\pi/a \leq k_i \leq 2\pi/a \quad . \tag{D.7}$$

Taking an additional next-nearest neighbor hopping t' along the edges of the cube into account the tight-binding dispersion relation gets modified to

$$t_{\underline{k}}^{fccsc} = -4t \sum_{i,j=1;j<i}^{d} \cos(k_i a/2)\, \cos(k_j a/2) - 2t' \sum_{i=1}^{d} \cos(a k_i) \quad , \qquad -2\pi/a \leq k_i \leq 2\pi/a \quad . \tag{D.8}$$

The Fermi surfaces, tight-binding DOS and dispersions are shown in figures D.2 and D.3.

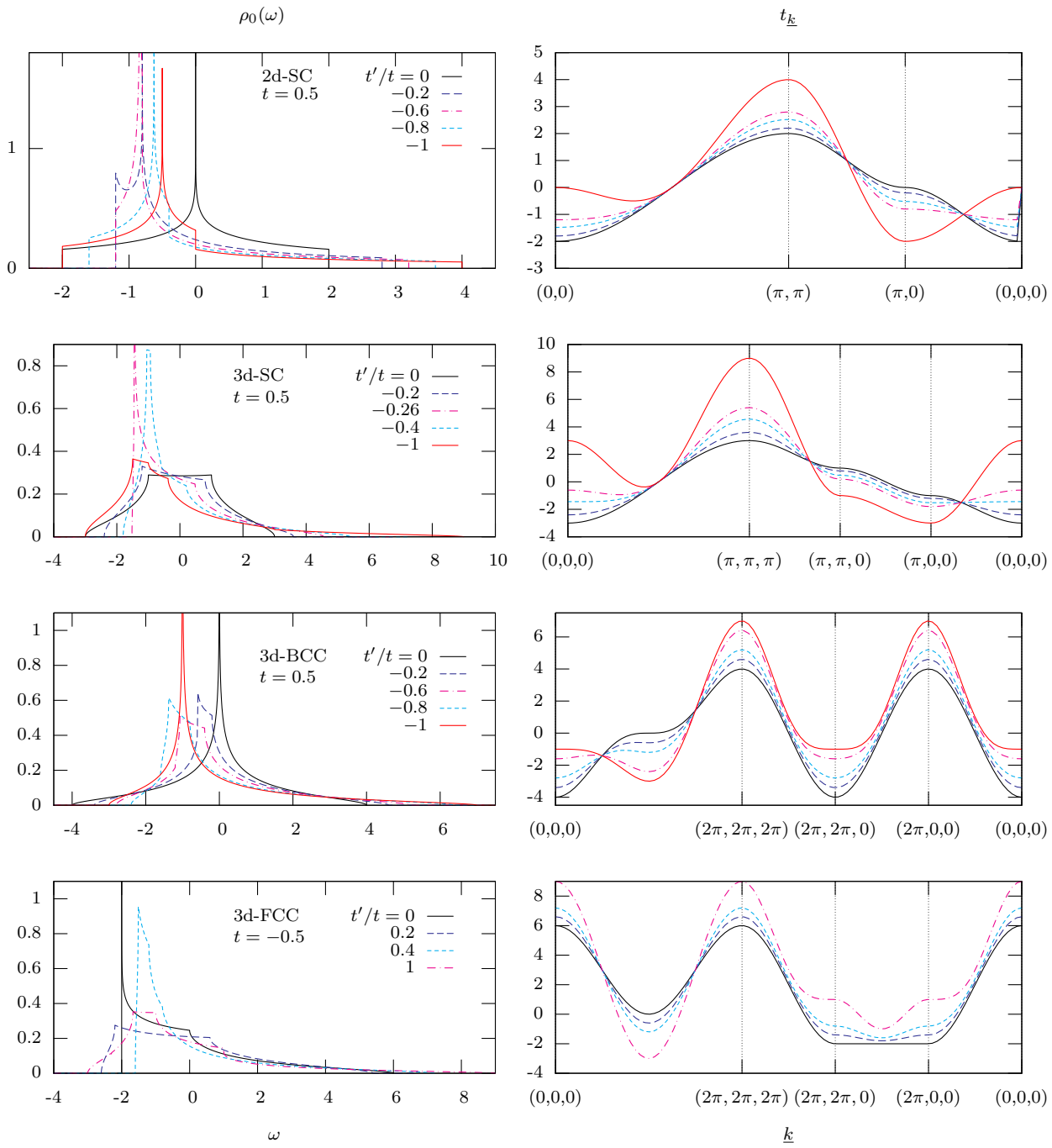

Figure D.3: Free density of states (left) and the associated dispersion relation $t_{\underline{k}}$ along a loop in the Brillouin zone (right) for the two-dimensional simple cubic (2d-SC), the three-dimensional simple cubic (3d-SC), the three-dimensional body centered cubic (3d-BCC) and the three-dimensional face centered cubic (3d-FCC) lattices for various next nearest neighbor hoppings t'.

Bibliography

[And61] P. W. Anderson, Phys. Rev. **124**(1), 41 (1961).

[And78] P. W. Anderson, Rev. Mod. Phys. **50**(2), 191 (1978).

[And83] N. Andrei, K. Furuya, and J. H. Lowenstein, Rev. Mod. Phys. **55**(2), 331 (1983).

[And95] F. B. Anders, J. Phys.: Condens. Matter **7**, 2801 (1995).

[And04] F. B. Anders, *On Wilson's Numerical Renormalization Group*, Lecture notes, Universität Bremen (2004).

[Ari00] R. Arita, S. Onoda, K. Kuroki, and H. Aoki, J. Phys. Soc. Jpn. **69**(3), 785 (2000).

[Ari06] D. N. Aristov and G. Khaliullin, Phys. Rev. B **74**(4), 045124 (2006).

[Aue98] A. Auerbach, *Interacting Electrons and Quantum Magnetism*, Springer-Verlag (1998).

[Bae95] D. Baeriswyl, D. K. Campbell, J. M. P. Carmelo, F. Guinea, and E. Louis (editors), *The Hubbard Model: Its Physics and its Mathematical Physics*, Springer-Verlag (1995).

[Bay61] G. Baym and L. P. Kadanoff, Phys. Rev. **124**(2), 287 (1961).

[Bay62] G. Baym, Phys. Rev. **127**(4), 1391 (1962).

[Bic87] N. E. Bickers, Rev. Mod. Phys. **59**(4), 845 (1987).

[Bic89a] N. E. Bickers and D. J. Scalapino, Ann. Phys. (N.Y.) **193**(1), 206 (1989).

[Bic89b] N. E. Bickers, D. J. Scalapino, and S. R. White, Phys. Rev. Lett. **62**(8), 961 (1989).

[Bic91] N. E. Bickers and S. R. White, Phys. Rev. B **43**(10), 8044 (1991).

[Bra89] U. Brandt and C. Mielsch, Z. Phys. B **75**(3), 365 (1989).

[Bra90] U. Brandt and C. Mielsch, Z. Phys. B **79**(2), 295 (1990).

[Bra91] U. Brandt and C. Mielsch, Z. Phys. B **82**(1), 37 (1991).

[Bru97] T. Brunner and D. C. Langreth, Phys. Rev. B **55**(4), 2578 (1997).

[Bul90] G. Bulk and R. J. Jelitto, Phys. Rev. B **41**(1), 413 (1990).

[Bul97] R. Bulla, T. Pruschke, and A. Hewson, J. Phys.: Condens. Matter **9**(47), 10463 (1997).

[Bul99] R. Bulla, Phys. Rev. Lett. **83**(1), 136 (1999).

[Bul01] R. Bulla, T. A. Costi, and D. Vollhardt, Phys. Rev. B **64**(4), 045103 (2001).

[Bul08] R. Bulla, T. Costi, and T. Pruschke, Rev. Mod. Phys. **80**, 395 (2008).

[Cit97] R. Citro and M. Marinaro, Z. Phys. B **103**(2), 153 (1997).

[Coj93] S. P. Cojocaru and V. A. Moskalenko, Theor. Math. Phys. **97**(2), 1290 (1993).

[Col84] P. Coleman, Phys. Rev. B **29**(6), 3035 (1984).

[Col07] P. Coleman, *Handbook of Magnetism and Advanced Magnetic Materials*, volume 1, John Wiley & Sons, Ltd. (2007), (preprint http://archiv.org/abs/cond-mat/0612006).

[Cox98] D. L. Cox and A. Zawadowski, Adv. Phys. **47**(5), 599 (1998).

[Dar00] A.-M. Daré and G. Albinet, Phys. Rev. B **61**(7), 4567 (2000).

[Dom74] C. Domb and M. S. Green (editors), *Phase transitions and critical phenomena*, volume 3, Academic Press, London (1974).

[Don74] S. Doniach and E. H. Sondheimer, *Green's Functions for Solid State Physicists*, W. A. Benjamin, Inc (1974).

[Eme90] V. J. Emery, S. A. Kivelson, and H. Q. Lin, Phys. Rev. Lett. **64**(4), 475 (1990).

[Ere01] M. Eremin, I. Eremin, and S. Varlamov, Phys. Rev. B **64**(21), 214512 (2001).

[Faz99] P. Fazekas, *Lecture Notes on Electron Correlation and Magnetism*, volume 5 of *Series in Modern Condensed Matter Physics*, World Scientific, Singapore (1999).

[Fre95] J. K. Freericks and M. Jarrell, Phys. Rev. Lett. **74**(1), 186 (1995).

[Fro91] H. O. Frota, Phys. Rev. B **44**(16), 8433 (1991).

[Ful91] P. Fulde, *Electron Correlations on Molecules and Solids*, Springer Verlag, Berlin (1991).

[Geb97] F. Gebhard, *The Mott Metal-Insulator Transition*, Springer Tracts in Modern Physics, Springer, Berlin (1997).

[Geo93] A. Georges and W. Krauth, Phys. Rev. B **48**(10), 7167 (1993).

[Geo96] A. Georges, G. Kotliar, W. Krauth, and M. J. Rozenberg, Rev. Mod. Phys. **68**(1), 13 (1996).

[Gou96] G. Goulb and C. V. Loan, *Matrix Computations*, Johns Hopkins Studies in Mathematical Science, The Johns Hopkins University Press, London, 3rd edition (1996).

[Gre81] N. Grewe and H. Keiter, Phys. Rev. B **24**(8), 4420 (1981).

[Gre83] N. Grewe, Z. Phys. B **53**(4), 271 (1983).

[Gre87] N. Grewe, Z. Phys. B **67**(3), 323 (1987).

[Gre88] N. Grewe, T. Pruschke, and H. Keiter, Z. Phys. B **71**(1), 75 (1988).

[Gre91] N. Grewe and F. Steglich, *Handbook on the Physics and Chemistry of Rare Earths*, volume 14, p. 343, North-Holland (1991).

[Gre96] N. Grewe, *Eine lokale Theorie des Festkörpers* (1996), internal Report.

[Gre08] N. Grewe, S. Schmitt, T. Jabben, and F. B. Anders, J. Phys.: Condens. Matter **20**, 365217 (2008).

[Gut63] M. C. Gutzwiller, Phys. Rev. Lett. **10**(5), 159 (1963).

[Hal94] E. Halvorsen and G. Czycholl, J. Phys.: Condens. Matter **6**, 10331 (1994).

[Han96] T. Hanisch, *Gitterabhängigkeit des Ferromagnetismus im Hubbad-Modell*, Ph.D. thesis, Universität zu Köln, Köln (1996).

[Han97] T. Hanisch, G. S. Uhrig, and E. Müller-Hartmann, Phys. Rev. B **56**(21), 13960 (1997).

[Hau01] K. Haule, S. Kirchner, J. Kroha, and P. Wölfle, Phys. Rev. B **64**(15), 155111 (2001).

[Hau03] K. Haule, A. Rosch, J. Kroha, and P. Wölfle, Phys. Rev. B **68**(15), 155119 (2003).

[Her97] T. Herrmann and W. Nolting, J. Magn. Magn. Mater. **170**(3), 253 (1997).

[Hew93] A. C. Hewson, *The Kondo Problem to Heavy Fermions*, Cambridge University Press, Cambridge (1993).

[Hir87] J. E. Hirsch, Phys. Rev. B **35**(4), 1851 (1987).

[Hon96] S.-P. Hong, H. Doh, and S.-H. S. Salk, Czech. J. Phys. **46**(4), 1855 (1996).

[Hor85a] B. Horvatic and V. Zlatic, J. Phys. **46**, 1459 (1985).

[Hor85b] B. Horvatic and V. Zlatic, Solid State Commun. **54**(11), 957 (1985).

[Hub63] J. Hubbard, Proc. Roy. Soc. A **276**, 238 (1963).

[Hub64a] J. Hubbard, Proc. Roy. Soc. A **277**, 237 (1964).

[Hub64b] J. Hubbard, Proc. Roy. Soc. A **281**, 401 (1964).

[Hub65] J. Hubbard, Proc. Roy. Soc. A **285**, 542 (1965).

[Hub67] J. Hubbard, Proc. Roy. Soc. A **296**, 82 (1967).

[Hus01] C. Huscroft, M. Jarrell, T. Maier, S. Moukouri, and A. N. Tahvildarzadeh, Phys. Rev. Lett. **86**, 139 (2001).

[Jar91a] M. Jarrell, J. Gubernatis, R. N. Silver, and D. S. Sivia, Phys. Rev. B **43**(1), 1206 (1991).

[Jar91b] M. Jarrell, J. E. Gubernatis, and R. N. Silver, Phys. Rev. B **44**(10), 5347 (1991).

[Jar92] M. Jarrell, Phys. Rev. Lett. **69**(1), 168 (1992).

[Jar93] M. Jarrell and T. Pruschke, Z. Phys. B **90**, 187 (1993).

[Jar95] M. Jarrell, Phys. Rev. B **51**(12), 7429 (1995).

[Jar01] M. Jarrell, T. Maier, M. Hettler, and A. Tahvildarzadeh, Europhys. Lett. **56**(4), 563 (2001).

[Kan63] J. Kanamori, Prog. Theor. Phys. **30**(3), 275 (1963).

[Kan96] K. Kang and B. I. Min, Phys. Rev. B **54**(3), 1645 (1996).

[Kar05] M. Karski, C. Raas, and G. S. Uhrig, Phys. Rev. B **72**(11), 113110 (2005).

[Kar08] M. Karski, C. Raas, and G. S. Uhrig, Phys. Rev. B **77**(7), 075116 (2008).

[Kaw81] N. Kawakami and A. Okiji, Phys. Lett. A **9**(14), 483 (1981).

[Kaw83] N. Kawakami and A. Okiji, Solid State Commun. **43**(6), 467 (1983).

[Kei70] H. Keiter and J. C. Kimball, Phys. Rev. Lett. **25**(10), 672 (1970).

[Kei71a] H. Keiter and J. C. Kimball, J. Appl. Phys. **42**(4), 1460 (1971).

[Kei71b] H. Keiter and J. C. Kimball, Int. J. Magn. **1**, 233 (1971).

[Kei84] H. Keiter and G. Morandi, Phys. Rep. **109**(5), 227 (1984).

[Kei85] H. Keiter, Z. Phys. B **60**(2-4), 337 (1985).

[Kei90] H. Keiter and Q. Qin, Z. Phys. B **79**(3), 397 (1990).

[Kha96] G. Khaliullin and P. Horsch, Phys. Rev. B **54**(14), R9600 (1996).

[Kim90] C.-I. Kim, Y. Kuramoto, and T. Kasuya, J. Phys. Soc. Jpn. **59**(7), 2414 (1990).

[Kla98] K. Kladko and P. Fulde, Int J. Quantum Chem. **66**(5), 377 (1998).

[Km80a] H. R. Krishna-murthy, J. W. Wilkins, and K. G. Wilson, Phys. Rev. B **21**(3), 1003 (1980).

[Km80b] H. R. Krishna-murthy, J. W. Wilkins, and K. G. Wilson, Phys. Rev. B **21**(3), 1044 (1980).

[Koj84] H. Kojima, Y. Kuramoto, and M. Tachiki, Z. Phys. B **54**(4), 293 (1984).

[Kol05] W. Koller, A. C. Hewson, and D. Meyer, Phys. Rev. B **72**(4), 045117 (2005).

[Kro97] J. Kroha, P. Wölfle, and T. A. Costi, Phys. Rev. Lett. **79**(2), 261 (1997).

[Kro05] J. Kroha and P. Wölfle, J. Phys. Soc. Jpn. **74**(1), 16 (2005), (preprint at http://arxiv.org/abs/cond-mat/0410273v2).

[Kub62] R. Kubo, J. Phys. Soc. Jpn. **17**(7), 1100 (1962).

[Kur83] Y. Kuramoto, Z. Phys. B **53**, 37 (1983).

[Kur84] Y. Kuramoto and H. Kojima, Z. Phys. B **57**, 95 (1984).

[Kur85a] Y. Kuramoto, in T. Kasuka and T. Saso (editors), *Theory of heavy fermions and valence fluctuation*, volume 62 of *Springer series in solid state sciences*, pp. 152–161, Springer, Berlin (1985).

[Kur85b] Y. Kuramoto and C. Horie, J. Magn. Magn. Mater. **47-48**, 343 (1985).

[Kur85c] Y. Kuramoto and E. Müller-Hartmann, J. Magn. Magn. Mater. **52**(1-4), 122 (1985).

[Kyu07] B. Kyung, Phys. Rev. B **75**(3), 033102 (2007).

[Lan66] D. C. Langreth, Phys. Rev. **150**(2), 516 (1966).

[Lee87] P. A. Lee and N. Read, Phys. Rev. Lett. **58**(25), 2691 (1987).

[Li08] G. Li, H. Lee, and H. Monien, arXiv:0804.3043v1 (2008).

[Lie68] E. H. Lieb and F. Wu, Phys. Rev. Lett. **20**(25), 1445 (1968).

[Lie03] E. H. Lieb and F. Y. Wu, Physica A **321**, 1 (2003).

[Lut60a] J. M. Luttinger, Phys. Rev. **119**(4), 1153 (1960).

[Lut60b] J. M. Luttinger and J. C. Ward, Phys. Rev. **118**(5), 1417 (1960).

[Lut61] J. M. Luttinger, Phys. Rev. **121**(4), 942 (1961).

[Mac06a] A. Macridin, M. Jarrell, and T. Maier, Phys. Rev. B **74**(8), 085104 (2006).

[Mac06b] A. Macridin, M. Jarrell, T. Maier, P. R. C. Kent, and E. D'Azevedo, Phys. Rev. Lett. **97**(3), 036401 (2006).

[Mai05] T. Maier, M. Jarrell, T. Pruschke, and M. H. Hettler, Rev. Mod. Phys. **77**(3), 1027 (2005).

[Man04] D. Manske, *Theory of Unconventional Superconductors: Cooper-Pairing Mediated by Spin Excitations*, volume 202 of *Springer Tracts in Modern Physics*, Springer, Berlin (2004).

[Mer06] J. Merino, B. J. Powell, and R. H. McKenzie, Phys. Rev. B **73**(23), 235107 (2006).

[Met89] W. Metzner and D. Vollhardt, Phys. Rev. Lett. **62**(3), 324 (1989).

[Met91] W. Metzner, Phys. Rev. B **43**(10), 8549 (1991).

[MH84] E. Müller-Hartmann, Z. Phys. B **57**(4), 281 (1984).

[MH89a] E. Müller-Hartmann, Z. Phys. B **74**(4), 507 (1989).

[MH89b] E. Müller-Hartmann, Z. Phys. B **76**(2), 211 (1989).

[MH95] E. Müller-Hartmann, J. Low Temp. Phys. **99**(3-4), 349 (1995).

[Mie93] A. Mielke and H. Tasaki, Commun. Math. Phys. **158**(2), 341 (1993), (preprint http://arxiv.org/abs/cond-mat/9305026).

[Mos97a] V. A. Moskalenko, Theor. Math. Phys. **110**(2), 243 (1997).

[Mos97b] V. A. Moskalenko and N. M. Plakida, Theor. Math. Phys. **113**(1), 1309 (1997).

[Mos98] V. A. Moskalenko, Theor. Math. Phys. **116**(3), 1094 (1998).

[Nag65] Y. Nagaoka, Solid State Commun. **3**, 409 (1965).

[Nag66] Y. Nagaoka, Phys. Rev. **147**(1), 392 (1966).

[Neg88] J. W. Negele and H. Orland, *Quantum Many-Particle Systems*, Frontiers in Physics, Addison-Wesley, New York (1988).

[Noz75] P. Nozières, J. Low Temp. Phys. **17**(1-2), 31 (1975).

[Obe97] T. Obermeier, T. Pruschke, and J. Keller, Phys. Rev. B **56**(14), R8479 (1997).

[Oki83a] A. Okiji and N. Kawakami, Solid State Commun. **43**(5), 365 (1983).

[Oki83b] A. Okiji and N. Kawakami, Phys. Rev. Lett. **50**(15), 1157 (1983).

[Ots06a] J. Otsuki and Y. Kuramoto, J. Phys. Soc. Jpn. **75**, 064707 (2006), (preprint http://arxiv.org/abs/cond-mat/0602584).

[Ots06b] J. Otsuki, H. Kusunose, and Y. Kuramoto, J. Phys. Soc. Jpn. Suppl. **75**, 256 (2006), (preprint http://arxiv.org/abs/cond-mat/0510424).

[Pan07] S. Pandey and A. Singh, Phys. Rev. B **75**(6), 064412 (2007).

[Pen66] D. R. Penn, Phys. Rev. **142**(2), 350 (1966).

[Pen96] K. Penc, H. Shiba, F. Mila, and T. Tsukagoshi, Phys. Rev. B **54**(6), 4056 (1996).

[Pet06] R. Peters, T. Pruschke, and F. B. Anders, Phys. Rev. B **74**(24), 245114 (2006).

[Pie96] P. Pieri, S. Daul, D. Baeriswyl, M. Dzierzawa, and P. Fazekas, Phys. Rev. B **54**(13), 9250 (1996).

[Pie99] R. Pietig, R. Bulla, and S. Blawid, Phys. Rev. Lett. **82**(20), 4046 (1999).

[Pru89] T. Pruschke and N. Grewe, Z. Phys. B **74**, 439 (1989).

[Pru93] T. Pruschke, D. L. Cox, and M. Jarrell, Phys. Rev. B **47**(7), 3553 (1993).

[Pru95] T. Pruschke, M. Jarrell, and J. Freericks, Adv. Phys. **44**, 187 (1995).

[Pru01] T. Pruschke, W. Metzner, and D. Vollhardt, J. Phys.: Condens. Matter **13**, 9455 (2001).

[Pru03] T. Pruschke and R. Zitzler, J. Phys.: Condens. Matter **15**, 7867 (2003).

[Pru05] T. Pruschke, Prog. Theor. Phys. Suppl. **160**, 274 (2005).

[Row68] D. J. Rowe, Rev. Mod. Phys. **40**(1), 153 (1968).

[Rus74] G. Rushbrooke, G. Baker, and P. Wood, in C. Domb and M. Green (editors), *Phase Transitions and Critical Phenomena*, volume 3, p. 245, Academic Press, London, New York (1974).

[Saa00] Y. Saad, *Iterative Methods for Sparse Linear Systems*, Cambridge University Press, 2nd edition (2000).

[Sad05] M. V. Sadovskii, I. A. Nekrasov, E. Z. Kuchinskii, T. Pruschke, and V. I. Anisimov, Phys. Rev. B **72**(15), 155105 (2005).

[Sai97] T. Saikawa, A. Ferraz, P. E. de Brito, and H. Kaga, Phys. Rev. B **56**(8), 4464 (1997).

[Sai98] T. Saikawa and A. Ferraz, Eur. Phys. J. B **3**(1), 17 (1998).

[Sak88] O. Sakai, M. Motizuki, and T. Kasuya, in J. Kanamori and A. Kotani (editors), *Core-Level Spectroscopy in Condensed Systems Theory*, p. 45, Springer, Heidelberg (1988).

[Sak89] O. Sakai, Y. Shimizu, and T. Kasuya, J. Phys. Soc. Jpn. **58**, 3666 (1989).

[Sak05] O. Sakai, Y. Shimizu, and Y. Kaneta, J. Phys. Soc. Jpn. **74**(9), 2517 (2005).

[San93] G. Santoro, M. Airoldi, S. Sorella, and E. Tosatti, Phys. Rev. B **47**(24), 16216 (1993).

[Sas92] T. Saso, Prog. Theor. Phys. Suppl. **108**, 89 (1992).

[Sch66] J. R. Schrieffer and P. A. Wolff, Phys. Rev. **149**(2), 491 (1966).

[Sch83] P. Schlottmann, Phys. Rev. Lett. **50**(21), 1697 (1983).

[Sch99a] S. Schäfer and P. Schuck, Phys. Rev. B **59**(3), 1712 (1999).

[Sch99b] P. Schlottmann, Phys. Rev. B **59**(19), 12379 (1999).

[Sch05] P. Schlottmann, J. Appl. Phys. **97**, 10A917 (2005).

[Ser91] J. W. Serene and D. W. Hess, Phys. Rev. B **44**(7), 3391 (1991).

[She05] A. Sherman and M. Schreiber, Int. J. Mod. Phys. B **19**(13), 2145 (2005).

[She06] A. Sherman, Phys. Rev. B **73**(15), 155105 (2006).

[She07] A. Sherman and M. Schreiber, Phys. Rev. B **76**(24), 245112 (2007).

[She08] A. Sherman and M. Schreiber, Physical Review B (Condensed Matter and Materials Physics) **77**(15), 155117 (2008).

[Shi75] H. Shiba, Prog. Theor. Phys. **54**(4), 967 (1975).

[Shi76] H. Shiba, J. Low Temp. Phys. **25**(5-6), 587 (1976).

[Ste01] G. R. Stewart, Rev. Mod. Phys. **73**(4), 797 (2001).

[Tas92] H. Tasaki, Phys. Rev. Lett. **69**(10), 1608 (1992).

[Tas98a] H. Tasaki, Prog. Theor. Phys. **99**(4), 489 (1998).

[Tas98b] H. Tasaki, J. Phys.: Condens. Matter **10**, 4353 (1998).

[Tsv83a] A. Tsvelick and P. Wiegmann, Adv. Phys. **32**(4), 453 (1983).

[Tsv83b] A. M. Tsvelick and P. B. Wiegmann, J. Phys. C **16**(12), 2321 (1983).

[TZ97] A. N. Tahvildar-Zadeh, J. K. Freericks, and M. Jarrell, Phys. Rev. B **55**(2), 942 (1997).

[Uld05] A. Uldry and R. J. Elliott, J. Phys.: Condens. Matter **17**, 2903 (2005).

[Ulm98] M. Ulmke, Eur. Phys. J. B **1**, 301 (1998).

[Vak90] S. I. Vakaru, M. I. Vladimir, and V. A. Moskalenko, Theor. Math. Phys. **85**(2), 1185 (1990).

[Var02] C. Varma, Z. Nussinov, and W. van Saarloos, Phys. Rep. **361**(5-6), 267 (2002).

[Vil94a] Y. M. Vilk, L. Chen, and A.-M. S. Tremblay, Phys. Rev. B **49**(18), 13267 (1994).

[Vil94b] Y. M. Vilk, L. Chen, and A.-M. S. Tremblay, Physica C **235-240**, 2235 (1994).

[Vil97] Y. Vilk and A. Tremblay, J. Phys. I **7**, 1309 (1997).

[Vir90] A. Virosztek and J. Ruvalds, Phys. Rev. B **42**(7), 4064 (1990).

[Vis74] P. B. Visscher, Phys. Rev. B **10**(3), 943 (1974).

[Vla90] M. I. Vladimir and V. A. Moskalenko, Theor. Math. Phys. **82**(3), 301 (1990).

[Voi95] Voit, Rep. Prog. Phys **58**, 977 (1995).

[Vol99] D. Vollhardt, N. Blümer, K. Held, M. Kollar, J. Schlipf, M. Ulmke, and J. Wahle, Advances in Solid State Physics **38**, 383 (1999).

[Wah98] J. Wahle, N. Blümer, J. Schlipf, K. Held, and D. Vollhardt, Phys. Rev. B **58**, 12749 (1998).

[Whi83] R. M. White, *Quantum Theory of Magnetism*, Springer, 2nd edition (1983).

[Wie83] P. B. Wiegmann and A. M. Tsvelick, J. Phys. C **16**(12), 2281 (1983).

[Wil75] K. G. Wilson, Rev. Mod. Phys. **47**(4), 773 (1975).

[Wis07] F. Wissel, *Transient and Stationary Properties of the Olami-Feder-Christensen Earthquake Model in One and Two Dimensions.*, Ph.D. thesis, TU Darmstadt (2007).

[Yus07] V. Yushankhai, A. Yaresko, P. Fulde, and P. Thalmeier, Phys. Rev. B **76**(8), 085111 (2007).

[Zit02] R. Zitzler, T. Pruschke, and R. Bulla, Eur. Phys. J. B **27**(4), 473 (2002).

[Zit04a] R. Zitzler, *Magnetic Properties of the One-Band Hubbard Model*, Ph.D. thesis, Mathematisch-Naturwissenschaftlichen Fakultät der Universität Augsburg (2004).

[Zit04b] R. Zitzler, N.-H. Tong, T. Pruschke, and R. Bulla, Phys. Rev. Lett. **93**(1), 016406 (2004).

[Zla90] V. Zlatić and B. Horvatić, Solid State Commun. **75**(3), 263 (1990).

Acknowledgment

This work would not have been possible without the assistance and help of several people.

First of all I would like to thank Professor Grewe for giving me the opportunity to work on this subject, the stimulating discussions and his continuous interest. Without his enduring urge to get to the bottom of things and to reconsider the basics, I would probably still be chasing rainbows.

I am especially indebted to Torben Jabben, with whom I had uncountably many fruitful discussions and who was a constant source of inspiration. Additionally, he was the one to bring the incredibly powerful numerical library *numpkg* into existence, without which my poor attempts to assemble some usable and efficient code would have been doomed to fail.

Pretty much the same is true for Eberhard Jakobi, who contributed a great deal to that library and also was always eager to engage in a discussion.

And certainly both friends were responsible for the pleasant atmosphere during the daily grind in the institute.

I would also like to thank Frithjof Anders for setting me up with his NRG-code and always being available for questions.

I must not fail to mention Felix Wissel. Apart from being the second-best "Muffgenosse in the whole Muff"[Wis07, page 130], his company during the last years and friendship means a lot to me.

I want to truly thank my parents, my brother and sisters and family Eilks for their enduring and unconditional support.

Most of all, I am infinitely grateful for the love and caring of Frauke Eilks, who suffered through this with me. She contributed a lot to this work and without her, I wouldn't have made it.

That's all, folks!

Lebenslauf

Name	Karl Sebastian Schmitt
Geburtsdatum	17. 12. 1975
Geburtsort	Bensheim
Familienstand	ledig

1982-1986	Joseph Heckler Grundschule in Bensheim
1986-1995	Altes Kurfürstliches Gymnasium (AKG) Bensheim
1995	Abitur am AKG Bensheim
1995	Beginn des Physik-Studiums an der TH Darmstadt
1995	Beginn des Wehrersatztdienstes beim Technischen Hilfswerk (THW), Ortsverein Bensheim
1997	Vordiplom an der TH Darmstadt
1998-1999	Auslandsstudium an der University of Illinois at Urbana-Champaign, USA
2001-2002	Diplomarbeit in der AG Prof. Grewe am Institut für Festkörperphysik, TU Darmstadt
2002	Ende des Wehrersatzdienstes beim THW Bensheim
2002	Beendigung des Studiums mit dem Abschluss Diplom
seit 2002	Wissenschaftlicher Mitarbeiter am Institut für Festkörperphysik der TU Darmstadt